TECHNISCHE UNIVERSITÄT MÜNCHEN

Max-Planck-Institut für Physik
(Werner-Heisenberg-Institut)

The Galactic Center resolved with MAGIC and a new technique for Atmospheric Calibration

Christian Fruck

Vollständiger Abdruck der von der Fakultät für Physik der Technischen Universität München zur Erlangung des akademischen Grades eines

Doktors der Naturwissenschaften

genehmigten Dissertation.

Vorsitzender:		Univ.-Prof. Dr. A. Ibarra
Prüfer der Dissertation:	1.	Hon.-Prof. A. Caldwell, Ph.D.
	2.	Univ.-Prof. Dr. E. Resconi

Die Dissertation wurde am 23.01.2015 bei der Technischen Universität München eingereicht und durch die Fakultät für Physik am 22.04.2015 angenommen.

Christian Fruck: *The Galactic Center resolved with MAGIC and a new technique for Atmospheric Calibration*, Doktorarbeit,

ABSTRACT

A new method has been developed, which allows for the correction of Imaging Air Cherenkov Telescope (IACT) data regarding the effect of time and altitude dependent atmospheric transmission by using Light Detection And Ranging (LIDAR). This method has been tested by applying it to data of the Crab Nebula observed with MAGIC during adverse atmospheric conditions. A major improvement in the reconstruction of the energy spectra could be achieved, even for observations that were performed with clouds of moderate optical thickness.

The Galactic Center (GC) has been observed with MAGIC at very large zenith distance (Zd). These observations were triggered by reports about a gas cloud, which is very closely approaching the GC super massive black hole (SMBH), giving astronomers a unique chance to study the effect of in-falling matter on the broad band emission of the SMBH. The high Zd dramatically increases the effective collection area, but increases the energy threshold as well. No significant variability could be detected during the first three years of this multi-year observation campaign. Nonetheless, a detailed study of the energy spectrum and morphology of the GC γ-ray source could be performed with 66 h of good quality data. A possible TeV counterpart of the elongated radio source called "the Arc", which is at about 0.2 ° from the GC has been detected. A new method for measuring the energy spectrum of this extended object has therefore been developed. The results indicate a hard γ-ray spectrum for energies between 0.5 TeV and 5 TeV for this new source.

The type Ia supernova SN 2014J has been observed with MAGIC, six days after the explosion. It has been the closest-to-Earth supernova of this type since at least 28 y. No signal could be detected, but it was possible to establish the most stringent upper limits on the direct emission of VHE γ-radiation for type Ia supernovae.

KURZZUSAMMENFASSUNG

In dieser Arbeit wird eine neue Methode vorgestellt, welche es erlaubt, mit Hilfe von Light Detection And Ranging (LIDAR) Messungen, Daten von abbildenden Luftschauer-Tscherenkov Teleskopen (eng. IACT) hinsichtlich des Einflusses der atmosphärischen Transmission zu korrigieren. Diese Methode wurde anhand von Beobachtungen des Krebsnebels, welche in Zeiten widriger Wetterbedingungen durchgeführt wurden, getestet. Sogar bei mäßiger Bewölkung konnte eine signifikante Verbesserung bei der Berechnung des Energiespektrums erzielt werden.

Des Weiteren wurden Beobachtungen des Galaktischen Zentrums mit den MAGIC Teleskopen bei sehr großem Zenitwinkel durchgeführt. Durch die Beobachtung bei großen Zenitwinkeln lässt sich die effektive Detektorfläche drastisch vergrößern, bei ebenfalls steigender Energieschwelle. Die Beobachtungen wurden durch Berichte über eine Gaswolke, welche sich dem Galaktische Zentrum bis auf sehr geringen Abstand nähert, ausgelöst. Dieses Ereignis bietet Astronomen die einmalige Gelegenheit die Auswirkungen von Materie, welche von einem Schwarzen Loch aufgesogen wird, mit Beobachtungen im gesamten elektromagnetischen Spektrum zu studieren. In den ersten drei Jahren dieser auf mehrere Jahre ausgelegten Beobachtungskampagne konnte keine signifikante Veränderung des γ-Strahlungsflusses beobachtet werden. Trotzdem konnten die insgesamt 66 Stunden Beobachtungszeit dazu verwendet werden das Spektrum und die Ausdehnung der Gammastrahlenquelle im Galaktischen Zentrum genau zu studieren. Dabei konnte unter anderem ein Gegenstück zur „Arc" genannten Radioquelle in hochenergetischer Gammastrahlung gefunden werden. Eine neue Methode zur Berechnung von Energiespektren wurde an diesem ausgedehnten Objekt getestet, mit dem Resultat eines harten Gammastrahlungsspektrum zwischen 0.5 TeV und 5 TeV.

Außerdem wurde die Supernova SN 2014J etwa sechs Tage nach ihrer Explosion mit den MAGIC Teleskopen beobachtet. Es handelte sich um die der Erde am nächsten gelegene Supernova vom Typ Ia seit mindestens 28 Jahren. Es konnte zwar keine Gammastrahlung detektiert werden, dennoch konnte mit dieser Messung, für solche Objekte, die bisher niedrigste Obergrenze für die direkte Emission von hochenergetischer Gammastrahlung festgelegt werden.

CONTENTS

LIST OF FIGURES

LIST OF TABLES

ACRONYMS

a.s.l.	above sea level
BH	black hole
CR	cosmic ray
CTA	Cherenkov Telescope Array
FADC	flash analog to digital converter – fast type of analog to digital converter
GC	Galactic Center
GCA	Galactic Center Arc
GDAS	Global Data Assimilation System
GMC	giant molecular cloud
HV	high voltage
IACT	Imaging Air(-shower) Cherenkov Telescope
IC	inverse Compton
LAT	Large Area Telescope, γ-ray telescope on-board the Fermi satellite
LIDAR	light detection and ranging
LoNS	light of night sky
MAGIC	Major Atmospheric Gamma Imaging Cherenkov
ORM	Observatorio del Roque de los Muchachos
PCB	printed circuit board
PDE	photon detection efficiency
PMT	photomultiplier tube
PSF	point spread function – instrumental response to a point source
SED	spectral energy distribution
TS	test statistic
SMBH	super massive black hole – typically BH with several $10^6\,M_\odot$
SN	supernova
SNR	supernova remnant
VHE	very high energy – energy range of IACTs ($\sim 100\,\mathrm{GeV}$ – $\sim 100\,\mathrm{TeV}$)
VHZD	very high zenith distance – used for $Zd > 60\,^\circ$
WC	Winston cone
WIMP	weakly interacting massive particle
Zd	zenith distance

1

GOALS AND STRUCTURE OF THIS THESIS

The first of the two main purposes of this thesis is to get a better understanding of the very high energy (***VHE***) γ-ray emission mechanisms in the Galactic Center (***GC***) region, by observing the GC with the Major Atmospheric Gamma Imaging Cherenkov (***MAGIC***) telescopes. The particle acceleration mechanisms and the γ-ray emission processes close to the GC black hole (***BH***) have been actively discussed in the recent years (Ballantyne et al., 2011; Chernyakova et al., 2011; Fatuzzo & Melia, 2012; Kusunose & Takahara, 2012; Guo et al., 2013). This is because of the availability of *Fermi* data in the GeV regime on one hand, but also because Gillessen et al. (2012) reported a compact gas cloud, approaching very closely the super massive black hole (***SMBH***) at the center of our galaxy. This event presents a unique opportunity for studying accretion and particle acceleration processes close to the event horizon of a SMBH. Observations with ground based Imaging Air Cherenkov Telescopes (***IACT***s), like those forming the basis of studies presented in this thesis, can help exploring such scenarios. The report about the GC observations can be found in chapters 9, 10, 11, and 12.

Apart from pure application of the experimental methods of γ-ray astronomy with IACTs, a lot of effort was made in order to improve the capabilities of these instruments. The second important goal was to develop a technique for correcting IACT data recorded during adverse weather conditions, using the information provided by an elastic low power light detection and ranging (***LIDAR***) system operated alongside with the MAGIC telescopes. Adverse atmospheric conditions, such as clouds and dust in the field of view of the telescope, reduce the useful observation time of MAGIC by a significant amount. Recovering part of that data can help increasing the scientific output of the experiment. In chapters 6, 7, and 8 I will report about this project.

1.1 GALACTIC CENTER OBSERVATIONS WITH MAGIC

The goals for the GC observation campaign are two-fold. The first goal is to search for spectral and flux variability of the γ-ray source associated with the region around the BH at the center of our galaxy, under the influence of possible accretion of material from the gas cloud G2 (Gillessen et al., 2012). For this study, multi-year monitoring of the source with very homogeneous temporal coverage is needed to produce a long-term light-curve of the TeV flux.

Apart from this important study with uncertain outcome, these observations also allow for exploring one of the densest astrophysical environments in our galaxy with one of the most sensitive instruments for VHE γ-ray astronomy. The GC region has already been observed with Cherenkov telescopes before (Enomoto et al., 2003; Kosack et al., 2004; Tsuchiya et al., 2004; Aharonian et al., 2004; Albert et al., 2006; Aharonian et al., 2009; Archer et al., 2014), but the emitting objects and mechanisms are still poorly understood.

The geographic location of the MAGIC telescopes implies observations at large zenith angle. As a result the energy threshold is relatively high, but on the other hand the sensitivity for energies above 1 TeV is significantly increased.

1.2 ATMOSPHERIC CORRECTION STRATEGY FOR MAGIC

With the new LIDAR system, the MAGIC telescopes have support by very powerful instrument for measuring atmospheric back-scattering profiles. In this thesis I pursue two goals which were necessary for making the LIDAR a really useful tool for the MAGIC data analysis.

The first important step was finding an automatic algorithm for extracting atmospheric transmission profiles from the back-scattering data. The next step was applying the transmission profiles to the MAGIC data in order to correct light absorption due to adverse atmospheric conditions. The energy bias, as well as the change of the instrument response (effective collection area), caused by absorbing aerosol layers have to be taken into account for recovering the correct spectrum.

Finally it is very important to test such a method with a well characterized source of VHE γ-radiation. The Crab Nebula is a perfect candidate for testing the capability of the method to reconstruct the original spectrum of a strong, non-variable γ-ray source.

1.3 OUTLINE OF THE THESIS

I am starting this thesis with a short introduction on cosmic rays, high energy astrophysics, and the MAGIC telescopes (part I). The second part (II) deals with the influence of adverse atmospheric conditions on data taken with IACTs. I am presenting methods for measuring variable atmospheric transmission with LIDAR and correcting Cherenkov telescope data accordingly. In part III of this thesis I am presenting the results of the first three years of a multi-year observation campaign targeting the unique event of a gas cloud interacting with the central black hole (BH) of our galaxy. Part IV is summarizing the work presented in this thesis. It is followed by an appendix (V) where, besides a few other auxiliary studies, I am reporting on observations of the closest supernova (***SN***) of type IA since 28 years, using the MAGIC telescopes.

Part I

BACKGROUND

The scientific results presented in this thesis are based on a large foundation of standard techniques and knowledge existing inside the MAGIC collaboration and the astrophysical community as a whole. In this part, I will try to give a short overview of the field. It will span from the astrophysical background over to the observational techniques of Cherenkov astronomy, including the acceleration and propagation of energetic particles throughout the Universe.

2

COSMIC RAYS AND HIGH ENERGY ASTROPHYSICS

Cosmic rays were discovered by Victor Hess during balloon flights in 1912. Until the 1950s, when developments in accelerator-physics finally allowed for probing the nuclear energy scale and above, many of the discoveries made in particle physics were based on observations of cosmic rays. Today it is known, that cosmic rays can reach enormous energies of over 10^{20} eV, far from ever being matched by human-made accelerators. Their influence on electronics as well as the human body is well studied, since they pose a threat to all space traveling activities(Cucinotta & Durante, 2006; Fleetwood et al., 2000). Even their influence on cloud formation and therefore on earth's climate is being studied (Carslaw, 2009). However, the most fundamental question is still not fully resolved: Where do they come from?

The definition of the term ***cosmic rays*** throughout literature is not always the same. In this introduction, I will use a very wide definition: All elementary particles and nuclei that reach earth from outside the atmosphere in the form of ionizing radiation. They are either charged particles accelerated in astrophysical sources (primary cosmic rays) or they are produced in interactions of the primary cosmic rays, like for example with magnetic fields or the interstellar medium (secondary cosmic rays). In addition, there is secondary radiation from cosmic ray interaction with the atmosphere. This is what terrestrial instruments usually detect.

The best candidates for cosmic ray accelerators within our galaxy are supernova remnants, interacting with interstellar gas and forming strong shocks (Blasi, 2013). Super massive black holes (SMBHs) in the centers of galaxies are among the most promising candidates for sources of CRs form outside our galaxy. Especially at ultra high energies of $E \approx 10^{20}$ eV the acceleration of atomic nuclei in the magnetospheres of SMBHs seems to be one of the few possible scenarios (Neronov et al., 2009). Unfortunately most active galactic nuclei (AGN) are far away from our galaxy, making it hard to study these processes. One exception is the central BH of our own galaxy, which despite its extremely low luminosity could help shedding light on BH accretion and CR acceleration mechanisms.

In the following sections I will first give a short historical introduction to cosmic ray physics, emphasizing also their importance for the development of fundamental particle physics. This section will then be followed by a short glance at the current status of our scientific knowledge of cosmic ray spectrum and composition.

2.1 HISTORICAL BACKGROUND

Until the early 1910s it was widely believed that ionizing radiation is coming from natural radioactivity only. That would have implied that their intensity decreases with altitude above the surface of the earth. The first measurements, which were performed at lower altitudes, seemed to support this assumption. Then in 1912, Victor Hess performed a series of balloon flights. On his first flight he ascended to 5 300 m altitude. Later in 1913 he went even higher. He was carrying an electroscope and measuring the discharge due to ionizing radiation. From above $\sim$ 1 km on the discharge was increasing significantly with altitude. Based on his observations he concluded that he had detected radiation coming from above, outside the earth's atmosphere. In 1914 Kolhörster was ascending up to 9 km, confirming Hess's results. The name ***cosmic rays*** goes back to Millikan in 1925. In 1936, Hess received the Nobel Prize in Physics for his discovery, which he shared with David Anderson (Longair, 2011).

Also the discovery of many fundamental particles goes back to that times and to cosmic ray research. In 1932, Carl David Anderson discovered the positron, when observing tracks from cosmic ray secondaries with opposite curvature in a cloud chamber (Anderson, 1933). Muons were first observed in 1936 by Anderson and Neddermeyer (Longair, 2011). Later on, also the first barionic and mesonic resonances were discovered in cosmic ray interactions (Rochester & Butler, 1947; Hopper & Biswas, 1950). Studying cosmic rays for the purpose of fundamental particle physics discoveries moved to the background when in the early 1950s the proton synchrotron was invented and could reach center of mass energies of several GeV (Wilson, 1996).

2.2 THE COMPOSITION AND SPECTRUM OF COSMIC RAYS

The differential energy spectrum of cosmic rays impinging on earth's atmosphere up to $\sim$ 1 PeV can be pretty well described by a single power law with a spectral index α of -2.7 (see fig. 2.1).

$$\frac{\mathrm{d}F}{\mathrm{d}E\,\mathrm{d}\Omega} = I_0 \left(\frac{E}{E_0}\right)^{\alpha} = 1.8 \cdot 10^4 \left(\frac{E}{\mathrm{GeV}}\right)^{-2.7} \mathrm{m}^{-2}\mathrm{s}^{-1}\mathrm{sr}^{-1}\mathrm{GeV}^{-1} \qquad (2.2.1)$$

For energies below 10 GeV, the cosmic ray flux is not constant, but depends on the solar activity. At energies between 1 and 10 PeV, the spectral index changes from -2.7 to about -3. This feature is also known as the knee of the cosmic ray spectrum. At energies above 1 EeV, the spectrum is again hardening a bit, a feature also known as the ankle of the CR spectrum (Beringer et al., 2012). The hadronic component of the cosmic ray flux at a given energy consists of 79% protons, 15% helium and heavier nuclei. The elemental distribution is relatively similar to the abundance of elements in the solar system, with higher values, where the abundance in the solar system is very low (fig. 2.2 (b)) (Simpson, 1983). The spectra of the different hadronic components of

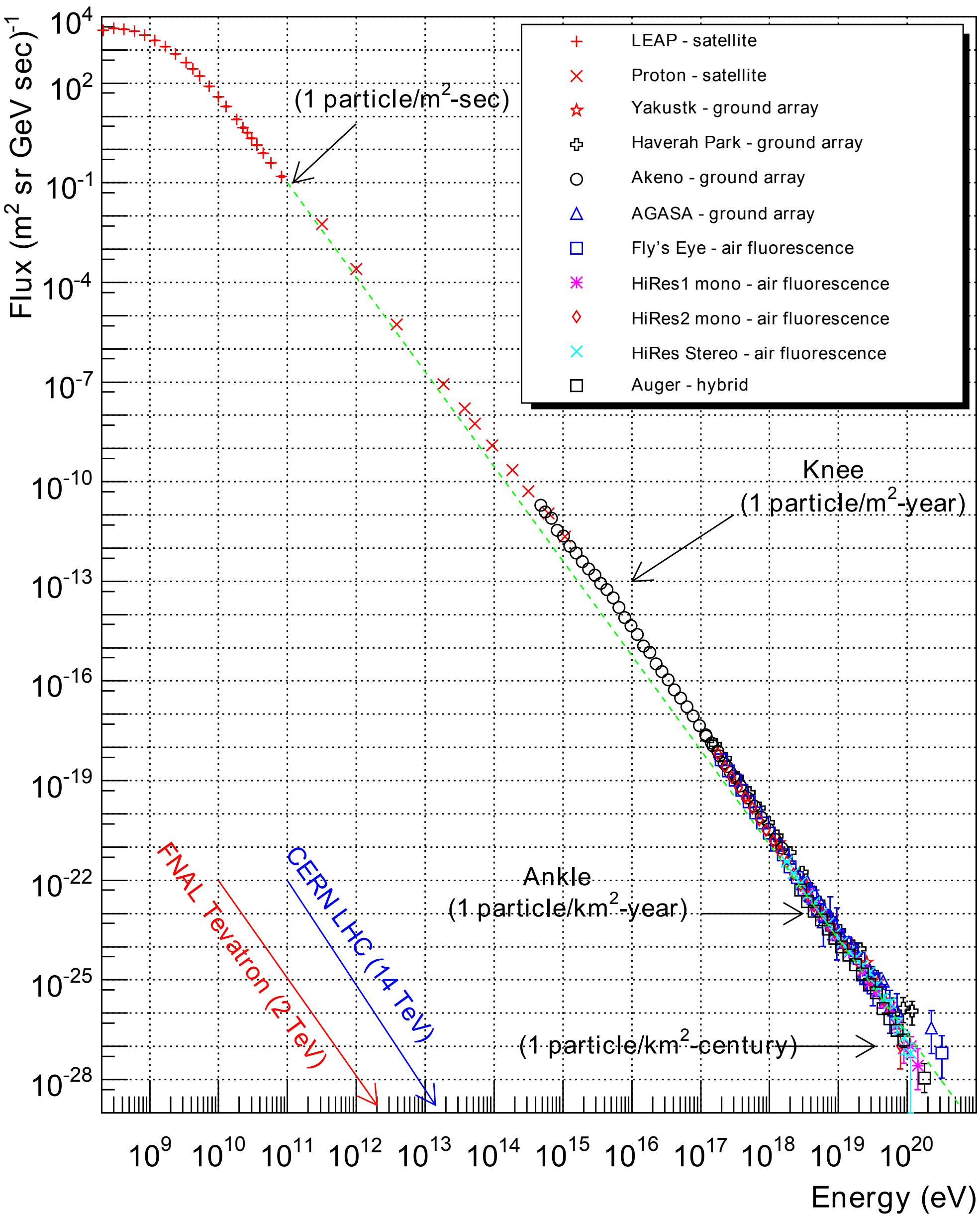

Figure 2.1: Cosmic ray spectrum over 12 orders of magnitude in energy and 30 orders of magnitude in differential flux, measured with different instruments, ground based as well as space borne (Hanlon, 2013). The overall spectral shape can be reasonably well described by a single power law with spectral index −2.7 for nearly the whole range.

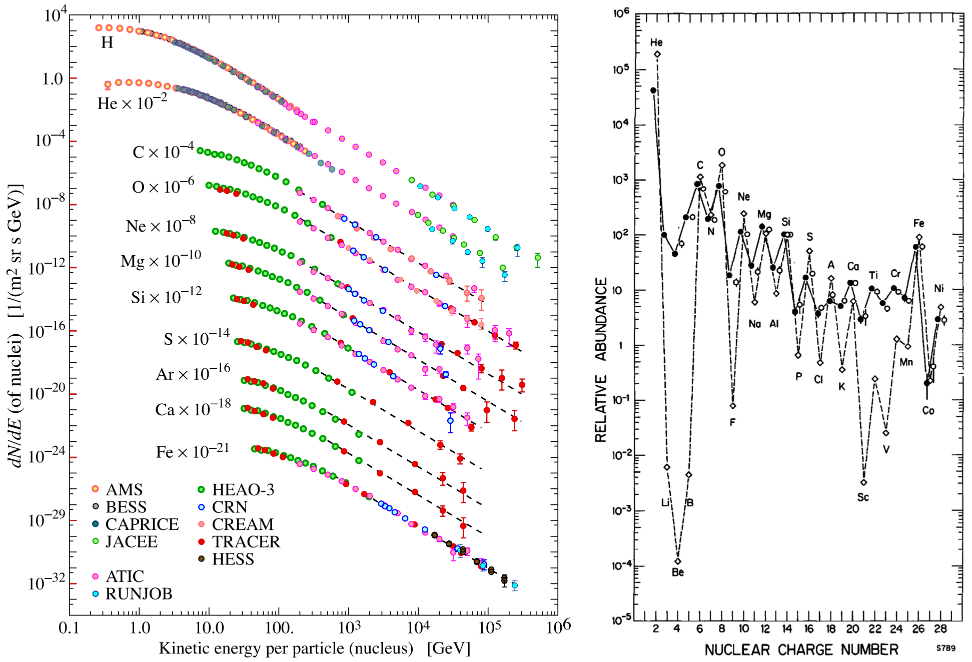

(a) (b)

Figure 2.2: Cosmic ray spectra for the different hadronic components, shifted on the y-axis for better readability (Beringer et al., 2012). The dashed lines are indicating the tentative spectral shape (a). Relative elemental distribution in cosmic rays (filled circles, solid line), compared to the distribution of elements in the solar system (empty circles, dashed line) (Simpson, 1983). The distributions are remarkably similar with the only exception being some elements like Li, Be, B and others that have a comparably low abundance in the solar system (b).

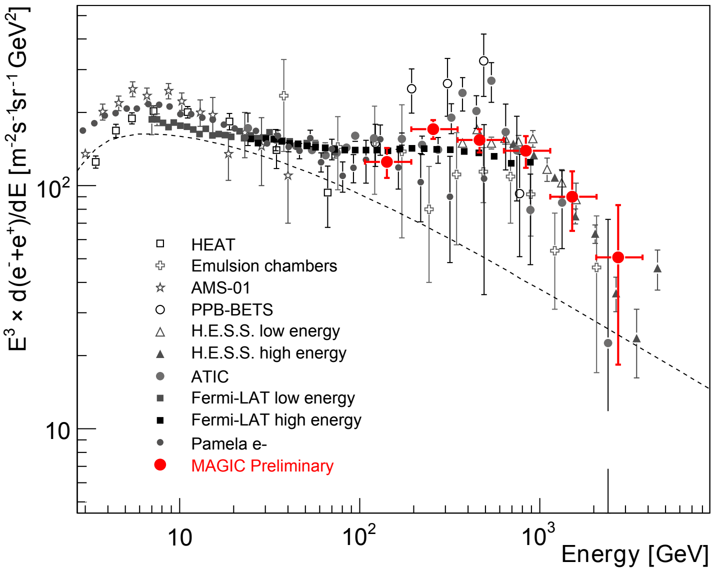

Figure 2.3: The cosmic $e^+ e^-$ spectrum observed with different instruments, including the MAGIC telescope (Tridon et al., 2011). The dashed line shows a typical prediction of a diffusive propagation model. The observed bump between 100 GeV and 1 TeV is rather unexpected and gives rise to speculations, ranging from the influence of a nearby pulsar wind to DM decay (Chowdhury et al., 2011).

cosmic radiation follow the same power-law shape, that can be observed in the overall spectrum (fig. 2.2 (a)) (Beringer et al., 2012).

A much smaller fraction (about 1% depending on the energy) of the total cosmic ray flux is contributed by electrons and γ-rays. The cosmic electron spectrum is different compared to the hadronic component. It shows a slightly steeper spectral index of < -3 and an interesting feature between 100 GeV and 1 TeV, which was first observed by the ATIC experiment (Chang et al., 2008) (see figure 2.3). This so-called ATIC peak, which has by now also been tentatively confirmed by other experiments like *Fermi* (Abdo et al., 2009b), H.E.S.S. (Aharonian et al., 2008) and MAGIC (Tridon et al., 2011), could be possibly explained by either nearby pulsars or DM decay (Chowdhury et al., 2011).

Finally, there must also be a neutrino component. These neutrinos are exclusively secondary cosmic rays from either hadronic interactions or they are so-called cosmogenic neutrinos from the interaction of hadronic cosmic rays with the cosmic microwave background. Due to their small interaction cross-section and the large background from hadronic CR-interactions in the atmosphere, the experimental data is still relatively poor. There are only upper limits on a diffuse cosmic neutrino flux component (Biagi, 2013; Aartsen et al., 2014) but there is evidence at a 4σ level from a search for point sources in ICE-cube data (Stecker, 2013).

2.3 COSMIC RAY ACCELERATION MECHANISMS

In this section, a very short introduction to theories that can explain observations by describing acceleration mechanisms for cosmic rays will be given. A more detailed discussion on that topic can be found for example in Longair (2011).

The exact physics of cosmic particle accelerators are not known, but there are certain requirements that theories explaining the acceleration of charged particles in astrophysical objects have to fulfill (Longair, 2011):

- The acceleration mechanisms should produce power-law spectra, as observed for all charged particles.
- Some should be able to reach energies of $\sim 10^{20}$ eV.
- They should reproduce similar chemical abundances as the observed cosmic abundance.

In all known mechanisms, the state of matter in the environment of cosmic accelerators is plasma. The interaction of particles with the surrounding material happens via collision-less deflection in magnetic fields or acceleration in electric fields.

It is impossible to cover all theories on mechanisms for cosmic ray acceleration. Therefore, in the following I will introduce only a few important examples.

2.3.1 *The Fermi mechanism*

The first stochastic mechanism, which can accelerate charged particles to extreme energies and naturally produce a power-law spectrum was proposed by Fermi (1949). In this mechanism, the acceleration happens in a turbulent plasma with "magnetic mirrors" moving at random velocities in random directions. After a large number of such reflections the particle will come out of such a region with increased kinetic energy.

The energy gain of a particle with momentum $\vec{p}$, which is reflected from a "magnetic mirror" moving in x-direction at a velocity u can be calculated by changing the frame of reference to the mirror, then inverting the x-component of the particles momentum and finally transforming back to the observer's frame:

$$\begin{pmatrix} \gamma & \beta\gamma \\ \beta\gamma & \gamma \end{pmatrix} \begin{pmatrix} 1 & 0 \\ 0 & -1 \end{pmatrix} \begin{pmatrix} \gamma & -\beta\gamma \\ -\beta\gamma & \gamma \end{pmatrix} \begin{pmatrix} E/c \\ p_x \end{pmatrix} = \begin{pmatrix} E''/c & p''_x \end{pmatrix} \qquad (2.3.1)$$

After the first Lorentz boost one obtains

$$E' = \gamma\,(E - u\,p_x)\,, \qquad (2.3.2)$$

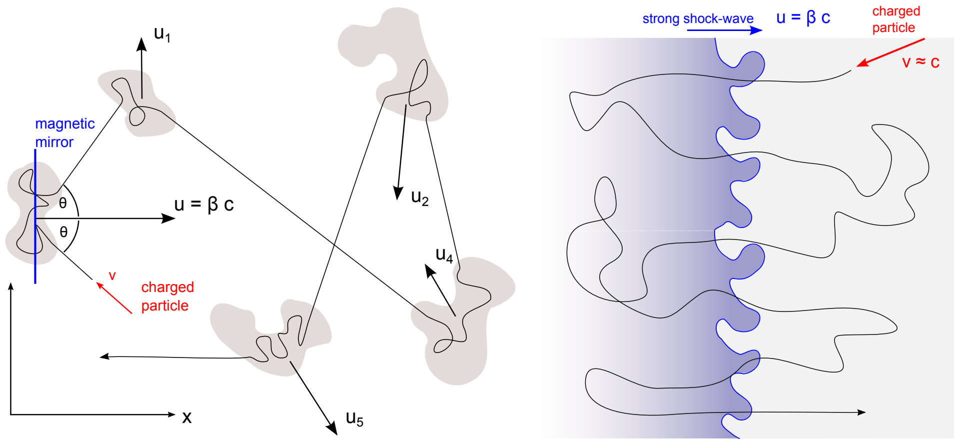

(a) (b)

Figure 2.4: Illustration of stochastic particle acceleration mechanisms. The mechanism, which was originally proposed by Fermi (1949), assumes randomly moving plasma clouds to act as "magnetic mirrors" for charged particles. Averaging over a large number of collisions, the energy gain per interaction of the particle is proportional to $\beta^2 = \overline{u}^2/c^2$ (a). In the diffusive shock acceleration mechanism, which was proposed in the late seventies, a charged particle is performing a random walk in the vicinity of a strong astrophysical shock. The energy gain per double crossing of the shock-front is proportional to $\beta = u/c$, where u is the relative velocity at which the upstream-side plasma and the downstream-side plasma are colliding (b).

for the energy of the particle and

$$p'_x = \gamma\,(-\beta\,E/c + p_x)\,, \tag{2.3.3}$$

for its momentum. After reflection and back-transformation, the Energy is

$$E'' = \gamma^2\,(E - 2\,u\,p_x + \beta^2\,E)\,. \tag{2.3.4}$$

Assuming very high energy particles ($c \approx v \gg u$) and random orientation of the particles momentum $\vec{p}$, the second term in the sum can be neglected when averaging [1].

$$E'' = \gamma^2\,E\,(1+\beta^2) = E\,\frac{1+\beta^2}{1-\beta^2} = E\,(1+2\beta^2+\mathcal{O}(\beta^4))\,. \tag{2.3.5}$$

The most important results are that the average energy gain in such a scenario is of the order of β^2 if β is the typical velocity of randomly moving "magnetic mirrors" and that the mechanism leads to a power-law spectrum as it is

---

[1] In fact there is a higher probability for head-on collisions compared to following collisions, which leads to a slightly different final result if taken into account. The fact that the energy gain is second order in β of the cloud remains unchanged.

shown by Fermi (1949). The major problem of this idea, also known as second order Fermi-acceleration, is that for realistic scenarios the energy losses in-between two interactions have to be unrealistically small (Longair, 2011). Also, acceleration to extreme energies would take very long. Those issues can be solved in the scenario that is described next.

2.3.2 *Diffusive shock acceleration*

The idea of particle acceleration in astrophysical shocks came up in the late seventies and was first suggested by Krymskii (1977); Bell (1978); Blandford & Ostriker (1978) and others. In this scenario, energetic charged particles are randomly scattered in strong magnetic fields that are present the vicinity of a shock-front passing through a plasma. The particles that are moving at velocities v close to the speed may pass the shock front several times during their random movement. The shock-front itself is moving only at much lower speed and, the plasmas on the up-stream and on the down-stream side of the shock are approaching each other at $u \ll c$, which appears as quasi static to the charged particles. When a particle passes once through the shock-front approaching in x-direction, according to equation 2.3.2, its energy gain is

$$E' = \gamma\,(E - u\,p_x) \approx\ (E + \beta\,E\,\cos\theta)\,. \tag{2.3.6}$$

I is assumed that the particle moves towards the non-relativistic shock ($\gamma \approx 1$) in $-x$-direction at ultra relativistic ($p \approx E/c$) speed and at an angle θ with respect to the normal to the plane of the shock. One can now average over all possible directions of incidence. For isotropically distributed directions of the particles, the probability to find a particle with direction in $[\theta, \theta + \mathrm{d}\theta]$ is proportional to $\sin\theta$. The probability for any particle to actually cross the shock front in a given time interval is proportional to $\cos\theta$. Therefore, the average energy gain is

$$\left\langle \frac{\Delta E}{E} \right\rangle = \beta \int_0^{\pi/2} 2\,\cos^2\theta\,\sin\theta\,\mathrm{d}\theta = \frac{2}{3}\,\beta\,. \tag{2.3.7}$$

After the next crossing of the shock-front, back to the original side, on average the energy increases by the same factor. On first order the average total energy gain is

$$\left\langle \frac{\Delta E}{E} \right\rangle = \frac{4}{3}\,\beta\,. \tag{2.3.8}$$

This means that the dependance of the energy gain per cycle on β is of first order. Therefore, this mechanism is also known as first order Fermi acceleration.

In order to establish a prediction of the energy spectrum that would be produced by this mechanism, one has to estimate the rate at which particles escape from the acceleration zone. The rate at which cosmic rays are removed from the shock region, because they are left behind, divided by the rate at which particles are passing the shock-front is the ratio of the velocity of the high energy particles over the velocity, at which the shock zone is propagating. This is on the order of $u/c = \beta$. It has been shown by Bell (1978) that the velocity of the shock-front v_s is $4/3$ of the relative collision speed u of the two plasmas, for a typical strong astrophysical shock. Therefore, rates at which particles are removed from the acceleration zone per cycle, on one hand, and gain energy, on the other, are

$$\Delta N = -a\,\beta\,N\,, \tag{2.3.9}$$

$$\Delta E = b\,\beta\,E\,. \tag{2.3.10}$$

The Energy spectrum is the solution to the differential equation, which can be obtained by dividing equation 2.3.9 by 2.3.10.

$$\begin{aligned} \frac{\mathrm{d}N}{\mathrm{d}E} &= -\frac{a}{b}\,N\,E^{-1}\,,\\ \Rightarrow\; N(E) &= -N_0\,E^{-a/b}\,,\\ \Rightarrow\; \frac{\mathrm{d}N}{\mathrm{d}E} &= N_0\,E^{-(a/b-1)}\,. \end{aligned} \tag{2.3.11}$$

For a ratio of a/b of the order of one, a power-law spectrum with spectral index $\alpha = -2$ is obtained. Modifying a bit the rate at which particles are removed from the zone of the shock, due to a limited spacial extension of the shock for example, moderate variation of the spectral index $\alpha \lesssim -2$ is possible.

It has now been shown that diffusive shock acceleration can produce a power-law spectrum as required. Another important aspect has not been treated yet: timescales. Typical astrophysical shocks travel at $\approx 10^4\,\mathrm{kms}^{-}1$ (Longair, 2011), which means that about 3% of the energy of a charged particle is gained per cycle in a cosmic accelerator. Drury (1983) showed that the average time needed for one full cycle of a particle traveling from the downstream region of the shock to the upstream one and back is

$$\Delta t = \frac{4}{v_p}\left(\frac{\kappa_1}{u_1} + \frac{\kappa_2}{u_2}\right)\,, \tag{2.3.12}$$

where v_p is the velocity of the charged particle $u_{1/2}$ and $\kappa_{1,2}$ are the in/out streaming velocities and the diffusion coefficients on the upstream/downstream side of the shock. For simplicity we assume that $v = c$, $\kappa_1 = \kappa_2 = \kappa$ and $u_1 = u_2 = u$, the velocity at which the shock-wave is traveling. Drury (1983) also states that assuming a totally random magnetic field on the scale of the scattering length of the charged particle one can assume $\kappa = \kappa_{\mathrm{B}} = r_g\,v/3$, the Bohm diffusion coefficient, where r_g is the particles Larmor radius. To get an estimate for the acceleration timescale for protons, one can now assume that

$$\Delta t = \frac{8}{3c}\,\frac{r_g\,c}{u} = \frac{8}{3c}\,\frac{p\,c}{e\,B\,u} = \frac{8}{3c}\,\frac{E[\mathrm{eV}]}{B\,u}\,. \tag{2.3.13}$$

In order to obtain the total time t_{acc}, needed by the particle in order to reach a certain energy E, one has to sum over all cycles while the energy is increasing according to equation 2.3.8.

$$\begin{aligned} t_{\mathrm{acc}} &= \frac{8}{3c}\,\frac{E_0}{e\,B\,u}\sum_{i=0}^{n} E_0\,\left(1+\tfrac{4}{3}\beta\right)^i \\ &= \frac{8}{3c}\,\frac{E_0}{e\,B\,u}\,\frac{1-(1+\frac{4}{3}\beta)^{n+1}}{-\frac{4}{3}\beta} \\ &\approx \frac{2\,E}{e\,B\,u^2}\,. \end{aligned} \tag{2.3.14}$$

In the second last step the formula for the geometric series has been applied and in the last step a factor $1+\beta$ has been neglected, assuming relatively small β. If one now assumes a magnetic field of $B = 10^{-8}$ T inside the shock region of an SNR and $u = 10^4\,\mathrm{kms}^{-1}$ (Longair, 2011), the timescale needed for reaching energies around the knee (10^{15} eV) is $t_{\mathrm{acc}} = \mathcal{O}(100\,\mathrm{y})$. This allows to explain cosmic ray energies up to the knee with SNRs. For reaching energies around the ankle timescales of the order of a million years would be necessary, which is far beyond the typical lifetime of these objects. Finally it can be concluded that the first order Fermi acceleration mechanism can explain cosmic-ray observations, but is a relatively slow process.

2.3.3 *Rotating magnetic fields*

Acceleration of charged particles can happen not only via stochastic mechanisms, but also in the vicinity of rotating, highly magnetized objects like neutron stars. It is argued by Goldreich & Julian (1969) that a neutron star can be considered as a perfect conductive sphere with extremely strong magnetic dipole field. This sphere is rotating at an angular velocity Ω, which induces an electric field

$$\vec{E} = \vec{v}\times\vec{B} = (\vec{\Omega}\times\vec{r})\times\vec{B}\,. \tag{2.3.15}$$

Due to its high conductivity a space charge forms inside the neutron star that exactly compensates the electric field. The field outside the neutron star would however not vanish, if the pulsar is surrounded by vacuum. It is shown by Goldreich & Julian (1969) that the force acting on an electron on the surface generated by the electric field would exceed the gravitational force by orders of magnitude. They argue that the magnetosphere of a neutron star cannot be empty, but must rather be filled with charged particles extracted

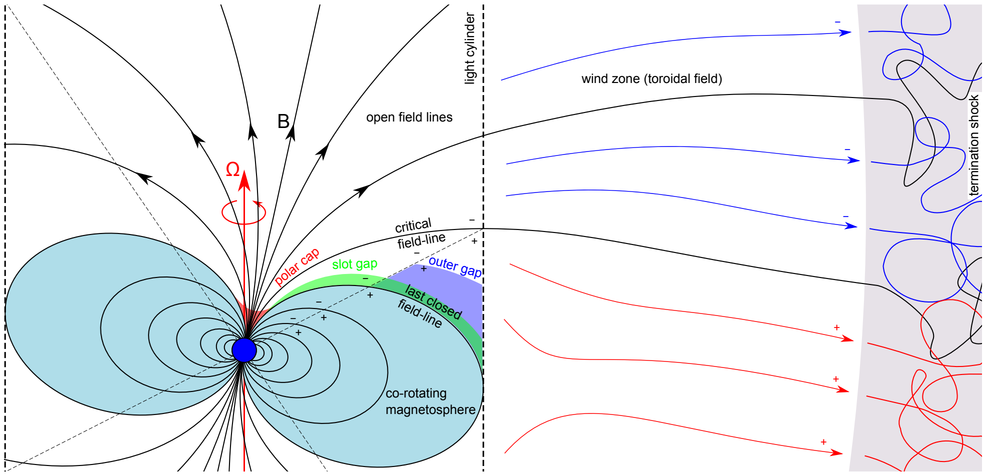

Figure 2.5: Pulsars are conductive rotating spheres with a very strong misaligned magnetic field. Due to strong induced electric fields, the surface of the pulsar is polarized and the surroundings of the neutron star are filled with charged particles. Within the co-rotating particles can be accelerated close to the polar cap or inside the slot gap or outer gap regions, where the charge density is too low to compensate the electric field. The light cylinder is the surface, on which the speed of light would be exceeded in case of co-rotation. Outside the light cylinder the poloidal field gets wound up into into a toroidal structure, pushing a wind of highly relativistic charged particles. This pulsar wind ends in the termination shock, where particles can be accelerated to very high energies.

from the surface. The resulting space charge, also referred to as Goldreich Julian charge density is

$$\rho_{GJ} = \frac{1}{2\,\pi}\,\vec{\Omega} \times \vec{B}\,. \tag{2.3.16}$$

In the magnetosphere of neutrons stars zones exist where the Goldreich Julian charge density cannot be established, due to a rapid escape or the lack of a source of in-streaming particles. In such regions, where the electric field strength can be enormous and the particle density is very low, charged particles can be accelerated while moving along the field lines. Three such regions have been suggested over the last decades: the polar cap region (Ruderman & Sutherland, 1975; Arons & Scharlemann, 1979), the slot gap (Arons, 1983; Muslimov & Harding, 2003) and the outer gap region (Hirotani, 2008) (see also figure 2.5). These co-rotating regions were mainly discussed in order to explain pulsed X-ray and γ-ray emission.

Outside the light cylinder, the magnetic field is forced into a toroidal shape by out-streaming charged particles that can not co-rotate at super-luminal speed. These particles form the pulsar wind, which ends in the termination shock where electrons are accelerated to very high energies (Aharonian et al., 2012) and might play a role for particle acceleration in the GC as well.

Mechanisms like this are probably not only at work in pulsars but also in BH magnetospheres (Neronov et al., 2009).

2.4 INTERACTIONS OF COSMIC RAYS

In addition to the collision-less MHD interactions, which are responsible for the acceleration of cosmic ray particles, there are also a number of important mechanisms of direct, inelastic interaction of cosmic rays with other particles and radiation fields. Here, an introduction will be given about the most important such processes, which usually lead to absorption of primary cosmic rays, but are also responsible for the creation of secondary cosmic rays.

A large fraction of this secondary radiation is γ-radiation. Processes like those described in this section are an essential perquisite, opening the opportunity to observe the extreme environments where charged particles are accelerated to high energies from the distance. This enables studies like the one reported on in this thesis.

This section is largely based on the books by Longair (2011) and Rybicki & Lightman (2008), where detailed discussions of the radiative processes can be found.

2.4.1 *Radiation of accelerated charge*

Charged cosmic rays, due to magnetic fields, are always subjected to acceleration and therefore emit photons. In the instantaneous rest frame, the power emitted from an accelerated charge q is described by Larmor's formula

$$P = -\frac{\mathrm{d}E}{\mathrm{d}t} = \frac{q^2\,|\vec{a}|^2}{6\pi\,\epsilon_0\,c^3}\,. \tag{2.4.1}$$

The angular density of the emitted power scales with $\sin\theta^2$, where θ is the angle, measured from the direction of the acceleration.

For an observer measuring the radiation emitted from a relativistic accelerated charge with Lorentz factor γ in his frame of reference S, the radiation power is

$$P_S = -\left(\frac{\mathrm{d}E}{\mathrm{d}t}\right)_S = \frac{q^2\,\gamma^4}{6\pi\,\epsilon_0\,c^3}\,(|\vec{a_\perp}|^2 + \gamma^2\,|\vec{a_\parallel}|^2)\,, \tag{2.4.2}$$

and the frequency spectrum of an accelerated charge is

$$I(\omega) = \frac{q^2}{3\pi\,\epsilon_0\,c^3}\,|\vec{a}(\omega)|^2\,, \tag{2.4.3}$$

where $\vec{a}(\omega)$ is the Fourier transform of the time profile of the acceleration $\vec{a}(t)$ (Longair, 2011).

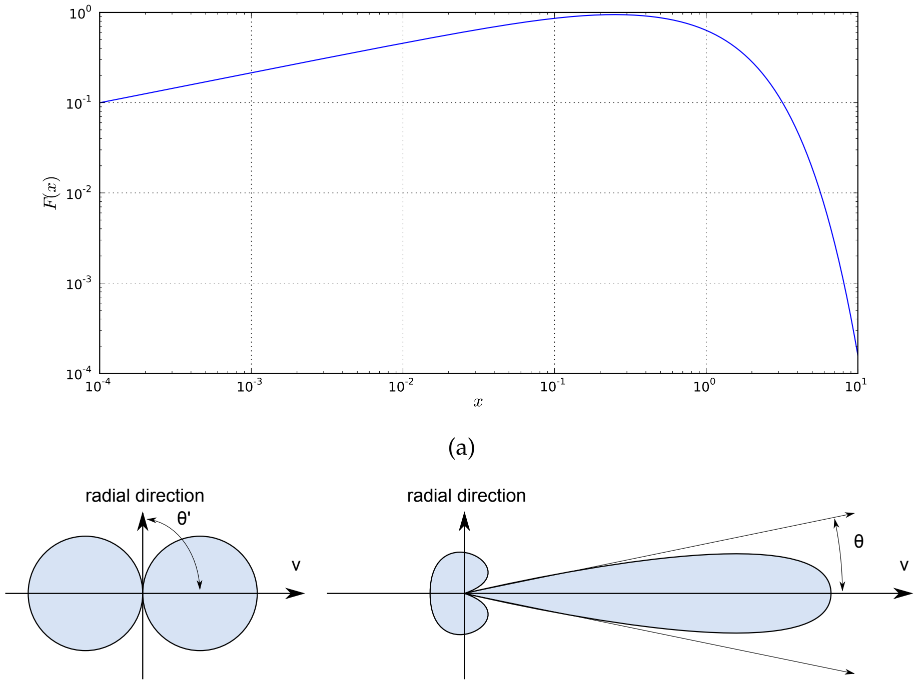

(a)

(b) (c)

Figure 2.6: Spectral shape of synchrotron radiation $F(x)$ as a function of $x = \omega/\omega_c$, with $\omega_c = (3\,\gamma^2\,q\,B\,\sin\alpha)/(2\,m\,c)$, the critical angular frequency (a). Sketch of angular distribution of radiant intensity of synchrotron radiation, in the rest-frame of the emitting particle (b) and in the lab-frame (c). The sketch is for the plane perpendicular to the magnetic field lines.

Bremsstrahlung

Bremsstrahlung is the radiation that is emitted by a charged particle in the Coulomb field of a nucleus. The spectrum radiated by a single particle is constant in ω up to a cutoff frequency $\omega_c = \gamma\,v\,/b$, which relates to the interaction time $\tau = 2\,b/\gamma\,v$. b is the collision parameter of the scattering

Synchrotron radiation

Synchrotron radiation is one of the most important mechanisms for the production of high energy γ-radiation, especially in combination with inverse Compton scattering (see section 2.4.2). It is the radiation emitted by relativistic charged particles gyrating in magnetic fields. The frequency of gyration of such a particle is

$$\omega_B = \frac{q\,B}{\gamma\,m}\,. \tag{2.4.4}$$

The acceleration, due to the direction of the Lorentz force, happens perpendicular to the magnetic field. Synchrotron radiation is emitted mainly perpendicular to the direction of the Lorentz force. Relativistic beaming is further confines the solid angle, where the particle emits with highest radiant intensity to an opening angle θ of about $1/\gamma$. See figure 2.6 (b,c) for illustration.

The total power of synchrotron radiation emitted by a particle gyrating at pitch angle α is

$$P(\alpha) = 2\,\sigma_T\,c\,U_{mag}\,\beta^2\,\gamma^2\,\sin^2\alpha\,, \tag{2.4.5}$$

and the Energy loss rate for randomly oriented magnetic fields is

$$P = -\frac{\mathrm{d}E}{\mathrm{d}t} = \frac{4}{3}\,\sigma_T\,c\,U_{mag}\,\beta^2\,\gamma^2\,, \tag{2.4.6}$$

where σ_T is the Thomson cross-section (see 2.4.12) and $U_{mag} = B^2/2\mu_0$ the energy density of the magnetic field. The spectral power distribution of synchrotron radiation is

$$\frac{\mathrm{d}P(\omega)}{\mathrm{d}\omega} = -\frac{\sqrt{3}\,q^3\,B\,\sin\alpha}{8\,\pi^2\,\epsilon_0 m\,c}\,F(\frac{\omega}{\omega_c})\,, \tag{2.4.7}$$

with the critical angular frequency

$$\omega_c = \frac{3}{2}\,\beta\,\gamma^3\,\omega_B\,\sin\alpha\,, \tag{2.4.8}$$

and

$$F(x) = x\int_x^{\infty} K_{\frac{5}{3}}(\xi)\,\mathrm{d}\xi\,, \tag{2.4.9}$$

where $K_\nu(\xi)$ are the modified Bessel functions. The function $F(x)$ (see figure 2.6 (a)), which is describing the spectral shape, can be approximate for very small and very large x in the following way (Rybicki & Lightman, 2008)

$$F(x) \approx \frac{4\,\pi}{\sqrt{3}\,\Gamma(\frac{1}{3})}\left(\frac{x}{2}\right)^{\frac{1}{3}} \approx 2.15\,\sqrt[3]{x}\,,\ \ x \ll 1\,, \tag{2.4.10}$$

$$F(x) \approx \sqrt{\frac{\pi}{2}}\,\sqrt{x}\,e^{-x} \approx 1.25\,\sqrt{x}\,e^{-x}\,,\ \ x \gg 1\,. \tag{2.4.11}$$

Curvature radiation

Curvature radiation is emitted by charged high energy particles moving in very strong magnetic fields (e.g. pulsar magnetospheres). Such particles will loose all momentum perpendicular to the magnetic field very quickly due to synchrotron radiation. They are constrained to only move along magnetic field lines, where no Lorentz force is acting on them. They follow the curvature of the magnetic field lines, which results in acceleration and thus emission of radiation, similar to synchrotron radiation.

2.4.2 *Photon scattering*

A second important production mechanism for high energy γ-radiation is direct interaction of photons with charged particles. At low photon energies ($h\,\nu \ll m_e\,c^2$), the energy of the photon is conserved in the interaction with an electron and the cross-section is given by the Thomson cross-section

$$\sigma_{\mathrm{T}} = \frac{8\,\pi}{3}\,r_e^2\,, \tag{2.4.12}$$

$$\frac{\mathrm{d}\sigma_{\mathrm{T}}}{\mathrm{d}\omega} = \frac{1}{2}\,r_e^2\,(1+\cos^2\theta)\,, \tag{2.4.13}$$

with the classical electron radius

$$r_e = \frac{e^2}{4\,\pi\,\epsilon_0\,m_e\,c^2}\,. \tag{2.4.14}$$

Compton-scattering

At higher energies, when the momentum transfer from the photon to the electron is not negligible ($h\,\nu \approx m_e\,c^2$), the process is referred to as Compton scattering. The energy after the collision is

$$h\,\nu' = \frac{h\,\nu}{1+\frac{h\,\nu}{m_e\,c^2}\,(1-\cos\theta)}\,, \tag{2.4.15}$$

θ being the deviation of the direction of propagation of the photon. The differential cross-section is described by the Klein-Nishina formula

$$\frac{\mathrm{d}\sigma}{\mathrm{d}\omega} = \frac{r_e^2}{2}\,\frac{\nu'^2}{\nu^2}\left(\frac{\nu}{\nu'}+\frac{\nu'}{\nu}-\sin^2\theta\right)\,. \tag{2.4.16}$$

In the ultra-relativistic limit ($h\,\nu \gg m_e\,c^2$) the total cross-section is given by (Rybicki & Lightman, 2008)

$$\sigma = \frac{3}{8}\,\sigma_T\,\frac{m_e\,c^2}{h\,\nu}\left(\ln\frac{2\,h\,\nu}{m_e\,c^2}+\frac{1}{2}\right)\,. \tag{2.4.17}$$

Inverse Compton-scattering

Inverse Compton-scattering is the most important mechanism for the production of very high energy γ-radiation in cosmic e^+/e^- accelerators. In the presence of an electromagnetic radiation field, energetic electrons or positrons can 'up-scatter' photons to very high energies. In astrophysical accelerators, this photon field is very often created via synchrotron radiation by the same population of electrons, also responsible for the 'up-scattering' (Synchrotron Self Compton - SSC). The spectral energy distributions (SEDs) of sources with the SSC mechanism at work show a typical two-bump structure (see figure 2.7 (b)).

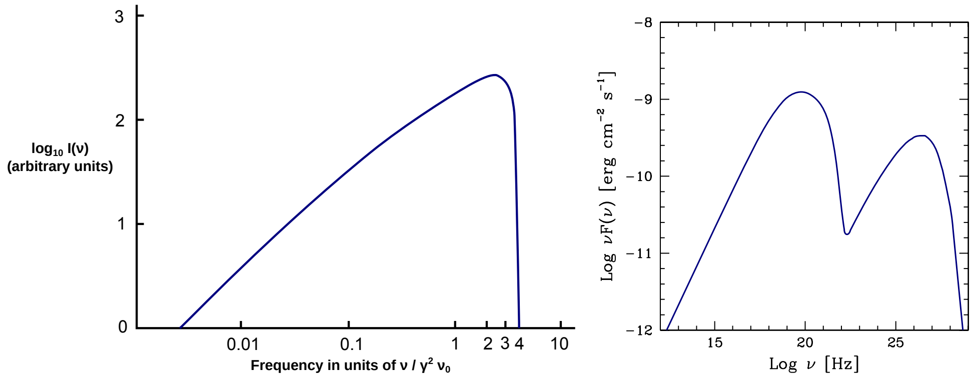

(a) (b)

Figure 2.7: Spectrum of inverse Compton radiation (a), adopted from (Longair, 2011). Typical Spectral Energy Distribution (SED) from a Synchrotron Self-Compton (SSC) model for explaining the broad band emission of an Active Galactic Nucleus (AGN) (b).

If in the rest-frame S' of the electron in its initial state the photon energy $h\,\nu' \ll m_e\,c^2$, the scattering can be treated as Thomson scattering. The energy loss rate for the electron can then be given as follows (Longair, 2011):

$$P = -\frac{\mathrm{d}E}{\mathrm{d}t} = \frac{4}{3}\,\sigma_T\,c\,U_{rad}\,\beta^2\,\gamma^2\,. \tag{2.4.18}$$

This result is remarkably similar to the energy loss rate of an electron gyrating in a magnetic field (synchrotron radiation). The only difference is that U_{rad} here is the energy density of the photon field. In the Thomson regime ($h\,\nu' \ll m_e\,c^2$) the mean and the maximum energy of the photons in their final state can be approximated by (Longair, 2011)

$$h\,\bar{\nu} \approx \frac{4}{3}\,\gamma^2\,h\,\nu_0\,, \tag{2.4.19}$$

$$h\,\nu_{max} \approx 4\,\gamma^2\,h\,\nu_0\,. \tag{2.4.20}$$

The spectrum emitted by mono-energetic electrons is shown in figure 2.7 (a). At higher photon energies (Klein-Nishina regime), the maximum energy transfer is limited by the energy of the electrons ($\gamma m_e c^2$).

2.4.3 *Hadronic interactions*

Apart from charged cosmic rays emitting synchrotron radiation or participate in Compton scattering, for the hadronic component, there is also the possibility to undergo hadronic interaction processes. In the interaction mechanisms described in the last two sections, the energy loss rate was proportional to the energy density of the electromagnetic field. Here the actual density of nuclear matter traversed by the cosmic ray particle is important.

The radius of a nucleus with mass number A is approximately

$$R_A = A^{\frac{1}{3}}\, 1.2 \cdot 10^{-15}\,\mathrm{m}\,. \tag{2.4.21}$$

Assuming only protons in the interstellar medium (ISM), the cross-section for hadronic interaction of two particles can be approximated by the area defined by the separation, at which of two protons ate still touching ($(2.4 \cdot 10^{-13}\,\mathrm{cm})^2 \cdot \pi = 1.8 \cdot 10^{-25}\,\mathrm{cm}^2$). With a particle density of $N = 1\,\mathrm{cm}^3$ the mean free path length for hadronic interactions in the ISM is on the order of Mpc. This mean free path length reduces to $\mathcal{O}(100\,\mathrm{pc})$ in dense molecular clouds with densities of the order $10^4\,\mathrm{cm}^3$ (Snow & McCall, 2006).

A more accurate formulation of the pp-interaction mechanism can be found for example in Aharonian et al. (2013).

2.5 COSMIC RAY DETECTION

This section will give a short overview on experimental techniques for studying the properties of cosmic rays. Because particle and astro-particle physics share the same origin, as described in section 2.1, it is not surprising that the experimental methods, at least in the beginning were very similar. Nearly all of the direct observations are based on recording ionization tracks using various techniques and estimating the energy by using calorimeters.

2.5.1 *Balloon experiments*

100 years ago, the whole field of cosmic ray research started with balloon flights and still today balloon experiments contribute important results. Balloon experiments present a low cost alternative so space-borne cosmic ray detectors. Important results about the chemical composition of the cosmic ray flux in the range between 10GeV and 10TeV per nucleon were contributed by balloon experiments like the RUNJOB (RUssian-Nippon JOint Balloon), CREAM (Cosmic Ray Energetics And Mass) and ATIC (Advanced Thin Ionization Calorimeter) experiment (Guzik et al., 2004; Derbina et al., 2005; Panov et al., 2007; Ahn et al., 2010).

Typically such experiments are carried out in the high altitude circumpolar air streams. Helium balloons can stay there at altitudes of 30-40km on a stable track around the north- or south-pole for several days or weeks. Experimental detection techniques are ranging from emulsion chambers (RUNJOB) to sophisticated multi-layer calorimeters (ATIC and CREAM).

2.5.2 *Space-borne instruments*

Space-borne experiments are useful, especially for long term monitoring or generally long integration times. Cosmic ray detectors were deployed in space already in the early times of the space traveling era, for example on the deep-space probes Voyager 1 and 2 (Stone et al., 1977).

Two important examples for cosmic ray observatories currently in space are AMS (Alpha Magnetic Spectrometer) and PAMELA (Payload for Antimatter Matter Exploration and Light-nuclei Astrophysics). Both were designed for searching for antimatter in the lower energy (100 MeV-100 GeV) cosmic ray regime (Bergström et al., 2013; Bruno et al., 2013).

The *Fermi* satellite is another prominent example for a space mission with big impact on the field of astroparticle research (see section 2.5.4).

2.5.3 *Large area ground-based arrays*

The highest energy regime of the cosmic ray spectrum is accessible only via large-scale ground-based facilities that detect Cherenkov light, fluorescence light and secondary particles. In most cases a combination of different detection channels is used together with Monte Carlo simulations in order to reconstruct the air-shower events and draw conclusions on the primary particles.

The most important instruments for Ultra High Energy Cosmic Ray (UHECR) research ($E \geq 1 \cdot 10^{18}$ eV) are the HiRes (High Resolution Fly's Eye Cosmic Ray Detector) (Sokolsky et al., 2010), the AGASA (Akeno Giant Air Shower Array) (Chiba et al., 1992), the Telescope Array (Kawai et al., 2008), and the Pierre Auger Observatory (Allekotte et al., 2008; Abraham et al., 2010). They could find strong evidence for the predicted cutoff of the cosmic ray spectrum around energies of $E \approx 10^{20}$ eV due to scattering of high energy particles at CMB photons (Abbasi et al., 2008; Aab et al., 2013).

It is possible that at the highest cosmic ray energies the deflection in galactic and extragalactic magnetic fields is not high enough any more for scrambling the direction of origin of those particles. Such a discovery would open the path to a new discipline in astronomy: cosmic ray astronomy. But until now, no significant correlation of UHECRs with astrophysical point-sources or any other large scale structures has been found (Neto et al., 2013).

2.5.4 *γ-ray astronomy*

The easiest and most obvious messenger particles for astronomy are photons, also in the regime of very high energies. γ-radiation is not deflected by magnetic fields throughout the cosmos and the observation techniques are very similar to the ones used for detecting charged cosmic rays of comparable energy. There is only one effect that strongly influences very high energy (VHE) γ-ray signals coming from large distances, namely interaction with extragalactic background light (EBL). VHE and EBL photons are interacting and thereby producing e^+/e^- pairs. This can strongly reduce the flux at energies above ~ 100 GeV for distant AGN sources.

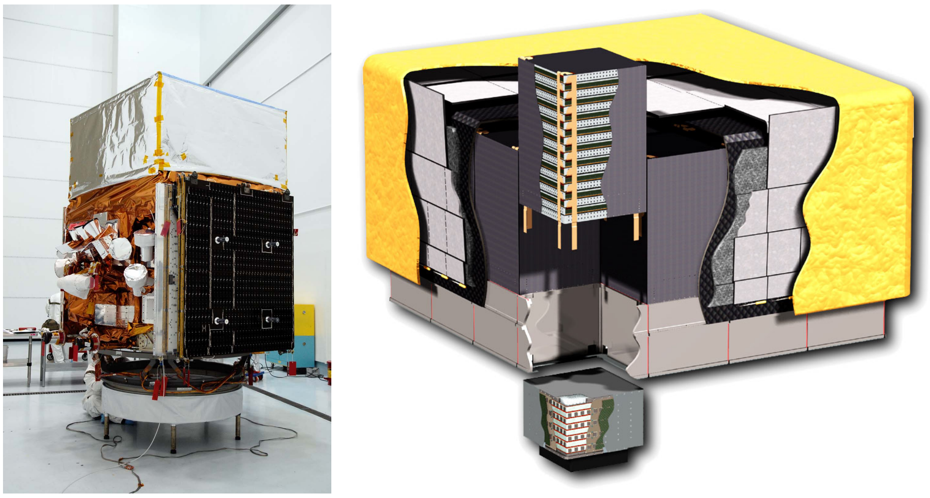

(a) (b)

Figure 2.8: The *Fermi* satellite being prepared for launch (a). The segmented detector of the Large Area Telescope (LAT) on board the *Fermi* satellite consists of Si tracker and CsI calorimeter modules (b). Sources: (Atwood et al., 2009), Wikipedia

The Fermi space telescope

Since 2008, the Large Area Telescope (LAT) on board the *Fermi* satellite is the most sensitive instrument for γ-ray astronomy in the energy range between 20 MeV and 300 GeV. It covers a total collection area of about $1\,\mathrm{m}^2$ with modular Si tracker and CsI calorimeter. The tracker consists of 16 layers of Wolfram foil, each followed by Si strip detectors. After the tracker follows an electromagnetic calorimeter made from CsI crystals with photo-diode readout. The instrument is operating in scanning mode, covering the whole sky in three hours due to its large field of view of 2.4 sr (Atwood et al., 2009).

Apart from the LAT, *Fermi* also hosts the Gamma-ray Burst Monitor (GBM), which allows for quick follow up observations by pointing the LAT at the γ-ray burst (GRB) as well as alerting other telescopes.

Before the launch of *Fermi*, already the Energetic Gamma Ray Experiment Telescope (EGRET) (Thompson, 2008) onboard the Compton Gamma Ray Observatory (CGRO) and later the Astro-rivelatore Gamma a Immagini LEggero (AGILE) satellite (Pittori & Tavani, 2004) were conducting observations in the medium to high (30 MeV - 50 GeV) energy γ-ray regime.

Cherenkov astronomy from the ground

At energies of more than 100 GeV, the flux of VHE γ-radiation from most sources is too small for significant detections with space telescopes of the size of LAT ($A_{\mathrm{eff}} \approx 1\,\mathrm{m}^2$). The signal to background ratio would be good enough, but integration times needed for a detection reach the typical time duration of the mission. It becomes therefore impossible to study source variability or fast transients. At these energies the Imaging Air Cherenkov Telescope (IACT) technique allows for observations from the ground, with collection areas exceeding that of satellites by over five orders of magnitude. A detailed description of the technique will be given in chaper 3.

2.5.5 *Neutrino telescopes*

Apart from γ-radiation, also neutrinos produced in cosmic ray interactions could serve as none-deflected messengers for high energy astronomy. Their big disadvantage is the extremely small interaction cross-section. Nevertheless there are projects that try to pioneer the field of neutrino astronomy. Such installations are IceCube at the geographic south pole and the future KM3NeT (Cubic Kilometre Neutrino Telescope) (Karle et al., 2014; Margiotta, 2013). Their working principle is filling large volumes of transparent media, such as water or ice, with fast and sensitive light detectors that can detect Cherenkov light from neutrino-induced particle showers.

3

γ-RAY ASTRONOMY FROM THE GROUND

This chapter will introduce the working principle of Imaging Air Cherenkov Telescopes (IACTs) for VHE γ-ray astronomy. The first part is an introduction about cosmic ray induced extended air-showers and the Cherenkov effect, followed by a general introduction to Cherenkov telescopes. The second part will give a deeper description of the MAGIC experiment and a short outlook to CTA. The last part is a brief summary of the objects and scientific topics that can be studied with Cherenkov telescopes.

3.1 THE IMAGING AIR CHERENKOV TELESCOPE TECHNIQUE

After Blackett (1948) pointed out that Cerenkov light could contribute to the light of the night sky (LoNS) with a fraction of around $1 \cdot 10^{-4}$, Jelley (1958a) suggested to use Cherenkov light for studying extensive air-showers of cosmic rays. It was in the same year when Morrison (1958) first suggested to observe the γ-ray sky for studying astrophysical phenomena. The first source of VHE γ-radiation detected from the ground was the Crab Nebula observed by the Whipple collaboration (Weekes et al., 1989)

IACTs offer all the solutions to problems of space-borne detectors (limited shower containment and collection area) at comparably low cost. Currently operating instruments are the High Energy Stereoscopic System (H.E.S.S.), the Major Atmospheric Gamma Imaging Cherenkov (MAGIC) telescope and the Very Energetic Radiation Imaging Telescope Array System (VERITAS).

3.1.1 *Extended air-showers*

Cosmic ray particles impinging on earth's atmosphere, starting from energies of the order of 1 GeV, trigger a whole cascade of secondary particles after their first interaction with air-molecules and atoms. The type of the primary particle has large influence on the development of such Extended Air-Showers (EAS), due to the different available interaction mechanisms. The strongest difference can be found between air-showers that are triggered by hadronic cosmic rays and those originating from electrons or γ-rays.

Electromagnetic showers

The highly dominant process for interactions of high energy γ-rays with the earth's atmosphere is the creation of electron-positron pairs in the electric field in air molecules and atoms. The two charged particles in turn loose energy via emission of photons due to Bremsstrahlung. These react again

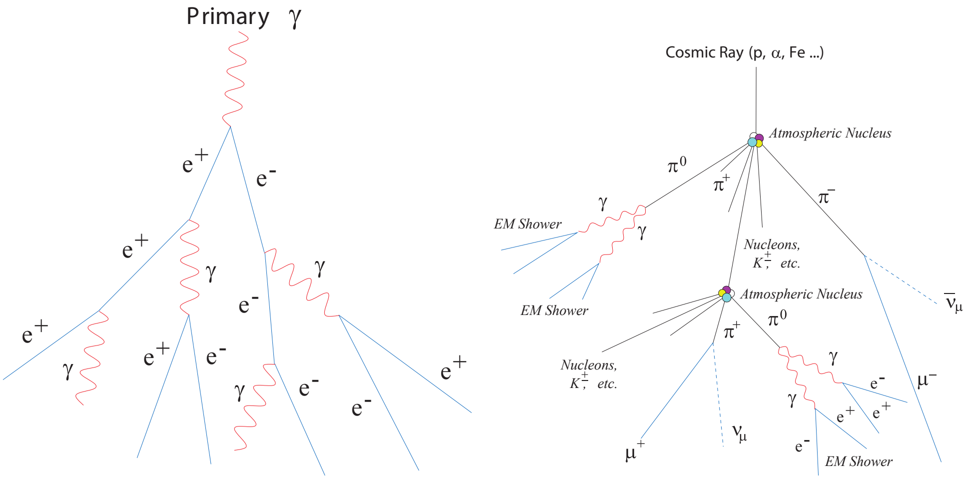

(a) (b)

Figure 3.1: Illustration of particle interactions in electromagnetic (a) and hadronic (b) air-showers. From Wagner (2006)

through pair creation, and so on, until the photon energy is not sufficient for pair creation ($E_\gamma > 1.022\,\text{MeV}$) any more. See figure 3.1 (a) for an illustration of the typical shower development.

The longitudinal development of electromagnetic cascades can be described with a simple model first proposed by Heitler (1954). The basic assumption is that after one radiation length X_0 a γ-ray is creating an $e^+ + e^-$ pair and e^+ or e^- are emitting a Bremsstrahlung photon. The energy of a particle, e^+, e^- or γ, gets distributed equally between the two outgoing particles ($e^+ + \gamma$, $e^- + \gamma$ or $e^+ + e^-$). This process repeats until a critical energy, when the ionization losses of the electrons reach about the same level as the radiation losses ($E_{e^-} = \mathcal{O}(100\,\text{MeV})$) and the shower dies out.

Hadronic showers

Hadronic cascades are initiated by deep inelastic scattering of cosmic ray nucleons on nuclei in air-molecules. All kinetic energy that is stored in a hadronic cosmic-ray particle is sooner or later transferred to pions. Those pions can carry relatively high transverse energy, due to their 3-particle production via the strong interaction. The total energy gets nearly equally distributed between π^0, π^+ and π^-. The life-times in the respective rest-frames are $8.4 \cdot 10^{-17}\,\text{s}$ for π^0 and $2.6 \cdot 10^{-8}\,\text{s}$ for charged pions. At large Lorenz factors, typically of the order of $\gamma = 1000$, the track lengths of charged pions are of the order of 10m, while those of neutral pions are negligible. 99.99% of the charged pions decay via

$$\pi^+ \to \mu^+ + \nu_\mu\,, \tag{3.1.1}$$

$$\pi^- \to \mu^- + \bar{\nu}_\mu\,, \tag{3.1.2}$$

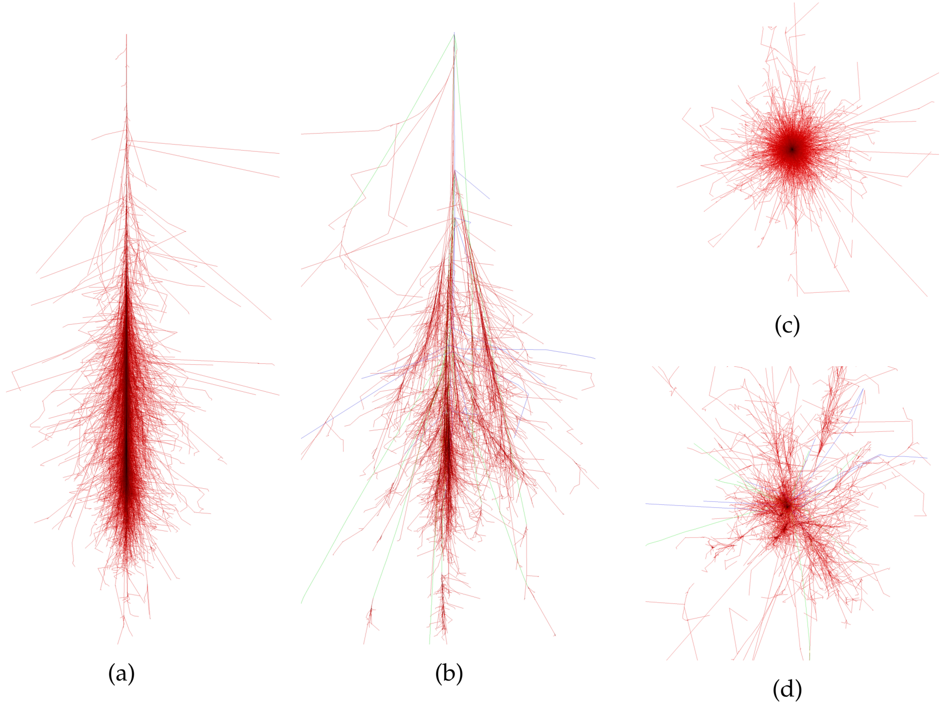

Figure 3.2: Side view (a,b) and bottom view (c,d) of particle tracks in electromagnetic (a,c) and hadronic (b,d) air-showers. The air-showers induced by primary particles of 100 GeV were simulated with CORSIKA and are available online (courtesy of Schmidt (2014)).

and 99.82% of the neutral pions decay via

$$\pi^0 \rightarrow 2\gamma\,. \tag{3.1.3}$$

Neutral pions are therefore very likely to create an electromagnetic subshower within the hadronic cascade. Figure 3.1 shows an illustration of the interaction mechanisms in hadronic, compared to electromagnetic air-showers. Figure 3.2 shows the results of Monte Carlo simulations of such events.

3.1.2 *The Cherenkov effect*

It was first observed by Cherenkov (1934) and later explained theoretically by Frank & Tamm (1937) that charged particles moving through a transparent, dielectric medium, at velocities greater than $v = c/n$, are emitting electromagnetic radiation, also in the optical. Cherenkov light is emitted at a characteristic angle from the direction of propagation of the particle.

$$\cos\theta_c = \frac{1}{n\,\beta}\,. \tag{3.1.4}$$

It is the direction, perpendicular to the surface of a cone, on which excitations of the microscopic dipoles in a medium traversed by a charged particle have

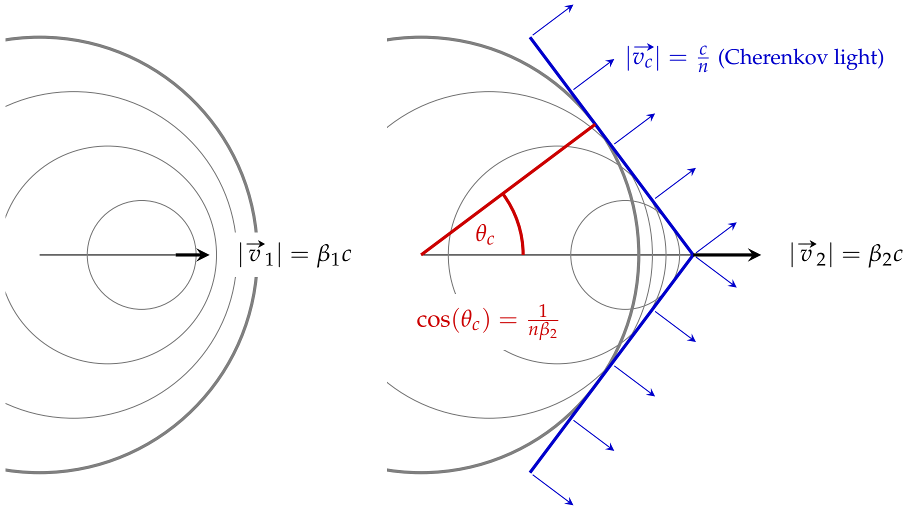

Figure 3.3: Huygens construction illustrating the production mechanism of Cherenkov radiation. When a charged particle travels through an optical medium with refractive index n at a velocity $\beta_1 < n^{-1}$, photons that are emitted as the dipoles in the dielectric medium react to the electric field of the particle interfere destructively. If the particle moves at a speed $\beta_2 > n^{-1}$, there is a cone on which the perturbations in the polarization caused by the same particle at different locations have the same phase. The constructive interference leads to the emission of an electromagnetic wave, propagating perpendicular to the surface of the cone.

the same phase (see figure 3.3 for illustration). The number of photons emitted by a particle of charge $z\,e$ and velocity β per unit distance and wavelength is (Jelley, 1958b)

$$\frac{\mathrm{d}^2 N}{\mathrm{d}x\,\mathrm{d}\lambda} = \frac{2\pi\,\alpha\,z^2}{\lambda^2}\left(1 - \frac{1}{\beta^2\,n^2(\lambda)}\right) . \tag{3.1.5}$$

The Cherenkov effect is not very important in terms of energy loss (Beringer et al., 2012), but it plays a key role for particle detection, especially in neutrino and γ-ray astronomy.

3.1.3 *Cherenkov telescopes*

The angle at which Cherenkov light is emitted in the atmosphere is 1.4° on sea level and decreasing with altitude. Typical showers from VHE γ-rays reach their maximum particle density on altitudes around 10km. This means, that most of the light gets distributed on an area of ∼150m radius at altitudes of 2000m a.s.l with a core density of 15 photons per m^2 for a 100GeV primary γ (see figure 3.4). The arrival time distribution is on the order of a few ns only. With a large enough light collector and ultra fast as well as sensitive detectors it is possible to detect the light flashes from such a shower. One can map the Cherenkov light image of such an air-shower onto a camera, which is a matrix of fast and sensitive detectors. For electromagnetic cascades,

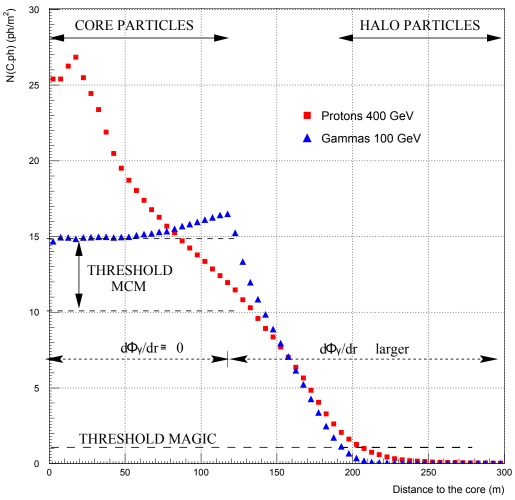

Figure 3.4: Distribution of Cherenkov light on the ground from MC simulations for a 400GeV proton-shower (red) and a 100GeV γ-shower (blue). Both particles are coming from zenith, adopted from (Barrio et al., 1998).

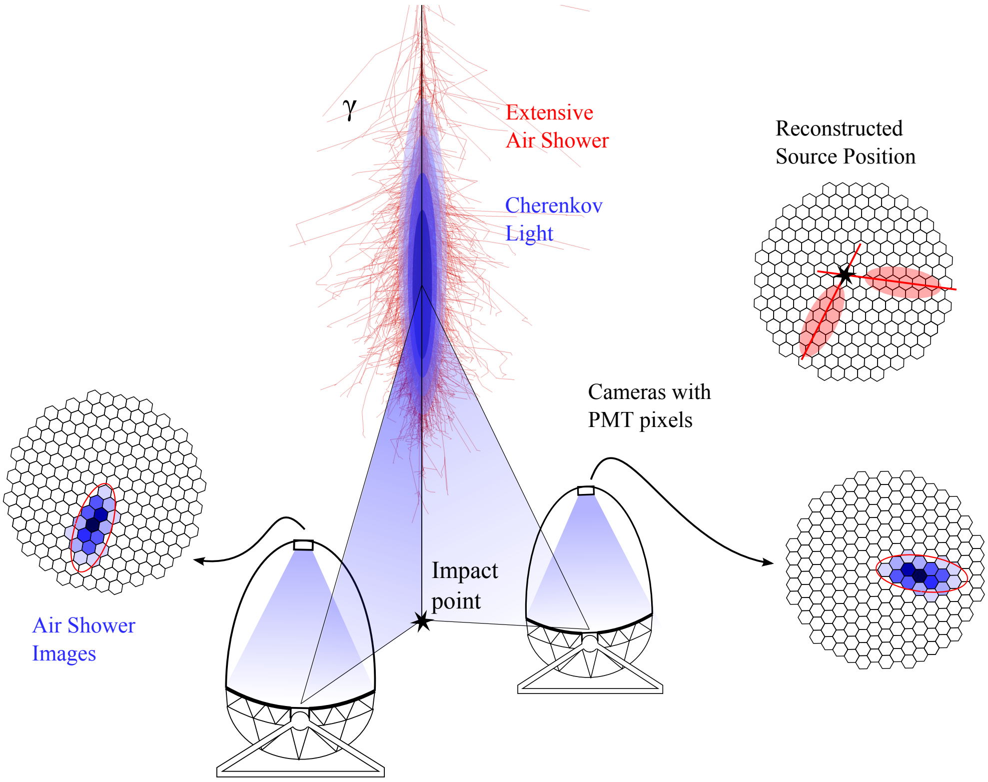

Figure 3.5: Illustration of the observation technique of an IACT in stereo mode. The telescopes are located inside the Cherenkov light pool of an extensive air-shower. The light that is collected by the big mirror dishes gets mapped on the fast and sensitive imaging cameras with photomultiplier pixels. The shape and orientation of the resulting images can be used to reconstruct the type, the direction of origin of the primary particle and its energy.

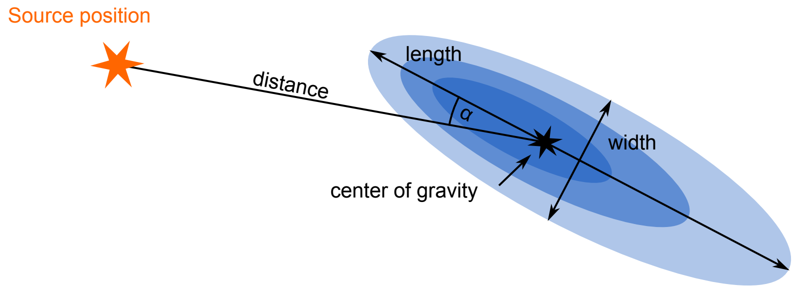

Figure 3.6: Mono parametrization scheme for IACT images, based mainly on Hillas (1985). An ellipse is fitted to the shower image. Parameters like length and width, but also the distance of the shower core from the expected source position or the angular miss-alignment of the major axis α can be used to distinguish signal from background.

such images usually have an elliptic shape. The shape and orientation of the ellipse carries information about the direction of origin of the primary particle as it is illustrated in figure 3.5. In addition the shape can also be used to discriminate background from hadronic events, that are on the order of 100 to 1000 times more frequent than the electromagnetic ones. The energy of the primary particle is proportional to the total light yield of the shower. The image parametrization and event reconstruction strategies will be explained in a bit more detail in the next section (3.1.4).

With present instruments, it is possible to cover the energy range between 50GeV and 100TeV and to obtain directional resolutions better than 0.05°.

3.1.4 *Image parametrization and event reconstruction*

The first parametrization scheme for air-shower Cherenkov light images that – with some minor changes – is still in use today is the so-called Hillas parametrization. Hillas (1985) suggested to fit an ellipse to the image after subtracting the background from the light of night sky (LoNS). He found that the two major axis of the ellipse, the misalignment of the ellipse, the light concentration, the distance of the center of the ellipse to the source and the RMS width projected along the axis connecting source and shower image, are good parameters for distinguishing γ-ray signal from hadronic background. First discoveries by the Whipple telescope were made by performing on-off scans of the source and then excluding a large number of hadronic events using simple cuts in the Hillas parameter space (Weekes et al., 1989). Figure 3.6 shows a slightly more modern image parametrization scheme, which is mainly based on the Hillas scheme and still used for single telescope data analysis by MAGIC. All recent instruments for VHE-γ observations are operating in stereo-mode. This means that two or more telescopes are observing the same source and images of atmospheric events will only be stored in case of coincidence of triggers from at least two or more telescopes. This mode of observation allows to introduce a couple of new parameters that allow

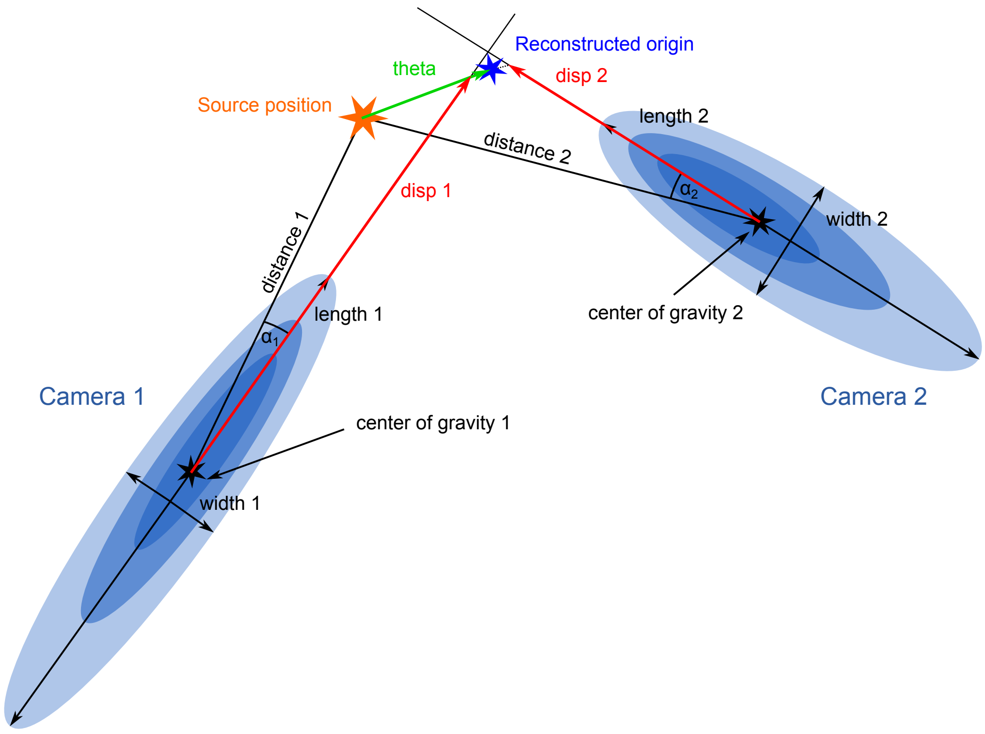

Figure 3.7: Stereo parametrization scheme as it is used in the MAGIC data analysis chain.

to reconstruct more precisely the arrival direction and to improve γ-hadron separation. The improvements are also coming from the fact that there is then more than one independent set of mono parameters for each event (see figure 3.7). Important new parameters are for example "disp1" and "disp2" (the angular distance of the shower image center of gravities from the reconstructed shower direction of origin) or θ (the angular distance of the reconstructed shower direction from the expected source position).

In addition, the stereo parameters allow for calculating secondary parameters like the height of the shower maximum, which is very useful for background suppression, because the shower cores of electromagnetic air-showers tend to happen at higher altitude for events with comparable light yield. For calculating the height of the shower maximum, it is necessary to calculate the impact parameter of the shower first. This can be done by simple triangulation as indicated in figure 3.5.

3.2 THE MAGIC TELESCOPES

The two Major Atmospheric Gamma Imaging Cherenkov (MAGIC) telescopes – or Florian Goebel telescopes – started operation in 2003 (MAGIC I) and 2009 (MAGIC II). They are hosted by the ORM (Observatorio Astrofisico del Roque de los Muchachos) on the Canary island La Palma (28° 45′ 42″N,

Figure 3.8: The MAGIC telescopes on top of the Roque de los Muchachos on the Canary island la Palma. From left: MAGIC I, MAGIC II and the LIDAR tower on top of the counting house. The Gran Telescopio Canarias (GTC), with 10.4 m main mirror largest single optical telescope world-wide, can be seen in the background. Image: courtesy of Robert Wagner

$18^\circ\, 53'\, 25''$W) at an altitude of 2200m above sea level. With a mirror diameter of 17 m each, they are the largest Cherenkov telescopes operating as a stereoscopic system in the world. One of their main characteristics is the low energy threshold of 50 GeV (Aleksic et al., 2012), which makes them the IACT with the largest overlap with space telescopes like *Fermi*. MAGIC II is almost a clone of the MAGIC I telescope. In 2011 the readout of both telescopes and in 2012 the camera of MAGIC I was upgraded, improving the performance and making both telescopes more similar to each other (Sitarek et al., 2013).

3.2.1 *Structure, reflector and drive system*

The MAGIC telescopes are two free-standing Ø17m parabolic dishes composed of single mirror facets on an Alt/Az mount, at a distance of 80m from each other. The dish and under-structure of both telescopes is a space-frame made from carbon fiber (dish) and steel tubes. The use of lightweight materials serves the purpose of enabling fast repositioning to any direction in the sky within 20-30 seconds (Lorenz, 2004), which allows fast follow-up observations after so-called Gamma-Ray Bursts (GRBs) (see section 3.4.4). The camera is mounted on a vertical Aluminum arch that is supported against horizontal oscillations by steel cables. The telescopes are moved by two 11 kW electric motors on the azimuthal and one electric motor on the elevation axis (Lorenz, 2004).

With only one mirror and $F/d = 1$, the optics of the telescope are kept very simple. For IACTs, timing conservation is even more important than optical resolution, giving preference to a parabolic mirror shape over such that offer better imaging quality. The overall parabolic shape is approximated

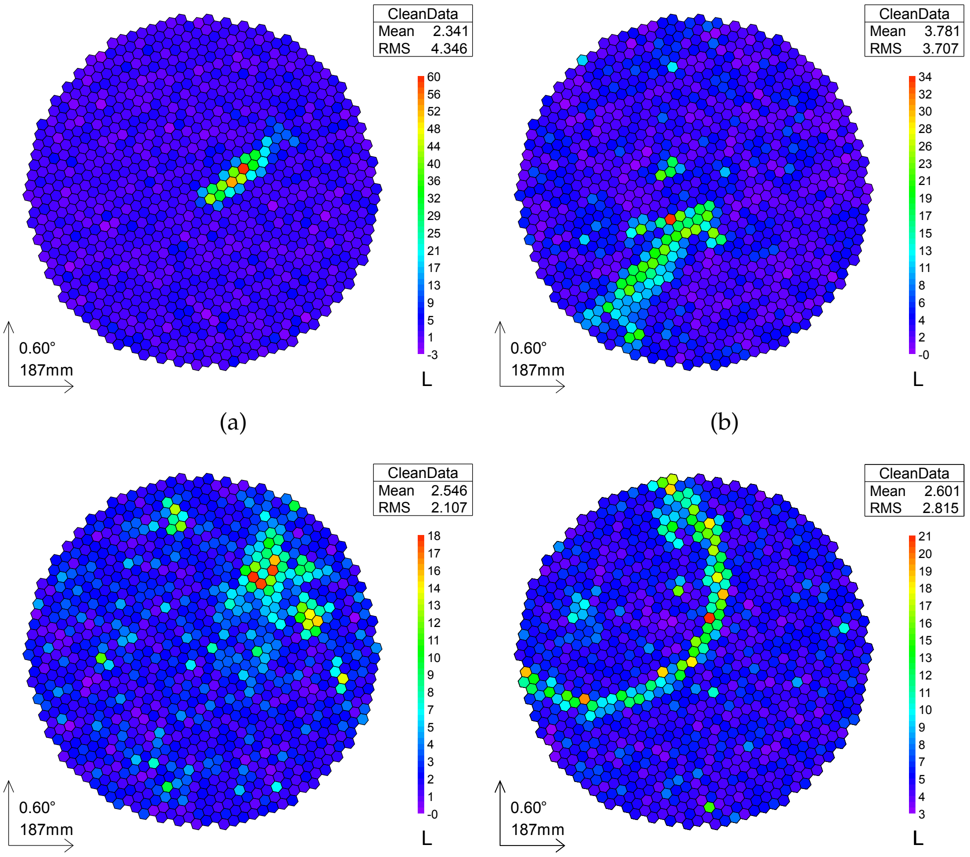

(a) (b)

(c) (d)

Figure 3.9: Images of air-showers observed with MAGIC. The images show: a γ-like event (a), two different hadronic events (b,c) and a muon ring (d).

by 964 0.5×0.5 m^2 (in case of MAGIC I) and 247 1×1 m^2 (in case of MAGIC II) spherical mirror facets of different radii of curvature (Kellermann, 2011). The single mirrors of MAGIC II and groups of 2×2 facets of MAGIC I are individually adjustable, in order to keep the point spread function (PSF) of the reflector constantly to a minimum. Look-up tables provide the information for an automatic adjustment of the mirrors during the observations (Biland et al., 2008).

3.2.2 *Camera*

Since the upgrade in 2012 both MAGIC telescopes are equipped with PMT cameras of 1039 pixels each (Sitarek et al., 2013). The PMTs are operated behind Winston cones (WC), which serve as light concentrators. The WCs have a hexagonal outer shape and are optimized for collecting light only from the solid angle occupied by the mirror. The angular diameter mapped onto a single pixel is about 0.1°, which corresponds to a field of view of the cameras of 3.5° (Tridon et al., 2010).

3.2.3 *Trigger and readout*

The standard trigger of the MAGIC telescope system is a digital coincidence trigger logic that requires groups of N next-neighbor pixels to each pass a certain trigger threshold simultaneously. In stereo mode also coincidence of both telescopes is required. In the first layer of the trigger chain, the single pixel or "L0" trigger, it is possible to apply individual thresholds for each pixel. This feature can be used to avoid high rates of accidental triggers in case of stars inside the field of view. The next stage is the next-neighbor or "L1" trigger. Next neighbors are defined as most closely packed groups of N pixels. $N = 2, 3, 4$ are the most popular choices. In the last step, the "L3" or stereo trigger, the geometric orientation of the telescopes has to be taken into account, in order to adjust the coincidence window to the time difference between the light flashes hitting both telescopes. When all these conditions are fulfilled, the event is recorded (Paoletti et al., 2007).

Since recently, there is also a second trigger available in MAGIC, which allows to trigger even fainter events. This so-called analog sum-trigger makes use of the fact that independent random noise only grows with the square-root of the number of channels that are summed up in an analog way, while the signal from an actual cosmic event, distributed among several pixels, grows linearly. For this new trigger, overlapping patches of always 19 pixels are summed up and checked against a discriminator threshold. This condition can replace the standard "L1" trigger or be used in addition (Haefner et al., 2011, 2012).

The core element of the MAGIC readout system is the DRS4 waveform digitizer chip. The DRS4 chip is a switched capacitor array, developed at the at the Paul Scherrer Institute that can store 1024 samples of the waveform and can be operated at sampling speeds of 0.7 to 5GHz. The sampling speed used in the MAGIC readout system is 2GSamples/s, which provides a buffer length of 512ns. In case of a trigger event, only a certain region of interest (30ns long), where the actual signal is expected, is stored. The readout process itself happens at a much lower frequency and generates a deadtime of about 30μs for each event. At a typical Trigger rate of 250Hz, the deadtime fraction stays well below 1% (Tescaro, 2012).

3.2.4 *Software and analysis chain*

The data analysis software package developed, maintained and used by the MAGIC collaboration (MARS) is a set of executables and macros written in C++ that make extensive use of the ROOT (CERN data analysis framework (Brun & Rademakers, 1997)) libraries and its C++ interpreter CINT. The whole analysis chain can be divided into the following steps:

(i) Calibration – "Callisto"

(ii) Image-cleaning and -parametrization – "Star"

(iii) Calculation of the stereo parameters – "Superstar"

(iv) Gamma-hadron separation and energy estimation – "Melibea"

(v) Final products: detection plots – "Odie", skymaps – "Caspar" and energy spectra – "Flute"

In appendix D the working principle of some of the programs is described in more detail. This is to motivate some of the analysis steps that lead to the final results presented in the two main parts of this thesis.

Calibration, image-cleaning and -parametrization

The first two steps are usually done automatically, either on site or at a data center. In the first step, calibration ("Callisto"), ADC counts of the raw data are converted into photoelectron counts for each individual pixel. The output of this step is stored in the ROOT file format. The image cleaning is done by a program called "Star". The cleaning algorithm is using two different cleaning thresholds, where the lower one is typically half of the higher one. For all pixels in the image that exceed the higher threshold, all neighboring pixels are required to pass the lower one only. The remaining pixels are discarded. The next and final step performed by the program "Star" is the image parametrization using Hillas parameters (see section 3.1.4) and additional parameters, like timing information. Only the image parameters of each event are stored. All single pixel information gets discarded, keeping the data volume comparably low in the following steps.

Data selection and stereo-parametrization

The typical individual data analysis for the astronomer starts at the level of cleaned and parametrized events or "Star-files". This data is available for each telescope separately. At this stage, usually also the data quality selection, based on information about camera DC-currents, trigger rates and from auxiliary instruments monitoring the atmospheric conditions, is performed (see chapter 5). The remaining events are combined to stereo-events by a program called "Superstar". In this step additional stereo parameters like the altitude of the shower maximum and the direction of the shower are calculated.

Monte Carlo production

At this level, Monte Carlo simulations come into play. A large number of γ-induced air-showers is simulated with the CORSIKA program (Heck et al., 1998). The Cherenkov photons, that are emitted in the direction of the simulated location of the telescopes are propagated by a ray-tracing code ("Reflector") and converted into signal waveforms for each pixel in the camera simulation program ("Camera"). After that, the events undergo the same calibration, cleaning and parametrization procedure, like the real data.

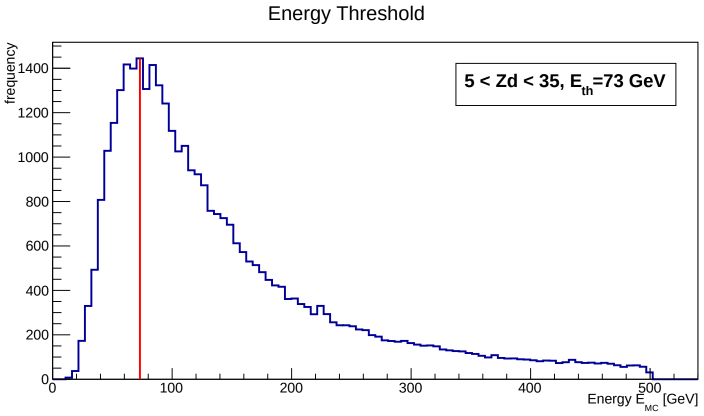

Figure 3.10: The energy threshold of an IACT is usually defined as the peak in the distribution of detected γ-ray events binned in energy. The energy threshold of the MAGIC telescopes was determined using MC data and reweighting the histogram to match the energy spectrum of the Crab Nebula.

Event classification and energy estimation

A machine learning algorithm called Random-Forests (Breiman, 2001) is trained with simulated γ-shower events and real data from a region in the sky where no source of γ-radiation is expected. Look-up tables are generated for the energy estimation. All this information is then used in a program called "Melibea" that later performs the energy estimation and stores a classifier to sort out hadron induced air-showers.

Final data products

There are a variety of programs for generating the final products of the analysis. Most recent and most popular are the following three: "Odie" for calculating excess and significance from a certain region around the source, "Caspar" for producing sky-maps of the source and searching for possible extension and "Flute" for computing energy spectra and testing time variation of the observed flux.

As already mentioned, a more detailed description of these final analysis steps can be found in appendix D.

3.2.5 *Sensitivity and performance of MAGIC*

For defining the scientific goals and for planning observations with MAGIC, it is important to know the performance of the telescope. For giving the reader an impression of what can be achieved with the MAGIC telescope system, a short overview of its sensitivity and performance will be given in the following.

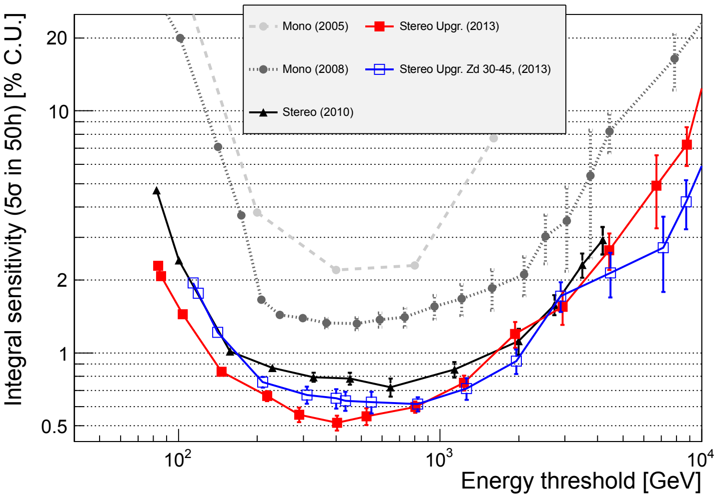

Figure 3.11: Integral sensitivity of the MAGIC telescopes after the last upgrade in 2012 (red, blue) and during previous development stages (black/gray). The Sensitivity is given in terms of an integral flux in units of the Crab Nebula flux, which is needed to reach a five σ detection within 50h. The plot has been taken from the post-upgrade MAGIC performance paper (Aleksic et al., 2014).

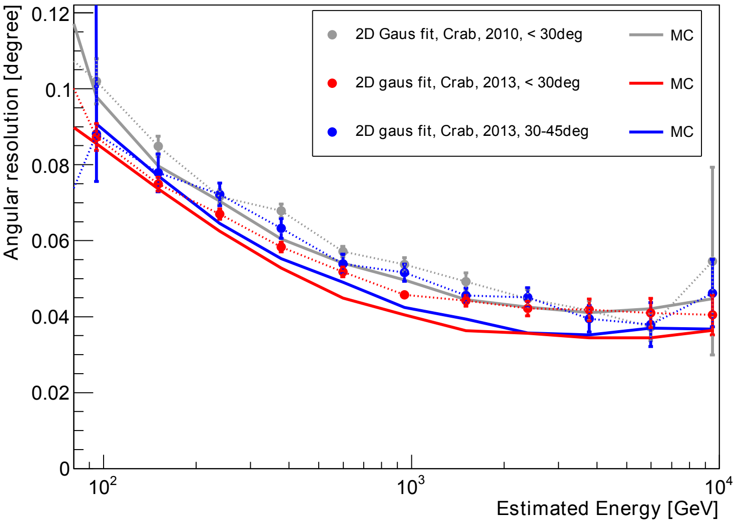

Figure 3.12: Angular resolution of the MAGIC telescope system, depending on the energy. The PSF has been determined by fitting a 2D Gaussian to the distribution of reconstructed directions from Crab nebula observations (datapoints) and MC (lines) for different Zd ranges. Plot taken from the post-upgrade MAGIC performance paper (Aleksic et al., 2014).

In the field of ground based γ-ray astronomy one usually defines the energy threshold as the location of the peak in the distribution of detected events binned in energy. This position is determined from MC simulations using a typical energy spectrum, similar to what is assumed from a potential source. Since the spectra of astrophysical sources of γ radiation usually have power-law shaped spectra with spectral indices typically between -2 and -3, this peak defines the low energy cut-off for the detectability of γ-rays. Figure 3.10 shows a histogram from which the energy threshold of the MAGIC telescopes can be determined. In this case a Crab-like spectrum is assumed and the Zd is between 5 ° and 35 °. The energy threshold in this typical example is 73 GeV.

In IACT astronomy, the integral sensitivity of a telescope is very frequently stated in units of Crab Nebula flux. This is then the minimum fraction of the Crab Nebula γ-ray flux, which is needed for detecting a source within 50 h on a 5σ significance level. In figure 3.11 the integral sensitivity curve for the upgraded MAGIC system, as determined by Aleksic et al. (2014), is shown.

The angular resolution or point spread function (PSF) of IACTs is the uncertainty of the arrival direction of γ-rays, as reconstructed from the air-shower images. Aleksic et al. (2014) have studied this using real Crab Nebula data and also MC simulations. The angular resolution or PSF is defined as the standard deviation of a 2D Gaussian fit to the distribution of reconstructed arrival directions. Depending on the observed energy it lies between 0.1 ° and 0.04 ° (see figure 3.12). The systematic uncertainty on the reconstructed source position is $\lesssim 0.02\,°$ (Aleksic et al., 2014)

The energy resolution of the MAGIC telescope system is a bit energy dependent. It is usually in the range between 15 % and 20 % on a relative scale. According to Aleksic et al. (2014), the systematic error is 10% on the energy scale and between 11% and 18% on the flux normalization.

All these parameters make MAGIC one of the most competitive telescopes for observing γ-rays above energies of about 70 GeV.

3.3 THE CTA PROJECT

In order to improve in sensitivity and resolution compared to the current generation of Cherenkov telescopes it is necessary to cover a large area on the ground and also to maximally exploit the advantages of stereoscopic observations. The Cherenkov Telescope Array (CTA), which is currently in the design an prototyping phase, will meet these requirements and enable astronomical studies with an increased sensitivity by about one order of magnitude. The plans foresee to install one array on each hemisphere for enabling observations of the entire sky. In its final phase of construction, each array will consist of a certain number of telescopes of three different size categories. The different size categories will allow to maximize sensitivity over a large energy range. The highest energy events ($E \gtrsim 5\,\mathrm{TeV}$) will be collected on a large area by about 30 so-called small size telescopes (SST). For improved

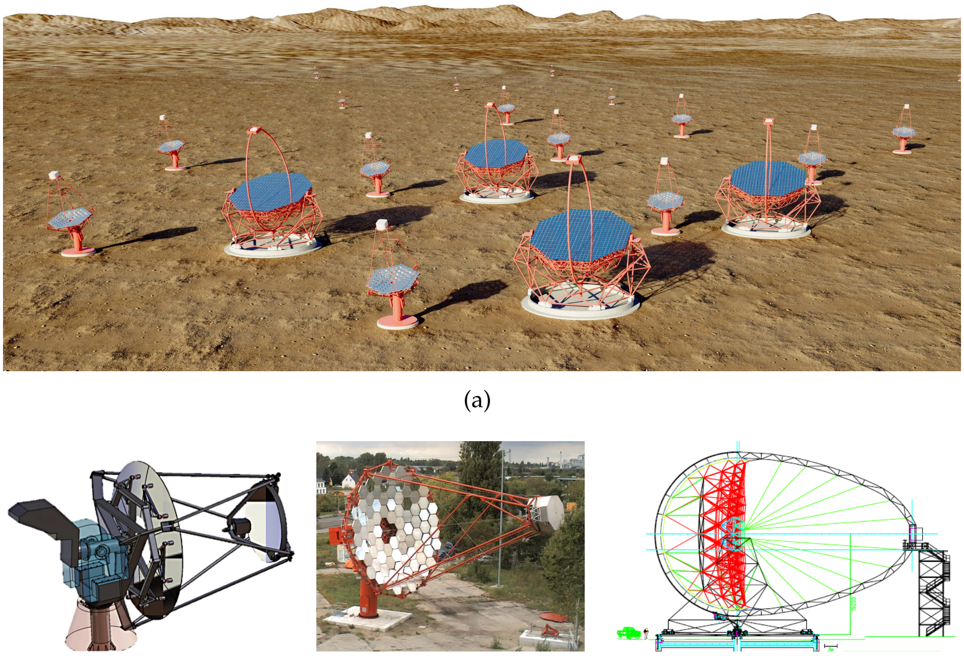

(a)

(b) (c) (d)

Figure 3.13: The Cherenkov Telescope Array (CTA) in its final state, 3D animation (a). Proposed design for the small size telescopes (SST) with Davis Cotton optics (b). Prototype for the mid size telescopes erected in 2013 in Zeuthen (Berlin) (c). Design concept of the 23m diameter large size telescope (d). Sources: CTA website (www.cta-observatory.org) and DESY website (astro.desy.de)

resolution in the mid energy range ($200\,\text{GeV} \lesssim E \lesssim 5\,\text{TeV}$) around 20 mid-sized telescopes (MST) will be employed. In order to establish maximum overlap with the *Fermi*-LAT, at the lowest energies ($30\,\text{GeV} \lesssim E \lesssim 200\,\text{GeV}$), ca. 5 large size telescopes (LST) will be placed in the middle of each array (Acharya et al., 2013) (see figure 3.13 for illustration).

3.3.1 *Hardware development for CTA*

In order to meet the technical requirements, necessary to ensure the desired high performance of CTA, many developments in hardware and technology were necessary. Most important was probably the improvement of light sensors in respect to the previous state-of-the-art designs. The peak quantum efficiency of the photo-cathode of photomultiplier tubes (PMTs) was increased from about 30% in current experiments to nearly 50% for the CTA candidate PMTs.

Not only the PMTs themselves have been optimized for their use in CTA, but also the light concentrators for maximizing the collection efficiency of the camera. In terms of this thesis work, a set of different designs of Winston cones has been characterized regarding their angular acceptance, also in combination with PMTs of different two different kinds of surface finishing. The results of this study can be found in appendix H.

3.3.2 *Site selection for CTA*

Another important aspect of the preparatory phase of the CTA project is the selection of the best suitable sites on both hemispheres. Requirements range from aspects like accessibility and political support/stability of the site/countries down to geographic latitude, altitude of the site, climatic conditions and light pollution. For evaluating the physically measurable parameters like weather and background light, apart from the extensive use of archival satellite data, also dedicated ground-based measurements were performed. For this purpose, grid independent solar-powered instrumented units, called ATMOSCOPEs were deployed at each site (Fruck, 2010). Their purpose was to collect data with uniform instrumentation from all sites, as well as to cross-calibrate already existing instruments for better comparison of archival data. For a detailed description of all aspects of the hardware of the ATMOSCOPEs refer to Fruck et al. (2015).

3.4 SOURCES OF VHE-γ RADIATION

This section will give a short summary of science goals pursued by Cherenkov telescopes and the astrophysical objects, which can be observed in order to accomplish them. As it is already motivated by chapter 2, a large part of the science goals of Cherenkov astronomy is strongly connected to the identification of the sources of cosmic rays. Nevertheless, Cherenkov telescopes, often in combination with data form other wavelengths, also allow for detailed studies of very high energy astrophysical phenomena and fundamental questions in physics, like dark matter searches and tests of Lorentz invariance.

3.4.1 *Active Galactic Nuclei*

Active Galactic Nuclei (AGN) are among the "classical" sources observed at VHE. There is a variety of astronomical classifications for those objects. All of them are thought to be galaxies having a super-massive black hole (SMBH) in their center, driving strong accretion-powered jets extending over several tens of kpc in length.

The objects, which are brightest in VHE γ-radiation are the so-called Blazars, AGN pointing their jets towards the observer. Those objects can reach super-Eddington luminosity and show ultra fast variability down to minute time-scale. Some of the nearest Blazars, when in high luminosity state, are the brightest objects that have ever been observed with IACTs. The large distance to those objects makes it impossible for Cherenkov telescopes to resolve them spatially. But the extremely broad band spectrum of electromagnetic emission that extends from radio waves up to VHE γ-radiation, in combination with fast spectral variability, enables to test models for jet-formation and particle acceleration inside those objects.

Apart from studying intrinsic physics of those objects, given the high luminosity, large distance, and high variability, they can also serve for more fundamental studies. One can probe the flux of the extra-galactic background light (EBL) by studying the attenuation of the VHE signal from very distant objects. The attenuation at $\sim$TeV energies is a result of the e^+e^--pair creation that can happen in $\gamma\gamma$ collisions of VHE radiation with optical photons (Ackermann et al., 2012; Mazin et al., 2013). The minute scale flares of very broad band electromagnetic radiation up to several TeV can be used to probe Lorentz invariance violation (Fairbairn et al., 2014). This is done by comparing the arrival times of γ-rays of different energies from a short-lived flare of a very distant AGN. Under the assumption that the production mechanism is emitting all energies at the same time, any possible delay would be due to Lorentz invariance violation or due to space-time micro-structure, which is only resolved by VHE γ-rays, due to their very short wavelength. A γ particle of 1 TeV can probe length scales of 10^{-18} m.

3.4.2 *Super Nova Remnants*

Super Nova Remnants (SNR) are the expanding leftovers of stars that experienced a supernova explosion. In-between a few hundred and several thousand years, those objects are ideal environments for cosmic ray acceleration. The reason is the formation of strong shocks, while they are expanding into the interstellar medium. SNRs are among the prime candidates for first order Fermi acceleration. Due to their typically large spatial extension, they can be resolved as extended sources with, even with the limited capabilities of

Cherenkov telescopes. This way it is possible to identify the emission regions of VHE γ-radiation, which can help to identify the production mechanisms.

In observations of the SNR W51C by MAGIC and other experiments it was possible to exclude all models, in which mostly electrons are accelerated. This source is the first clear candidate for galactic hadronic cosmic ray acceleration (Krause, 2012).

3.4.3 *Pulsars and PWN*

At the center of SNRs, a compact massive object is left behind. In-between the Chandrasekhar mass limit of $\sim 1.4\,m_\odot$ and the critical mass limit that will lead to the creation of a black hole, a neutron star is formed. Those objects that can be described as gravitationally bound states of pure nuclear material with increased electron concentration towards their crust have extremely strong magnetic fields ($B \approx 10^7 \,..\, 10^9\,\mathrm{T}$) and spin at high frequencies ($T \approx \mathrm{ms} \,..\, \mathrm{s}$). Even with surface temperatures of the order of $1 \cdot 10^6\,\mathrm{K}$, most of them are dominated by non-thermal emission of electromagnetic radiation. The first such objects were discovered as strong sources of pulsed radio emission, for example by Hewish et al. (1968). About one year later, optical and X-ray counterparts were discovered for the pulsar situated inside the Crab Nebula (Cocke et al., 1969; Fritz et al., 1969). It is the same object, in which also the first pulsed component was discovered in the VHE range by the MAGIC telescopes (Aliu et al., 2008). A little bit more detailed description of the physics inside pulsar magnetospheres can be found in chapter 2.3.3.

Apart from the pulsed emission of the neutron stars, young pulsars power large pulsar wind nebulae (PWN) of very energetic electrons an positrons. At the termination shock of these objects, particles can be accelerated to very high energies and emit synchrotron and inverse Compton radiation. One such object is the Crab Nebula, the brightest steady source that can be observed by Cherenkov telescopes. It therefore serves as standard candle for the field. While for the current generation of IACTs it is not possible to resolve the extension of this source, for CTA it might be, giving deeper insight into the production mechanisms of VHE γ-radiation.

3.4.4 *GRBs*

Gamma ray bursts (GRB) are very short lasting (seconds to minutes) events with extremely strong emission of electromagnetic radiation, mostly at high and very high energies (keV to GeV). They are usually observed at very large redshift ($\overline{z} = 2.8$, as stated by Jakobsson et al. (2006)), making them good probes for studying cosmology or Lorentz invariance. After studies by Kouveliotou et al. (1993), it is generally accepted that there are at least two different types of GRB events, so-called long and short GRBs. There is evidence that the long GRBs happen in supernova explosions (Pian et al., 2006) of extraordinarily massive stars (Fruchter et al., 2006), where the high energy emission is generated in bipolar jets breaking through the hulls of the progenitor star (Bromberg et al., 2012).

Cherenkov telescopes, so far, were not able to detect VHE γ-radiation from GRBs. This is, on one hand, due to the small FoV and the short durations of these events. On the other hand, also due to the large distance of the objects and thus the EBL absorption that swallows most of the VHE emission. The MAGIC telescopes run a unique alert and follow up program, that allows for pointed observations as fast as 20-30s after the detection by satellite experiments.

3.4.5 *Dark matter interaction/decay*

The most recent analysis of the data from the *Planck* mission have determined the matter density parameter of the universe to $\Omega_m = 0.315 \pm 0.017$ (Ade et al., 2013). Visible matter (i.e. stars, gas, dust etc.) can only account for a small fraction of this. A widely accepted model for explaining the missing matter fraction is the ΛCDM model, which assumes a cosmological constant Λ and dark matter (DM) that consists of weakly interacting heavy dark matter particles. Structure formation implies, that DM inhomogeneities must have played an important role in locally increasing the concentration of visible matter. Therefore, one expects high DM concentrations at places, where also the concentration of baryononic matter is high. Many theories predict decay or interaction channels that allow DM to be converted into Standard Model (SM) particles.

In such scenarios, depending on the exact mass and interaction/decay channels of the DM particles, also VHE γ-radiation could be produced. By observing regions with high matter concentration, IACTs can help probing the parameter space of ΛCDM models (Aleksić et al., 2011).

Part II

ATMOSPHERIC CALIBRATION

If one looks at Cherenkov telescopes from the particle physics point of view, rather than the astronomy one, the actual detector extends far outside the telescope or camera. Namely, it contains the atmosphere too. From this point of view, the air above the telescopes is part of the instrument. As simple and at the same time convincing this may sound, it imposes quite some problems when it comes down to calibration issues. In this part I will present the results from the effort that was made throughout this thesis in order to improve the accuracy of atmospheric calibration during adverse weather conditions in order to maximize observation time with the MAGIC telescopes.

4

THE INFLUENCE OF THE ATMOSPHERE

This chapter shall motivate briefly the importance of knowing the exact condition of the atmosphere for IACT astronomy and give a short characterization of the MAGIC site at the ORM on la Palma based on literature.

4.1 PRODUCTION AND TRANSMISSION OF CHERENKOV LIGHT

Cherenkov light, which is used for detecting VHE γ-rays by IACTs is typically emitted at $\approx 10\,\mathrm{km}$ above sea level (a.s.l.). for energies of the order of 100 GeV. See figure 4.1 (a) for an example profile. The spectral composition is shown in 4.1 (b). The unabsorbed spectral intensity strongly increases towards smaller wavelengths. At small wavelengths also the light extinction is very high, which leads to a peak in the absorbed spectrum a bit above 300 nm. Below 300 nm, absorption by ozone molecules is very strong. At longer wavelengths it is molecular Rayleigh scattering, which contributes most to the extinction of Cherenkov light (see figure 4.1 (c)). The impact of Mie and aerosol scattering can be highly variable. It depends on the dust/aerosol contamination of the atmosphere as well as on the formation of clouds and haze.

Also changes in the vertical atmospheric molecular density profile, depending on the temperature profile and geographic latitude, can have strong impact on the Cherenkov light intensity measured on the ground as it is shown by Bernlöhr (2000).

4.2 CHARACTERIZATION OF THE LA PALMA ORM SITE

Viewed form a global climatological perspective, the Canary islands are located at the border between the Hadley cell and the Ferrel cell, two of the three large scale atmospheric cells rotating in meridional direction. The Hadley cell is driven by hot, moist air rising to the top of the troposphere over the tropics and descending as cold and therefore dense air over the subtropics. The Ferrel cell in turn is not driven directly by thermal convection, but indirectly through the Hadley cell (Peixdto & Oort, 1992). The thermally driven meridional rotation under the effect of Coriolis forces gives rise to the well known zonal component of the dominant wind direction at different latitudes (Trade winds at typically $< 30\,^{\circ}$ latitude, Westerlies at typically $> 30\,^{\circ}$ latitude).

This global system of air circulation has two important implications for observational conditions on La Palma, given it's geographic location. First, La

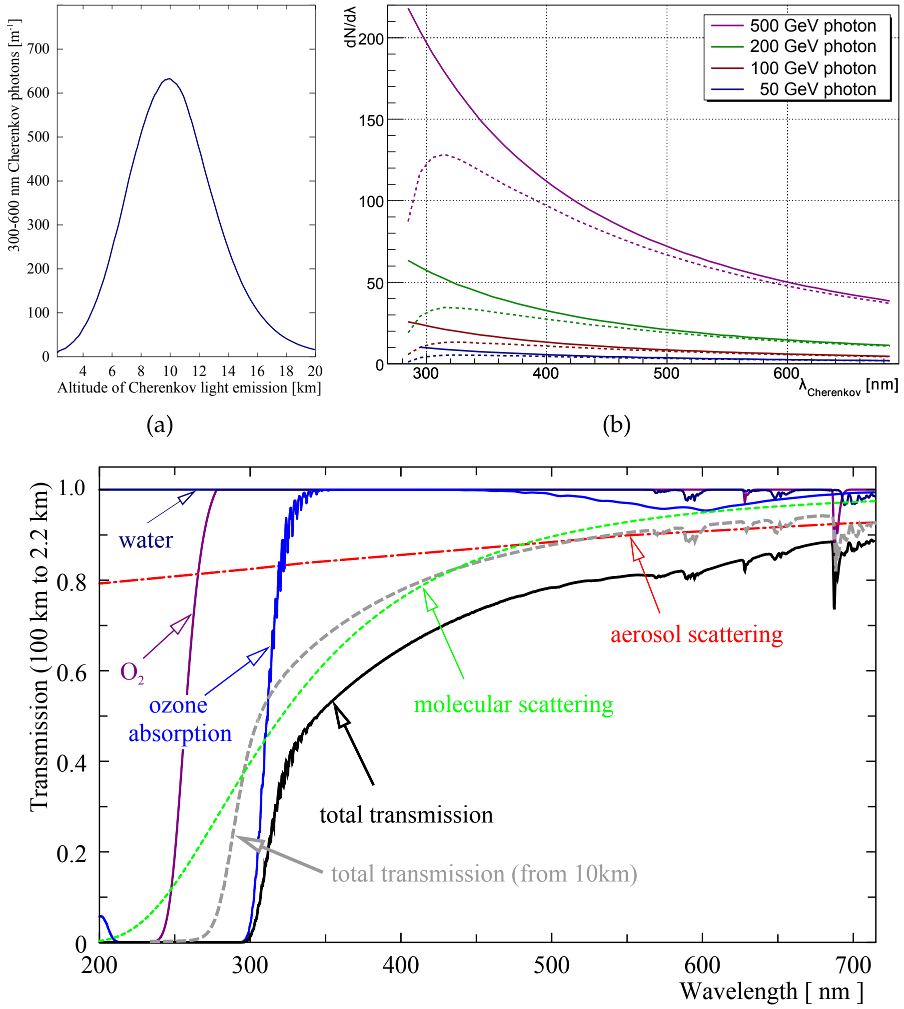

(a)

(b)

(c)

Figure 4.1: Average vertical light emission profile of a 100 GeV electromagnetic air-shower (a), unabsorbed (solid) absorbed (dashed) Cherenkov light spectra for different energies (b) and different mechanisms that lead to extinction of Cherenkov light, as well as the total extinction from 10 km and 100 km vs. wavelength (b). Data and plots taken from Bernlöhr (2000) (a,c) and Wagner (2006) (b).

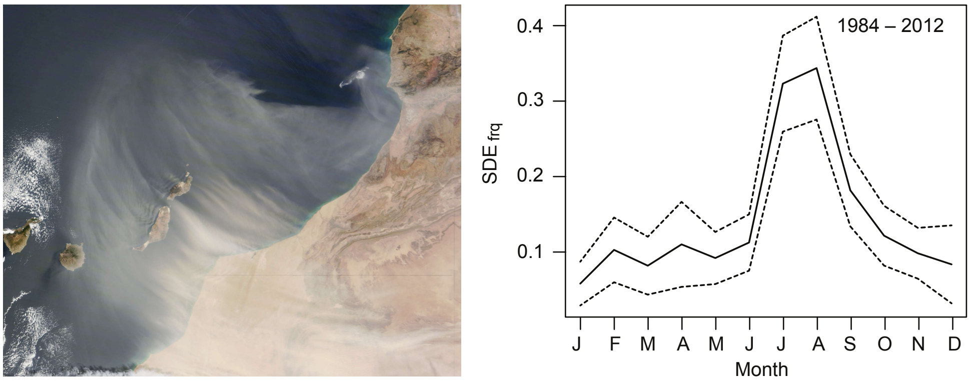

(a) (b)

Figure 4.2: Satellite image of a Saharan dust event over the Canary islands (a) (image source: NASA Earth Observatory[1]and average time fraction of Saharan dust influence throughout the year (solid line) with 1σ error region (dashed lines)(b), found in Laken et al. (2014).

Palma is located in a latitudinal zone of descending dry air originating from the top of the troposphere. Therefore typically very dry and nearly dust-free air is prevailing at the top of the mountain. Second, since La Palma is on the border of two zonal wind direction domains, influence from both, trade winds and Westerlies is possible. During the summer months the trade wind influence extends further north, while during the winter months influence of the Westerlies is strongest.

Both seasons bring different weather phenomena that can have negative influence on the observations by optical telescopes and IACTs. Moist maritime air brought over the Atlantic ocean by Westerlies during the winter months carries clouds also at medium and high altitudes, while trade winds often carry big amounts of Saharan dust over the Canary islands during the summer months (Fernandopullé, 1976). See figure 4.2 for a satellite image of a typical Saharan dust event.

4.2.1 *Clouds at the Roque de los Muchachos*

Generally, clouds are rare at the top of the Roque de los Muchachos, especially during the summer months when the trade wind influence is strong. Usually the ocean is covered by strato-cumulus clouds at altitudes of about 1 000 m a.s.l. where the temperature inversion is typically located (Fernandopullé, 1976). During the winter months Westerlies can bring cyclonic depressions over the Atlantic ocean with clouds at all altitudes. Also cirrus cloud bands passing over the Canaries from western directions are common during the winter.

---

[1] `http://earthobservatory.nasa.gov/`

4.2.2 *The Calima weather phenomenon*

Saharan dust events, often referred to as ***Calima*** by the local population, are characterized by decreased optical transmission and increased vertical extension of the planetary boundary layer (PBL) above the Canary islands. The Sahara is responsible for about half of the amount of desert aerosols that end up in the oceans world-wide (Goudie & Middleton, 2001). In the summer months (July – September) the average fraction of nights influenced by Saharan dust is about 30% during the last three decades (Laken et al., 2014).

4.2.3 *Night sky brightness on La Palma*

The light of the night sky (LoNS) brightness on the Roque de los Muchachos, with 21.9 mag arcsec^{-2} in the V-band, 22.7 mag arcsec^{-2} in the B-band and 22.0 mag arcsec^{-2} in the U-band during low solar activity and off-the galactic plane, is one of the lowest of all astronomical sites world-wide (Benn & Ellison, 1998). This is mainly due to special legislation, which regulates the type and brightness of outside lighting, especially street lights (Diaz-Castro, 1998).

5

INSTRUMENTATION FOR ATMOSPHERIC MONITORING

This chapter gives a brief overview of instruments used for atmospheric monitoring in the MAGIC experiment and describe a bit more in detail the MAGIC LIDAR system, which can provide precise and useful information that can be used for applying spectral corrections (see chapters 6 and 7).

Observations with imaging air-shower Cherenkov telescopes (IACTs) require the atmosphere as part of the detector for γ-radiation of cosmic origin. It provides target material for the high energy particles, is crucial for the emission of Cherenkov radiation and has to transmit Cherenkov light to the telescopes on the ground. Monitoring the weather and especially the optical properties of the atmosphere is necessary as part of the calibration of the overall detection method. Another reason, why monitoring the weather conditions on the MAGIC site is important, is that the MAGIC telescopes are operated in the open, without protective dome. Extreme conditions like strong wind, high humidity or ice formation may endanger safe operation. A variety of different instruments are operated alongside with the telescopes.

5.1 THE MAGIC WEATHER STATION

The MAGIC weather station provides basic weather information like outside temperature, humidity, wind speed and direction. The station is located outside on the control building and communicates to the central control computer via Ethernet. Reports from the weather station that are sent every second, are mainly used for assuring that the telescope is operated within safety limits. If any of those limits gets exceeded, a warning message for the operators is displayed and the observations are interrupted automatically. Figure 5.1(a) shows a picture of the Reinhardt[1] MWS 5MV weather station, which is used for MAGIC.

5.2 THE PYROMETER

Ambient temperature in the atmosphere is strongly altitude dependent. Inside the troposphere it decreases by about 1 °C every 200 m. The air in each layer radiates a characteristic thermal spectrum corresponding to the ambient temperature T. The total emitted power per unit area j^*, according to the Stefan–Boltzmann law is

$$j^* = \epsilon \cdot \sigma \cdot T^4 \,, \tag{5.2.1}$$

---

[1] `http://reinhardt-testsystem.de/`

(a) (b)

Figure 5.1: The weather station installed on the MAGIC control house is a Reinhardt MWS 5MV that can measure: wind speed and direction, temperature, relative humidity, dew point and barometric pressure. (a) The Heitronics KT19.82 pyrometer is mounted coaxially on the MAGIC I telescope and serves for detecting clouds by their thermal radiation, which is increased compared to the clear sky (b). (images: Reinhardt (2013); Heitronics (2013))

with σ the Stefan–Boltzmann constant and ϵ the emissivity. The emissivity depends on the thickness of the observed layer, as well as the constitution and the density of the air inside. When the layer contains big amounts of water vapor, dust or haze, the emissivity increases and with it the emitted radiance. Additionally, clouds are also reflecting partially the heat radiation emitted by the ground, which further increases their luminosity, also at higher altitudes. For this reason, a pyrometer can be used for detecting clouds in the line of sight if pointing up to the sky.

In the MAGIC experiment a Heitronics[2] KT19.82 pyrometer (fig. 5.1(b)) with a FoV of 2° is mounted coaxially on the MAGIC I telescope. The sky temperature is measured every 10 seconds and converted into an arbitrarily scaled floating point value between ~ 0 and ~ 100 that is already corrected for the effect of the zenith distance. That value is then written into the data stream and can later on be used for data quality selection.

5.3 OTHER TOOLS FOR JUDGING DATA QUALITY

Apart from the pyrometer data, there is a variety of other instruments and secondary information in the data, that can be used for quality selection. One of these values is the number of stars identified by the star-guider cameras of the MAGIC telescopes. To improve the pointing accuracy, both MAGIC

---

[2] `http://www.heitronics.com/`

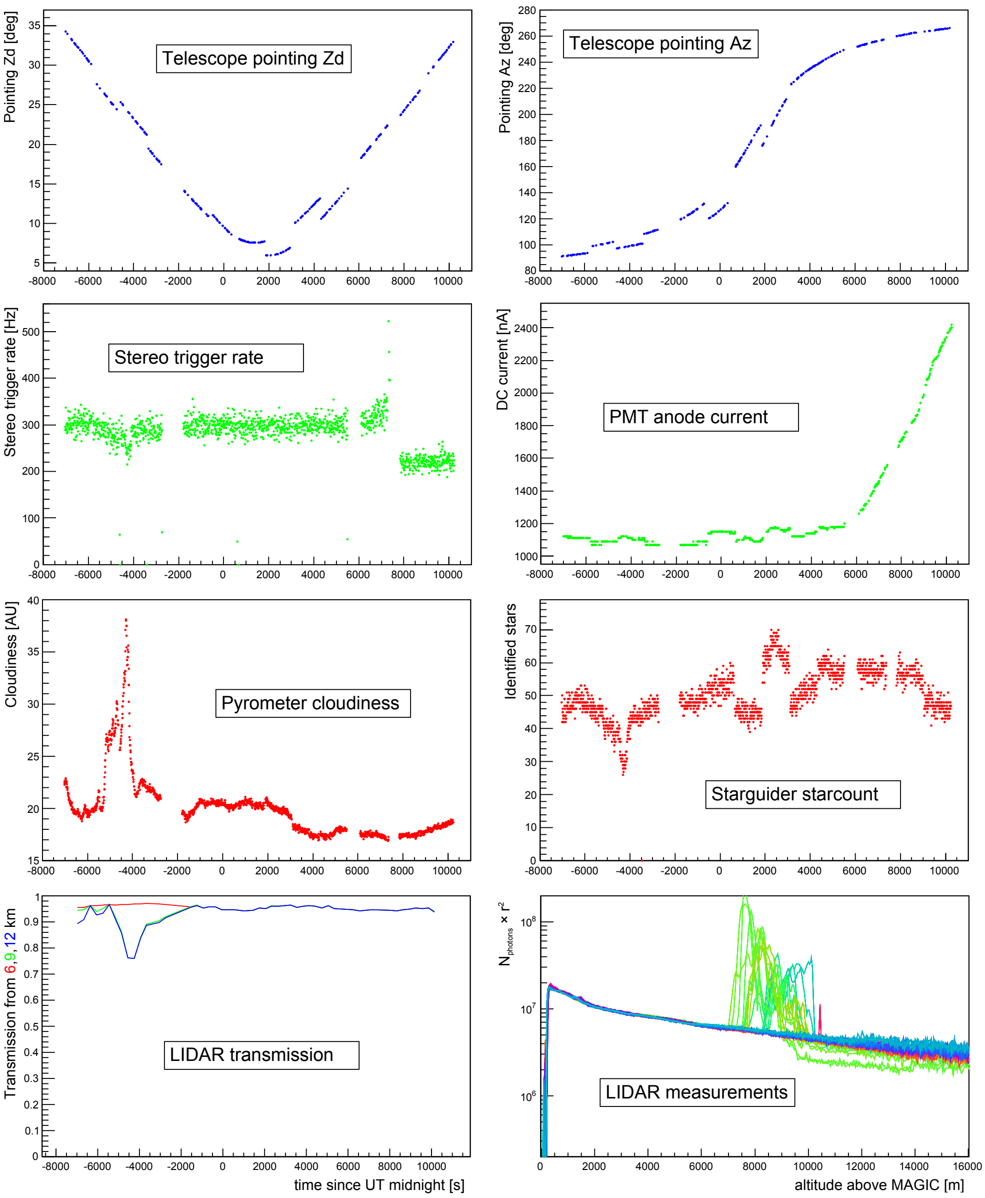

Figure 5.2: Auxiliary information that can be used for pre-selecting MAGIC data for analysis. Top to bottom: Pointing position of the telescopes. Stereo trigger rate and camera mean pixel DC current (system stability and light conditions). Pyrometer "cloudiness" and number of stars identified by star-guider (clouds/transparency of the atmosphere). Integral LIDAR transmission from different altitudes and single LIDAR measurements. The cloud at about 8 km altitude that enters the field of view of the telescopes at about $-5 \cdot 10^3$ s is very well visible in the LIDAR data. It reflects in an increased "cloudiness" value as well as a slightly reduced number of identified stars. A tiny effect is even visible in the stereo trigger rates. Moonrise at about $6 \cdot 10^3$ s reflects in the DC current, while the rate jumps to a lower value due to a change in the discriminator thresholds.

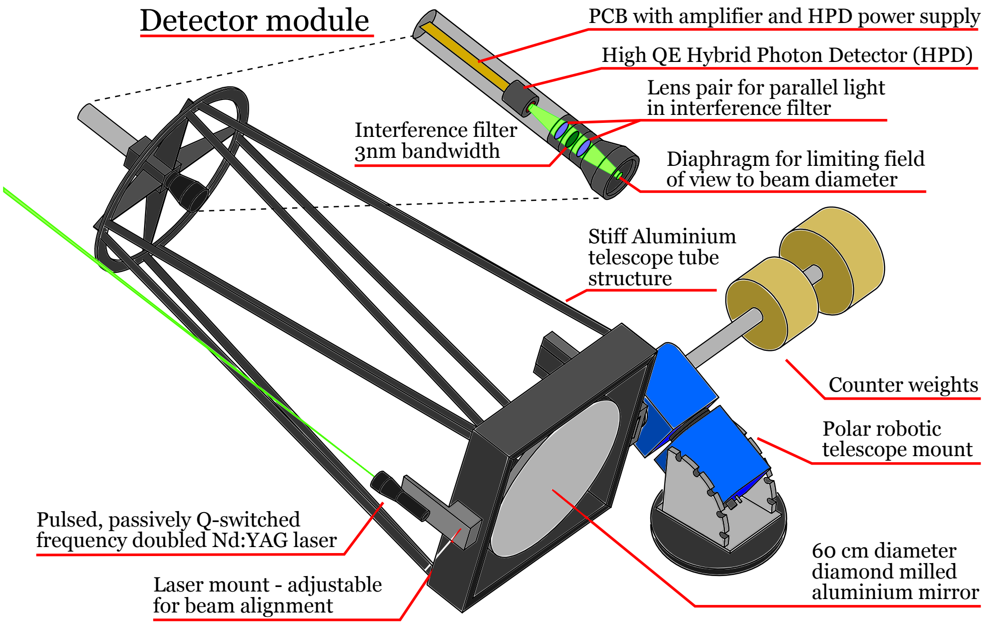

Figure 5.3: The MAGIC LIDAR system is based on a commercially available but reinforced equatorial telescope mount, the NTM 500 and a custom design telescope tube and mirror with 60cm in diameter. A frequency doubled Nd:YAG laser with a pulse width of 0.5 ns and 5μJ pulse energy is mounted on the side of the tube, parallel to the optical axis. The detector at the focal point uses a Hybrid Photo Diode (HPD) with a peak Quantum Efficiency (QE) of $> 50\%$ at the laser wavelength of 532 nm. It is operated behind a narrow band filter, in order to reduce background from the light of the night sky (LoNS).

telescopes use sensitive CCD cameras, mounted coaxially with the telescopes in the mirror dish. The star-guider program identifies a number of bright to medium faint stars and compares their location in the image to a star catalog. This information is then used for applying pointing corrections to the observational data. Apart from it's main purpose, the star-guider data can be used for judging the transparency of the atmosphere. The number of identified stars inside the field of view can be used to check the data quality when compared to a reference value for the same star-field corresponding to perfect conditions.

Other useful parameters for judging the quality of the data are the trigger rate of the system, as well as the PMT anode DC currents in the pixels. The latter can be used to quantify the light conditions during the observations. Figure 5.2 shows an example set of secondary data from observations of a single source that extended over nearly a whole night.

5.4 THE MAGIC LIDAR SYSTEM

The majority of the other instruments for atmospheric monitoring can provide

(a)

(b)

Figure 5.4: The upper image (a) shows the LIDAR telescope with laser and receiver, inside the dome, on top of the LIDAR tower. The MAGIC 2 telescope is visible in the background. The lower image (b) shows the LIDAR control room inside the lidar tower, below the platform. From left to right: mount control unit, NIM crate with trigger module, laser controller and HV supply, LIDAR PC hosting 4 GB of memory and a FADC card for digitizing and analyzing the analog signal.

information that is useful for data quality selection, but these cannot be used for recovering bad quality data. This is partially due to the qualitative nature of those parameters, but also because for correcting data from Cherenkov telescopes, knowing the integral atmospheric transmission alone is not enough. Cherenkov light from particle showers detected on the ground is generated at different altitudes. Therefore, an instrument is required that is able to measure a transmission profile of the atmosphere in the field of view of the telescopes. Light detection and Ranging (LIDAR) can provide such information but has two main disadvantages (see chapter 6 for a mathematical introduction to LIDAR). First of all, LIDAR as an active measurement technique has the potential to interfere with MAGIC data-taking or even disturb the observations of other near-by telescopes on the Roque de los Muchachos. Second, the inversion of LIDAR return signals is in general not an easy task. One usually applies techniques that require more powerful lasers in order to measure atmospheric transmission with high accuracy.

For the MAGIC experiment we managed to overcome these difficulties by using a custom design elastic "μ-LIDAR", based on single photon counting, and developing a specialized signal analysis algorithm. This combination allows for measuring atmospheric cloud/aerosol transmission profiles with reasonable precision, while keeping light pollution to a minimum. The LIDAR system is installed inside a small tower, on top of the MAGIC control building, $\sim$ 70m from both telescopes. The LIDAR telescope is located inside a protective dome that can be opened and closed remotely (see fig. 5.4(a)). The electronics and the computer running the control software are installed below the LIDAR platform, inside the tower (see fig. 5.4(b)). The LIDAR is operated together with the telescopes on a nightly basis.

Its operation has been automatized as far as possible as part of this thesis and is now part of the standard nightly observation procedure. Standard operation foresees one LIDAR measurement every 5 minutes, firing 50000 laser shots distributed over 3 minutes. The raw signal is analyzed online and the information is stored locally, as well as written into the data stream of the telescopes.

5.4.1 *The hardware components of the MAGIC LIDAR system*

This section provides a short overview of the most important hardware components on the LIDAR system.

the LIDAR mount

The MAGIC LIDAR system is based on a commercially available but reinforced[3] equatorial telescope drive, the NTM 500. The mount can carry the weight of all the other components, which is about 50 kg and still track positions in the sky with astronomical precision. It uses a gear-less electric drive

---

[3] An increase in motor power by a factor two was requested to the company.

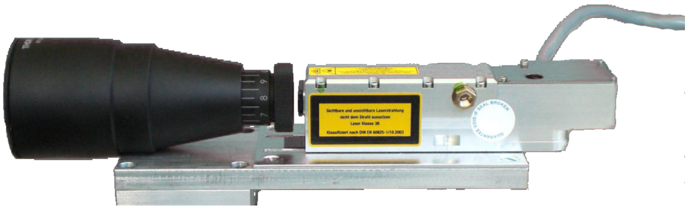

Figure 5.5: LIDAR laser with 10x beam expander. The laser is a frequency doubled Nd:YAG with 1μJ pulse energy and 500 ps pulse duration and can be fired at rates up to ∼2kHz. The 10x beam expander helps to reduce the light flux density, in order to enhance eye safety and to reduce the beam divergence to about $0.05\,^{\circ}$.

(direct drive) that allows for very fast repositioning and has a pneumatic braking system. The mount is connected to a computer control unit, that also provides power and pressurized air for the brakes. This control unit is connected to the main computer via Ethernet.

the LIDAR telescope

For collecting back-scattered light, the MAGIC LIDAR system uses a custom design telescope with a 60 cm spherical mirror made of a solid piece of Al. The optics are designed for LIDAR application. A single mirror helps minimizing the reflection losses and in addition is coated for maximum reflectivity at the laser wavelength of 532 nm. The F over d ratio of the system of 2.5 allows for a relatively compact size at maximum light collection.

the LIDAR laser

The laser, which is used in the MAGIC LIDAR system is a passively Q-switched, frequency doubled (532 nm) Nd:YAG laser, capable of firing pulses of 5μJ energy and 500 ps duration at a repetition rate of up to 2 kHz. The actual rate at which the laser is operated is reduced to $\sim$ 250 Hz, in order to not overload the MAGIC DAQ in the rare cases, when the LIDAR can stereo-trigger the telescopes[4]. The laser is combined with a $10\times$ beam expander, in order to lower the light flux density for eye safety reasons and to reduce the beam divergence to about 0.87 mrad.

the light detector unit of the LIDAR

The LIDAR detector is based on a so-called Hybrid Photo Diode (HPD), the Hamamatsu R9792U-40, which has already been discussed and tested as a possible future replacement for the MAGIC camera pixels (Orito et al., 2009). It provides a peak Quantum Efficiency (QE) of over 50% and is capable of

---

[4] In late 2013 an optical fiber transporting a trigger feedback from the LIDAR laser has been connected to the MAGIC trigger system. This enables to write a veto flag into the trigger pattern of affected events.

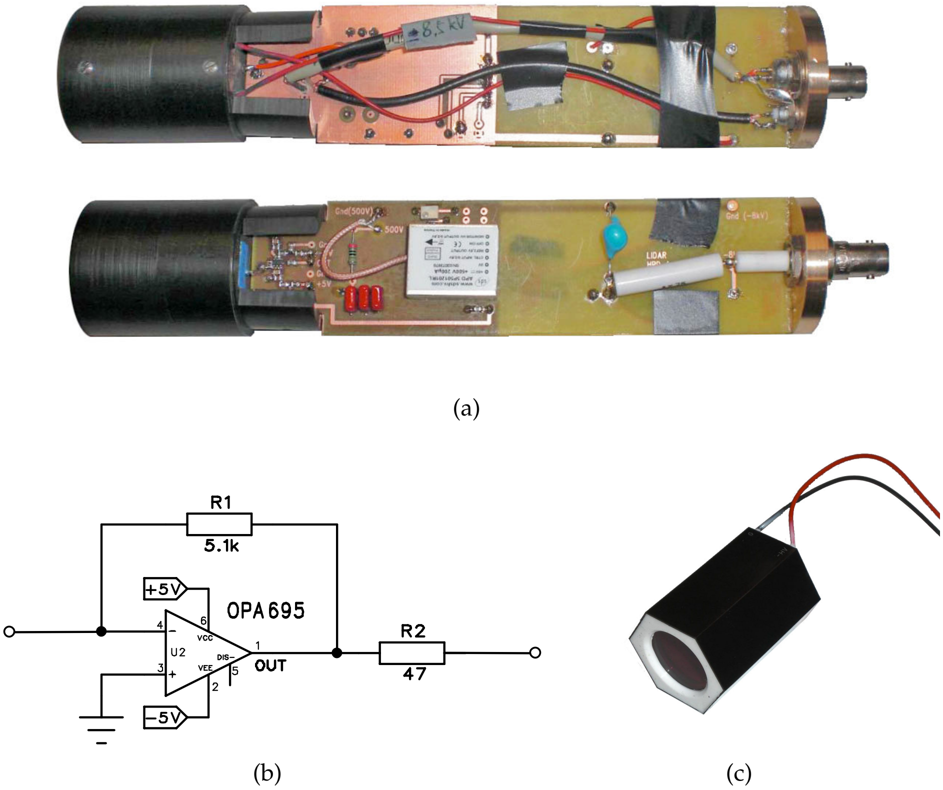

(a)

(b)

(c)

Figure 5.6: Front- and backside view of the LIDAR detector PCB, with the HPD on the left and the back-plane on the right side (a). The PCB is divided into 3 sections (from left): pre-amplification, as close as possible to the detector, AD bias supply with Cockcroft–Walton generator, producing ∼400V and HV area for connecting the photo-cathode to the external 6.5kV supply. As amplifier a OPA695 is used in trans-impedance mode with 5.1kΩ in the feedback (b). The actual detector, a Hamamatsu R9792U-40 Hybrid Photo Diode is shown in the right figure (c).

resolving single photon events. The HPD is installed behind a diaphragm and an interference filter with 3 nm bandwidth, for reducing the background from the Light of the Night Sky (LoNS). The electronic signal ($\sim 80000e^-$ in 2 ns for a single photo electron (ph.e.)) is pre-amplified right after the detector, for minimizing the effect of pickup noise.

The amplifier is an OPA695, which is operated in trans-impedance mode. It is directly connected to the HPD and uses 5.1kΩ as feedback resistor. See figure 5.6(b) for the schematics.

In addition to the amplifier, the detector unit also houses a Cockcroft–Walton generator for the AD bias voltage of about 400 V. The HV of 6.5 kV for the photo-cathode is provided by an external NIM module and fed through the back-plane.

For dealing with the strong temperature dependance in the gain of the avalanche diode (AD) of the HPD a temperature compensation circuit, similar to the one described by Saito et al. (2009) was added to the detector PCB, for compensating variations of the reverse bias voltage for the AD, due to temperature changes. The remaining effect has been treated by software (See section 5.4.2).

the LIDAR PC

The LIDAR main computer is a standard PC with 4GB of RAM and a 2.4GHz CPU (Intel Core 2 Quad). It serves for performing the online analysis of the LIDAR return, as well as running the operating software of the system. It also hosts important hardware elements for communication with the subsystems: A second Ethernet adapter, a 200 MSamples/s FADC card and a TTL IO card.

5.4.2 *LIDAR Software*

Major parts of the control and data analysis software for the LIDAR system were rewritten in the scope of this thesis, in order to establish automatic measurements, alongside with the observations by the MAGIC telescopes. The programming languages used for these programs are C++, partially making use of the ROOT data analysis framework libraries and LabVIEW. In the following, there will be a short summary of the LIDAR programs, describing their basic functionality.

the LIDAR measurement and data acquisition program

This program, written in C++, performs the actual LIDAR measurements. It reserves enough memory for storing one whole raw data-set before firing the laser for the desired number of shots. After each single shot, the signal waveform from the FADC is transferred to memory. Only when the recording of all shots has finished, the actual low-level data analysis starts.

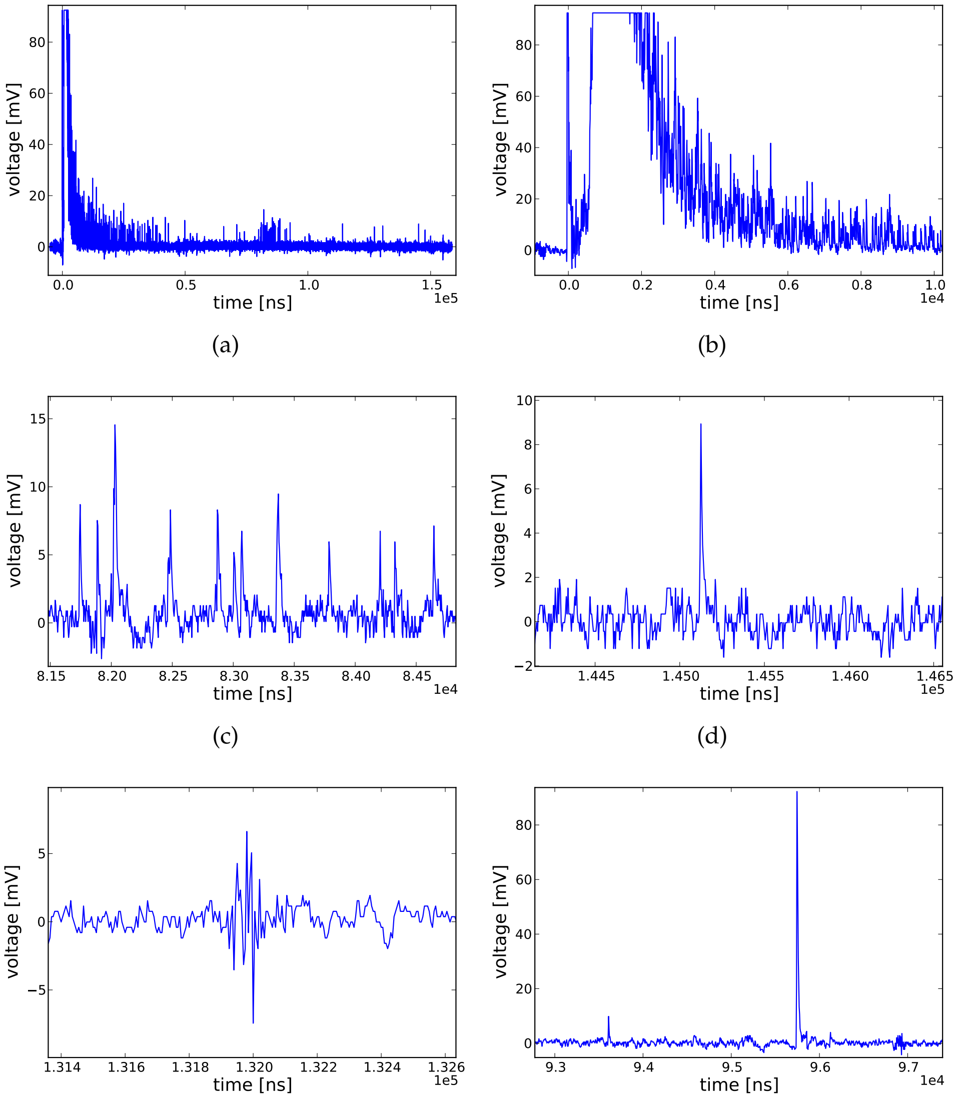

(a) (b) (c) (d) (e) (f)

Figure 5.7: FADC waveforms extracted from single LIDAR shots. The plots show: Full waveform of a single measurement (a). Near field region where charge integration rather than photon counting needs to be applied (b). Sample from the far field region where photon counting is applied with several single ph.e. events (c). Close up of one single ph.e. event (d). High frequency ringing noise that can be rejected using special photon counting algorithms (e). Ion feedback event in comparison to a single ph.e. event (f).

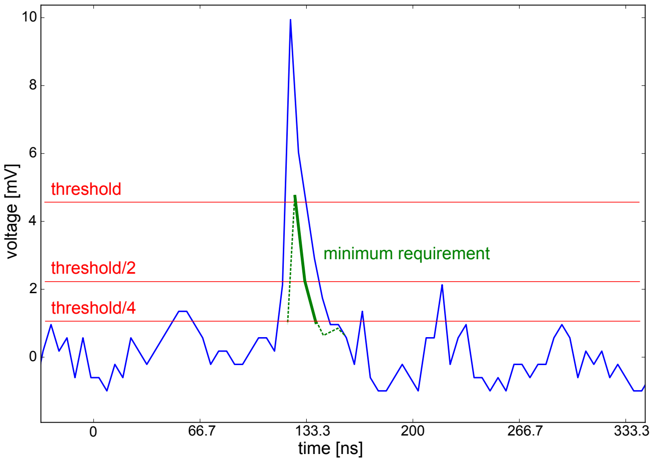

Figure 5.8: Photon counting algorithm for LIDAR using a multi-threshold criterion. This new algorithm accounts for the limited bandwidth of the amplifier, leading to a short exponentially behaving fall time of the pulses.

This second step has been improved in order to lower the background photon counts due to electronic noise and for providing a more reliable cross-calibration between single photon counting and charge integration mode. Because binary data of a single LIDAR measurement of 50000 shots consumes about 2 GB of memory, not all raw waveforms can be written to hard disk. For tracking hardware problems and optimizing the low level analysis methods, 20 waveforms are archived in binary format for each measurement as test sample. Figure 5.7(a) shows an example waveform of a single measurement.

LIDAR in general has to deal with a dynamic range of the return signal which is on the order of 10^6. On top, a low power system like the one described in this text is operating close to the noise limit at relatively long range, which is between 15 km and 20 km. These two facts have to reflect in the signal extraction algorithms, in order to cover a maximum dynamic range and at the same time suppress background/noise. The general concept for signal extraction is the following: The whole signal range is divided into two regions: a low and a high signal region. The near field/high signal region extends from 0 km to about 4 km distance from the telescope. In this region photons are detected at rates, which are so high that pileup of single ph.e. events occurs and charge integration, rather than single ph.e. counting is necessary (fig. 5.7(b)). In the far field region single ph.e. counting provides a better background rejection and is less sensitive to ion feedback events, which generate a lot charge concentrated in a single short pulse (fig. 5.7c,f). In addition to the back-scatter signal which is fully contained in the post-trigger region, both the pre- and post-trigger region contain background ph.e. counts from LoNS. This rate can be measured in the pre-trigger region and subtracted from the signal.

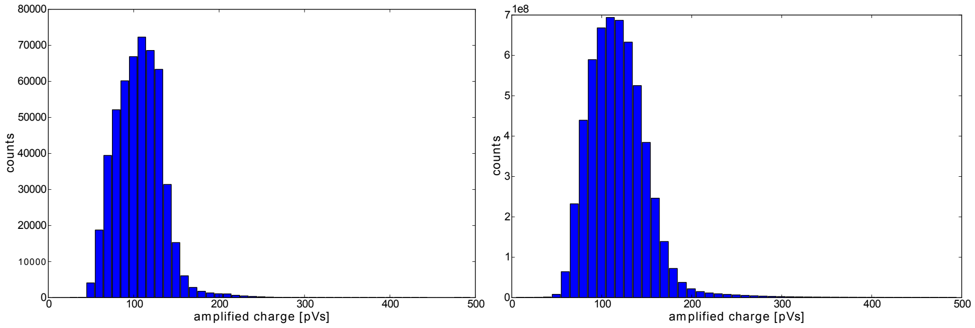

(a) (b)

Figure 5.9: LIDAR single photon charge histograms for a single measurement (a) and a larger sample covering about a year of LIDAR data.

The single ph.e. counting method has been improved in order to better reject high frequency noise as shown in figure 5.7(e) while still preserving maximum sensitivity, also for small amplitude ph.e. events. Such events are an unavoidable side effect of HPDs and occur when electrons are scattered back, off the avalanche diode, without depositing their full energy. Such events can also sum up with noise in a destructive way, further decreasing their amplitude. Single ph.e. events have a minimum width, as a result of the limited bandwidth of the amplifier. This can be used for distinguishing ph.e. from high frequency noise by requiring the following criterion:

$$V_{i-1} < V_i \cap V_i > V_{th} \cap V_{i+1} > \frac{V_{th}}{2} \cap V_{i+2} > \frac{V_{th}}{4}\,. \tag{5.4.1}$$

This concept is illustrated in figure 5.8. A second improvement to the low level LIDAR data analysis could be achieved by establishing better matching between the single ph.e. counting and the charge integration method. As mentioned in the description of the LIDAR hardware (section 5.4.1), the strong dependance of the overall gain on temperature could be counteracted by automatically adjusting the AD bias of the detector. The still remaining effect could be absorbed in the photon counting method. Instead of using a fixed ph.e. charge for conversion, this charge is now measured inside a reference region by integrating and averaging a large number of single ph.e. events. Again, for maintenance reasons the charge histograms that are recorded in that reference region for each LIDAR measurement are written to a file. The histograms for a single LIDAR measurement and for a large sample, which covers nearly a whole year are shown in figure 5.9. From comparing the width of the single measurement histogram to the width of the average one, one can conclude that the HPD gain stays reasonably stable.

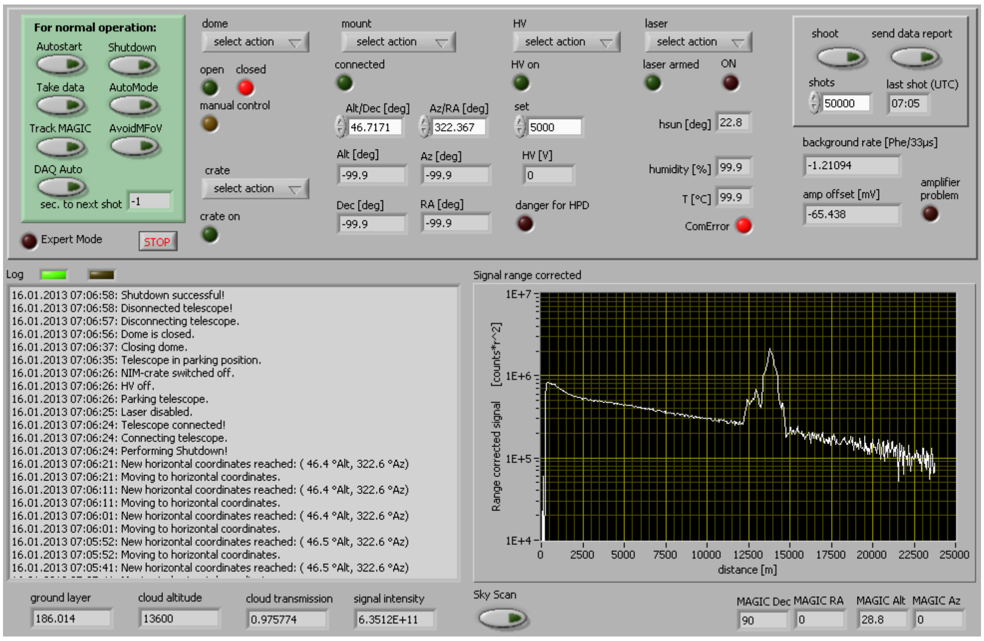

sec. to next shot -1

Alt/Dec [deg] 46.7171
Az/RA [deg] 322.367
Alt [deg] -99.9
Az [deg] -99.9
Dec [deg] -99.9
RA [deg] -99.9

set 5000
HV [V] 0

hsun [deg] 22.8
humidity [%] 99.9
T [°C] 99.9

shots 50000
last shot (UTC) 07:05
background rate [Phe/33µs] -1.21094
amp offset [mV] -65.438

```
16.01.2013 07:06:58: Shutdown successful!
16.01.2013 07:06:58: Disonnected telescope!
16.01.2013 07:06:57: Disconnecting telescope.
16.01.2013 07:06:56: Dome is closed.
16.01.2013 07:06:37: Closing dome.
16.01.2013 07:06:35: Telescope in parking position.
16.01.2013 07:06:26: NIM-crate switched off.
16.01.2013 07:06:26: HV off.
16.01.2013 07:06:26: Parking telescope.
16.01.2013 07:06:25: Laser disabled.
16.01.2013 07:06:24: Telescope connected!
16.01.2013 07:06:24: Connecting telescope.
16.01.2013 07:06:24: Performing Shutdown!
16.01.2013 07:06:21: New horizontal coordinates reached: ( 46.4 °Alt, 322.6 °Az)
16.01.2013 07:06:21: Moving to horizontal coordinates.
16.01.2013 07:06:11: New horizontal coordinates reached: ( 46.4 °Alt, 322.6 °Az)
16.01.2013 07:06:11: Moving to horizontal coordinates.
16.01.2013 07:06:01: New horizontal coordinates reached: ( 46.4 °Alt, 322.6 °Az)
16.01.2013 07:06:01: Moving to horizontal coordinates.
16.01.2013 07:05:52: New horizontal coordinates reached: ( 46.5 °Alt, 322.6 °Az)
16.01.2013 07:05:52: Moving to horizontal coordinates.
16.01.2013 07:05:41: New horizontal coordinates reached: ( 46.5 °Alt, 322.6 °Az)
```

ground layer	cloud altitude	cloud transmission	signal intensity
186.014	13600	0.975774	6.3512E+11

MAGIC Dec	MAGIC RA	MAGIC Alt	MAGIC Az
90	0	28.8	0

Figure 5.10: New user interface, developed in the frame of this thesis, of the MAGIC LIDAR system. The graphical user interface is based on LabVIEW, which then accesses separate executables and and drivers for communication with the hardware components. The most important automatic procedures are highlighted for the operator by placing them inside the green box in the top left. These commands are also available through TCP/IP commands received from the MAGIC central control program and do not need direct interaction of the user with the LIDAR computer. More specific functionality, mainly for testing and maintenance is available from the sub-system drop-down menus. Important parameters and system state indicators are displayed below the drop-down selector for the corresponding subsystem. The two big windows display the system log, listing the latest commands, actions and error messages (left) and the latest LIDAR measurement as range corrected photon counts (right).

the LIDAR control program and graphical user interface

Another piece of software that needed to be heavily modified in order to allow for leaving the test-phase and entering normal operation is the LIDAR control program. It is written in LabVIEW and serves as user interface, as well as for managing the interaction of all LIDAR subsystems. A variety of safety checks and automatic routines have been added in order to simplify operation for the user and for preventing damage to the hardware. Humidity and the detector DC current are constantly monitored and a safety ramp-down of the high voltage is issued whenever the limits are exceeded. The LIDAR is also receiving information from the central control (CC) of the telescopes. This information includes the pointing position of MAGIC as well as weather data. During strong winds, high humidity or with sunrise approaching, the whole system shuts down automatically. Another advantage of the data-stream that is received from the CC is that it allows for slave-tracking of the pointing position of the telescopes. Normally, the LIDAR is not pointed exactly at the observed sky coordinates. Its pointing is off-set by 5 ° towards a direction that does also take into account the relative geographic position of the telescopes, for not shooting the laser inside or through the MAGIC FoV.

Figure 5.10 shows the user interface of the new LIDAR program. All subsystem functionality can be accessed through drop-down menus. Additionally, in order to simplify operation, automatic routines for start-up, shutdown and continuous data-taking are available. In fact, for standard observations with MAGIC, operating the LIDAR does not even require the shifters to access the LIDAR user interface. All automatic routines can be launched directly over Ethernet from the CC interface.

6

ANALYZING LIDAR DATA

This chapter covers analysis methods for deriving physical information like back-scattering and attenuation coefficients from LIDAR return signals. In the first section the LIDAR equation is introduced as well as some standard inversion algorithms and LIDAR techniques. In the second section a new method, which was developed for testing energy corrections for MAGIC data, to be discussed in chapter 7, is presented. Finally, LIDAR data recorded during a full year of parallel operation with MAGIC is used for characterizing the MAGIC site from the cloud/aerosol points of view.

6.1 THEORETICAL INTRODUCTION TO LIDAR

This section will give a theoretical introduction to LIDAR and shortly introduce some standard techniques for analyzing LIDAR returns, starting from the LIDAR equation.

6.1.1 *The LIDAR equation*

In general, LIDAR needs a light emitter, usually a pulsed laser, and a receiver, in most cases using light concentrating optics that are aligned with the light beam, for increasing the collection efficiency for back-scattered light. The transmitted light pulse (N_0 photons) is affected by scattering and absorption on its way through the examined optical medium. Part of that light gets back-scattered to the detector where it is recorded in the form of a photon counting rate $\mathrm{d}N(t)/\mathrm{d}t$. This number can be converted to photons per distance element $\mathrm{d}N(r)/\mathrm{d}r$, $\mathrm{d}r = 1/2\, c\, \mathrm{d}t$. The rate measured by the receiver is determined by the volume back-scattering coefficient $\beta(r)$, the solid angle of the detector as seen from the point of scattering A/r^2, where A is the collection area of the receiver, the overall photon counting efficiency C and the geometric overlap of emitted beam and detector FoV $G(r)$. In addition, the light is affected by attenuation all along its path up to the point of scattering and back. The total extinction τ is determined by the exponential of minus two times the integral over the volume extinction coefficient $\alpha(r)$.

$$\tau(r) = \exp\left(-2\int_0^r \alpha(r')\mathrm{d}r'\right) . \tag{6.1.1}$$

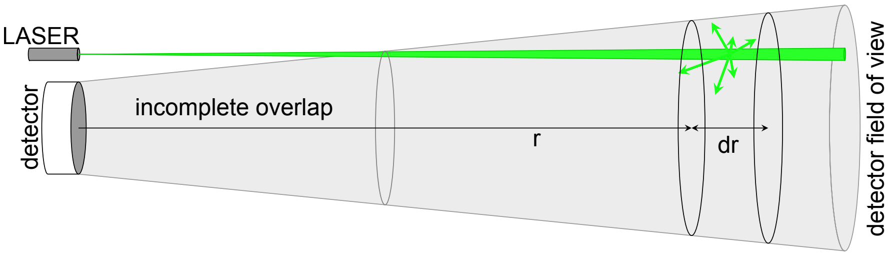

Figure 6.1: LIDAR uses short pulses of light, usually emitted by a laser, that are then back-scattered in a medium at a distance r and received by a detector. The detector counts photons per time element $\mathrm{d}t$, which corresponds to a range element $\mathrm{d}r = 1/2 \cdot c \cdot \mathrm{d}t$. The laser beam is not necessarily contained inside the field of view of the detector for the whole range. This behavior is described by an overlap function or geometric factor $G(r)$.

Putting everything together, the full LIDAR equation for single scattering is obtained (see figure 6.1 for illustration).

$$\frac{\mathrm{d}N(r)}{\mathrm{d}r} = N_0\, C\, G(r)\, \frac{A}{r^2}\, \beta(r)\, \exp\left(-2\int_0^r \alpha(r')\mathrm{d}r'\right) . \tag{6.1.2}$$

For most applications, the strongest dependency of $\mathrm{d}N/\mathrm{d}r$ is the one on the square of the distance to the detector. On the other hand, this dependency does not carry any information about the physical properties of the atmosphere. It is therefore convenient to introduce the so-called range-corrected LIDAR return

$$S(r) = \frac{\mathrm{d}N(r)}{\mathrm{d}r}\, r^2 . \tag{6.1.3}$$

The LIDAR equation can be brought into an even more mathematically elegant form, where the r^2 dependency and the exponential function are absorbed into a signal function $\Sigma(r)$[1].

$$\begin{aligned} \Sigma(r) &= \ln(N(r)\, r^2) \\ &= \ln\left(N_0\, A\, l\right) + \ln\left(\beta(r)\right) - 2\int_0^r \alpha(r')\mathrm{d}r' . \end{aligned} \tag{6.1.4}$$

In the following last step, differentiation by r removes the integral and reveals the basic structure of the differential equation, as well as the main problem for finding analytic solutions.

$$\frac{\mathrm{d}\Sigma}{\mathrm{d}r} = \frac{1}{\beta}\frac{\mathrm{d}\beta}{\mathrm{d}r} - 2\alpha . \tag{6.1.5}$$

In the most general case $\beta(r)$ and $\alpha(r)$ are independent, which makes it impossible to invert LIDAR returns without any additional information available.

---

[1] In the literature one also finds S as symbol for the signal function. Here, for convenience S is chosen for the range corrected return.

The next section will deal with some special cases, assumptions and methods that allow for calculating β and α from Σ.

6.1.2 *Inversion of the LIDAR equation for some special cases*

Inversion of the LIDAR equation is possible, whenever there is a known relation between the volume back-scattering β and the volume attenuation coefficient α. The quotient of α over β is also called LIDAR ratio K. For a given type of scatterer and wavelength, the LIDAR ratio is constant. This allows for inverting the LIDAR equation for special situations like for example pure Rayleigh scattering.

Slope method

For a homogenous atmosphere where $\mathrm{d}\beta/\mathrm{d}r$ is zero, equation 6.1.5 becomes

$$\alpha = -\frac{1}{2}\frac{\mathrm{d}\Sigma}{\mathrm{d}r}\,. \tag{6.1.6}$$

The inversion of the LIDAR equation for that simple case is called slope method, because the slope of $\Sigma(r)$ determines the volume attenuation coefficient $\beta(r)$. However, for practical application, this method can not be used because the LIDAR returns are usually dominated by variations in the density of scatterers (Kunz & de Leeuw, 1993).

Forward integration

Klett (1981) pointed out that for applications, where aerosol-scattering is the subject of interest, a power-law relation between β and α can be assumed.

$$\beta = \text{const.}\ \alpha^k\,. \tag{6.1.7}$$

It is also stated there that k usually lies in the range 0.67 .. 1. With such a relation, the differential equation 6.1.5 is no longer under-determined and can now be written as follows:

$$\frac{\mathrm{d}\Sigma}{\mathrm{d}r} = \frac{k}{\alpha}\frac{\mathrm{d}\alpha}{\mathrm{d}r} - 2\alpha\,. \tag{6.1.8}$$

This differential equation can be solved more easily by introducing a new function y that is the inverse of α.

$$\frac{\mathrm{d}y}{\mathrm{d}r} = -\frac{1}{k}\frac{\mathrm{d}\Sigma}{\mathrm{d}r}x - \frac{2}{k}\,. \tag{6.1.9}$$

The following function solves the homogenous part of the equation.

$$y_h(r) = C\exp\left(-\frac{1}{k}\,\Sigma(r)\right). \tag{6.1.10}$$

A particular solution for the non-homogeneous part can be obtained by the method of variation of parameters.

$$C(r) = \frac{2}{k} \int^{r} \exp\left(\frac{1}{k}\,\Sigma(r)\right) \mathrm{d}r' . \tag{6.1.11}$$

Then the general solution for y is

$$y(r) = \left(C_0 - \frac{2}{k} \int^{r} \exp\left(\frac{1}{k}\,\Sigma(r)\right) \mathrm{d}r'\right) \cdot \exp\left(-\frac{1}{k}\,\Sigma(r)\right) . \tag{6.1.12}$$

The still open boundary condition can be chosen such that $\alpha_0 = \alpha(r = r_0)$ is known for some distance r_0. C_0 can then be determined to

$$C_0 = \frac{\exp\left(\frac{1}{k}\,\Sigma_0\right)}{\alpha_0} . \tag{6.1.13}$$

Taking the inverse of Eq. 6.1.12 and inserting C_0 results in the solution for $\alpha(r)$.

$$\alpha(r) = \frac{\exp\left(\frac{\Sigma(r)-\Sigma_0}{k}\right)}{\frac{1}{\alpha_0} - \frac{2}{k} \int_{r_0}^{r} \exp\left(\frac{\Sigma(r)-\Sigma_0}{k}\right) \mathrm{d}r'} . \tag{6.1.14}$$

As nicely demonstrated by Klett (1981), this form of the solution tends to be numerically unstable even for small errors. The author argues that this is because α is the ratio of two numbers that become smaller and smaller, while the numerical algorithm progresses to smaller r. The denominator being the difference of two large numbers then leads to numerical instability.

The Klett algorithm

In order to circumvent the difficulties regarding numerical instabilities of the forward integration method, Klett (1981) proposed a new method, where the integration constant C is not evaluated close to the detector but at some distant reference range r_m

$$C_m = \frac{\exp\left(\frac{1}{k}\,\Sigma_m\right)}{\alpha_m} . \tag{6.1.15}$$

The solution for $\alpha(r)$ is then obtained by back-integration from r_m.

$$\alpha(r) = \frac{\exp\left(\frac{\Sigma(r)-\Sigma_m}{k}\right)}{\frac{1}{\alpha_m} - \frac{2}{k} \int_{r}^{r_m} \exp\left(\frac{\Sigma(r)-\Sigma_m}{k}\right) \mathrm{d}r'} . \tag{6.1.16}$$

Using this method, the denominator and the enumerator become successively larger in each step. This leads to numerically more stable results that converge to the correct values, even for slightly wrong starting values α_m and k or noisy signal at large distance.

Unfortunately, this method is suitable only for single component atmospheres. Such conditions are given for aerosol LIDARs operating at near infrared wavelengths for example. At 532 nm aerosol scattering and Rayleigh scattering are different mechanisms of comparable influence and can not be well described by a single power-law index k. For analyzing the signals obtained with the LIDAR system operated at the MAGIC site, a specialized method has been developed that explicitly benefits from the two component nature of the scattering mechanisms (see section 6.2).

6.1.3 *Techniques using multiple wavelengths*

There are a many different LIDAR techniques available for a large variety of applications, many of them using relatively powerful lasers and multiple wavelengths for dealing with multi-component atmospheres. The most common of them, for completeness, will be described shortly in the following. More information can be found for example in Measures (1992).

Raman LIDAR

The Raman LIDAR technique can separate aerosol from molecular scattering by observing the Raman part of the molecular scattering. Raman scattering is inelastic molecular scattering, where in addition to the re-emission of a photon, also rotational or vibrational states of the molecule are excited/relaxed, resulting in a characteristic shift of the wavelength. The intensity of the Raman signal is about three orders lower than the Rayleigh one. Aerosol scattering does not contribute light in the wavelength regime of the Raman lines and can therefore be separated from the molecular part. Using multiple wavelengths, comparing the relative strength of Raman scattering or looking at specific Raman lines, one can even examine the molecular composition of the atmosphere, scanning for water vapor for example.

High spectral resolution LIDAR

This technique is again aiming at spectroscopically separating the molecular part from aerosol scattering using differences in the physical properties of air molecules compared to aerosol particles. Here the characteristic average velocity of gas molecules due to thermal motion compared to aerosol particles is used. While the velocity of aerosols is negligible, molecular motion leads to a spectral broadening of the order of 10^{-6}. If one manages to cut out the central wavelength with sufficient precision, one can again separate the molecular from the aerosol scattering part.

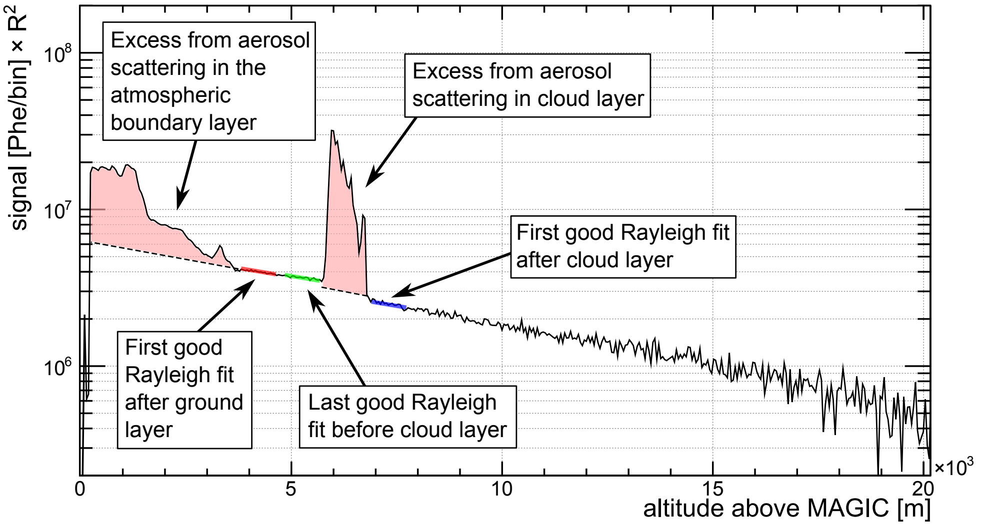

Figure 6.2: Example of a real data LIDAR return with cloud profile at mid altitude. The cloud transmission measurement algorithm is explained by means of this example. Regions with clear air have a highly dominant Rayleigh scattering contribution to the back-scattering cross-section. For this reason, the signal nearly perfectly scales with the exponential density profile of the atmosphere. This property can be used for measuring the transparency of cloud layers, in between two clear air regions by fitting an exponential air density model. The ratio of the scaling constants of the fits gives the relative light attenuation for double transmission (up and down after Rayleigh scattering).

Differential apsorption LIDAR

Differential absorption LIDAR is used to measure concentrations of chemical substances throughout the atmosphere. The two laser wavelengths are chosen such that one lies directly on top of an absorption line of the gas that one likes to search for and the other one is of similar wavelength but not affected by absorption. The ratio of the two LIDAR returns is directly linked to the concentration of the gas of interest.

6.2 ANALYZING DATA FROM THE MAGIC LIDAR SYSTEM

This section will introduce a method for analyzing the return signals of single-wavelength, "micro"-power Rayleigh LIDAR, in this context meaning wavelengths with comparable back-scattering contribution from molecular and aerosol scattering at very low power, which makes single photon counting inevitable.

The raw information from LIDAR, which is stored together with MAGIC data for analysis, is in the form of photon counts in bins of 48m distance. This number, as already described in section 6.1.1, spreads over a very large dynamic range. It's magnitude is mainly dominated by geometry and only secondarily by the atmospheric profile in the line of sight in front of the instrument. For this reason it is more convenient to use the so-called range corrected LIDAR return $S(r)$ (eq. 6.1.3). This is already corrected for the dominant r^{-2} scaling of solid angle that the mirror of the LIDAR telescope offers to the back-scattered light. Interpretation of the LIDAR return becomes easier when displaying the signal with logarithmic axis scaling on the signal-axis like in the real-data example in figure 6.2.

In regions with clear air, where Rayleigh scattering is dominating at 532nm, two effects lead to a very close to exponentially decreasing value of $S(r)$. The first and more important one is the density profile $\rho(h)$ of the atmosphere that roughly follows the barometric formula

$$\rho(h) \approx \rho_0 \exp \frac{h - h_0}{h_s} = \rho_0 \exp \frac{h - h_0}{\frac{RT}{Mg}} . \tag{6.2.1}$$

ρ_0 is the air density at reference altitude h_0 and h_s is the scale height of the atmosphere, containing the universal gas constant R, the temperature T (assumed to be constant here), The molar mass of air molecules M and the gravitational acceleration g. h_s is typically of the order of 8 km. In a real atmosphere, the temperature is of course altitude dependent, which results in a slightly different density profile that can be approximated with an exponential one with larger scale height. The second one is the attenuation of the light pulse by the total Rayleigh scattering cross-section α_{mol} on the way, which is similar to exponential too but less important, due to the relatively high transparency of air at 532nm. In result, clear-air regions appear as straight line sections in the semi-logarithmically scaled signal plot. Every atmospheric impurity, like from clouds or aerosols, adds additional back-scattering to the signal and causes an increase in magnitude of $S(r)$. Of course, the increase in back-scattering inevitably adds to the total scattering cross-section and therefore to the extinction coefficient $\alpha(r)$ as well. This leads to a drop of $S(r)$ below the extrapolation of the previous straight line fit from the clear air region, latest if a second clear air region after the region with enhanced back-scattering is reached (see figure 6.2). The ratio of the scaling constants of the fits, using the same slope/atmospheric scale height, gives the relative light attenuation for transmission up through and back through the cloud layer.

An automatic LIDAR data analysis algorithm has been developed and implemented in MARS (the MAGIC standard analysis framework) in the scope of this thesis. The final product of this algorithm is a transmission profile of the non-Rayleigh scattering components (i.e. clouds, aerosols, etc.) of the atmosphere for each LIDAR measurement. The algorithm uses a sliding window for fitting a clear-air pure-Rayleigh barometric-density-profile model $S_{\text{mol}}(r)$ to the selected regions.

$$S_{\text{mol}}(r) = C \cdot \exp \frac{r}{r_s} = C \cdot \exp \frac{r}{\frac{h_s}{\cos Zd}} . \tag{6.2.2}$$

Zd is the Zenith distance of the observed direction and h_s is the scale height of the barometric atmosphere model (compare eq. 6.2.1). The length of the fitting window was varied and the best results could be obtained for 500 m to 1 km, which corresponds to about 10 to 20 range bins, depending on the Zd. The value of χ^2/N_{df} of the fit[2] is used to identify clear-air regions and such regions with non negligible cloud/aerosol content, while moving the fitting window over the signal towards larger distance from the receiver. In the following, the single steps of the algorithm will be described in detail. A real data example can be found in figure 6.3.

6.2.1 *Identification of clouds*

The beginning of a cloud layer is detected if the following two criteria are fulfilled: $\chi^2/N_{df} > 2.5$ for the local fit and positive excess of the last bin over the fitted curve. The end of the cloud layer is then defined as follows: $\chi^2/N_{df} < 1.5$ and the first data-point of the fit lying below the last pre-cloud fit. This is done because clouds should always decrease and never increase the amount of transmitted light. In the next section it will be described how to extract transmission profiles, using two different methods, from the "enhanced back-scattering" regions defined in that way. The first such method is not making use of these regions directly, but of those with pure Rayleigh scattering before and after the cloud. The second one extracts the extinction coefficient $\alpha_a(r)$ directly making some assumptions, but in practice needs to be calibrated with the first method.

6.2.2 *Measuring the transmission of clouds*

For a single wavelength low-power LIDAR system like the one described in this context, all real signal inversion algorithms like the Klett method (Klett, 1981) cannot be used without additional assumptions, like for example a fixed LIDAR ratio plus a model for the molecular profile. This is because the use of laser light at 532nm in a partially very clear atmosphere consists of two distinct components of scatterers (Rayleigh and Mie/aerosol).

Two new methods for extracting transmission profiles from LIDAR data have been studied and are used in the analysis algorithm for MAGIC. Both make use of the clear-air model fit described above as well as the signal excess from additional aerosol back-scattering. The fits used for these methods have only one free parameter, the scaling of the molecular model C. The scaling factor of the pre-cloud fit C_1 should always have a higher value than the post-cloud one C_2. The losses are reflecting the attenuation of the light inside the cloud/aerosol layer.

---

[2] The statistical error for the fit is determined by $\sqrt{N}$, the number of counted photons before background subtraction. N is typically larger then 500 and a simple χ^2 fit is therefore appropriate.

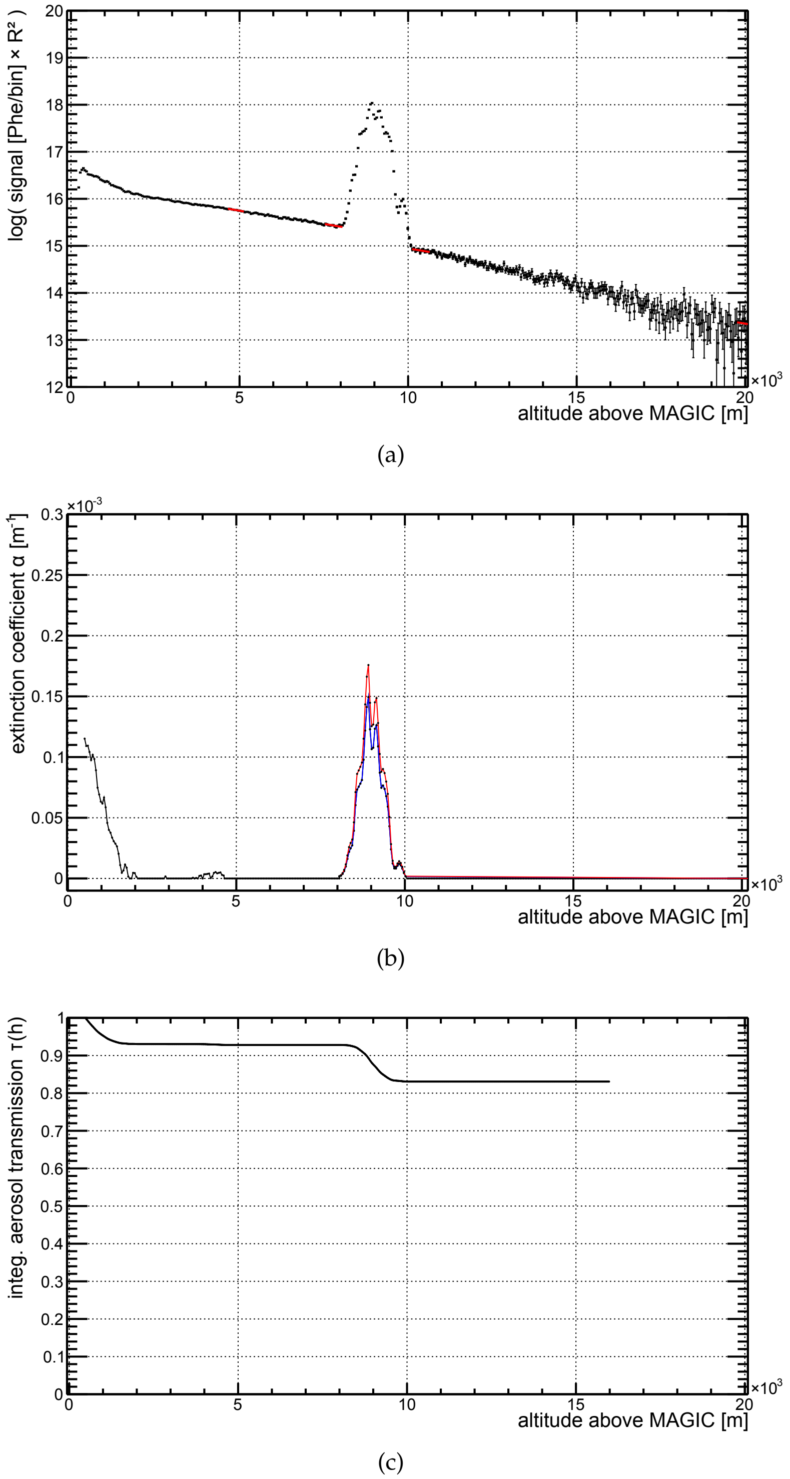

(a)

(b)

(c)

Figure 6.3: Methods for determining the light attenuation from LIDAR measurements in short: Clouds are detected by fitting a clear air model to the range corrected photon counts graph (upper plot) in a sliding window. The total extinction of the cloud layer can be measured by comparing the fit parameters before and after the cloud. The extinction coefficient (center plot) is estimated by normalizing the back-scattering excess of the cloud to the total extinction (blue line) or by scaling the back-scattering excess with the LIDAR ratio (red line). The integral extinction curve (lower plot) can be used for energy corrections to IACT events.

Extinction method

The first method, in the following called "extinction method", makes use of the assumptions already mentioned in the beginning of 6.2:

- In signal regions with clear air only Rayleigh scattering is important, all other scattering contributions as well as multiple scattering can be neglected.
- The range-corrected signal from pure Rayleigh scattering can be well described by a barometric altitude profile: $S(h) = C \cdot \exp h/h_s$. Losses due to Rayleigh scattering at 532 nm are small compared to the effect of the signal scaling due to changes of air density.
- Light that is Rayleigh scattered behind a cloud/aerosol layer is attenuated two times with the layer's opacity: $C_2 = S_2(0) = C_1 \cdot \tau_{\text{aer}}^2$

With these assumptions, the transmission of any cloud can be calculated by taking the square-root of the ratio of two clear-air fits, before and after the cloud.

$$\tau_{\text{aer}} = \sqrt{\frac{C_2}{C_1}} \, . \tag{6.2.3}$$

The extinction coefficient $\alpha_{\text{aer}}(h)$ can be estimated from the LIDAR signal $S(h)$ by distributing the total extinction proportionally to the magnitude of the cloud/aerosol back-scattering excess over the mean of the Rayleigh fit.

$$\overline{S}_{\text{mol}}(h) = \frac{C_1 + C_2}{2} \cdot \exp \frac{h}{h_s} \, , \tag{6.2.4}$$

$$\alpha_{\text{aer}}(h) = \sqrt{\frac{C_2}{C_1}} \cdot \frac{S(h) - \overline{S}_{\text{mol}}(h)}{\int_{h_1}^{h_2} \left(S(h) - \overline{S}_{\text{mol}}(h)\right) \, \mathrm{d}h} \, . \tag{6.2.5}$$

One of course introduces an error if assuming that the signal excess from aerosol scattering,

$$S_{\text{aer}}(h) \approx S(h) - \overline{S}_{\text{mol}}(h) \, , \tag{6.2.6}$$

is directly proportional to the attenuation coefficient α_{aer}. This assumption is completely neglecting the fact that S_{aer} is also modified by attenuation of the cloud itself and values from higher altitude do actually correspond to larger values of α_a. However, this effect does not modify the integral transmission of the cloud, because it was measured independently from the value of S in the cloud region. This way, the error is only affecting the spacial distribution of α_{aer}, but not its normalization. Furthermore, if only cloud layers with relatively high transparency are concerned, also the error on the spatial distribution is of second order only.

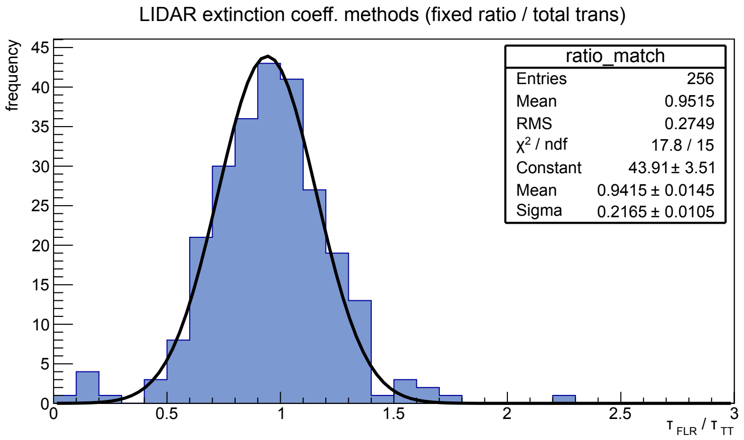

Figure 6.4: Comparison of extinction and LIDAR-ratio method by taking the ratio of the transmission values obtained for the same cloud using both methods. The sample ($0.8 < \tau_{\mathrm{tot}} < 0.9$) has been chosen such that both methods have a chance to perform properly in order to estimate the uncertainty on the LIDAR ratio, which has to be inserted as constant in the LIDAR ratio method.

LIDAR ratio method

In a second approach, from now on referred to as "LIDAR ratio method", the LIDAR ratio is assumed to be known and constant inside a given cloud/aerosol layer. Also, the total transmission of the cloud is assumed be close to unity, so that back-scattered light from the far end of the cloud does not get attenuated much by the rest of the cloud. In other words, this method is suitable only for optically thin clouds. For such objects, the extinction coefficient α_{aer} can be calculated from the back-scattering excess S_{aer} on top of Rayleigh scattering $\overline{S}_{\mathrm{mol}}$ pedestal directly, assuming that the LIDAR-ratio of cloud scattering K_{aer} is known, as well as the molecular back-scattering coefficient β_{mol}.

$$\alpha_{\mathrm{aer}}(h) = K_{\mathrm{aer}} \cdot \beta_{\mathrm{mol}}(h) \cdot \frac{S(h) - \overline{S}_{\mathrm{mol}}(h)}{\overline{S}_{\mathrm{mol}}(h)} . \tag{6.2.7}$$

The LIDAR ratio method does of course only make sense if the assumption of a known and stable value of the LIDAR ratio is valid. Therefore, a typical value for the LIDAR ratio was chosen from a test sample and the resulting total cloud transmission for both methods over a large sample of LIDAR measurements has been compared. The data has been preselected to contain only clouds within a range of $0.8 < \tau_{\mathrm{tot}} < 0.9$ to make sure that both methods perform in an optimal way and the resulting difference is mainly due to an uncertainty in the LIDAR ratio. The result of this comparison shows that the relative difference between both methods follows pretty well a Gaussian distribution with a standard deviation of 0.22 times the mean (figure 6.4). This relative error may seem quite large, but for optically thin clouds it is acceptable since the absolute error on the total transmission is low.

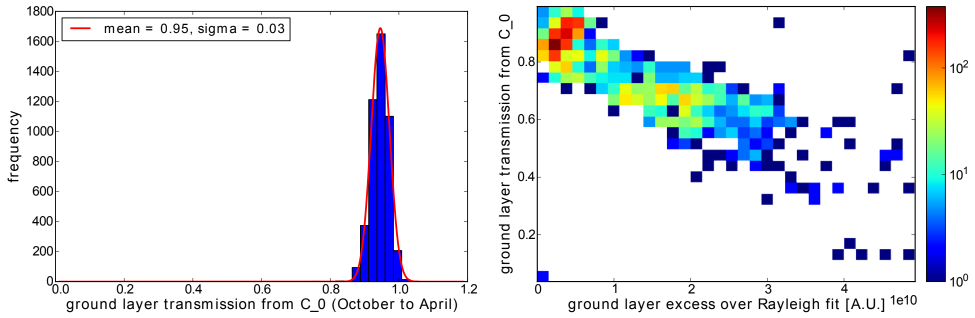

(a) (b)

Figure 6.5: Distribution of planetary boundary layer transmission values for the Calima free season (October 1st to May 1st). The LIDAR measurements were preselected, cutting in the integral boundary layer excess in order to exclude low level clouds. The distribution can be fitted with a Gaussian, resulting in a mean value of 0.95 and a standard deviation of 0.03 (a). Plotting the estimated boundary layer transmission versus the integral boundary layer excess reveals, behind some scattering, of the values a linear correlation (b).

Both methods have to be applied in different situations. The extinction method performs well for clouds of moderate extinction, because it really measures the transmission correctly within the errors of the fit, which is on the order of 3 % on an absolute scale. It is obvious that if the actual transmission approaches 100 %, the relative error on the measurement becomes very large. for clouds absorbing less than 10 % of the light it is more sensible to use the LIDAR ratio method, which is what is done in practice for MAGIC.

For correcting energy spectra of sources of VHE γ-radiation, it is useful to calculate the integral aerosol transmission to the ground as function of the altitude h.

$$\tau_{\mathrm{aer}}(h) = \int_{\mathrm{h_0}}^{h} \alpha_{\mathrm{aer}}(h)\mathrm{d}h \tag{6.2.8}$$

In chapter 7 it will be shown how this number can be used for correcting the light yield and thus energy estimation of single events.

6.2.3 *The transmission through the atmospheric boundary layer*

Apart from clouds in the field of view of MAGIC there is another, maybe even more important, target for LIDAR measurements. This is the atmospheric boundary layer, which on la Palma, in some periods, has a relatively high probability to contain large concentrations of Saharan dust. This effect, also called “Calima”, can cause high atmospheric opacity (up to 50 %) all over the optical spectrum.

In contrast to clouds, for boundary-layer aerosols it is not possible to perform a reference measurement right before the deviation from pure Rayleigh

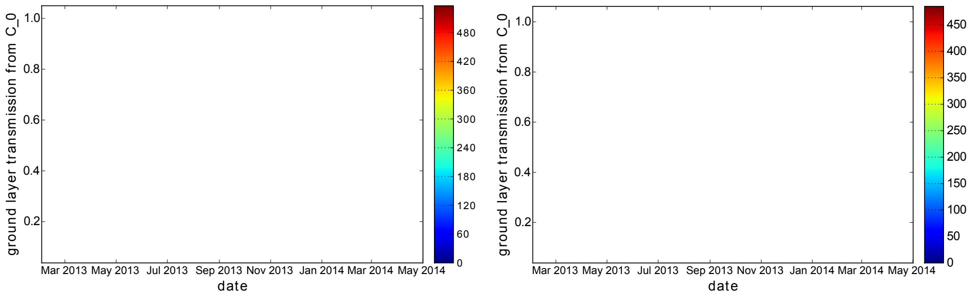

(a) (b)

Figure 6.6: Seasonal variation of the atmospheric boundary layer transmission, before (a) and after (b) correcting for the effect of varying air density with temperature. A cut was applied selecting only measurements with relatively small boundary layer back-scattering excess. A simple inverse proportionality between temperature and density has been assumed, using monthly mean night temperature at ORM (Jabiri et al., 2000). The effect of this correction is barely visible and the apparently lower transmission in the summer months stays more or less constant.

scattering starts. That is because the telescopes are located right inside the boundary layer and thus measuring an undisturbed signal on ground level is impossible. In order to still measure the total transmission of the aerosol layer above the site, one has to find another way. One option is using another measurement that has been performed during perfect clear sky conditions as reference. From this measurement a reference scaling constant for the molecular model fit $C_{0,\text{ref.}}$ is extracted. The total transmission of the boundary layer can then be calculated in the usual way:

$$\tau_{\text{b.l.}} = \sqrt{\frac{C_0}{C_{0,\text{ref.}}}} . \tag{6.2.9}$$

This is of course not unproblematic, since it requires to assume that the system has been perfectly stable in-between the two measurements and that the reference is indeed corresponding to perfectly clear conditions. After having studied LIDAR data from over one year, a good value for $C_{0,\text{ref.}}$, corresponding to clear conditions could be identified and it can be concluded that the assumption of stability is valid within certain error limits. The precision and stability of the transmission estimate obtained with this method can, for example, be tested by making a histogram of the distribution of ground layer transmission values from measurements with similar, low back-scattering excess from the boundary layer (fig. 6.5 (a)). The Calima season (May to September) was excluded from that study. The distribution can be nicely fitted with a Gaussian, which peaks at 0.95 with a standard deviation of 0.03. There is also a strong correlation between the planetary boundary layer excess and C_0 as expected (fig. 6.5 (b)). On the other hand, it cannot be finally excluded that there is a dependency of C_0 on other parameters than just the

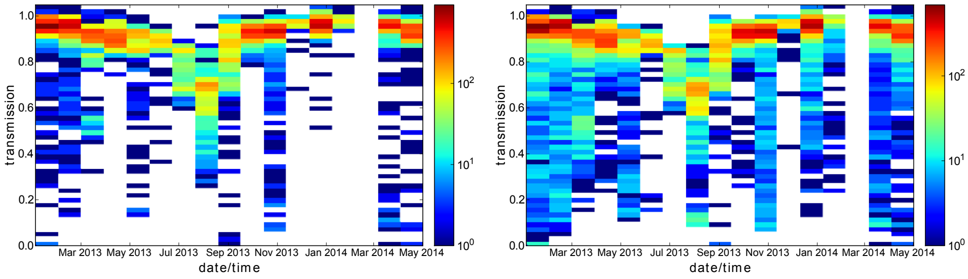

(a) (b)

Figure 6.7: Entire LIDAR data sample from 14 months. Transmission from 3 (a) and 8 (b) km to the ground. While winter moths show a higher frequency of high cirrus clouds, the summer is mostly affected by Saharan dust intrusion (Calima). Especially the months July and August of 2013 were heavily affected.

extinction in the ground layer. There is an expected correlation with ambient temperature, due to a change in air density with temperature. But applying corrections to the extinction values based on the average night temperatures at ORM does have much effect on the seasonal variations, which indicates that this effect is rather due to real changes in the boundary layer dust concentration (fig. 6.6). One important conclusion that can be drawn from these measurements is that there is no observed degradation of the laser/detector after one year, which would lead to large systematic errors when using this method.

6.3 ONE YEAR LIDAR DATA FROM THE MAGIC SITE

Apart from the final goal of applying atmospheric corrections to the MAGIC data, the large sample of automatically recorded LIDAR data, which at the moment of writing this thesis covers a period of more than a year, can also be used for more general studies of the atmospheric conditions in la Palma.

6.3.1 *Statistics on data quality and potential of corrections*

The full LIDAR data-set is visualized in figure 6.7. It shows a histogram in time and integral optical transmission from 3 km and from 8 km above the site to the ground. The influence of Calima is strongest in July and August, leading to lower integral transmission values for both starting altitudes, 3 and 8 km. In the winter on the other hand there is a larger fraction of nights with higher altitude clouds. This effect is only visible in the transmission values from higher altitude (figure 6.7 (b)).

A statistical analysis of the whole set of LIDAR data can be found in figure 6.8. Transmission values of $1.0 > \tau > 0.9$ can be considered close to perfect conditions (Moderate absorption inside the atmospheric boundary layer is taken into account in MC simulations.). $0.9 > \tau > 0.8$ means that data

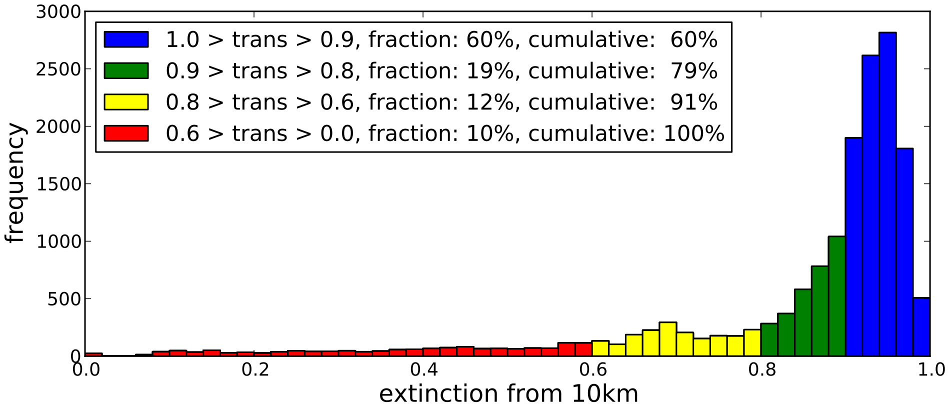

Figure 6.8: Overall transmission statistics from all available LIDAR data. Displayed is the integral transmission from 10km. Different colors are indicating the impact on MAGIC data and possibilities for corrections: blue – perfect conditions, green – data useful even without corrections, yellow – corrections mandatory, red – very bad conditions.

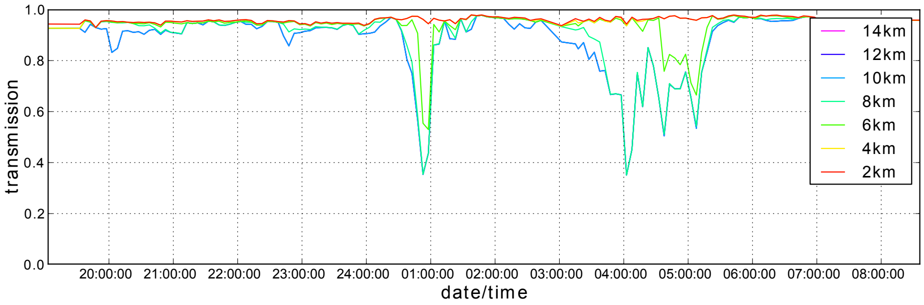

(a)

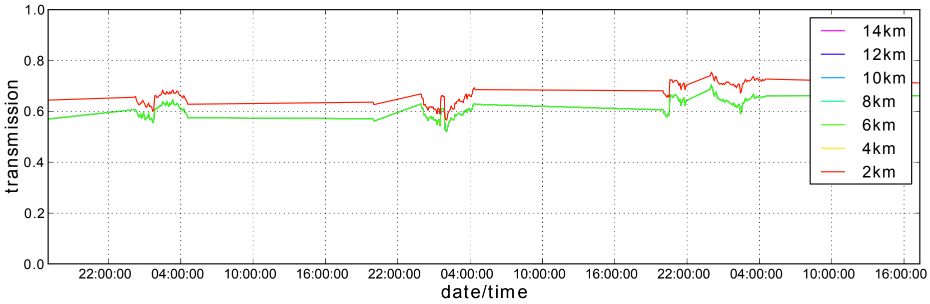

(b)

Figure 6.9: Examples for time development of integral transmission from different altitudes for one winter night with cirrus clouds (a) and three consecutive summer nights with strong Calima (b). High altitude clouds typically show variability timescale of the order of minutes, while for Calima important changes happen on timescales of the order of days.

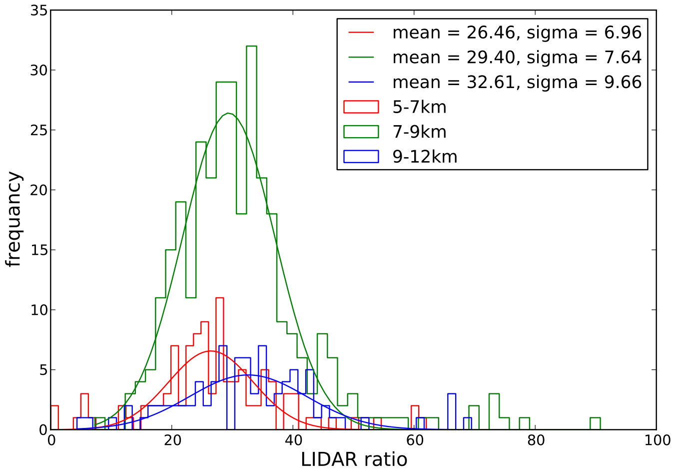

Figure 6.10: Measurements of the LIDAR ratio of typical cirrus clouds for three different altitude ranges, fitted with a Gaussian.

analysis would already profit from LIDAR corrections, regarding systematic errors on the energy scale. $0.8 > \tau > 0.6$ defines a regime where corrections become mandatory or one would have to discard the data otherwise. At transmissions lower than 0.6, even the LIDAR corrections might not help to fully recover the data. Undisturbed observational conditions could only be found in a fraction of 60% of the LIDAR data, for the observed period under investigation. The fraction of useful data could probably be increased to about 90% using atmospheric corrections. The sample is probably biased, compared to a multi-year average, due to the relatively short duration of only a bit more than a year and gaps in the LIDAR measurements.

Figure 6.9 shows two examples, one winter night with very clean air, but cirrus clouds moving through the field of view at high altitude, and three consecutive days in summer with strong Calima. From these plots it becomes clear that while clouds are a highly variable phenomenon, the atmospheric boundary layer during the Calima season typically remains relatively stable over several days.

6.3.2 *Statistics of the LIDAR ratio*

The availability of the two methods for measuring cloud transmission also allows for estimating the average LIDAR ratio for scattering inside clouds. Figure 6.10 shows histograms of measured values of the LIDAR ratio for different cloud altitudes. It is more or less Gaussian distributed around a mean value on the order of 30 sr and tends to slightly increase with altitude. It can however not be excluded that this effect is due to systematic errors.

7

EVENT BY EVENT LIDAR-BASED CORRECTIONS

This chapter covers a newly developed method for correcting the MAGIC data recorded during adverse atmospheric conditions using LIDAR data. First, a detailed description of the method for event-wise corrections of energy and estimated collection area is given. Then, the results of the first tests of this method, using Crab Nebula data, are be presented. Finally the systematic errors of the new method are discussed in detail.

7.1 CORRECTION OF IACT ENERGY SPECTRA

Having access to the full information about the current state of the atmosphere, one can adjust the analysis to the variable conditions in order to produce reliable energy spectra or light-curves. The natural and most complete way would be to produce tailored MC events for all the different situations. The data could then be split up and each fraction could be analyzed using the right set of MC events for the given atmospheric situation. Unfortunately, this procedure would require an immense amount of MC data, using too much time for production and disk-space for storage, in order to make sense for the present generation of IACTs. For that reason, another more practical solution was developed and will be presented in the following.

7.1.1 *Correcting the energy bias*

The primary energy estimation for air-shower events recorded with MAGIC is based on look-up tables that are created using Monte Carlo events, where the "true" energy information E_{true} is available as initial parameter for the production. For similar geometric constellations of telescopes and air-showers, the size parameter of the image scales roughly proportionally to the energy of the primary γ-particle[1]. A transmission-energy-correction on event basis, requires additional information about the shower development throughout the atmosphere. For optimal correctional precision, apart from exact transmission profiles $\tau(h)$ from LIDAR, also the light emission profile that contributes to the camera image $\epsilon(h)$ needs to be known. The integral over the product of the normalized light emission profile and the total transmission curve gives a good estimate of the atmosphere-induced light yield bias (see Fig.: 7.1).

$$\overline{\tau} = \int_0^\infty \epsilon(h) \cdot \tau(h) \, \mathrm{d}h \, . \tag{7.1.1}$$

---

[1] This is of course only valid if the air-shower is observed at the same viewing angle.

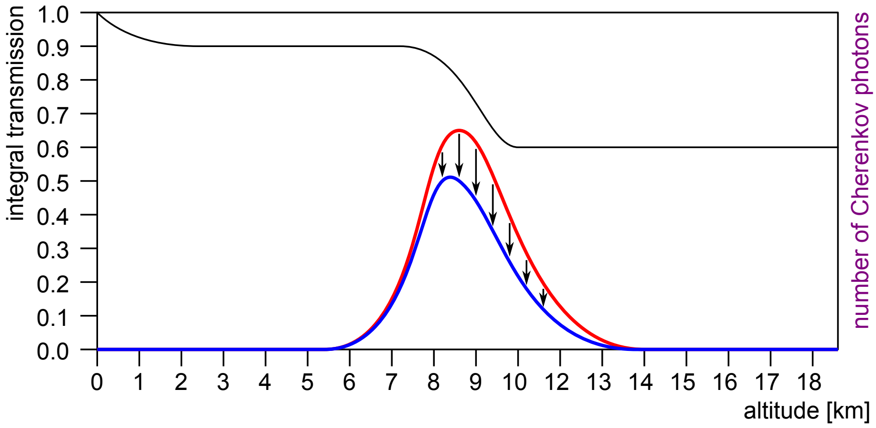

Figure 7.1: The profile of the total transmission from the location of light emission to the ground (black curve) modifies the emission profile (red curve) of Cherenkov photons produced by an extended air-shower arriving at the telescope (blue curve). The ratio of the integral values of both profiles gives a good estimate for the energy bias that is introduced in the data analysis of such events.

$\overline{\tau}$ is the average transmittance for Cherenkov light produced in the air-shower and arriving at the telescopes. It can be directly used to calculate a new energy estimation E_{corr} from the previously estimated energy using the look-up tables E_{est}, assuming that the light yield is proportional to the energy.

$$E_{\text{corr}} = \frac{E_{\text{est}}}{\overline{\tau}} \,. \tag{7.1.2}$$

The exact spatial distribution $\epsilon(h)$ of the origins of Cherenkov photons arriving at the telescopes is not known. Still, using stereoscopy it is possible to estimate the altitude of the shower maximum. The longitudinal distribution can be studied from MC simulations and approximated by a Gaussian profile, with an energy dependent width. Because the true energy of the events is unknown, and thus also the best estimate for the width, the correction method can be applied recursively several times for improving the accuracy.

7.1.2 *Restoring the correct effective collection area*

The correction of the energy estimate for each event is not sufficient for recovering the correct energy spectra from observations with IACTs during adverse atmospheric conditions. Even if all events are migrated to their correct energy bins, the resulting flux for each bin will be wrong. This is due to the fact, that the MC simulations that were used for determining the effective collection area for each energy bin were produced assuming optimal atmospheric conditions. Therefore, the collection area, which especially at low energies, strongly depends on the trigger efficiency, is then overestimated compared to the real data. The trigger efficiency mainly depends on the total

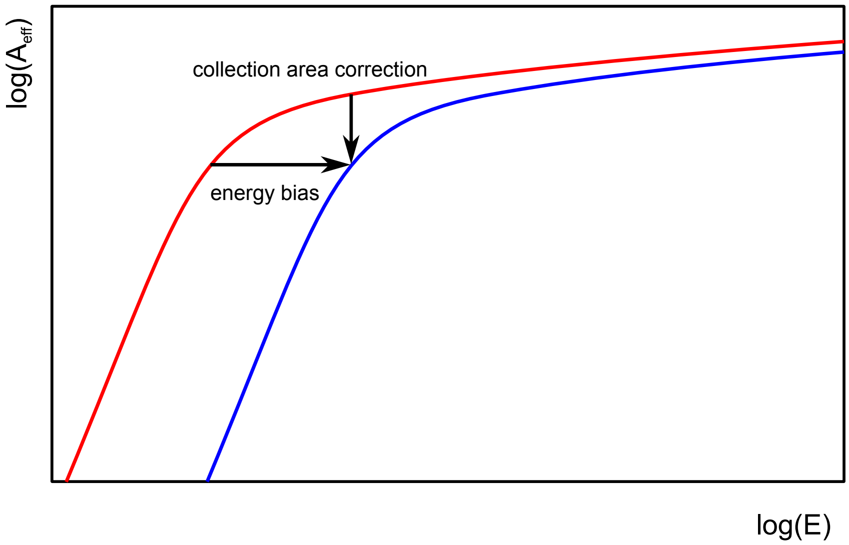

Figure 7.2: This sketch illustrates, how to do a first order correction to IACT events that are affected by aerosol extinction. The energy has to be up-scaled to correct for the aerosol extinction but the collection area should be evaluated at the apparent (smaller) energy. As a result, the curve that describes the effective collection area $A_{eff}(E)$ gets simply shifted to the right.

light yield of the events, which now is reduced by clouds or aerosols. As a result the flux, especially in the lower energy bins, is underestimated.

In order to correct for this effect one has to assume that the effective collection area calculated for the wrongly reconstructed value of the "estimated energy" is very close to the true one. This assumption becomes plausible, considering showers affected by clouds or aerosols as "mimicking" showers of lower energy. Even if this assumption is not correct for large energy biases, it stays valid for small corrections, where the altitude of the shower core is not significantly different for showers of "estimated" and "true" energy. In this context "true" means the actual energy of the primary γ particle, which is unknown for real data but a known initial parameter for MC-simulations. The "estimated" energy is the value provided by the look-up tables during the data analysis, assuming perfectly clear sky conditions.

The full correction can be described as follows: The energy is corrected using the estimated light yield bias, i.e. the events are migrated to different energy bins. The resulting migration matrix is then used for calculating a new effective collection area for each bin, by averaging the original collection area over all events migrating to that bin. In the following, I will show that this way of averaging the collection area is actually valid.

An instantaneous rate of events $R(E,t)$ of a given energy E after atmospheric correction can be written as follows:

$$R(E,t) = \frac{\mathrm{d}N(E,t)}{\mathrm{d}t}\,. \tag{7.1.3}$$

The time average is given by the total number of events $N(E)$, divided by the time interval T.

$$\langle R(E)\rangle = \frac{\displaystyle\int_0^T \frac{\mathrm{d}N(E,t)}{\mathrm{d}t}\,\mathrm{d}t}{T} = \frac{N(E)}{T}\,. \tag{7.1.4}$$

The particle flux $F(E,t)$ is obtained when dividing by the collection area $A(E-\Delta E(t),t)$ evaluated at the estimated energy, before atmospheric energy correction $E-\Delta E(t)$. $\Delta E(t)$ is the energy bias that has been applied during the energy correction.

$$F(E,t) = \frac{\mathrm{d}N(E,t)}{\mathrm{d}t}\cdot\frac{1}{A(E-\Delta E(t),t)}\,. \tag{7.1.5}$$

Averaging is performed by time integration. Here, the time element dt can be eliminated in the denominator and the averaging can be done by integrating over the event number N.

$$\langle F(E)\rangle = \frac{\displaystyle\int_0^T \frac{\mathrm{d}N(E,t)}{\mathrm{d}t}\cdot\frac{1}{A(E-\Delta E(t),t)}\,\mathrm{d}t}{T} \tag{7.1.6}$$

$$= \frac{\displaystyle\int_{N(E,0)}^{N(E,T)} \frac{\mathrm{d}N(E)}{A(E-\Delta E(N))}}{T}\,. \tag{7.1.7}$$

Finally, the transition to a discrete number of events can be performed.

$$\langle F_i\rangle = \frac{\displaystyle\sum_{j=0}^{N_i}\frac{1}{A_{i-\delta_j,j}}}{T}\,. \tag{7.1.8}$$

Here, i is the energy binning, while j runs over the single events. δ_j is the energy correction bias of event j in terms of energy binning.

The time-averaged flux $\langle F_i\rangle$ can therefore be calculated by using an event averaged collection area $\overline{A_i}$.

$$\overline{A_i} = \frac{N_i}{\displaystyle\sum_{j=0}^{N_i}\frac{1}{A_{i-\delta_j,j}}}\,. \tag{7.1.9}$$

7.2 TESTS ON DATA FROM CRAB NEBULA OBSERVATIONS

The performance of this new method had to be evaluated by reconstructing the spectrum of a known and stable source of VHE-γ radiation. In the field of IACT astronomy, the Crab Nebula serves as such standard candle since decades. It is observed regularly by the MAGIC telescopes for scientific but also for technical reasons. From this data, observations affected by clouds or aerosols were selected and a modified version of the MAGIC data analysis tool-chain, including LIDAR corrections, was applied to the analysis.

7.2.1 *Selected specific examples*

The Crab Nebula is observable from La Palma only from September to April. Therefore the LIDAR corrections could not be tested during strong Calima. On September 6th 2013 however there was one hour of Crab data which was affected by moderate Calima. The flux without corrections is reconstructed to a value, nearly a factor two lower than the known flux (Albert et al., 2008). Applying the LIDAR corrections, the SED fit recovers to the expected flux within errors (figure 7.3 (a)).

In winter 2013/14 there were some interesting observations for tests with clouds too. Figure 7.3 (b) shows an example from December 24th 2013 with highly variable cloud coverage. Given the mixed conditions it is remarkable that the LIDAR corrections allow for recovering the expected Crab spectrum within errors. It was however necessary to release a bit the cuts on the "hadronnes" parameter (see chapter 3.2.4), which has no big impact on the sensitivity, at least for strong sources. The "hadronnes" parameter is very sensitive on the shape of the images, which is an important property for distinguishing electromagnetic from hadronic air-showers. Clouds can slightly distort the shape of the air-shower images and therefore increase the rejection probability. This can be compensated by relaxing the cut and thereby reducing the sensitivity of the analysis for small inconsistencies between simulated and real air-shower images.

Another quite extreme example is data observed in March 22nd 2014 7.3 (c). Here the observations were longer and the cloud coverage relatively stable, fluctuating around a value of 0.5 with clouds at about 8km. Again, the cuts for the γ-hadron separation had to be relaxed in order to keep all γ-ray events. The effect of the corrections is large but in this case the spectrum could not be fully reconstructed. There is a remaining flux bias of about 15%.

7.2.2 *Tests with a long term heterogeneous data-set*

Figure 7.4 shows a combined data sample from more than 7h of observations mostly affected by adverse atmospheric conditions of different kinds (Calima, low and high level clouds but also containing a small fraction of clear skies). The corrections manage to reproduce the Crab Nebula spectrum well with possibly some over-correction at low energies. The largest impact comes from

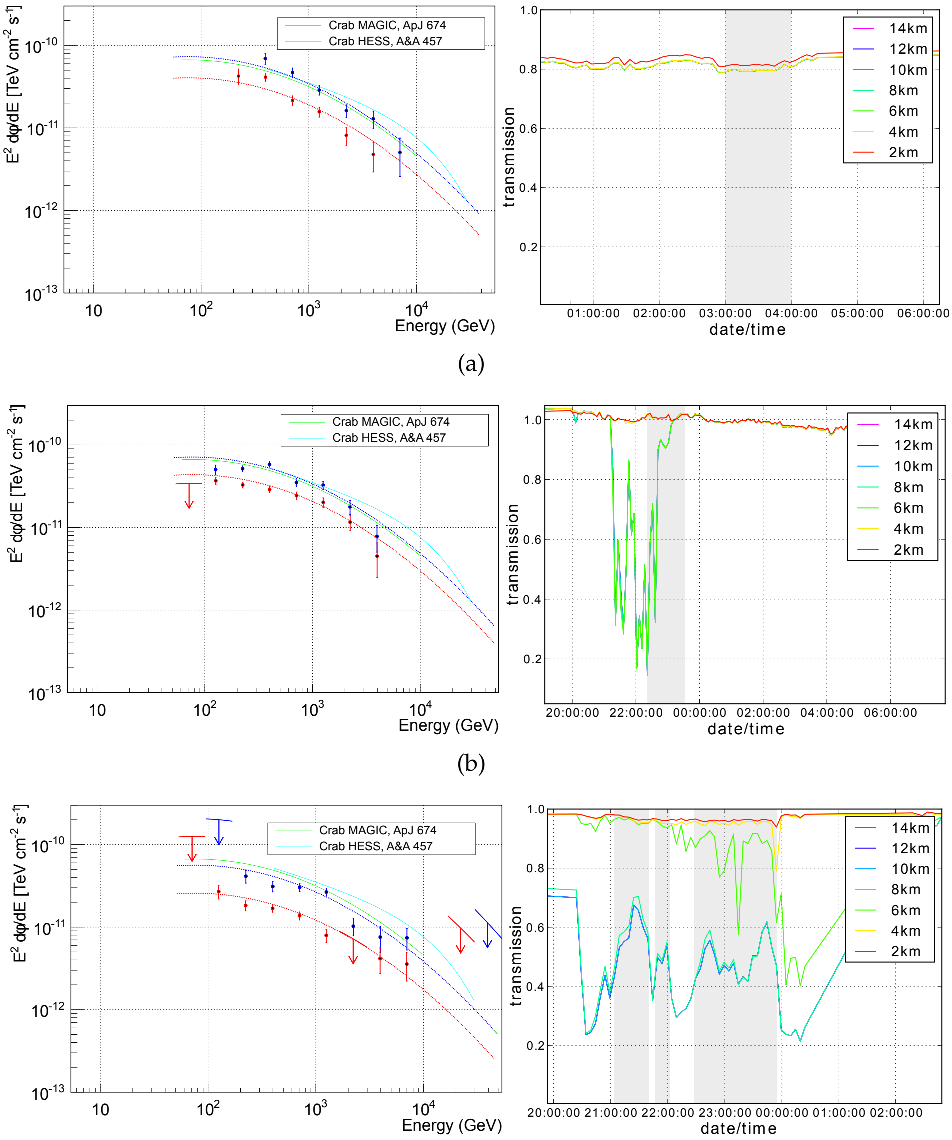

(a)

(b)

(c)

Figure 7.3: Three LIDAR correction examples with different atmospheric conditions, all using Crab Nebula data. The SED before (red) and after (blue) correction is shown on the left, with the corresponding results of the spectral fits and previously published spectra from MAGIC and HESS. On the right side, the the LIDAR transmission curves are shown, with the data-taking period marked in gray. The first example (a) shows data from September 6th 2013 affected by moderate Calima. The second example (b) from December 24th 2013 has medium level clouds inside the FoV, with very variable transmission. The last example (c) shows data, which is strongly affected by clouds of only $\sim 50\%$ transmission.

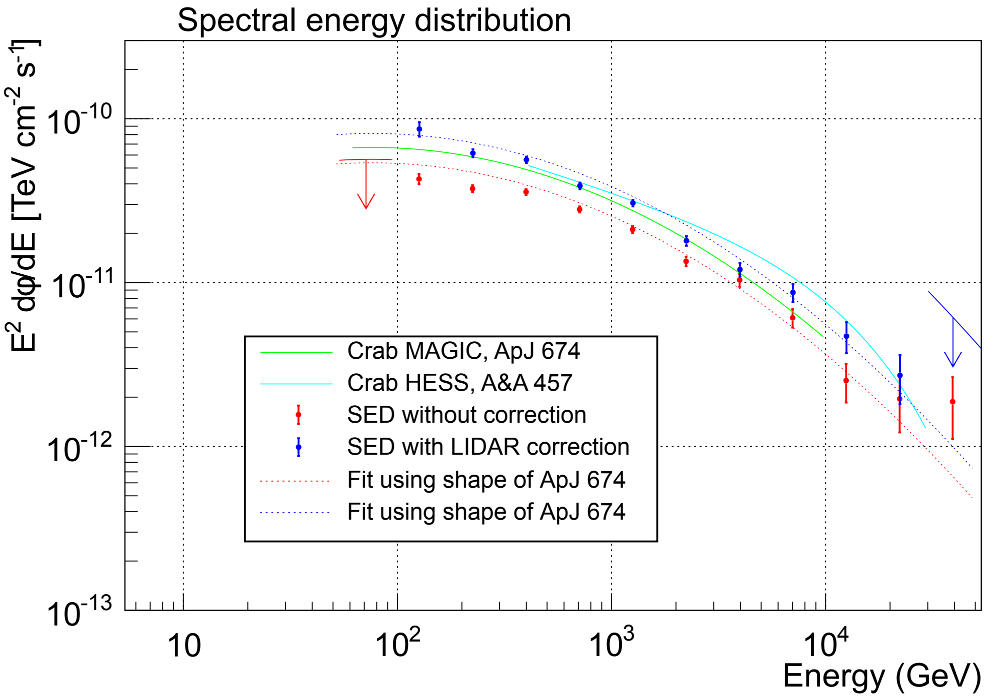

Figure 7.4: Crab SED from a 7h data sample, with and without LIDAR corrections, compared to spectra previously published by MAGIC and HESS.

the first data-point in the SED which is known to be affected by systematic uncertainties most.

From this sample it can be observed that the flux error introduced by atmospheric absorption is largest at low energies, where the impact of changes in the estimated collection area is largest. Relaxed γ-hadron separation cuts had to be used in order to cope for different degrees of selective absorption along the shower axis.

The actual improvement using the LIDAR corrections becomes clear when comparing the values of χ^2 calculated for the differences with respect to the published Crab spectrum (Albert et al., 2008). For the uncorrected SED the χ^2 yields a value of 458 with 10 spectral points. The SED after correction produces a χ^2 of 22.7 with 10 spectral points (see figure 7.5).

7.3 DISCUSSION OF THE UNCERTAINTIES OF THE METHOD

Despite the good overall performance of the LIDAR correction method presented above, it is based on a large number of assumptions and simplifications, all of them introducing systematic errors. In the following I will give a comprehensive summary of those uncertainties, which strongly depend on the situation in which the method is applied.

The first category of systematic uncertainties contains all sorts of errors of the transmission profile extraction method, from the photon counting method,

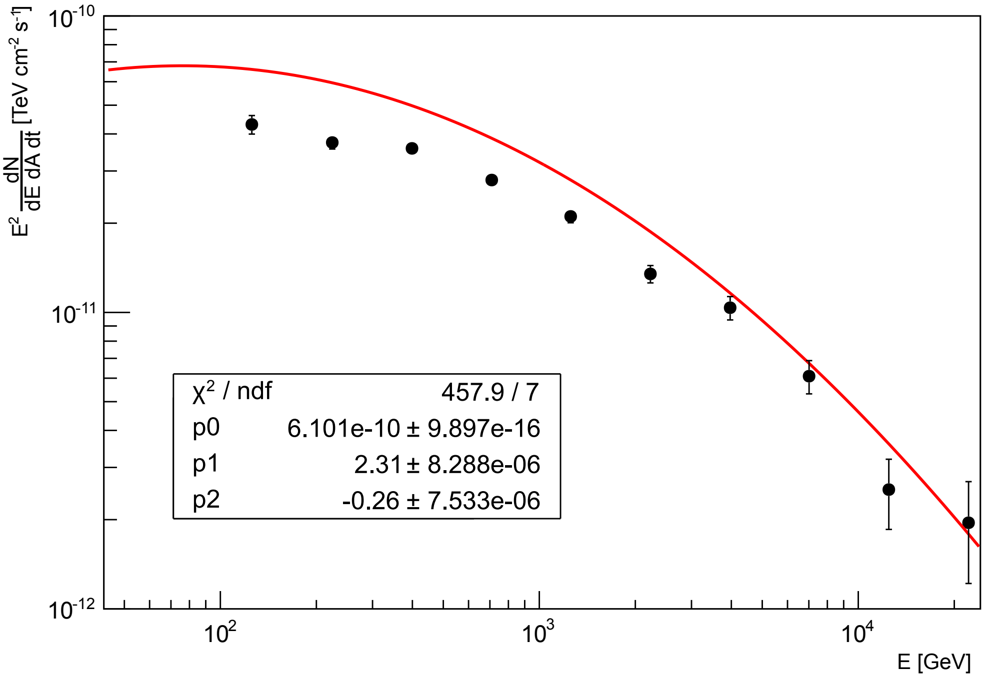

(a)

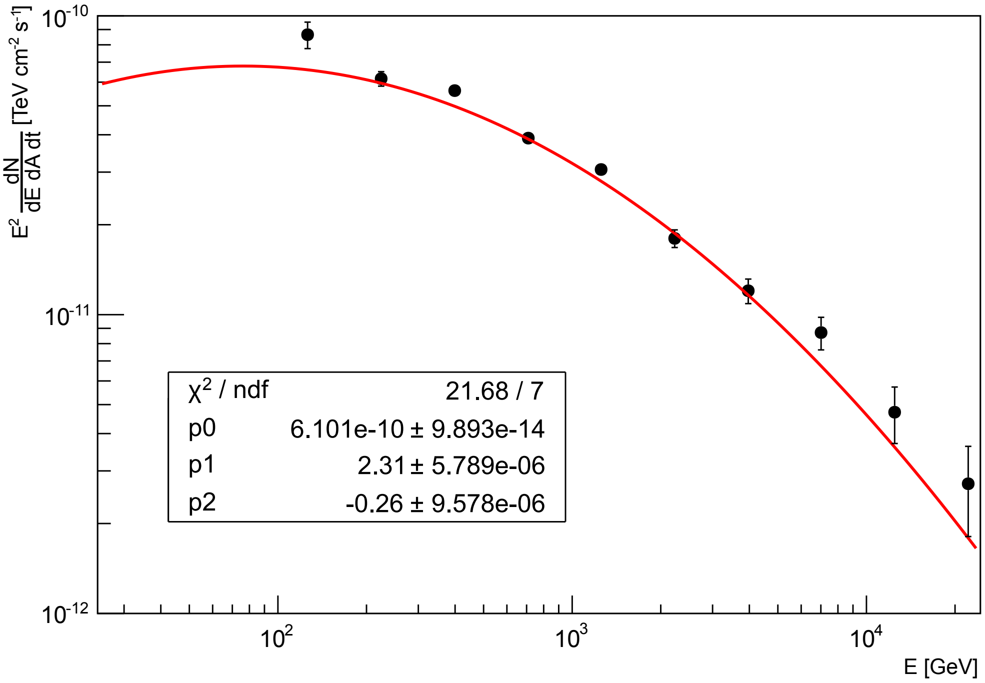

(b)

Figure 7.5: Quantification of the improvement due to LIDAR corrections using χ^2 of deviations from published Crab spectrum (Albert et al., 2008). SED before (a) and after (b) correction. When applying the LIDAR corrections, χ^2 reduces from 458 to 22.7 with 10 spectral points.

over the background, up to the fitting of the Rayleigh model atmosphere. The second category consists of errors introduced by the assumptions, which are made when the transmission profiles are applied to MAGIC data for performing the correction on the energy scale.

7.3.1 *Photon counting efficiency*

The charge amplification of avalanche diodes is highly temperature dependent. In order to ensure stable operation, a temperature stabilization circuit has been installed in the LIDAR detector module (see chapter 5.4.1). Even after applying this compensation, strong temperature differences can still lead to variations of the charge gain of up to 30%. This would in principle be covered by the signal extraction technique, because one part of the signal is obtained through single photon counting and the other part is calibrated with the average charge measured in the single photon counting region. But the overall gain distribution of HPDs shows a characteristic tail towards small charge, which is an unavoidable effect of electron back-scattering from avalanche diode. As a consequence, for a given photon counting threshold there will always be a considerable fraction of events, which surpass that threshold. If the AD gain varies, so does the photon counting efficiency.

The back-scattering probability at normal incidence for $\sim 10\,\mathrm{keV}\,e^-$ from Si is on the order of 20% (Darlington, 1975). The energy distribution of back-scattered e^- is relatively flat (Darlington, 1975; d'Ambrosio & Leutz, 2000), meaning that the deposited energy in the AD for those 20% is more or less homogeneously distributed between zero and the full available kinetic energy. Assuming that during normal operation the threshold for detecting single photo-electrons is around $1/2$ of the typical charge and can go up by 20% at higher ambient temperatures, due to decreasing amplification, the resulting uncertainty on the photon counting efficiency is about 2%.

In the latest version of the LIDAR readout software, this effect has been further reduced by also adapting the photon counting threshold to the variable overall charge gain (see also chapter 8.2.1).

7.3.2 *Improper background subtraction*

Another source of systematic uncertainties in the LIDAR measurements is the error on the estimated background photon rate. Here two effects have to be taken into account: the statistical error from the number of background photon counts inside the pre-trigger region, which is on the order of 10 counts, and systematic variations of the background low to high altitude due to variations in the pedestal. This effect has been reduced in a recent software upgrade (see chapter 8.2.1). An uncertainty of 5% plus the statistical uncertainty is assumed for error on the background subtraction.

7.3.3 *Thermal expansion of the atmosphere*

The absolute calibration of the method for the calculation of transmission profiles strongly depends on the stability of the molecular density profile of the atmosphere. This assumption is of course not true in reality. The largest effect leading to a systematic uncertainty on the calibration constant $C_{0,\mathrm{ref}}$ is the variation of the air temperature, varying also the air density. Typical variations throughout the year lead to changes of the molecular density on the order of 4%.

This error has to be summed up linearly with the 2%, coming from the photon counting efficiency, because the two are highly correlated. Also here, software improvements, currently being worked on have large potential for improvements. Instead of fitting an exponential atmosphere with fixed calibration, in the future a realistic density profile, based on radiosonde measurements will be used (see chapter 8.2.2).

7.3.4 *Reconstruction of the cloud profile*

For optically thick clouds ($\tau \lesssim 0.7$) also the reconstructed shape of the cloud profile does not perfectly match the real shape. Even if the integral transmission of the cloud can be measured with reasonable precision, in this case the shape assigned to the cloud gives more weight to lower altitudes compared to higher ones. The reason for this is that the estimated profile uses the shape of the excess over the average Rayleigh fit, instead of the real density profile of the cloud, which is unknown. The center of gravity shift, which is introduced by this error is difficult to quantify, but can be estimated to be

$$\Delta h_{\mathrm{cog}} \lesssim 0.5 \cdot W \cdot \tau \,, \tag{7.3.1}$$

where W is the vertical extension and τ the transmission of the layer.

Errors listed until this point are systematic errors of the method for extracting transmission profiles from LIDAR data. Plots of examples can be found in figures 7.6 and 7.7. The absolute systematic uncertainty on the atmospheric transmission is typically on the order of 5% at low altitude, after the atmospheric boundary layer, and may increase up to 10% at high altitudes after optically thick clouds. Those errors are entering into the LIDAR corrections performed on MAGIC data, on top of other uncertainties.

7.3.5 *Assumptions on the air-shower geometry*

For performing the atmospheric energy correction on γ-ray events recorded with MAGIC, a light emission model of the air-shower is needed. It can be shown with simple 1D simulations of air-showers that their average longitudinal development can be described reasonably well with a Gaussian profile (see appendix F). The width of this profile (typically around 5 km FWHM) is energy dependent and fluctuating around the mean value with a standard

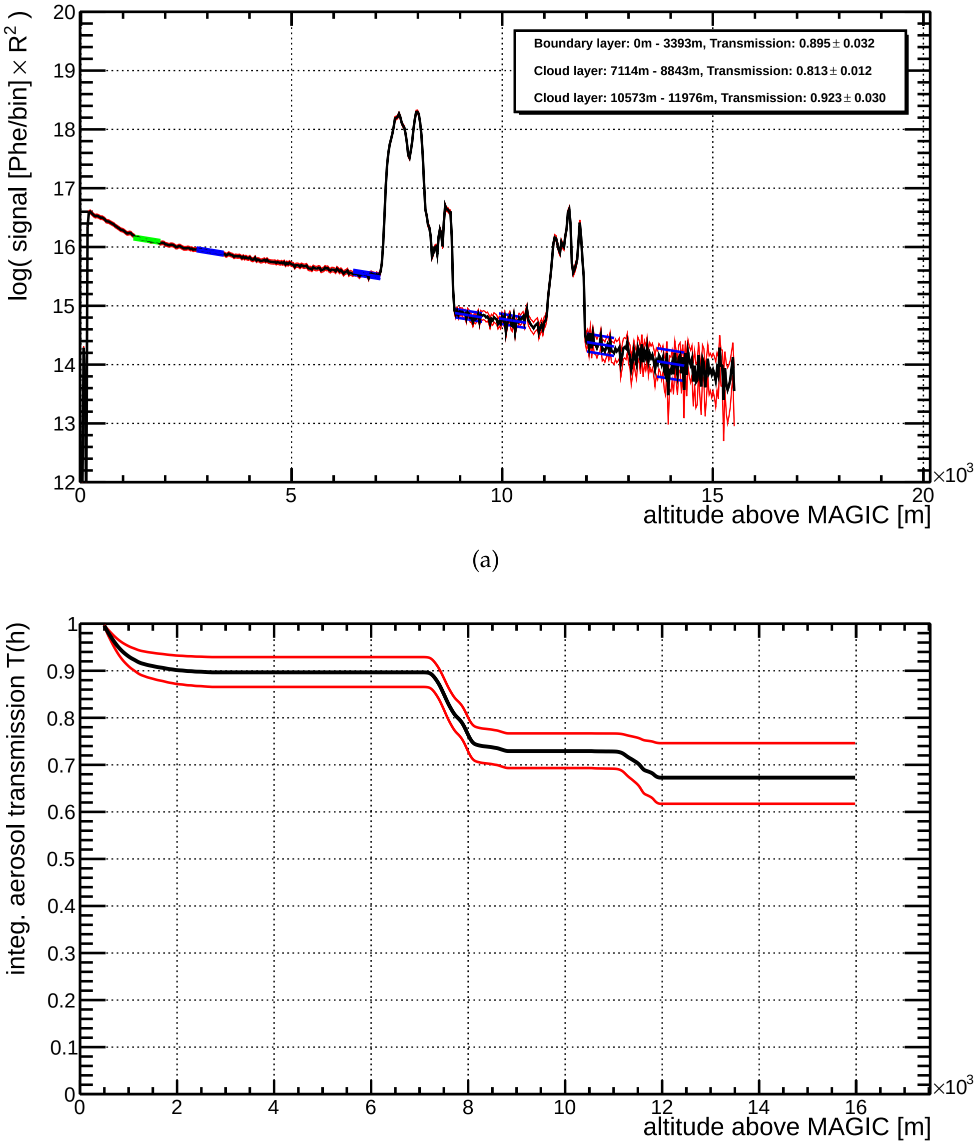

(a)

(b)

Figure 7.6: Typical example of systematic uncertainties of a LIDAR transmission measurement with two cloud layers. Error margins for the range corrected LIDAR return (a) including the uncertainty on the photon counting efficiency and the background subtraction are shown as red line. The reference regions for the fitting an exponential atmosphere are shown in blue (boundary layer transmission reference, before and after cloud layers) and green (defining the end of the planetary boundary layer). The errors for the transmission measurements (text box) and on the integral transmission to ground measurement (b, red lines) also contain the uncertainty on the calibration constant $C_{0,\mathrm{ref}}$.

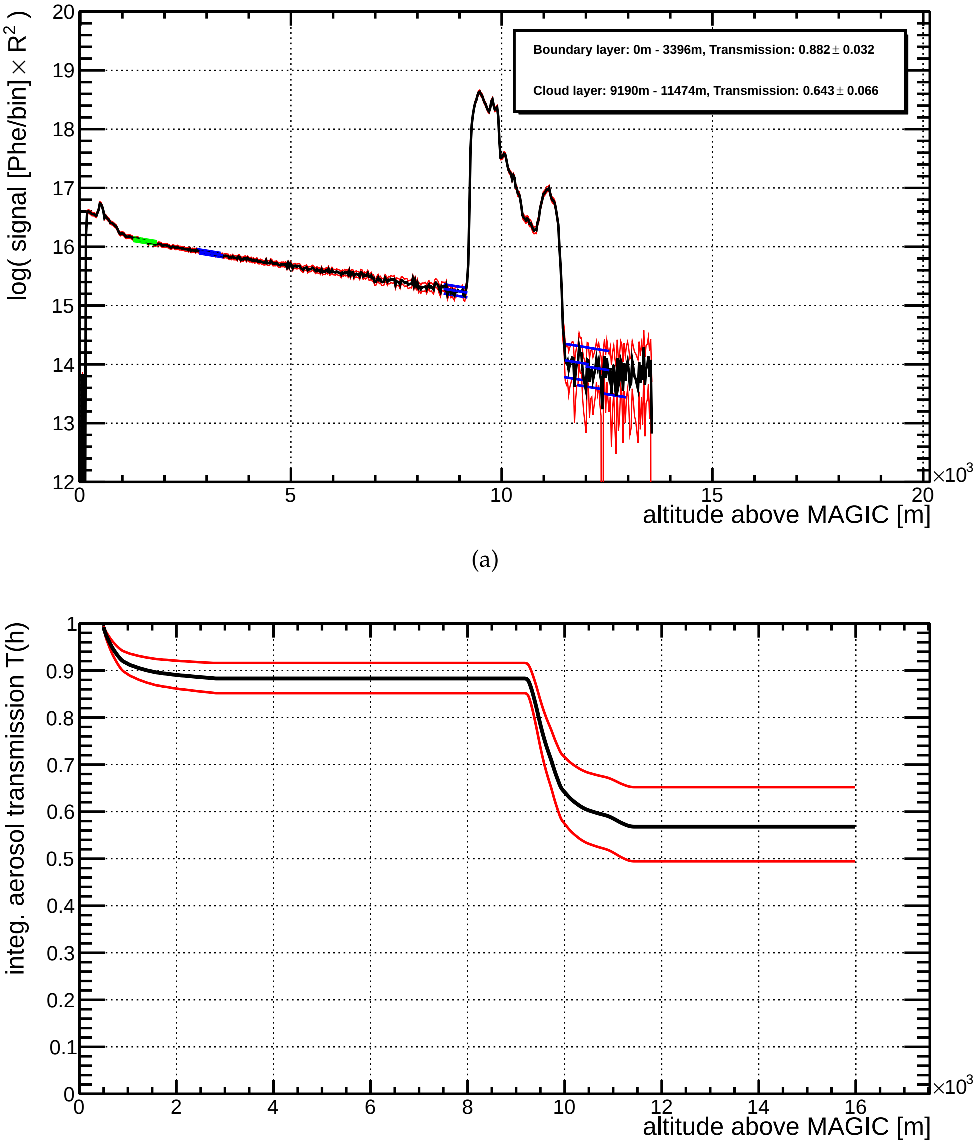

(a)

(b)

Figure 7.7: Another example of systematic uncertainties of a LIDAR transmission measurement at larger Zd and with relatively thick cirrus cloud. Error margins for the range corrected LIDAR return (a) including the uncertainty on the photon counting efficiency and the background subtraction are shown as red line. The reference regions for the fitting an exponential atmosphere are shown in blue (boundary layer transmission reference, before and after cloud layers) and green (defining the end of the planetary boundary layer). The errors for the transmission measurements (text box) and on the integral transmission to ground measurement (b, red lines) also contain the uncertainty on the calibration constant $C_{0,\mathrm{ref}}$.

deviation of $10 - 15\%$. The position of the mean (shower maximum) can be obtained from the stereo parameters of MAGIC data. For this value a systematic uncertainty of ± 1 km has to be considered.

Fluctuations of the width of the shower profiles mainly lead to a worsening of the energy resolution of the analysis, while a systematic shift of the position of the shower maximum can create an energy bias. A systematic bias in the position of the assumed shower maximum of 1km can in the worst case (step-like shape in the transmission profile, at the position of the shower maximum) lead to an energy bias of $\sim 10\%$ at a cloud transmission of 50% and $\sim 4\%$ at 25% transmission. This effect does only account for cirrus clouds, not for the effect of the atmospheric boundary layer or Calima.

In summary, the systematic uncertainties of the LIDAR corrections in their current state (results presented in this thesis) can be estimated as follows (absolute error on the energy scale):

- Moderate Calima ($\tau \lesssim 75\%$): $\sim 5\%$
- Strong Calima ($\tau \approx 50\%$) / mid-altitude cirrus ($\tau \lesssim 75\%$): $\sim 10\%$
- strong mid-altitude cirrus ($\tau \approx 50\%$) / high altitude cirrus: $\sim 15\%$

8

CONCLUSIONS AND POSSIBLE IMPROVEMENTS

In the previous chapters I presented a technique for correcting measurements of IACTs, performed during adverse atmospheric conditions, using a low-power single-wavelength LIDAR system. The technique was tested by applying it for reconstructing the VHE γ-ray spectrum of the Crab Nebula. After applying all corrections as described in Section 7.1 it was possible to reconstruct the Crab spectrum, even for data that were heavily affected by clouds. These first tests can be regarded as prove of principle, for atmospheric calibration of IACTs. The availability of such a powerful tool opens a new window for useful observations, also during none optimal atmospheric conditions and will help reducing the systematic errors of current and future instruments.

First tests of the method already showed good results, but there is still room for improvements, in hardware as well as in software.

8.1 HARDWARE IMPROVEMENTS

One may assume that better hardware will provide improved measurement results. In case of an auxiliary instrument like the MAGIC LIDAR system one also has to consider if a possible upgrade can justify its cost/effort and if better instrumentation can really improve the scientific output of the experiment as a whole. In the following I will present some ideas for upgrades that would, at low to moderate cost, bring considerable improvements.

8.1.1 *Increasing the Zd range of the LIDAR*

Mechanical constraints imposed by the size of the dome and the length of the telescope tube did not allow to go below a Zd of 55 °, making it impossible to use the LIDAR for VHZD observations, such as the GC observations, in a proper way. The solution to this problem was relatively simple and has already been implemented. A larger Zd range (5 °/15 ° depending on the azimuth) is achieved by lifting the LIDAR mount on 32 cm with respect to its old position.

8.1.2 *Improved photo detector module*

The custom made HPD detector module, which is described in chapter 5.4.1 showed a good performance during most of the first 1.5 years of regular LIDAR measurements. But it has some disadvantages for automatic, maintenance free operation.

The biggest disadvantage is its sensitivity to humidity. Since the LIDAR is a custom development, the detector PCB was designed in a way that allows for modifications/exchange of the electronic components. Currently neither the PCB, nor the housing are perfectly sealed. This imperfect protection against humidity, together with the applied HV of up to 8 kV leads to malfunction when the ambient relative humidity rises over 85 %.

Another problem, partially related to the previously mentioned one is the acceptable but not optimal signal to noise ratio. It is connected to the bad protection against humidity, because the HV and therefore the charge amplification had to be decreased to 5 kV during regular operation, in order to avoid problems. Other aspects are proper screening, galvanic decoupling, avoidance of ground loops and tuning of the bandwidth of the amplifier.

A new detector design should incorporate both aspects. Utmost effort should be made in order to improve the signal quality and the signal to noise ratio of the detector. Best possible protection against humidity can be achieved by sealing all electronic parts after the final lab tests.

8.1.3 *More powerful laser*

It is obvious that the useful range of the LIDAR could be increased by choosing a more powerful laser. This step might be necessary if using the LIDAR for VHZD observations. In this case the air-shower maximum is located at distances of 20 km or more. Due to the $1/r^2$ decrease of the signal a stronger light source might be necessary.

Use of a stronger laser should be evaluated carefully, considering the increased influence on the MAGIC telescopes as well as possible influence on other instruments at the ORM. Another issue is the reduction of saturation of the detector at close range. For possible solutions to this problem see the next two subsections.

8.1.4 *Second readout channel*

The ultimate solution to several problems of LIDAR, namely saturation and the incomplete overlap[1] at close range and generally limited dynamic range could be the use of different receiver channels with their own optical system and detector. If one wants to decrease the lower range limit of the LIDAR, this can be done by simply adding a second detector with own receiver optics to the system. It should be installed as close as possible to the laser optical axis in order to achieve full geometric overlap, already at relatively close distance. For such a short range detector, PDE and background-light suppression are less important due to the strong back-scattered signal.

---

[1] Part of the light scattered at short distance from the LIDAR is not mapped correctly onto the detector. This is due to the offset between the axis of the laser and the telescope on one hand and because for close distances the light is not focused to the plane of the detector on the other hand.

8.1.5 *Higher FADC resolution*

A higher than 8 bit resolution of the FADC would have two advantages. The first and most important is the higher dynamic range for the charge integration mode of operation (close range region). The second is that it would allow for more sophisticated pedestal subtraction algorithms that can deal better with low frequency noise. In the current situation subtracting a time dependent pedestal can cause step like features in the signal. This happens if the photon counting threshold, in this case also time dependent, crosses a digitization step and the acceptance for photons and especially noise suddenly changes.

8.2 SOFTWARE IMPROVEMENTS

The above mentioned improvements are already being developed and are partially implemented and tested. It will still require some final testing before they can be released with the latest MARS version. Changes in the LIDAR data recording routine are already implemented in La Palma but those only affect the most recently taken data.

8.2.1 *Improved background and pedestal subtraction*

For some LIDAR measurements it was found that the baseline of the FADC curve is not flat, but changes throughout the signal that is recorded for a single laser shot. Usually it tends to increase towards the far end of the curve. This leads to an underestimation of the background, which is extracted from the pre-trigger region at the very beginning of the signal. Due to the variable baseline the probability for noise triggering the photon counting is increased at the far end of the signal, compared to the close range. This may lead to a systematic overestimation of the photon counts from very high altitude and therefore to a too small slope or an upward bending of the range corrected signal from high altitude ($h \gtrsim 15\,\mathrm{km}$).

The exact electronic reason for this effect is unknown - probably a very slow ringing effect after the laser shot. But the problem can be tracked software-wise in two different ways. The first, lower level approach uses a linear interpolation between the beginning and the end of the recording range for the pedestal subtraction. The second method uses the assumption of pure Rayleigh scattering at very high altitude for estimating the background, instead of using the pre-trigger region. The first method is the preferred one because it is more fundamental and uses less assumptions. But it is not applicable to archival data since the raw FADC data is usually not stored to hard disk, due to its large data volume (1.6 GB) per measurement.

Both methods are already implemented and currently being tested. For the first method the pedestal is simply evaluated for the first and the last 512 FADC slices and the linear interpolation is being subtracted from each bin. Additionally the photon counting threshold needs to be slightly adjusted in order to avoid it crossing an FADC bin edge. The second method works as follows: Assume that one is evaluating the signal (incl. background) at two different distances r_1, r_2 at the far end of the range, where only Rayleigh scattering is expected. The photon counts should be given by

$$N_{\mathrm{ph},1} = A \cdot \frac{\exp(-\cos(Zd)\, r_1/h_\mathrm{s})}{r_1^2} + B\,, \tag{8.2.1}$$

$$N_{\mathrm{ph},2} = A \cdot \frac{\exp(-\cos(Zd)\, r_2/h_\mathrm{s})}{r_2^2} + B\,, \tag{8.2.2}$$

where A is an arbitrary scaling to match the real signal, B is the background that one is interested in and h_s is the scale height of the atmosphere. This set of equations can be solved for B, using

$$E = \frac{\exp(\cos(Zd)\, r_2/h_\mathrm{s}) \cdot r_2^2}{\exp(\cos(Zd)\, r_1/h_\mathrm{s}) \cdot r_1^2} = \exp\left(\frac{\cos(Zd)\,(r_2 - r_1)}{h_\mathrm{s}}\right) \cdot \frac{r_2^2}{r_1^2}\,. \tag{8.2.3}$$

$$B = \frac{N_{\mathrm{ph},1} - E\, N_{\mathrm{ph},2}}{1 - E}\,. \tag{8.2.4}$$

Using this method one has to be aware of the limitations. The true scale height for a given measurement is usually not known a priori and has to be estimated. Furthermore it is also altitude dependent, due to the temperature inversion starting at around 10 km altitude. Assuming a typical scale height for the molecular density profile in the stratosphere of about 8 km, with an uncertainty band of 1 km, the error on the background subtraction is on the order of 10% of the back-scattered signal.

8.2.2 *Fitting real atmospheric density profiles*

This second software/analysis based improvement is also already being worked on. The goal of it is fitting accurate atmospheric density profiles, which are available from contemporary GDAS (Global Data Assimilation System) data, to the LIDAR profiles. The GDAS profiles are mainly based on radiosonde measurements from the neighboring island Tenerife and available on a daily basis. Using real atmospheric profiles instead of the simple exponential function for fitting the Rayleigh part of the LIDAR measurements will help further decreasing the systematic errors.

Part III

GALACTIC CENTER OBSERVATIONS

Only a few decades ago Imaging Air-shower Cherenkov Telescopes opened a new observational window for astronomy, adding about three decades to the available energy spectrum. Only non-thermal processes in very extreme environments are able to accelerate charged particles that are able to produce γ-radiation of TeV energies. Such processes must be at work in the central few parsecs of our galaxy, which is known as a source of VHE γ-radiation since a few years already. The exact nature of these processes however stays unknown. An exceptional event happening in the GC currently presents an unprecedented opportunity to shed light on those processes, if observed with a large number of instruments covering radio to very high energy γ-rays. MAGIC can play a crucial role in bringing information from the processes producing the highest energy radiation.

9

MOTIVATIONS FOR OBSERVING THE GC WITH MAGIC

Triggered by an unprecedented event, the central region of our galaxy has been observed with MAGIC in the years 2012, 2013 and 2014. It has been reported by Gillessen et al. (2012) that a gas cloud of several times the Earth's mass is on a highly eccentric orbit towards the compact radio source SgrA*, which is thought to be the dynamic center of our galaxy, a black hole (BH) (Schödel et al., 2002) with $4.3 \cdot 10^6\,\mathrm{M}_\odot$ (Gillessen et al., 2009). All the time since its discovery, there have been speculations about the fate of the cloud and if it will be subjected to accretion by the central BH of our galaxy (Gillessen et al., 2012).

These observations had to be carried out under special conditions, because the Galactic Center (GC) is culminating at 58° zenith distance (Zd) when observed by the MAGIC telescopes (La Palma, 28.7616° N, 17.8905° W). Observing at that large Zd, the Cherenkov light is more widely spread on the ground. This results in a higher energy threshold but also an increased effective collection area. These circumstances make MAGIC a very competitive instrument if compared to the Cherenkov telescopes in the southern hemisphere, if the focus is on the highest energies.

9.1 ASTROPHYSICAL ENVIRONMENT IN THE CENTER OF OUR GALAXY

The central region of our galaxy is very densely populated by a large variety of astrophysical objects. Observations as well as interpretation have always been challenging for this part of the sky due to source confusion and absorption by other objects in the line of sight. Especially in the optical, all light from the GC is absorbed by interstellar dust in the Galactic plane (Genzel et al., 2010). Only in radio, infrared, X-ray and γ-rays, observations are possible. It is remarkable that in spite of all those challenges, the GC region has been studied with such high observational precision over the last three decades. The most precise data, especially regarding angular resolution, are coming from observations in near IR (40 marcsec resolution, Genzel et al., 2003) and radio (0.5 marcsec resolution, Bower et al., 2014) using large scale instruments like the Very Large Telescope (VLT, near IR), the Very Large Array (VLA, radio) and the Very Long Baseline Array (VLBA, radio). For comparison, the expected apparent size of the event horizon is about 10 μarcsec (Fish et al., 2011). Since 1999 the Chandra satellite offers an unprecedented angular resolution of 0.4 arcsec in the X-ray regime (Baganoff et al., 2000; Weisskopf et al., 2000).

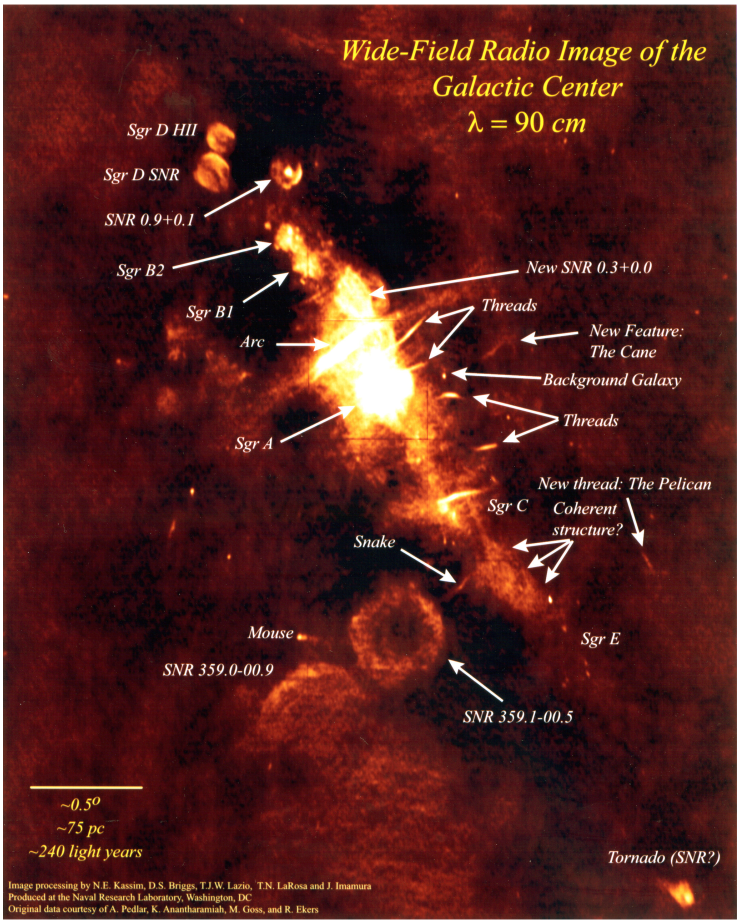

Image processing by N.E. Kassim, D.S. Briggs, T.J.W. Lazio, T.N. LaRosa and J. Imamura
Produced at the Naval Research Laboratory, Washington, DC
Original data courtesy of A. Pedlar, K. Anantharamiah, M. Goss, and R. Ekers

Figure 9.1: 90 cm radio image of the GC from observations with the very large array VLA. Many different sources of radio emission, like super nova remnants and giant molecular clouds cluster along the Galactic plane. Image: Kassim et al. (1998)

9.1.1 *The Galactic disk, bulge and nuclear bulge*

The Milky-way is thought to be a spiral type galaxy with a central bar extending out to about 4.5 kpc and a thicker $\sim$ 1.5 kpc radius bulge in it's center. (Cabrera-Lavers et al., 2008; Martinez-Valpuesta & Gerhard, 2011). Star formation is significantly stronger in the disc compared to the Galactic bulge, which is gas depleted and containing mostly metal rich old stars. Star forming regions reappear when going even closer to the center. There is a narrow band of molecular clouds extending $\sim 1.5\,^{\circ}$ left and right from the GC. The densest structures there are SgrA, SgrB and SgrC (Mezger et al., 1996).

9.1.2 *The SgrA radio complex*

The central $\sim$ 500 pc region of our galaxy contains a variety of strong radio sources. The 90 cm VLA image in figure 9.1 published by Kassim et al. (1998) can be used for orientation. The brightest region is at the dynamical center of the Milky-way galaxy, the SgrA radio complex. The three most dominant radio features are the SNR SgrA East, which is about 2 arcmin in diameter, the mini-spiral or SrgA West with three arms (45 arcsec) and the point like radio source SgrA* (Davies et al., 1976; Ekers et al., 1983). SgrA East, which is emitting a non-thermal radio spectrum and strong K_α-lines in X-ray is thought to be the SNR of a powerful supernova with a $13 - 20\,M_\odot$ progenitor star, about 10 000 y old (Maeda et al., 2002). SgrA West is thought to be connected to the so-called circumnuclear disk consisting of mostly molecular gas. It consists of ionized and atomic gas, as well as dust, emitting thermal spectra of temperatures between 100 an 10 000 K (Kunneriath et al., 2012). SgrA* was detected as bright, sub-arc-second radio source by Balick & Brown (1974) using data from the National Radio Astronomy Observatory (NRAO). Since then it has been hypothesized to be linked to a super massive black hole (SMBH) at the dynamical center of our galaxy. Recent evidence has been found that a parsec scale jet exists, which originates from SgrA*(Yusef-Zadeh et al., 2012; Li et al., 2013).

Very recently, observations using very long baseline interferometry (VLBI) in radio reach angular resolutions comparable to the scale of the event horizon of the SMBH ($\sim$ 10 μarcsec) (Doeleman et al., 2008; Fish et al., 2011). Future interferometers like GRAVITY will reach similar resolutions also in infrared (Eisenhauer et al., 2008). This will allow for resolved observations of processes happening at or very close to the event horizon of SgrA*.

9.1.3 *The S-star cluster and the SMBH*

Another very important piece of evidence for the black hole hypothesis were measurements of the velocity dispersion of stars in the central parsec (Krabbe et al., 1995). The most compelling evidence for a black hole of about $4 \cdot 10^6\ M_\odot$ comes from the direct observation of orbits of very bright stars around SgrA*, the so-called S star cluster (Genzel & Eckart, 1999). Schödel et al. (2002)

reported the observation of the pericentre passage at a distance of only 124 AU from SgrA*. This observation excludes most alternative scenarios, other than a SMBH.

One still unresolved mystery about the GC black hole is its relative weak activity (Genzel et al., 2010). Maeda et al. (2002) suggest that SgrA East might be responsible for increased activity of the SMBH SgrA* about 1000 years ago, sweeping over it with the shock of the SNR. At the same time this might be the reason for present inactivity, because gas that would otherwise be available for accretion has been pushed away.

9.1.4 *Dark matter searches in the GC region*

Apart from astrophysical studies, the GC is also a popular target for searching for dark matter decay/annihilation. If assuming a λCDM model for the evolution of the universe in which weakly interacting massive particles (WIMPs) that can either annihilate or decay to standard model particles, the highest flux of decay products is expected in places where also the concentration of visible matter is high (see also chapter 3.4.5). The interaction rates should scale proportionally to the density ρ for decay and like ρ^2 for annihilation. The dark matter halo of the Milky Way should have a density profile which is roughly scaling with $r^{-0.5}$, given the fact that the rotation curve is flat (Trimble, 1987). Because it is relatively close by, and given the high density, the GC is a good place for searching for DM annihilation. For this purpose γ-rays are good messenger particles. In the GC region also the background from astrophysical sources is quite high, therefore other objects like dwarf galaxies are also good targets due to the expected low background (Aleksić et al., 2011; Ackermann et al., 2011).

Experiments like the *Fermi* telescope have been searching for traces of annihilating DM since the start of the mission. Weniger (2012) found a 4.6σ local significance excess in the γ-ray spectrum at 130 GeV in *Fermi* data from within a few degrees from the GC. These findings are still being actively discussed as possible effect of some sort of systematic error. No effect, which has large enough impact on the spectrum could be found yet (Finkbeiner et al., 2013).

9.2 PREVIOUS VHE OBSERVATIONS OF THE SGRA REGION

The GC has been a popular target for observations with IACTs from the very beginning. The first strong hints for a detection were reported by CANGAROO II (Enomoto et al., 2003), and one year later by the Whipple collaboration ($3.7\,\sigma$) (Kosack et al., 2004). Detection was claimed in the same year by CANGAROO II (Tsuchiya et al., 2004), who reported a very steep spectral index of $\alpha = -4.6$, which was clearly ruled out by later observations. The H.E.S.S. collaboration, also in the same year, reported a highly significant ($\sim 10\,\sigma$) detection of a source at the GC with spectral index $\alpha = -2.2$ (Aharonian et al., 2004). They gave the name HESS J1745-290 to the source. MAGIC I mono observations could largely confirm the detection by H.E.S.S. with compatible flux and spectral index (Albert et al., 2006).

More recently new observations have been reported on by H.E.S.S. (Aharonian et al., 2009) and VERITAS (Archer et al., 2014). Acero et al. (2010b) claimed to be able to rule out SgrA East as main contributor to the TeV emission from the GC, making black-hole accretion scenarios even more likely.

9.3 THE GAS CLOUD G2

It was first reported by Gillessen et al. (2012) that VLT observations in the infrared have revealed a gas cloud on a highly eccentric orbit towards the central BH of our galaxy. They estimated a mass of about three times the Earth's and extrapolated the orbit, which resulted in a pericentre passage around mid 2013 at a distance of about 3100 Schwarzschild radii (R_S) or 36 light hours. These numbers were later updated and the predicted pericentre passage was shifted to September 10th 2013 and an even closer approach to the BH was predicted 2200 R_S (Gillessen et al., 2013a). Finally Gillessen et al. (2013b) reported that they could already observe part of the gas of G2 on the blue-shifted side in April 2013 and that the whole pericentre passage would probably extend over at least one whole year.

Predictions about the exact fate of that gas cloud and its possible effect on the accretion rate of the GC black hole depend a lot on the assumed models for the cloud and the environment around the BH. Therefore, predictions diverge from very little to no effect until possible strong flaring activity of SgrA* (Schartmann et al., 2012; Giannios & Sironi, 2013). Some models also predict the interaction of G2 with stellar mass black holes (SMBH) expected to exist in the vicinity of SgrA* (Bartos et al., 2013).

Given this unprecedented chance, observations in as many wavelengths as possible are being conducted in order to study the nature of the central BH of our galaxy.

10

THE MAGIC OBSERVATION CAMPAIGN AND DATA SET

The proposal of observing the GC was accepted in spring 2012. The campaign was intended as long-term monitoring program spanning over several years. Since then 66 h of good quality data were recorded. In the following I will first introduce the observation strategy, highlighting some of the major challenges that come with the low culmination altitude of the source. Thereafter the individual data sets recorded in the three years of observation will be presented and the quality selection cuts will be motivated.

10.1 THE OBSERVATION STRATEGY

When observed from the MAGIC telescope site, the GC culminates at 57.78 ° Zd. This has many implications for the observation conditions and the available time slot for the observations. The time window for observing the GC with MAGIC when setting the Zd limit to 70 ° is roughly from mid February until end of September.

The observation strategy proposed in 2012 was to start a longer term monitoring program that extends over a minimum of 5 years with 20h dedicated to GC observations each year. The goal of this proposal was two-fold. First of all, the VHE-γ flux of the GC is monitored in order to search for variability or flaring activity that could be caused by the interaction with the gas cloud G2. Second, the large data set can be used for a deep study of the morphology and spectrum of the sources of VHE-γ radiation in the vicinity SgrA*. Such a deep study can help to find an answer to the question about the origin of the γ-radiation that is observed from the GC, and also shed light on possible more active states of the GC in the recent past.

In order to achieve an extended and homogenous light curve, the source was observed on as many of the available days as possible, spanning over the whole observability period from end of February to end of July. See figure 10.1 for an illustration of the available period. The area filled in red is not available due to the trigger issue described below.

10.1.1 *The "L3 Deadzone"*

GC observations by MAGIC are further restricted in time by a problem that is very specific for the electronic design of the trigger and readout system of the MAGIC telescopes. As it is described in chapter 3.2.3, MAGIC uses the so-called Domino 4 analog ring sampler chip with an analog buffer of 1024 time slices, which gives a time budget of 512 ns when operated at a sampling rate of

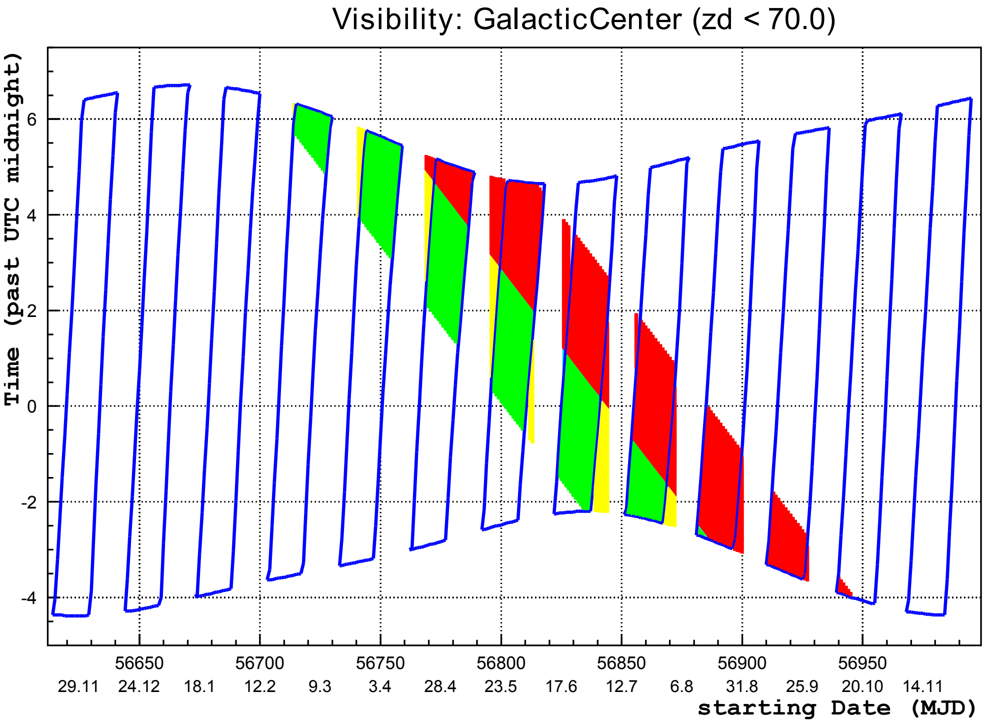

Figure 10.1: This is an exemplary visibility plot for MAGIC GC observations in 2014. The x-axis shows the observation date and the y-axis the intra-night time in hours from UTC midnight. The observation limit is set to 70 ° Zd. Dark time before culmination is shown in green, acceptable moon time and twilight in yellow and post culmination time, which is not available due to the "L3 Deadzone" issue, in red.

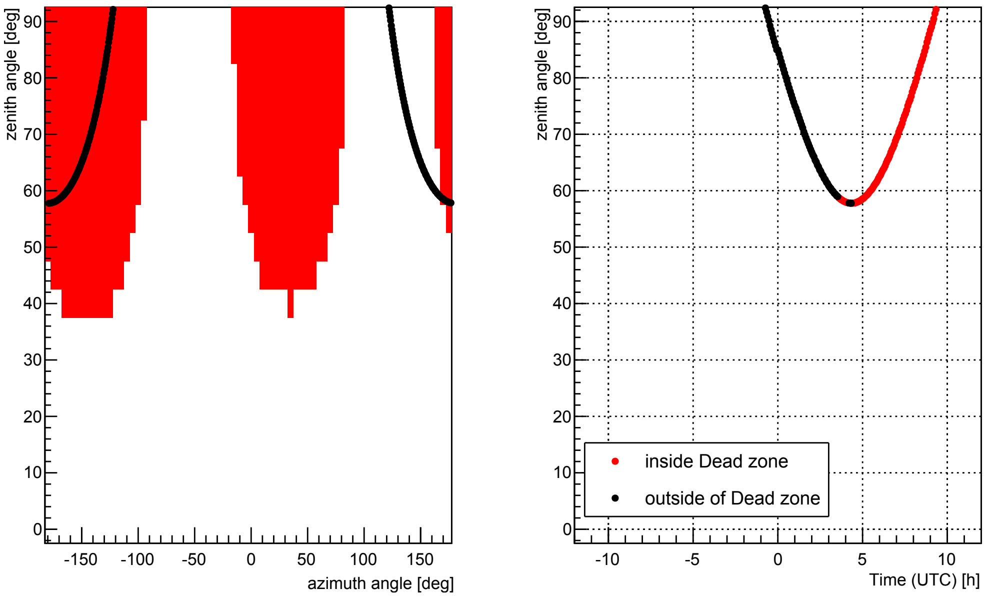

Figure 10.2: The "L3 Deadzone" (red) and observable time windows (black) for the GC. Source trajectories in Zd vs. azimuth and Zd vs. time from UT midnight. Plots courtesy of Daniel Mazin

2 GHz. When the signal of a given telescope arrives at the readout electronics, it is stored in the analog buffer and subsequently overwritten when the buffer is used up. This happens in parallel to the formation of a stereo trigger decision. Because the telescopes are located at a distance of 80 m, depending on the observed Zd and azimuth, the signal delay between the two telescopes can be up to 250 ns. Additional time is lost in the trigger electronics and for transmitting the trigger decision to the DAQ. In very unfortunate cases, where the projected distance between the telescopes is close to maximum, the whole time budget gets used up and there is not enough buffer length left for the 30 ns ROI readout. Inside this "L3 Deadzone", it is impossible to take stereo data with MAGIC.

The implication of this problem for the GC observations was that MAGIC could only observe the source before culmination, i.e. in a configuration where the telescopes are not lined up with the observational direction. See figure 10.2 for an illustration of the available time windows.

10.1.2 *The implications of the very large zenith distance*

Because of it's low culmination (57.78 ° Zd), the GC does not leave one much choice for observational Zd range. Being forced to observe under such extreme zenith angles, at first seems to be a clear drawback when compared to the performance of low zenith angle observations of telescopes on the southern hemisphere. The total available time slot of only $\sim$ 2 h per night is rather short and the energy threshold is certainly increased by a large factor. Also stereoscopy could be affected, due to the larger distance to the shower core and the therefore smaller relative separation of the telescopes. Finally, also the distance through the atmosphere is enlarged, which amplifies all atmospheric effects and uncertainties.

Naively one can expect that the distance to the shower core scales with $\cos(\theta_{\mathrm{Zd}})^{-1}$ and therefore the Cherenkov light flux density on the ground with $\cos(\theta_{\mathrm{Zd}})^{2}$. The area of the Cherenkov light pool on the ground on the other hand will scale with $\cos(\theta_{\mathrm{Zd}})^{-2}$. This means that for a Zd of 60 °, the energy threshold should go up by a factor four and at the same time, the effective collection area should increase by the same factor. In reality, the decrease in sensitivity at low and the increase at high energies depends on a few more parameters, such as the atmosphere, the L3 trigger sensitive area on the ground, the altitude of the shower maximum, focusing of the telescopes, and of course also the effectiveness of the gamma-hadron separation.

A better approximation for the scaling of the light yield and the collection area can be found in appendix G. In result the scaling of light yield and geometric collection area can be better approximated by a $\cos(\theta_{\mathrm{Zd}})^{3.5-4}$ dependence. These numbers however are only for the geometric scaling of the light pool and are neglecting absorption effects, as well as the change in trigger efficiency when decreasing the light yield.

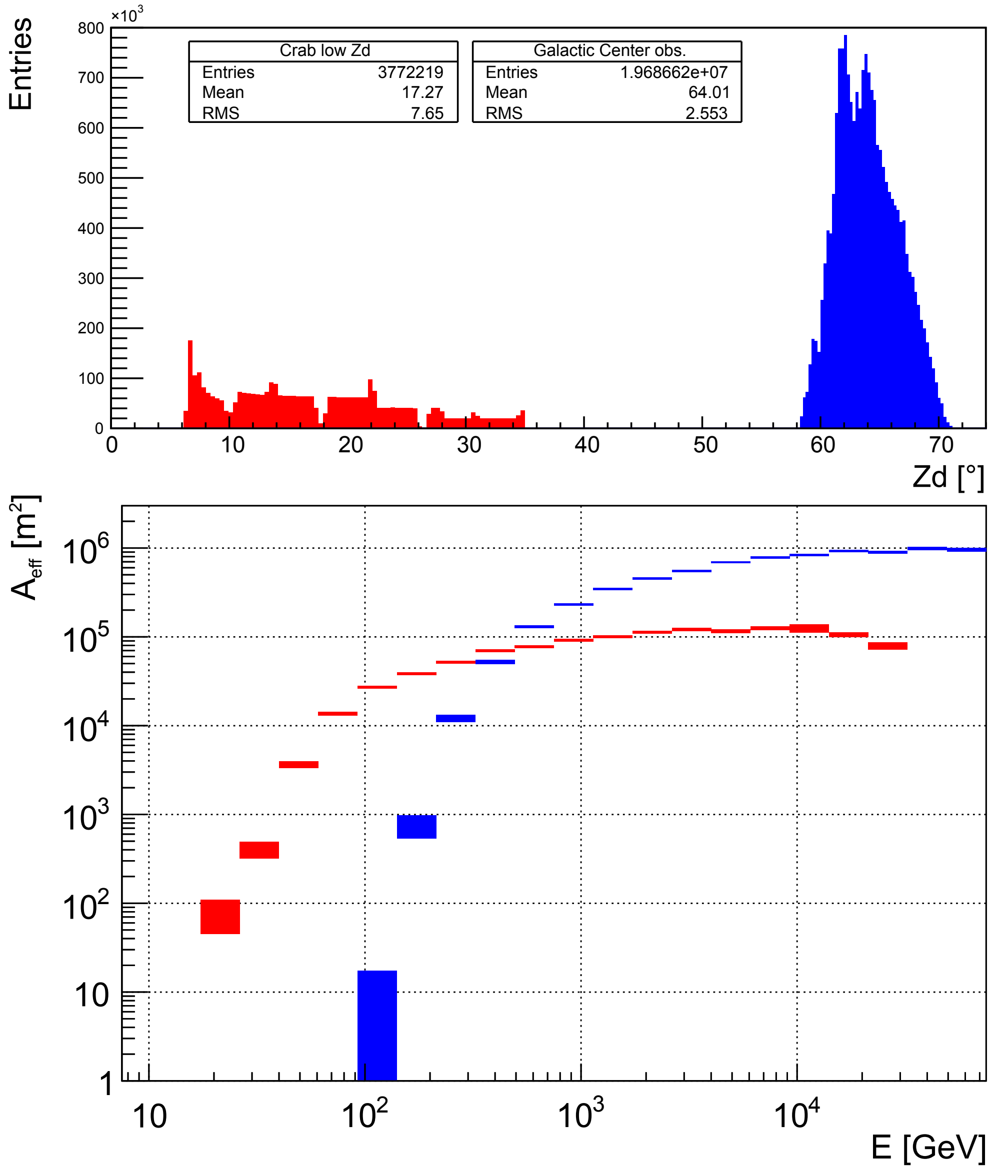

Figure 10.3: Zenith distance distributions of the events and collection areas after analysis for the Zd range $5 - 35\,^\circ$ (Low Zd Crab sample, red) and $58 - 70\,^\circ$ (2013 GC sample, blue) estimated from Monte Carlo γ-events. These results have been obtained using similar background subtraction (90 % survival efficiency for MC gammas). The collection area for high energies ($\gtrsim$ 10 TeV) increases by nearly a factor ten, while the energy threshold rises by about the same factor when going to extremely high Zd. Both observations perform similar at 500 GeV.

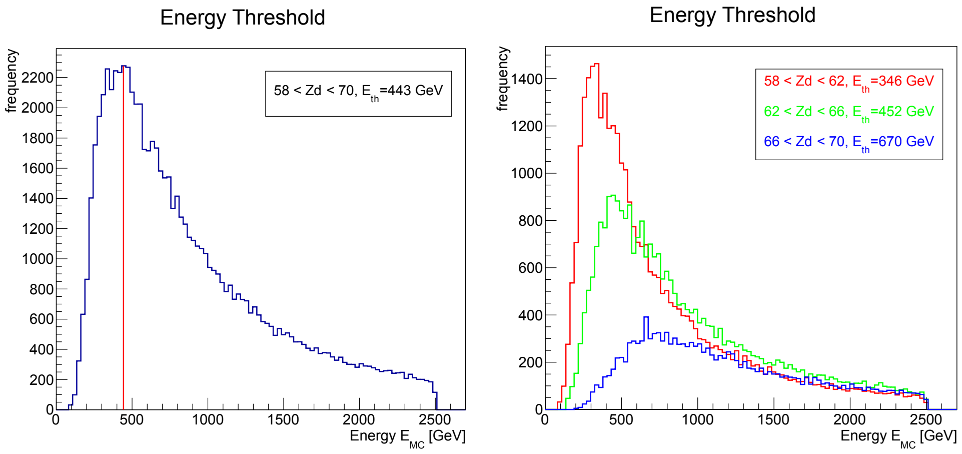

(a)

(b)

Figure 10.4: Energy threshold for very high Zd observations with MAGIC. The histograms were generated from MC, reweighting the energy spectra to match the spectral index of the Crab Nebula, $\alpha = -2.6$. The energy threshold for the whole Zd range of the GC observations is around 0.44 TeV (a). The energy threshold at this high Zd has a very strong dependence on Zd (b).

A better estimation of the trigger threshold and the effective collection area can be obtained by analyzing Monte Carlo data. As it can be seen in figure 10.3 the Zd range used in the GC observations compared to low Zd observations gives an increase of a bit less then a factor ten in energy threshold, but also shows an improvement in effective collection area at the highest energies by at least the same factor. A more exact determination of the energy threshold, defined as the maximum in the MC-event distribution after applying typical γ-hadron separation cuts, can be found in figure 10.4. The energy threshold for the whole Zd range covered by the GC observations is around 0.44 TeV. It is strongly Zd dependent as it can be seen from figure 10.4 (b).

10.2 DATA SAMPLE AND QUALITY CUTS

In this observation campaign, so far, the GC was observed in the years 2012, 2013 and 2014. for a total of about 66 hours. In the meantime the hardware and the telescope performance were changing due to various upgrades. In the following I will present the data-sets separately for each year and motivate the data quality selection cuts. In order to improve readability the tables summarizing the observations can be found in appendix B.

10.2.1 *2012 data sample*

The observations in 2012 were the shortest and least successful but could serve well to help improving the scheduling scheme for the following years. The idea for the proposal was triggered by the first reports about the gas cloud G2, but the observations were only possible due to a shift in the MAGIC upgrade schedule that was generating some left over observation time in spring 2012. The proposal was finally accepted and granted 20 h in an accelerated evaluation procedure and observations could start in mid April. One of the biggest issues in 2012 was that the "Deadzone" problem was not fully understood and therefore not taken into account correctly by the scheduler. Data taken after culmination had to be discarded. Quality cuts were applied to the remaining sample mainly based on the number of identified stars in the star-guider images ($> 0.66\times$ the saturation value for the corresponding star-field), rate of events with size greater 100 (only safety limits) and camera DC currents ($\sim 2.5\times$ the typical dark time value). LIDAR information was not yet available for that data-set. Additionally, LIDAR can only be used for $\lesssim 60\,^{\circ}$Zd, because of mechanical constraints of the movement of the telescope by the dome. The remaining observation days with the remaining effective observation times can be found in table B.1 in the appendix.

10.2.2 *2013 data sample*

After the 2012 observations could prove the expected good performance of the MAGIC telescopes above ~ 1 TeV at very large Zd, the proposal for 2013 was accepted as part of a multi-year campaign with the aim of monitoring the activity of SgrA* and granted a minimum of 20 h. With the experience gained in 2012, the 2013 observations could be scheduled much more efficiently. The whole available time window from March to July could be covered relatively homogeneously. For the quality cuts, the same scheme as for the 2012 data was applied, with the only difference, that cutting on the azimuth direction was not necessary any more, because the "Deadzone" could already be prevented in scheduling. The full post-analysis data-set is summarized in table B.2 (appendix).

10.2.3 *2014 data sample*

The time granted to the proposal is again 20 h like in the years before. The goal pursued in scheduling was again to cover the whole available period as homogeneously as possible. The already available data-set was filtered with the same already proven effective quality cuts as in the years before. Remaining times are summarized in table B.3.

11

DATA ANALYIS AND RESULTS

In this chapter I present the details of the GC data analysis, starting from preselected data runs, according to quality selection criteria (see chapter 10). This overview starts from source detection plots, continues with the presentation of γ-ray skymaps and energy spectra and finishes with searches for variability of the γ-ray flux from the GC. In order to improve readability, some of the tables and figures containing supplementary information can be found in appendix B.

11.1 DATA ANALYSIS AND SOURCE DETECTION

After applying quality cuts as described in chapter 10 the data could be analyzed with the standard MAGIC software tools (see chapter 3.2.4 and appendix D), starting from image parameter files (Star output level). After joining the single telescope information and calculation of the stereo parameters it was necessary to train dedicated Random Forests (RFs) for the gamma-hadron separation and the direction reconstruction. Finally, the location of SgrA* (RA 266.4168 °, Dec -29.0078 °) was searched for a significant γ-ray excess using θ^2-histograms. θ^2 detection plots show the number of events in bins of squared angular distance to an assumed source position. They have become a common tool for probing sky positions for significant excess in VHE γ-ray astronomy. See appendix D for a more detailed description of the method.

11.1.1 *2012 data*

For the 2012 data, which was taken during a period of frequent hardware changes, no appropriate source free sample for the Zd range above 58 ° was available. A subset of the GC data itself had to be selected as hadron sample for the calculation of the RFs. One usually tries to avoid this practice, especially if the source in scope is expected to contribute significantly to the cosmic ray flux. In this case however there was no other choice if one wanted to avoid using background data that was recorded with different camera geometry or readout electronics. Also, as described above, only a relatively small sample of useful data could be extracted from the 2012 observations. Still it was possible to make a $\sim 5\sigma$ detection from the remaining 6 h after quality cuts for both, full range and low energy optimized cuts. The corresponding θ^2 detection plots can be found in figure 11.1 (a,b).

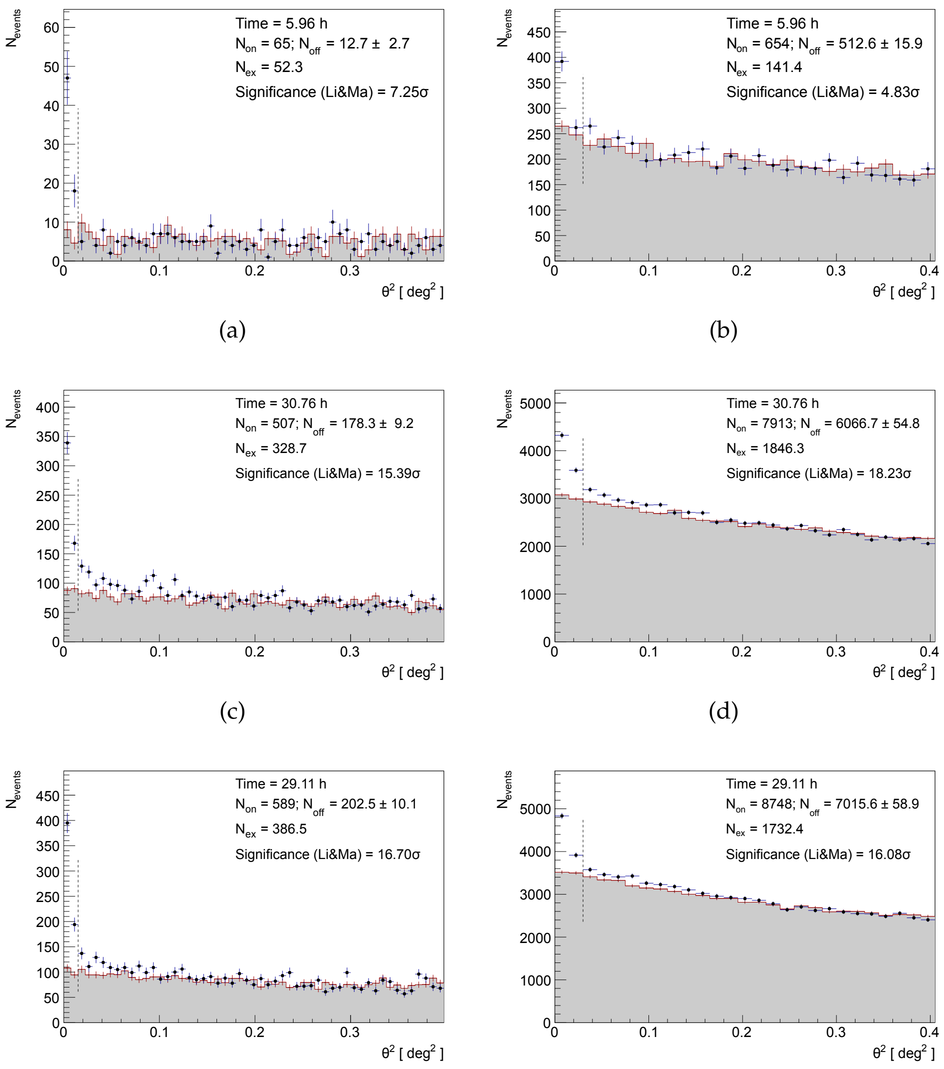

(a) (b)

(c) (d)

(e) (f)

Figure 11.1: Detection (θ^2) plots for the GC observations in the years 2012 (a,b), 2013 (c,d) and 2014 (e,f). The detection plots were made with different sets of cuts. The left side shows θ^2 histograms after applying cuts optimized for good sensitivity over the full spectral range. The right side is using cuts that were optimized for good sensitivity close to the energy threshold. The on-source histogram is displayed as data-points only, while the background histogram is displayed with data-points and gray bars.

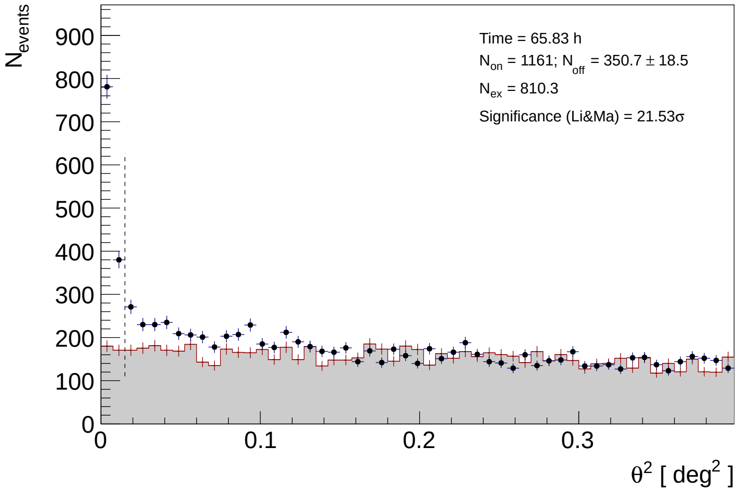

Figure 11.2: Detection (θ^2) plot for the set of GC observations. The none zero excess, which extends out until $\theta^2 \approx 0.15$ already gives a hint for extended emission from regions around the central source.

11.1.2 *2013 data*

For the 2013 data-set dedicated MC events as well as off-source observations are available for the generation of specialized RFs. Within the 31 h of good quality data, the GC γ-ray source could be detected on a 15σ level for full range optimized cuts and with 18σ for low energy cuts (see figure 11.1 (c,d)).

11.1.3 *2014 data*

For the 2014 data, dedicated MC simulations for the running period with very large Zd are not yet available. Therefore the same RFs that were used for analyzing the 2013 data had to be applied to this sample as well. This is not too problematic in this case, since, except for some minor adjustments in the focusing of the mirrors there were no big hardware changes in the meantime. The 2013 RFs seem to work well for the 2014 data-sample, yielding a 17σ detection applying full range cuts and 16σ with low energy cuts.

In summary, one can say that significant γ-ray emission from within $\sim 0.1\,^\circ$ from the location of SgrA* could be detected in all three years. The θ^2 plot for the complete data-set is shown in figure 11.2 with a 21.5σ detection. There is already a hint for extended emission in the θ^2 histograms. For values of $\theta^2 < 0.15$ there are always slightly more counts in the on, compared to the off histogram. The source extension will become obvious when looking at the sky-maps, which will be presented in the next section.

11.2 SKYMAPS

For studying more deeply the morphology of the γ-ray source at the Galactic Center and for searching the region for additional sources lying inside the

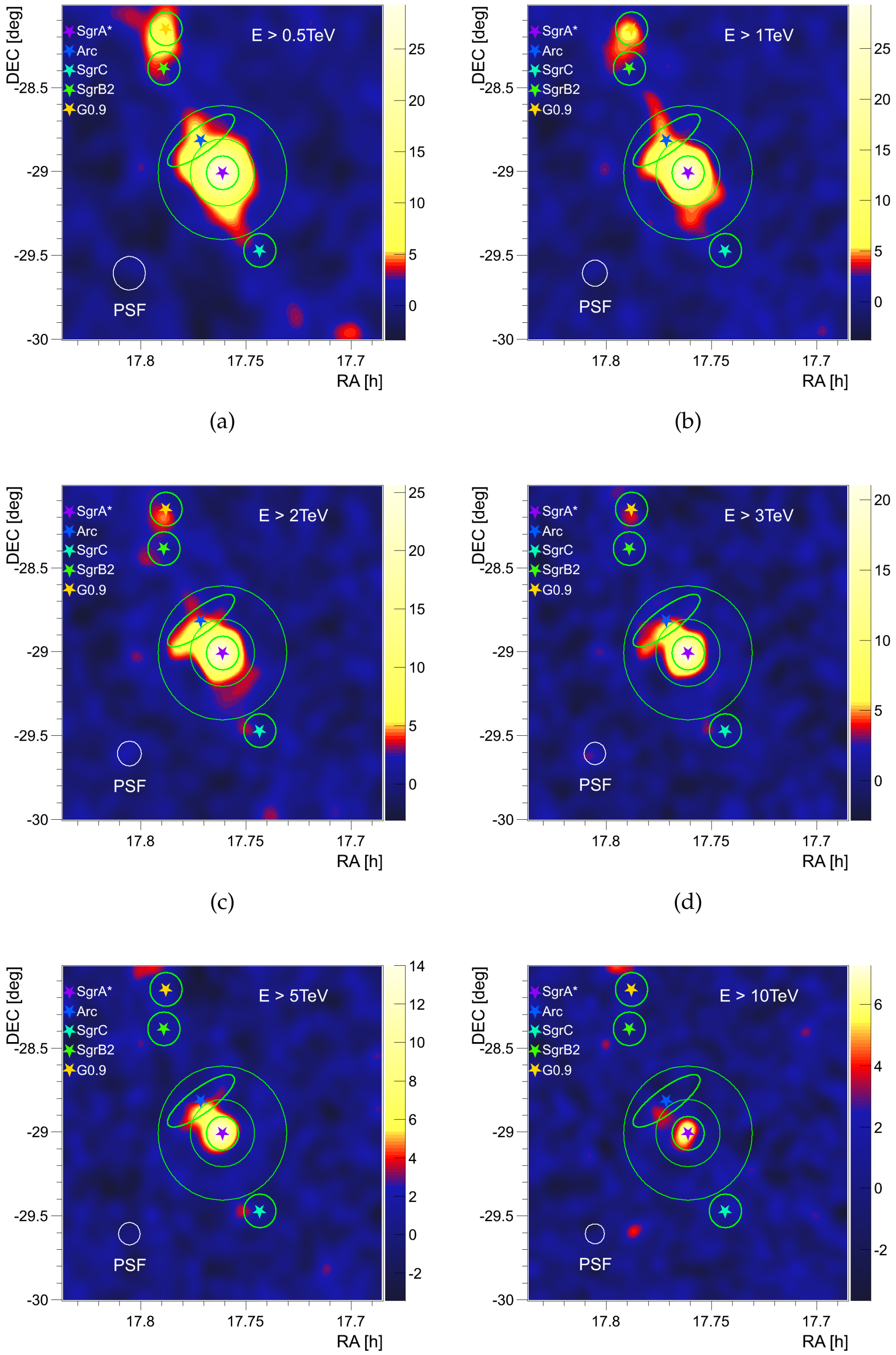

(a) (b) (c) (d) (e) (f)

Figure 11.3: Test statistic (TS)-value map of the central 2° × 2° of our galaxy for different cuts in energy. The TS value can be interpreted as a local significance of the smeared γ-ray excess, assuming a Gaussian distribution of the background. The coordinates of important radio sources are highlighted with markers and circles of 0.1° radius. The Arc radio feature is marked by an ellipse of 0.5° length. Additional circles of 0.2° and 0.4° radius are drawn around SgrA* for indicating the different integration radii, from which the events for the energy spectra have been extracted. The coordinates of the radio sources have been taken from Law et al. (2008) and Petrov et al. (2011).

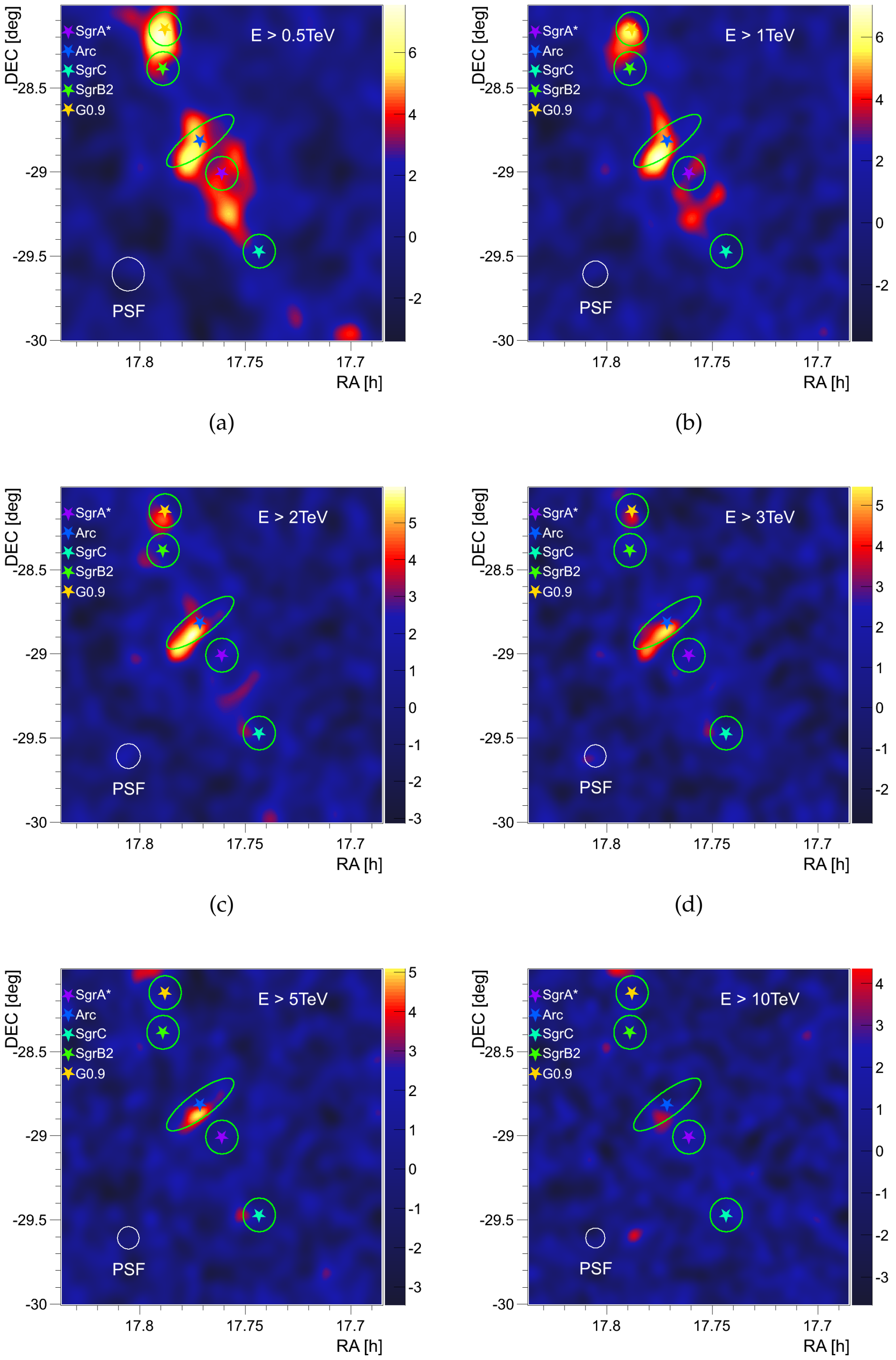

(a) (b)

(c) (d)

(e) (f)

Figure 11.4: Test statistic (TS)-value map of 2 ° × 2 ° around the GC for different cuts in energy. The 2D Gaussian resulting from a fit to the central source has been subtracted in order to highlight other features. Important sources known from radio observations are highlighted with markers and circles of 0.1 ° radius. The Arc radio source is marked by an ellipse of 0.5 ° length. The coordinates of the radio sources have been taken from Law et al. (2008) and Petrov et al. (2011).

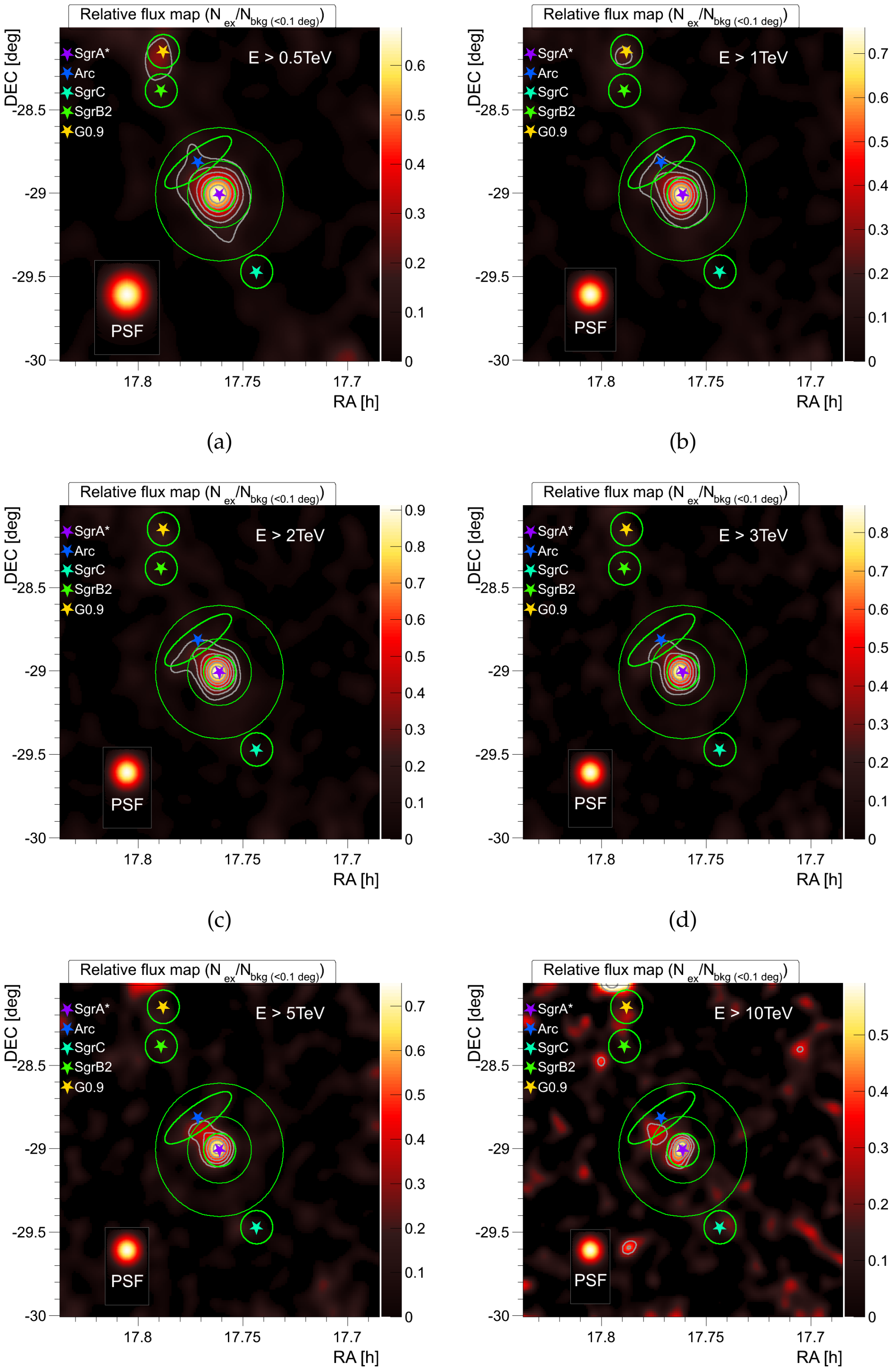

(a) (b)

(c) (d)

(e) (f)

Figure 11.5: Relative flux maps of the GC for different cuts in energy. The relative flux is the smeared excess map divided by the background map. The gray contours indicate the local significance of the excess starting from 5σ (3σ for the 10 TeV map (f)) and spaced by 1σ. Important radio source are highlighted with markers and circles of 0.1 ° radius. The Arc radio feature is marked by an ellipse of 0.5 ° length. Additional circles of 0.2 ° and 0.4 ° radius are drawn around SgrA* for indicating the different integration radii, from which the events for the energy spectra have been extracted. The coordinates of the radio sources have been taken from Law et al. (2008) and Petrov et al. (2011).

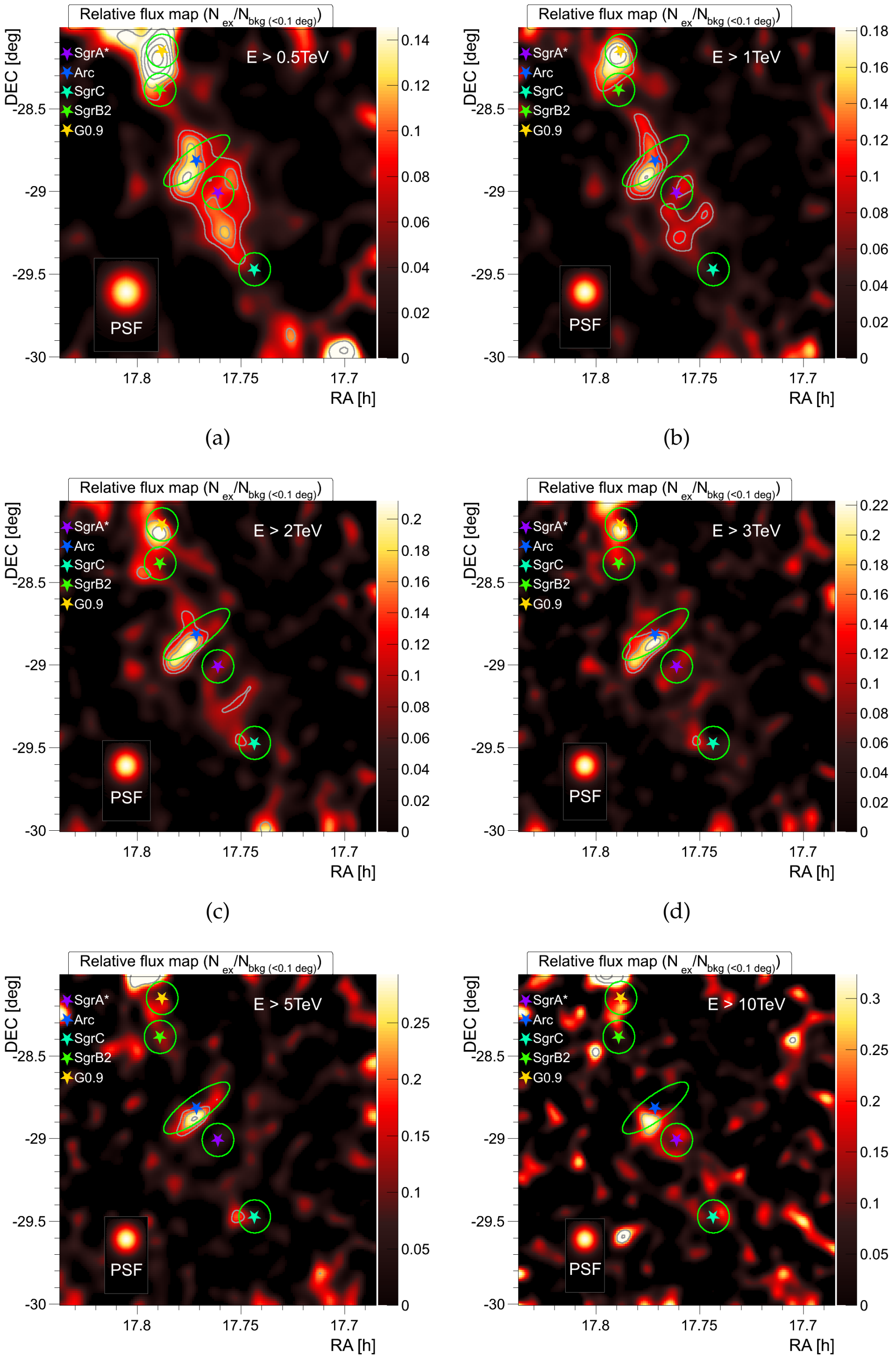

(a) (b) (c) (d) (e) (f)

Figure 11.6: Relative flux maps of the GC for different cuts in energy. The 2D Gaussian resulting from a fit to the central source has been subtracted. Bright radio sources are indicated with markers and circles of 0.1 ° radius. The gray contours show the local significance of the excess starting from 3σ. The Arc radio source is marked by an ellipse of 0.5 ° length. The coordinates of the radio sources have been taken from Law et al. (2008) and Petrov et al. (2011).

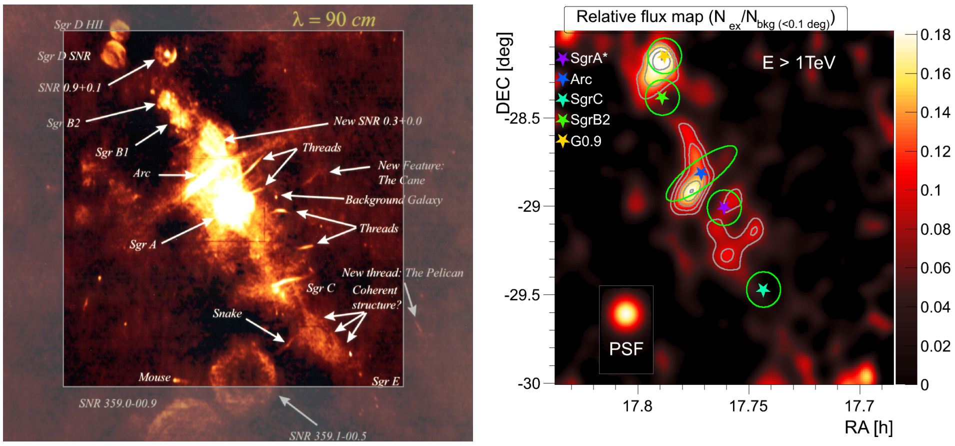

(a) (b)

Figure 11.7: Relative flux map of events with $E > 1\,\mathrm{TeV}$ and point source at the location of SgrA* removed (b) for direct comparison with VLA 90 cm radio image (Kassim et al., 1998) (a). The radio image has been clipped in order to show exactly the same FoV as shown by the γ-ray skymap.

	RA [°]	Dec [°]	δRA [°]	δDec [°]	offset [°]
SgrA*	266.417	-29.008	0.000	0.000	0.000 ± 0.000
($E > 500\,\mathrm{GeV}$)	266.4303	-29.002	0.014	0.006	0.013 ± 0.004
($E > 1\,\mathrm{TeV}$)	266.433	-29.010	0.017	-0.002	0.015 ± 0.003
($E > 2\,\mathrm{TeV}$)	266.436	-29.004	0.019	0.004	0.018 ± 0.003
($E > 3\,\mathrm{TeV}$)	266.440	-29.003	0.023	0.005	0.021 ± 0.004
($E > 5\,\mathrm{TeV}$)	266.439	-28.996	0.022	0.012	0.023 ± 0.007
($E > 10\,\mathrm{TeV}$)	266.439	-29.010	0.023	-0.002	0.020 ± 0.011

Table 11.1: Position fit results of the central source in the GC skymaps with different cuts in energy. The central 0.15° radius has been fitted with a 2D Gaussian in order to determine the location of the γ-ray emission. The coordinates (J2000) of SgrA* are taken from Petrov et al. (2011). δRA and δDec are indicating the signed offset of the fitted position from the coordinates of SgrA*.

useful FoV of MAGIC (2 ° × 2 °), skymaps were generated using the method described in appendix D. In order to study the energy dependence of the morphology, skymaps were generated for six different cuts in energy: $E > 0.5\,\text{TeV}$, $E > 1\,\text{TeV}$, $E > 2\,\text{TeV}$, $E > 3\,\text{TeV}$, $E > 5\,\text{TeV}$ and $E > 10\,\text{TeV}$.

The central source within a radius of 0.15 ° has been fitted with a two dimensional Gaussian. Table 11.1 shows the centroid positions of the fits and the offset with respect to the coordinates of SgrA* published by Petrov et al. (2011). The offset from the location of SgrA* ($\sim 0.02\,°$) is still covered by the systematic uncertainty on the reconstructed source position ($\lesssim 0.02\,°$, see 3.2.5 and Aleksic et al. (2014)). For dealing with the fact that the central source outshines the rest of the skymap by about one order of magnitude, dedicated skymaps have been generated, where the fitted Gaussian has been subtracted from the images.

Skymaps are shown here in two different representations: Significance or TS-value maps (figure 11.3, and with the central source removed figure 11.4) and relative flux maps with significance contours (figure 11.5, and with the central source removed figure 11.6). The TS-value maps show the deviation of the excess counts from zero in units of standard deviations of the background histogram, which is assumed to follow a Gaussian distribution for this purpose. The TS-value can therefore be interpreted as local significance of the excess. The color scale is chosen such that whenever the local significance exceeds 3σ, it changes from shades of blue to reddish colors and reaches yellow, wherever 5σ local significance are reached. The relative flux maps, as well as the TS-value maps show the result after smearing with a Gaussian kernel. Relative flux is defined as number of excess counts, within the range of the effective PSF after smearing, divided by the number of background events expected from the same region. In addition to the color coded relative flux, these skymaps are also showing significance contours. The contours usually start at 3σ and are spaced by 1σ. For strong sources, as it is usually the case in the skymaps without removing the central source, the threshold moves to 5σ. See appendix D for a more detailed description of the procedure of producing the skymaps.

Superimposed to the γ-ray skymaps the coordinates of the most important radio features (Law et al., 2008; Petrov et al., 2011) are marked for orientation in the images. Circles with 0.1 ° radius are drawn around those coordinates. For the elongated radio feature (Yusef-Zadeh et al., 1984) called the Galactic Center Arc (GCA), an elliptical shape of the length (0.5 °) and orientation of the GCA is drawn. Two additional circles with radius 0.2 ° and 0.4 ° are drawn around the coordinates of SgrA*. This is for indicating the integration radii for the extraction of the energy spectra (see next section).

11.2.1 *Morphology of the central source*

From the relative flux maps and also from the significance contours therein (figure 11.5), one can see that the major fraction of the flux is concentrated

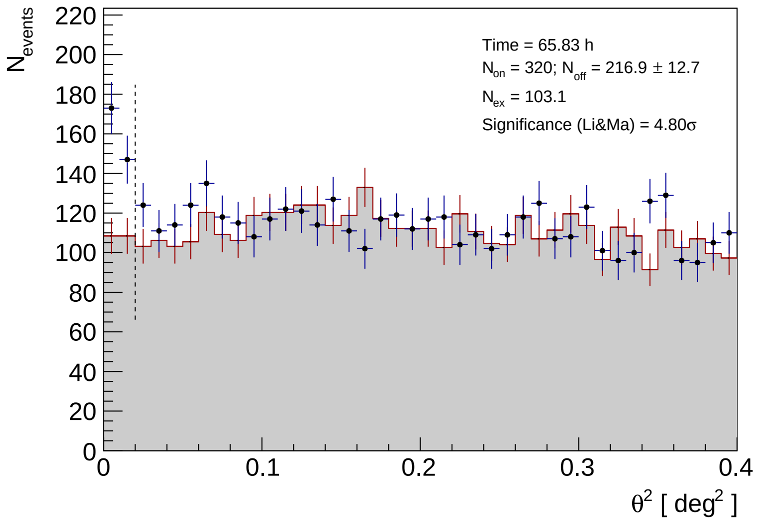

Figure 11.8: θ^2 plot for the coordinates of the SNR G0.9+0.1, which lie 0.9 ° from the actual observation target SgrA*.

within a central PSF-like shaped peak. This point-like contribution, within systematic errors, coincides with the location of SgrA*.

The TS-value maps (figure 11.3) show significant excess ($\sim 5\sigma$ local significance) from an asymmetric, slightly elongated region around SgrA*. This excess is concentrated mainly along the galactic plane, which passes through SgrA* from the upper left to the lower right with an inclination of 60 ° versus the horizontal direction.

This additional, extended component becomes even more obvious when looking at the skymaps with the central point-like source removed (figures 11.6 and 11.4). There is one component stretching along the galactic plane and another feature more perpendicular with respect to the galactic plane offset towards the upper right and well coinciding with the known elongated radio feature called Arc.

11.2.2 *Other sources in the field of view*

Apart from the γ-ray feature coinciding with the radio Arc, there is also significant γ-ray excess from the location of the supernova remnant G0.9+0.1. Despite the decreased sensitivity at 0.9 ° from the actual observation target SgrA*, G0.9+0.1 could be detected at about to 5σ significance level (see figure 11.8).

This source has been previously detected in VHE γ-rays by the H.E.S.S telescope (Aharonian et al., 2005) and has been identified as VHE counterpart of the PWN. An extension, meaning contribution from the shell of the SNR could be excluded by the authors. This was possible because HESS directly targeted the SNR with their observation and could therefore achieve a better angular resolution.

In the MAGIC skymaps, the signature of G0.9+0.1. is much stronger at lower energies and it completely vanishes from the skymaps above 5 TeV, indicating a much softer energy spectrum than for example the GC point-source or the Arc feature (see also section 11.3.2).

The excess from the location of the GCA is elongated along the direction of the orientation of the radio feature in all energy bands. It can be detected with more than 5σ local significance (TS value) for all energy cuts except for $E > 10\,\mathrm{TeV}$, where still a feature remains with 3σ local significance.

Figure 11.7 shows the point-source subtracted VHE skymap in comparison to the 90 cm VLA radio image from Kassim et al. (1998). No other objects detected in other wave-bands could be associated with significant γ-ray excess. Objects that one might expect to emit VHE γ-radiation are for example the molecular clouds SgrB1, SgrB2 and SgrC (due to CR interaction with the dense molecular gas and resulting π_0 decay) and SNRs SgrD as well as SNR 0.3+0.0. There is a hint for excess from SgrB2, given by the elongation of the signal of G0.9+0.1 (see for example figure 11.6 (a-d)) but the excess is not significant. Another hint for an association with a known object is the extension of the excess, north of the Arc feature at lower energies, which could be due to γ-ray emission of the SNR 0.3+0.0. But again this feature is not significant. Any weak excess along the galactic plane is highly prone to source confusion and could just be an upward fluctuation of the extended, elongated γ-ray background referred to as the Galactic Center Ridge by Aharonian et al. (2006a).

11.3 ENERGY SPECTRA AND SEDS

The actual γ-ray flux in physical units is determined by estimating the collection efficiency by using MC simulations. Apart from statistical errors from the limited number of recorded events in the signal as well as the background region, here also systematical uncertainties become important. This is because not all physical parameters of the MAGIC telescopes are known with perfect precision and therefore MC simulations do not perfectly match real data. For all energy spectra in this analysis a statistical uncertainty on the energy scale of $< 15\,\%$ and $< 25\,\%$ on the flux calculation can be assumed.

For normal point-source analysis in MAGIC the integration radius (or θ^2-cut) for extracting the signal of each spectral point is varied with energy. That is because the angular resolution is also changing with energy and therefore the signal to noise ratio can be optimized this way. Changing the θ^2-cut influences also the collection efficiency for γ-rays. This effect is compensated by calculating the effective collection area based on MC data, where a point source is assumed. In result, ideally, changing the θ^2-cut should not influence the obtained spectral points when the MC data matches the real data with

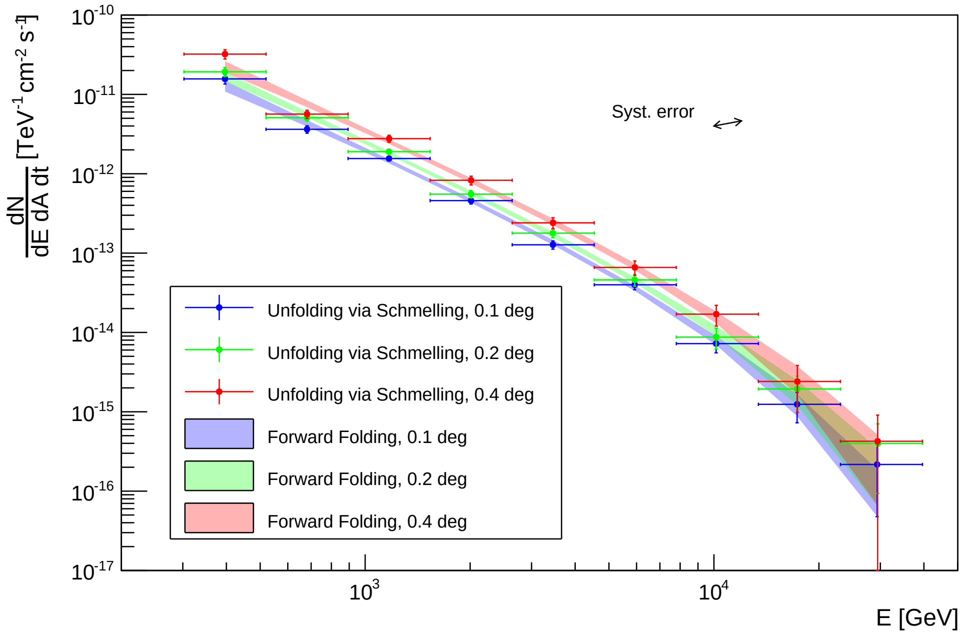

Figure 11.9: Differential energy spectra of the GC for different integration radii. The data-points are for the Schmelling unfolding method and the shaded regions correspond to the uncertainty areas of the forward folding method.

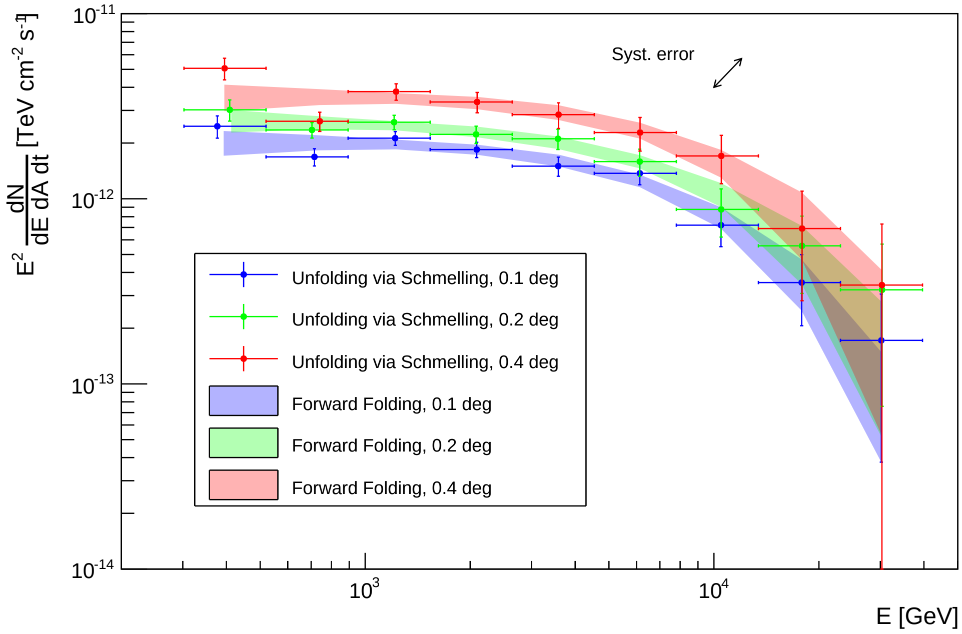

Figure 11.10: Galactic center SEDs for the three different integration radii. The data-points were obtained using the Schmelling unfolding algorithm and the shaded regions correspond to the uncertainty area of the forward folding method, using a power-law with exponential cut-off as spectral assumption.

integration radius 0.1 °

unfolding method	f_0 [cm^{-2}s^{-1}TeV^{-1}]	α	E_{cut} [TeV]	χ^2/n.d.f
Bertero	$(2.18 \pm 0.15) \cdot 10^{-12}$	-1.95 ± 0.013	9.9 ± 3.4	5.1/6
Forward	$(2.25 \pm 0.16) \cdot 10^{-12}$	-1.94 ± 0.015	8.8 ± 3.3	—
Schmelling	$(2.23 \pm 0.09) \cdot 10^{-12}$	-1.96 ± 0.010	9.5 ± 2.7	6.3/6
Tikhonov	$(2.25 \pm 0.12) \cdot 10^{-12}$	-1.98 ± 0.016	9.9 ± 4.4	5.8/6

integration radius 0.2 °

unfolding method	f_0 [cm^{-2}s^{-1}TeV^{-1}]	α	E_{cut} [TeV]	χ^2/n.d.f
Bertero	$(2.72 \pm 0.19) \cdot 10^{-12}$	-1.98 ± 0.013	11.4 ± 4.9	4.0/6
Forward	$(2.80 \pm 0.21) \cdot 10^{-12}$	-1.99 ± 0.015	10.5 ± 5.0	—
Schmelling	$(2.79 \pm 0.13) \cdot 10^{-12}$	-2.02 ± 0.010	11.4 ± 4.2	3.1/6
Tikhonov	$(2.83 \pm 0.17) \cdot 10^{-12}$	-1.98 ± 0.016	10.1 ± 4.9	3.6/6

integration radius 0.4 °

unfolding method	f_0 [cm^{-2}s^{-1}TeV^{-1}]	α	E_{cut} [TeV]	χ^2/n.d.f
Bertero	$(3.74 \pm 0.32) \cdot 10^{-12}$	-1.94 ± 0.016	11.61 ± 6.24	9.46/5
Forward	$(3.92 \pm 0.35) \cdot 10^{-12}$	-1.94 ± 0.017	9.99 ± 5.14	—
Schmelling	$(3.90 \pm 0.20) \cdot 10^{-12}$	-1.94 ± 0.012	10.66 ± 4.16	14.74/6
Tikhonov	$(3.96 \pm 0.28) \cdot 10^{-12}$	-1.95 ± 0.019	10.22 ± 5.84	4.15/6

Table 11.2: Parameter results of the correlated fits to the GC energy spectra for three different integration radii and 3 different unfolding methods plus forward folding. The fitted function is a power-law with exponential cut-off in all cases. The flux normalization is at 1 TeV.

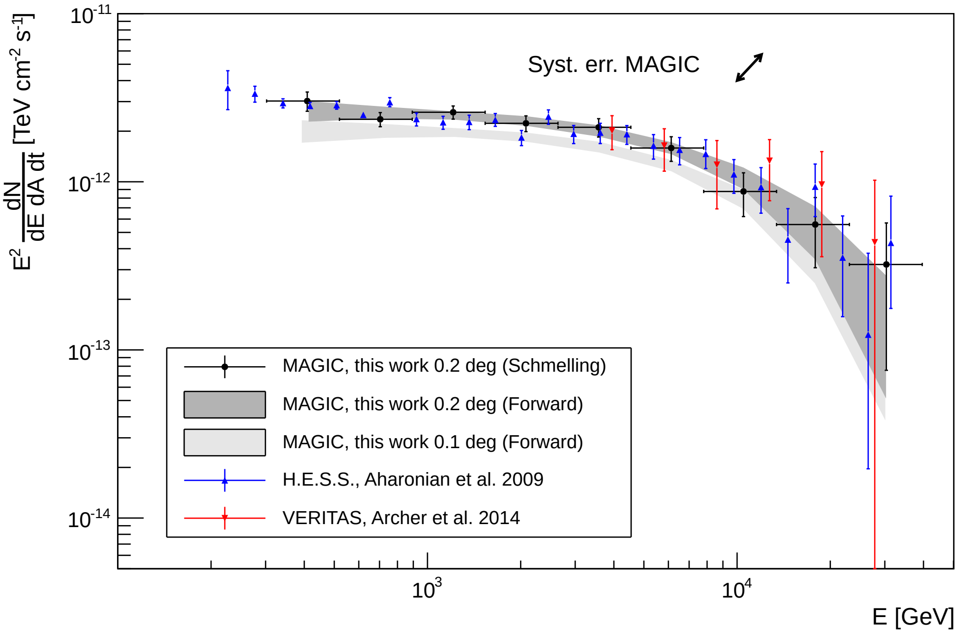

Figure 11.11: Galactic center: MAGIC SED compared to the SEDs published by H.E.S.S. (Aharonian et al., 2009) and VERITAS (Archer et al., 2014).

good precision. Apart from statistical fluctuations, only the significance of the data-points should change (see also chapter D).

For the Galactic Center the situation is a bit more complicated, due to the obvious extension of the source (see section 11.2). It is a matter of definition, what to count in for the extraction of the energy spectrum. It is also unwise to choose variable θ^2-cuts as it is usually done for point-sources. This way, the different spectral points would also correspond to different integration radii, probably leading to a flux overestimation at low energies compared to that at high energies.

Ideally one would have to generate MC data that exactly match the real extension of the source for the determination of the collection efficiency. In the frame of the analysis of a single source that was observed by MAGIC this is impractical. Another option would be to model the instrument response as a function of the image/camera coordinates with high detail and for a large parameter space, instead of calculating the collection efficiency from MC "on the fly". This would allow for fitting models to the data, similar to how it is done in the analysis tools of *Fermi*. However, such tools are not available for the MAGIC data analysis and the realization might prove even more difficult than in the case of *Fermi*.

Therefore, the only option for extracting energy spectra from MAGIC GC observations was to use fixed integration radii for all energy bands. Three different integration radii were chosen, resulting in three different energy spectra (0.1 °,0.2 ° and 0.4 ° integration radius). The integration radius of 0.1 ° should be mainly sensitive to the contribution of the central source only. However, at lower energies imperfect matching of data and MC might lead to systematic errors in the spectrum. The 0.2 ° integration radius presents a compromise in terms of fully integrating the central source and not too much from the extended emission. The 0.4 ° integration radius was chosen in order to include all of the extended components in the spectrum. The different integration radii are also indicated in the skymaps of figures 11.3 and 11.5.

The differential energy spectra have been found to match best a power-law spectrum with exponential cut-off:

$$\frac{\mathrm{d}F}{\mathrm{d}E} = f_0 \left(\frac{E}{1\,\mathrm{TeV}}\right)^{\alpha} \exp -\frac{E}{E_{\mathrm{cut}}} \,. \tag{11.3.1}$$

Therefore, a spectrum of this type was used for the forward folding method. The energy spectra for all three integration radii, after unfolding with different methods are presented in figure B.1. All unfolding results are in good agreement, which serves as confirmation that the algorithms performed in a stable way. The table with the parameter results of the correlated fits and the forward folding are summarized in table 11.2.

Depending on the input spectrum and other parameters, it can happen that one of the unfolding/regularization methods fails, giving wrong results.

For this reason it is common practice within the MAGIC collaboration to use different methods with orthogonal approaches to the regularization. When however all different methods give consistent results, the spectrum can be trusted without problems. See appendix D for more information and references on the unfolding methods.

The Spectral Energy Density (SED) (see also appendix D), which is defined as:

$$E^2\,\frac{\mathrm{d}F}{\mathrm{d}E} = E^2\,\frac{\mathrm{d}N}{\mathrm{d}E\,T_\mathrm{eff}\,A_\mathrm{eff}} \tag{11.3.2}$$

is better suited for studying details in, and differences between energy spectra. Therefore, SEDs for different integration radii and different unfolding methods are presented in figures B.2 and 11.10.

The energy spectra are remarkably similar for all three integration radii. Only the total Flux is changing by nearly a factor two when comparing the smallest and the largest integration radius. The difference between the flux from a 0.1 ° and a 0.2 ° integration radius of about 25 % could be possibly explained by a systematic error in the estimation of the collection area due to data/MC mismatch. The increase by another factor close to two when going to 0.4 ° on the other hand is a clear hint for the extension of the emission region. There is no hint for different production mechanisms for γ-radiation in the central source compared to the extended emission region from these SEDs, since the spectral shape is not changing when changing the integration radius.

Figure 11.11 serves for comparing the new MAGIC results with previously published SEDs observed with other instruments. Within errors, the results from the three instruments are in good agreement, if using the 0.1 ° or 0.2 ° integration radius.

11.3.1 *SED including Fermi data*

The most recently published *Fermi* spectrum of the GC point source is the one by Chernyakova et al. (2011). In the following, the spectral points therein are used for an interpretation of the broad band γ-ray emission spectrum of the GC. The overall spectral range covered by both instruments ranges from 100 MeV to 40 TeV, with a non-perfect coverage around 100 GeV.

As first approach to the combined data, a single power-law fit was fitted to the data points.

$$\frac{\mathrm{d}F}{\mathrm{d}E} = f_0\left(\frac{E}{10\,\mathrm{GeV}}\right)^{\alpha}\,. \tag{11.3.3}$$

Partially correlated statistical and systematical errors have been considered in the fit (see below). For all three integration radii with MAGIC the fit is not

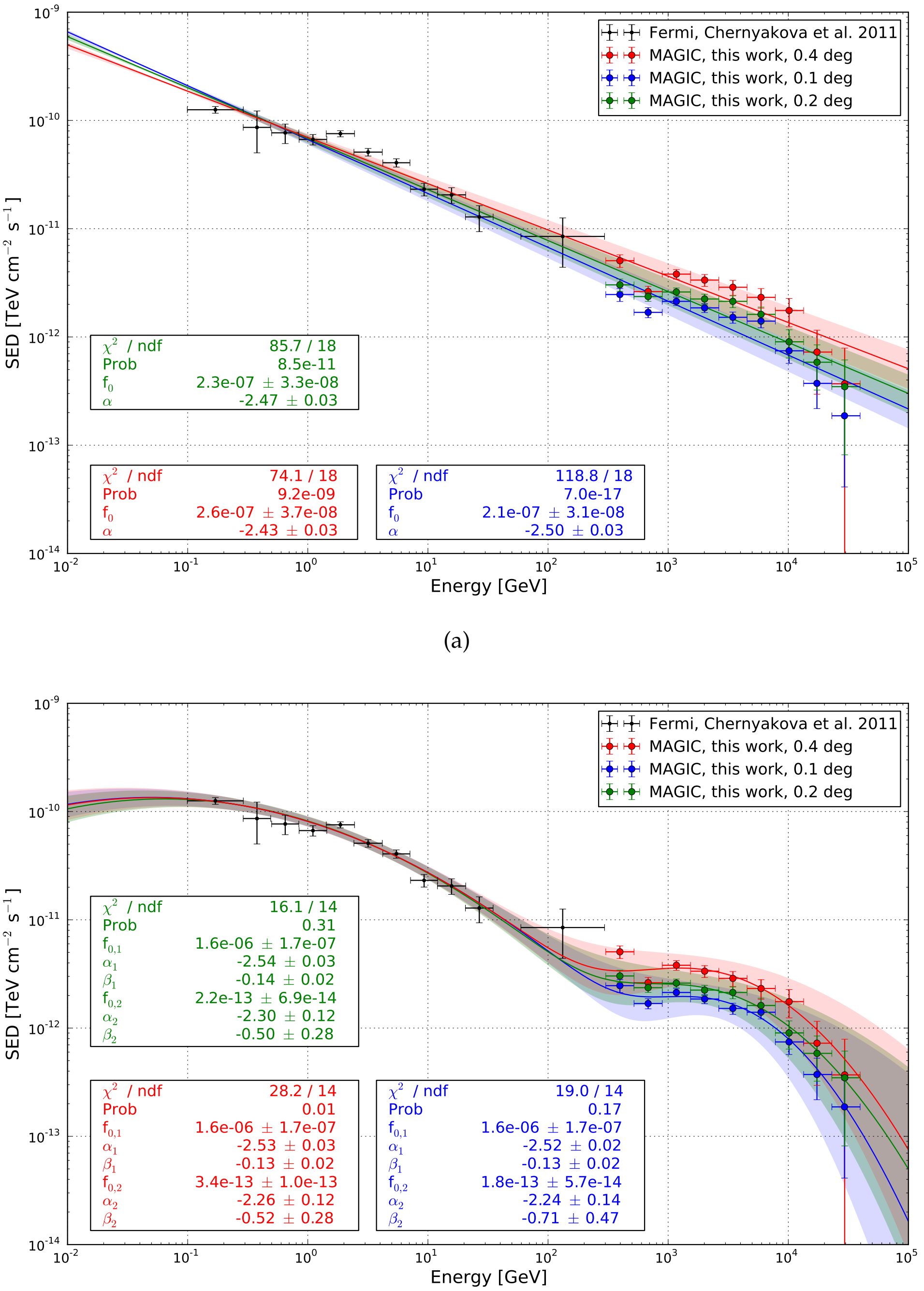

(a)

(b)

Figure 11.12: SED with different spectral fits to the combined MAGIC and *Fermi* data points from Chernyakova et al. (2011). Single power-law (a) and sum of two log-parabola functions (b) are fitted to combinations with all three integration radii on the MAGIC data side. The shaded areas indicate 1σ deviations from the best fit parameters, considering statistical and systematic uncertainties and parameter correlation.

matching the data at all with p-values indicating a more than 5σ exclusion for all three cases (see figure11.12 (a)).

In order to better account for the apparent shape of the spectrum, a double log-parabola function was fitted to the data.

$$\frac{\mathrm{d}F}{\mathrm{d}E} = f_{0,1}\left(\frac{E}{5\,\mathrm{GeV}}\right)^{\alpha_1+\beta_1\,\log\left(\frac{E}{5\,\mathrm{GeV}}\right)} + f_{0,2}\left(\frac{E}{3\,\mathrm{TeV}}\right)^{\alpha_2+\beta_2\,\log\left(\frac{E}{3\,\mathrm{TeV}}\right)}\,. \tag{11.3.4}$$

The double log-parabola fits the data much better, with p-values between 0.31 and 0.01. The best match is achieved for the 0.2 ° integration radius data-points (see figure 11.12 (b)). The Energy normalization was chosen such, that the parameter correlation is relatively small.

Due to the good energy resolution and the comparably large bins, the statistical errors of *Fermi* data were assumed to be uncorrelated. The statistical errors of MAGIC data after unfolding are correlated. For the fits, the correlated statistical errors of MAGIC data have been taken into account. In order to estimate the influence of systematic uncertainties, the fits have been repeated adding and subtracting each of the systematic error margins in energy scale and flux normalization for MAGIC and *Fermi* (see section 11.5 for a discussion of the systematic errors). The resulting parameter deviations were added in quadrature to the parameter errors of the initial fit. The maximal deviations from the best fits, within the resulting parameter uncertainties are indicated by the shaded regions. Parameter correlations have been taken into account for calculating the shaded regions.

Due to the two-bump shape of the GC SED and given the limited resolution of the instruments (MAGIC and *Fermi*) together with the very densely populated GC region it is quite reasonable to assume two distinct sources for the GeV and for the TeV emission. At the same time it is not excluded that the data can be also explained by a single γ-ray source.

11.3.2 *Extracting energy spectra from skymaps - new experimental method*

Using normal ring-wobble MC simulations (γ-rays are simulated to originate from a ring in camera coordinates, which corresponds to the wobble distance of 0.4 °.) it is not possible to calculate energy spectra of very extended or off-center sources. This could be achieved by using diffuse MC simulations (γ-rays are simulated with homogeneously distributed direction of origin). But in this case it is still impossible to calculate a clean spectrum of a source with possible contribution of another nearby source. Therefore it is desirable to be able to subtract point sources in the FoV, similar to what current software (*Caspar*) allows one to do in skymaps.

What I am presenting in the following is a new experimental technique that uses data from intermediate steps in the programs *Caspar* and also *Flute* and which allows one to generate energy spectra for arbitrary source locations and

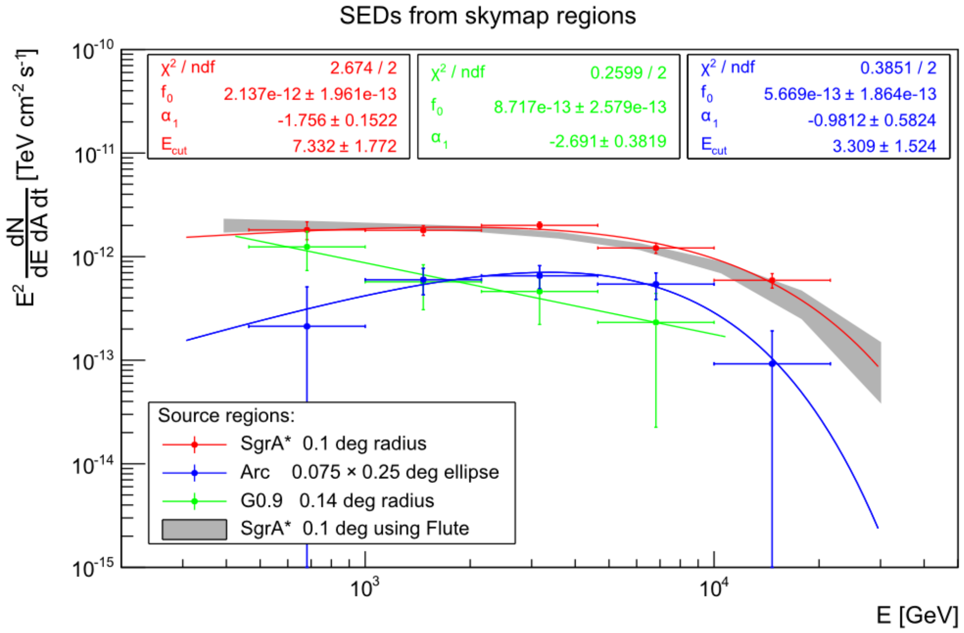

Figure 11.13: Three SEDs extracted from GC skymaps using the novel method. The SED of the GC source, coinciding with the coordinates of SgrA*, has been extracted using the same integration radius as in *Flute* (0.1 °, red data points). The result from using *Flute* (after forward folding) with the same integration radius is shown as shaded gray area. Another SED has been generated for the coordinates of SNR G0.9+0.1, using a slightly bigger integration radius due to the degeneracy of the PSF at large offset from the center of the observations (green data points). An elliptical shape has been used for extracting an SED of the γ-ray excess, coinciding with the GCA radio feature (blue data points).

geometries. It even allows for subtracting point-source contributions from the data. The two 2D histograms of on-events and oversampled background estimation (*Caspar*, see appendix D), as well as the effective on-time and collection area estimation based on MC simulations computed by the program *Flute*, serve as input for this new method. The skymaps have to be generated with the same energy binning and same hadronnes cuts as it is used by *Flute*.

For calculating the γ-ray flux from the skymaps, first the correct background scaling has to be found for subtracting the oversampled background map. This is done by comparing signal free regions, which have to be defined by the user first. Then the background corrected on-skymap is divided by a normalized version of the background map, similar to how the relative flux map is generated by *Caspar* (see appendix D). Point sources can be removed by using Crab Nebula skymaps from data, which were recorded with similar observational conditions as PSF model. Finally custom defined regions can be used for extracting acceptance corrected excess events. The procedure is also illustrated in figure B.3 in the appendix.

The effective collection area and observation time has to be adopted from the program *Flute*. Special care has to be taken in order to use a signal integration region of similar size in *Flute* as it is used in the skymap. Integration regions should not be smaller than the PSF of the instrument for this method to work. An additional error on the collection area is considered in the final spectrum/SED.

Figure 11.13 is showing three different SEDs that were calculated using the above described method. The SED of the central source at the coordinates of SgrA* agrees well with the result obtained with *Flute* for the same source. Also a spectrum of the coordinates of SNR G0.9+0.1 has been calculated and fitted with a single power-law. The resulting spectrum ($f_0(1\,\mathrm{TeV}) = (8.80 \pm 2.52) \times 10^{-13}\,\mathrm{TeV}^{-1}\mathrm{cm}^{-2}\mathrm{s}^{-1}$, $\alpha = -2.69 \pm 0.38$) is in good agreement with results that were previously published by the H.E.S.S. experiment (Aharonian et al., 2005). A third, this time extended region was used for calculating the SED of the region of the radio Arc. The signal extraction region is an ellipse with semi major axes $0.25\,^\circ$ and $0.075\,^\circ$. The dimensions of the integration radius are motivated by the extensions of the radio Arc ($0.5\,^\circ$ length) and chosen in order to match approximately the same collection area as for the point sources. For this source the central point source has been subtracted because it might have some overlap. The spectrum shows evidence curvature and could therefore be better fitted with a power-law with cut-off than with a simple power-law (spectral index: 2.3 ± 0.1). Using such a function the parameter results are:

$$\begin{aligned} f_0(1\,\mathrm{TeV}) &= (5.7 \pm 1.9) \times 10^{-13}\,\mathrm{TeV}^{-1}\mathrm{cm}^{-2}\mathrm{s}^{-1}\,, \\ \alpha &= -1.0 \pm 0.6\,, \\ \text{and } E_{cut} &= 3 \pm 2\,\mathrm{TeV}\,. \end{aligned}$$

Energy cut	F_{2012} [$\mathrm{cm}^{-2}\,\mathrm{s}^{-1}$]	F_{2013} [$\mathrm{cm}^{-2}\,\mathrm{s}^{-1}$]	F_{2014} [$\mathrm{cm}^{-2}\,\mathrm{s}^{-1}$]
$E > 1\,\mathrm{TeV}$	$1.44 \pm 0.44 \cdot 10^{-12}$	$2.11 \pm 0.23 \cdot 10^{-12}$	$2.11 \pm 0.26 \cdot 10^{-12}$
$E > 2\,\mathrm{TeV}$	$4.17 \pm 1.74 \cdot 10^{-13}$	$8.10 \pm 1.04 \cdot 10^{-13}$	$8.93 \pm 1.20 \cdot 10^{-13}$
$E > 5\,\mathrm{TeV}$	$1.53 \pm 0.73 \cdot 10^{-13}$	$1.81 \pm 0.34 \cdot 10^{-13}$	$2.16 \pm 0.42 \cdot 10^{-13}$
$E > 10\,\mathrm{TeV}$	$5.60 \pm 3.32 \cdot 10^{-14}$	$4.35 \pm 1.46 \cdot 10^{-14}$	$4.98 \pm 1.71 \cdot 10^{-14}$

Table 11.3: Integral γ-ray flux observed from within 0.2° of the direction to the GC for the three different observation seasons with different lower cuts in energy. The errors given in the table do not contain the additional systematic uncertainty on the flux normalization of $\sim 25\%$.

11.4 VARIABILITY SEARCHES

One of the main goals of this observation campaign is searching for variability of the GC γ-ray source, triggered by possible accretion of parts of the previously discovered gas cloud G2. At this stage the GC has been observed for three years, which in an optimistic scenario could be enough to see possible variability.

Figure 11.14 shows nightly light curves of the GC γ-ray flux for $E > 1\,\mathrm{TeV}$ and $E > 2\,\mathrm{TeV}$. For better clarity, due to the otherwise large error bars of the nightly data points, in figure 11.15, a re-binned version light curves with 15 d bins can be found. Figure 11.16 shows light curves for 5 TeV and $E > 10\,\mathrm{TeV}$ using the same 15d binning. The statistical error bars of the nightly flux measurements have been summed in quadrature with a 25% night-to-night variance, which has to be introduced due to nightly changes in the observation conditions (see section 11.5)

In general, at lower energies, the light curves seem to indicate a slight increase of the flux, when comparing the 2012 data to the rest of the data set. All light curves have been fitted with a constant flux and a linear time dependence. The introduction of a linear time dependence does not imrove the fit significantly. The somewhat lower flux measured in 2012 can probably be explained with the relatively poor data quality of the first year of observations and the imperfect random forests, for which no suitable background data sample was available.

For comparison of the fluxes measured during the three different observation seasons (2012, 2013, 2014), the flux averages for different lower energy integration boundaries are listed in table 11.3. From this table it becomes clear that there is no significant flux change, especially when comparing the 2013 and 2014 data sets, which are much larger then the 2012 one and where also the systematics are better under control. From the tabulated values of 2013 and 2014 one can exclude a flux increase by more than $\sim 30\%$ for $E > 1\,\mathrm{TeV}$ and $E > 2\,\mathrm{TeV}$, on a 2σ level and by more than $\sim 70\%$ for $E > 5\,\mathrm{TeV}$ and $E > 10\,\mathrm{TeV}$, also on a 2σ level. Compared to 2012, the flux did at least not increase by more than $\sim 150\%$.

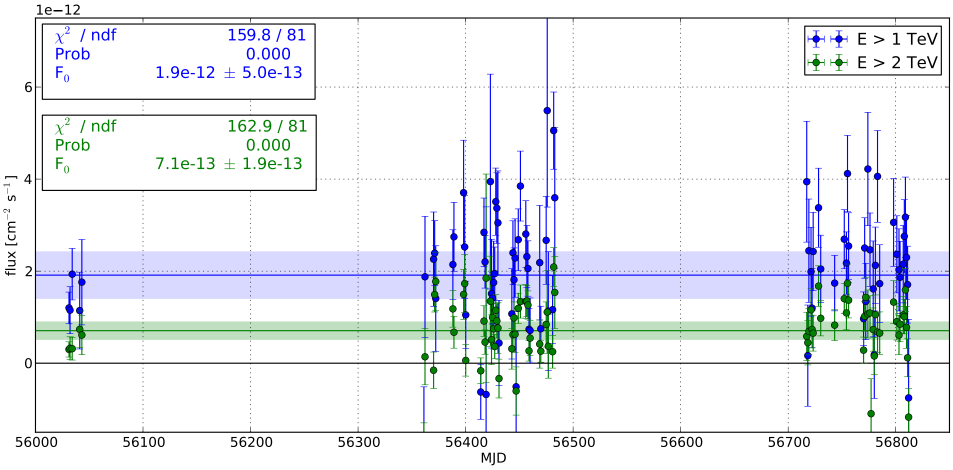

(a)

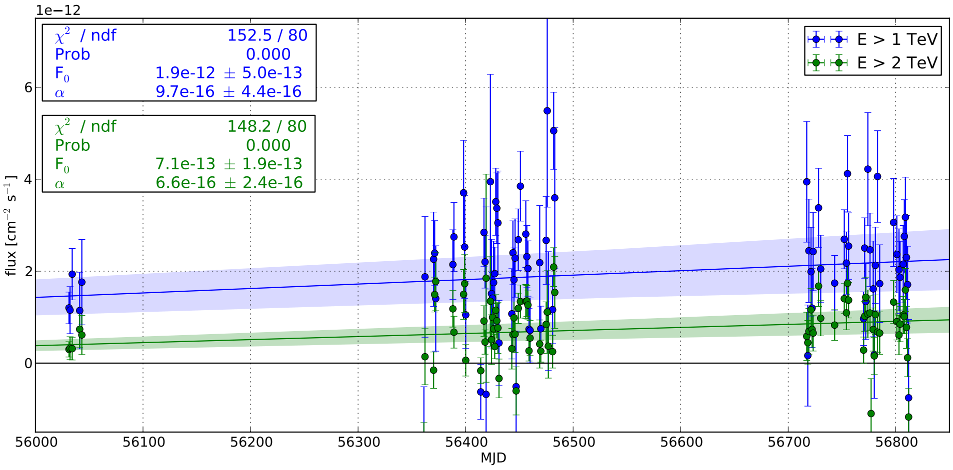

(b)

Figure 11.14: Nightly light curves of the GC γ-ray flux for $E > 1\,\text{TeV}$ (blue) and $E > 2\,\text{TeV}$ (green). The light curves have been fitted with a constant flux (a) and a linear time dependence (b). The shaded areas represent the parameter uncertainties, taking into account statistical and systematic errors.

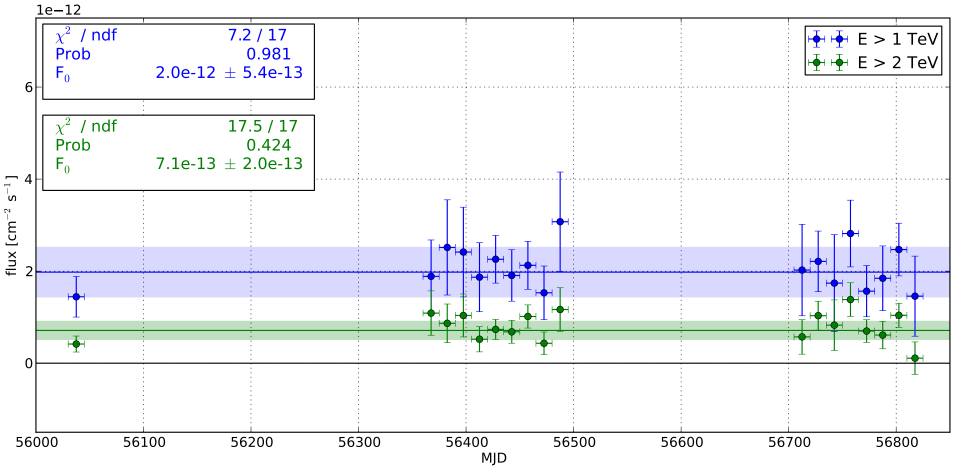

(a)

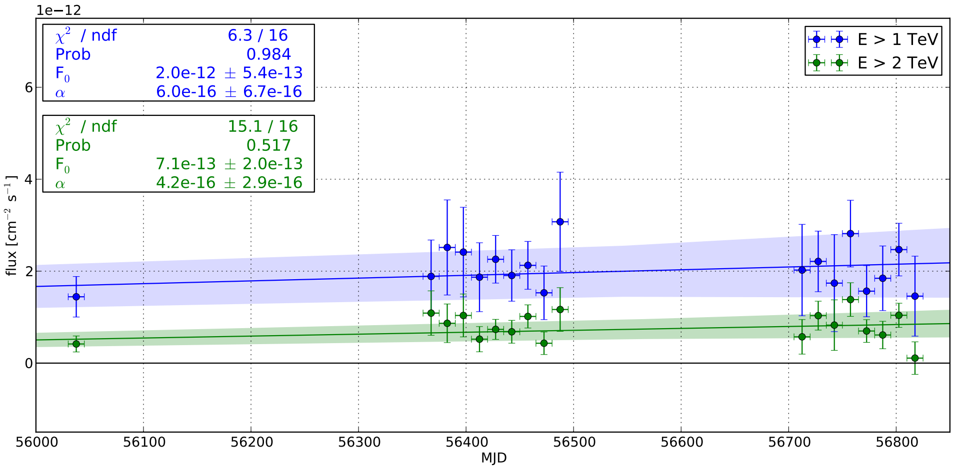

(b)

Figure 11.15: Light curves with 15 d binning of the GC γ-ray flux for $E > 1\,\mathrm{TeV}$ (blue) and $E > 2\,\mathrm{TeV}$ (green). The light curves have been fitted with a constant flux (a) and a linear time dependence (b). The shaded areas represent the parameter uncertainties, taking into account statistical and systematic errors.

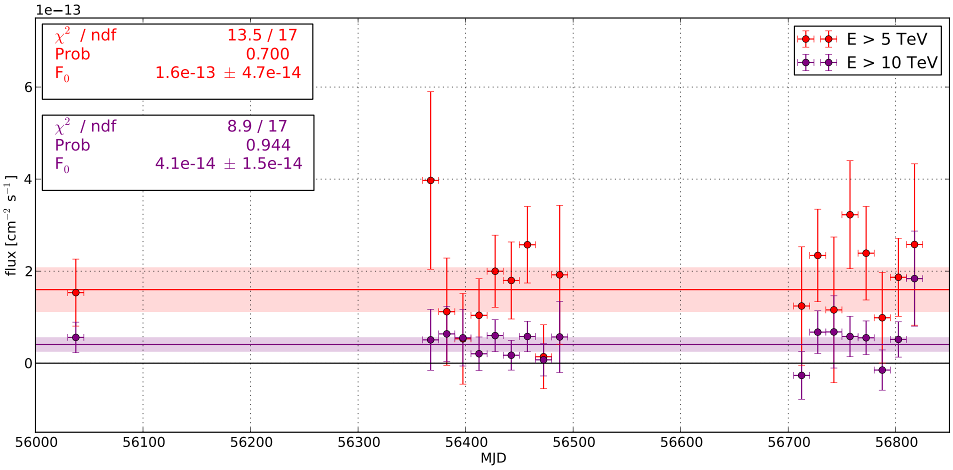

(a)

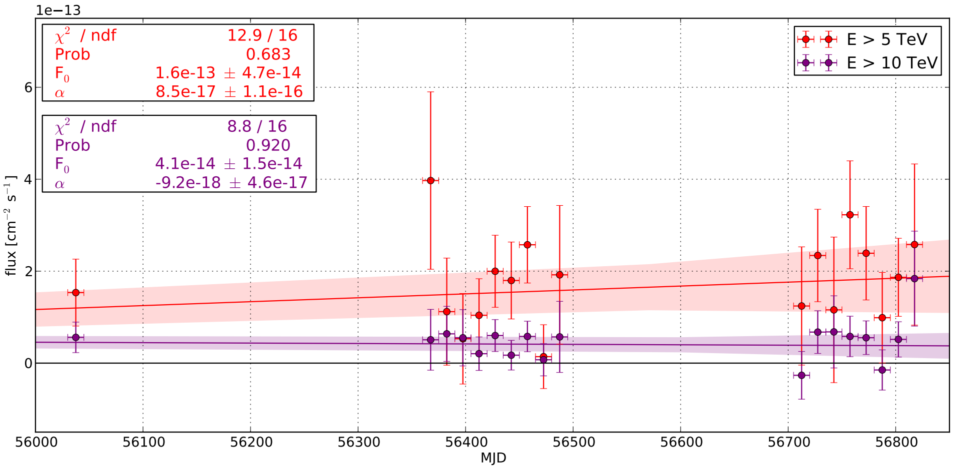

(b)

Figure 11.16: Light curves with 15 d binning of the GC γ-ray flux for $E > 5\,\mathrm{TeV}$ (red) and $E > 10\,\mathrm{TeV}$ (purple). The light curves have been fitted with a constant flux (a) and a linear time dependence (b). The shaded areas represent the parameter uncertainties, taking into account statistical and systematic errors.

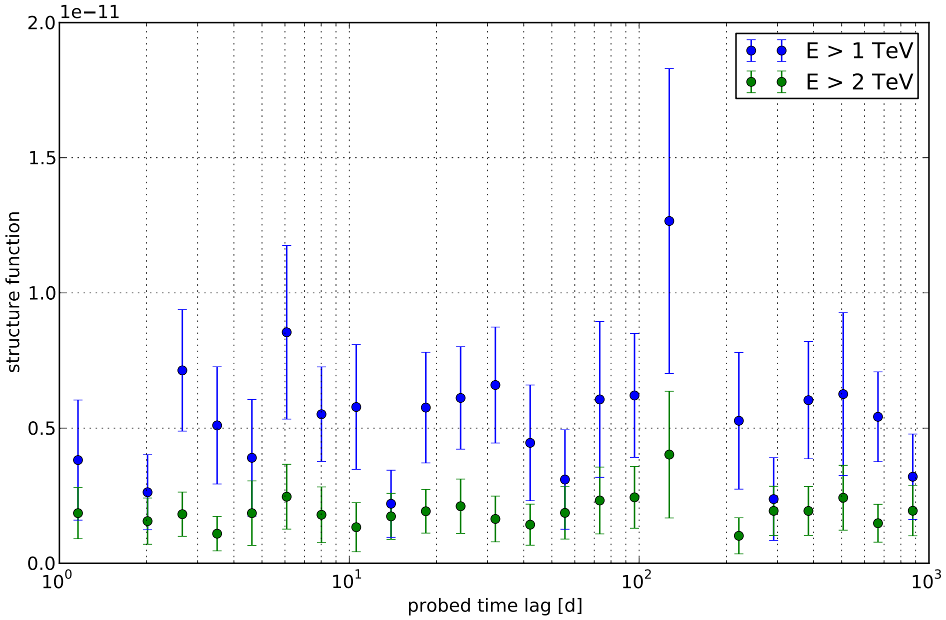

(a)

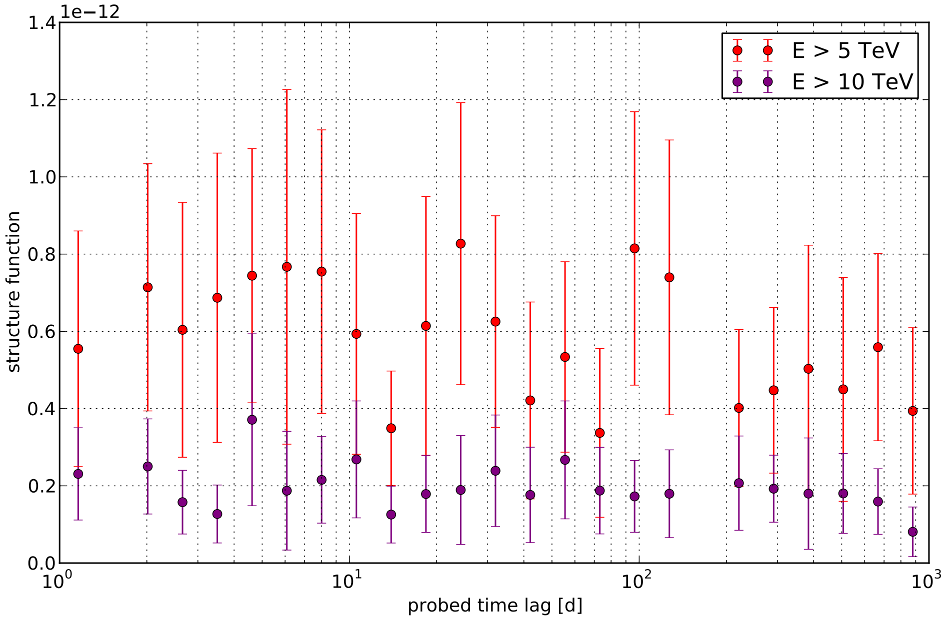

(b)

Figure 11.17: Structure function analysis of the nightly light curves of the GC flux for $E > 1\,\text{TeV}$, $E > 2\,\text{TeV}$ (a) and $E > 5\,\text{TeV}$, $E > 10\,\text{TeV}$ (b).

Finally, also a technique, which is quite common in astronomy for examining variability and variation timescales, was applied to the GC light curves: the so-called Structure Function (SF) analysis (Emmanoulopoulos et al., 2010, and references therein). The SF is defined as:

$$SF(\tau) = \frac{1}{N(\tau)} \sum \omega(t) \cdot \omega(t+\tau) \left(F(t+\tau) - F(t)\right)^2 , \tag{11.4.1}$$

$$N(\tau) = \sum \omega(t) \cdot \omega(t+\tau) , \tag{11.4.2}$$

$$\omega(t) = \frac{F(t)}{\delta F(t)} . \tag{11.4.3}$$

In practice, the sum runs over all flux measurement pairs $(F(t), F(t+\tau))$ with a time separation τ, which lies within the probed time lag bins. As is can be seen in figure 11.17, there is no hint for a significant variation or a significant variation timescale, which would be indicated by an increase of the SF until the characteristic timescale and a subsequent break.

One can conclude that there is no significant deviation from the assumption of a constant flux. Especially at energies above 10 TeV, where some models predict possible variability on a timescales of years, the light curve is perfectly consistent with constant emission.

11.5 DISCUSSION OF SYSTEMATIC ERRORS

Instruments for observing high and very high energy γ-rays have the advantage of covering several orders of magnitude of the energy spectra of astrophysical sources. A weak point, especially when comparing them to lab experiments is the relatively large uncertainty in their calibration. This is strongly related to the detection method (recording of particle showers) which on the other hand allows for covering a very wide spectral range.

For satellite detectors like the Fermi LAT it is possible to calibrate the detector in a test beam facility, which allows for reducing the systematic uncertainties of the energy scale. For IACTs it is impossible to calibrate the entire system as a whole. The individual components and steps have to be examined carefully in order to achieve a reasonably good calibration, which is then still not comparable to what could be achieved in an experiment conducted at lab conditions.

11.5.1 *Fermi*

The calibration of the energy scale for the Fermi LAT was performed by exposing part of the instrument to a test beam at CERN. This way also the energy resolution could be determined ($\sim$ 15% at 100 MeV, $\sim$ 9% 1–10 GeV, $\sim$ 18% at 300 GeV) (Atwood et al., 2009). The systematic error on the energy scale can be considered negligible due to precise calibration.

Systematic effect	Uncertainty low Zd	Uncertainty high Zd
F-factor	10% ES	10% ES
atmospheric transmission	$5-10\%$ ES	$12-25\%$ ES
mirror reflectivity	8% ES	8% ES
PMT electron collection efficiency	5% ES	5% ES
light collection in a Winston Cone	5% ES	5% ES
PMT quantum efficiency	4% ES	4% ES
charge flat-fielding	$2-8\%$ ES FN	$2-8\%$ ES FN
analysis and MC discrepancies	$10-15\%$ FN	$15-20\%$ FN
background subtraction	$1-8\%$ FN	$5-10\%$ FN
Total (ES)	$16-20\%$ ES	$20-30\%$ ES
Total (FN)	$10-19\%$ FN	$16-24\%$ FN

Table 11.4: Most important sources and estimated values of systematic uncertainties of the absolute energy scale (ES) and the flux normalization (FN) as measured by the MAGIC telescopes. Values for low zenith observations are adapted from Aleksic et al. (2012). Adaptations to high Zd observations are motivated in the text.

The systematic uncertainty on the collection area, and therefore flux normalization of the Fermi telescope is 10% below 100 MeV, 5% at around 500 MeV and 20% above 10 GeV (Abdo et al., 2009a).

11.5.2 *MAGIC*

In case of MAGIC a large number of sources contribute to the overall systematic uncertainty. A comprehensive list of such sources can be found in Aleksic et al. (2012), of which the most important ones are listed in table 11.4. Many of those uncertainties are only relatively poorly known and hard to estimate, others could be determined in MC studies by the authors of Aleksic et al. (2012). The largest systematic uncertainties are introduced by the F-factor calibration method (see appendix E for an explanation), transmission of the atmosphere, mirror reflectivity, and data-MC miss-match. It is generally assumed that the different sources of systematic uncertainty are statistically independent and can therefore be summed quadratically. The overall systematic uncertainty on the energy scale for low Zd observations is about $16\%-20\%$ and the uncertainty on the flux normalization is $10-19\%$.

At large Zd some of the systematic uncertainties are increased with respect to low Zd. In this situation, the biggest contribution comes from variability in the transmission of the atmosphere. Compared to low Zd, the optical depth of the atmosphere increases by a factor 2 when observing at 60° Zd, and by a factor 3 when observing at 70° Zd. Therefore the uncertainty on the energy scale increases from $5-10\%$ to about $12-25\%$. In contrast to most of the other systematic uncertainties, the error introduced by the uncertainty in the transmission of the atmosphere is strongly varying from night to night, as the state of the atmosphere is changing. One expects larger systematic variations from night to night compared to the overall shift when measuring the spectrum averaged over time. For simplicity, half of the uncertainty is assumed to be due to statistical nightly fluctuations and the other half is assumed to be an overall systematic bias. Therefore, the error on the energy scale is larger when producing a nightly light-curve than it is for the differential energy spectrum or SED.

Also discrepancies between data and MC become more important and are not studied well for high Zd. Due to the larger distance to the showers, the geometrical size of the camera images decreases and therefore the optical PSF of the system becomes more important. This optical PSF has also day to day fluctuations, coming from imperfect focusing of the automatic mirror control (AMC). These fluctuations are impossible to match with MC simulations. Therefore also flux normalization error, which originates from analysis and MC discrepancies has been increased from $10 - 15\%$ to $15 - 20\%$. Larger variations are expected from night to night, while the systematic bias for long term averaging is expected to be lower.

The last contribution to the systematic error, which increases due to HZD observations is the uncertainty of the background subtraction. For data taken with the so-called wobble mode (see chapter 3), the background, which has to be subtracted from the signal region is extracted from the corresponding Off-wobble positions. These in turn are typically at a distance of 0.8° from the source. If, at around 65° Zd, this small deviation lies in the vertical direction, it can cause differences in the energy threshold and collection area of about 10%. Therefore, the systematic error estimation of the background subtraction has been increased to $5 - 10\%$ for the Zd range of the GC observations. Again, fluctuations are expected to be higher when only a limited number of wobble-pairs is available, while averaging eliminates part of the uncertainties after long-term observations.

The overall systematic uncertainties for MAGIC observations at $60^\circ - 70^\circ$ Zd can be assumed to be 20% on the energy scale as well as 16% on the flux normalization for long-term average (spectrum/SED) and 30% on the energy scale as well as 24% on the flux normalization in terms of night-to-night fluctuations (nightly light-curves). All plots in this thesis show only 1σ statistical errors on the error bars. Some plots contain an arrow, indicating the systematic uncertainty region of all MAGIC data-points.

It should be mentioned that due to error propagation, the resulting uncertainties on SEDs and integral fluxes can be much larger than the individual errors on energy scale (ΔE) and flux normalization (ΔF). The error propagation into the SED is for example

$$\Delta SED = \sqrt{\left(\Delta E \cdot \frac{\mathrm{d}}{\mathrm{d}E}\left(E^2 \frac{\mathrm{d}F}{\mathrm{d}E}\right)\right)^2 + \left(\Delta F \cdot \frac{\mathrm{d}}{\mathrm{d}F}\left(E^2 \frac{\mathrm{d}F}{\mathrm{d}E}\right)\right)^2} \tag{11.5.1}$$

$$= \sqrt{\left(2 \cdot \frac{\Delta E}{E} E^2 \frac{\mathrm{d}F}{\mathrm{d}E}\right)^2 + \left(\frac{\Delta F}{F} E^2 \frac{\mathrm{d}F}{\mathrm{d}E}\right)^2} . \tag{11.5.2}$$

The resulting systematic uncertainty for an SED measured over long time is therefore as much as 43%.

12

INTERPRETATION, DISCUSSION AND CONCLUSIONS

One of the main scientific questions asked in this thesis is about variability of the GC γ-ray flux due to the interaction of the SMBH with the G2 gas cloud. So far, no significant deviation from a constant flux could be detected, neither at lower (> 1 TeV) nor above 10 TeV (see chapter 11.4). But the new extensive GC observations allow for addressing also other questions concerning the γ-ray sources in that region. Apart from testing models of different production mechanisms of VHE γ-radiation at the GC, also the discovery of a possible new source very close to SgrA could help improving our picture of the GC environment from the high energy point of view.

12.1 MODELS PREDICTING γ-RAY EMISSION FROM SGRA*

Before the publication of the *Fermi* spectrum, theoretical models were built mainly around the TeV emission observed by H.E.S.S. (Aharonian et al., 2004, 2009). Already at this stage hadronic as well as leptonic emission mechanisms were proposed for explaining the VHE-emission. Atoyan & Dermer (2004) proposed that TeV γ-rays are the result of inverse Compton scattering of high energy electrons that are accelerated by first and second order *Fermi* processes occurring inside the accretion disk of the SMBH and in the termination shock of the out-flowing wind of the hypothetical black-hole plerion.

In most hadronic scenarios like the one proposed by Ballantyne et al. (2011), γ-rays are produced by π_0 decay in interactions of CRs, accelerated in the vicinity of the BH with the dense environment close to the GC. In this specific model, the TeV spectrum is obtained by switching on and off CR acceleration close to the BH, at specific times in the past. The energy dependance of the diffusion coefficient is then responsible for the spectral shape. The authors find two possible scenarios in which it can match the H.E.S.S. spectrum. In the first scenario, they require a steady state, low luminosity accelerator that was switched on about 10^4 y ago with an unusually hard spectral index ($\alpha = -0.75$). In the second scenario they are able to explain the data, requiring relatively fast variability, namely switching on the acceleration for 10 y and observing 7 y after switching it off again. In this scenario a relatively soft CR spectral index of $\alpha = -2.7$ is needed. An interesting implication of the model by Ballantyne et al. (2011) is that for the second case variability of the TeV spectrum is expected on timescales of the order of 10 y, in case the accelerator stays quiet, but also if a new flare of CR acceleration occurs.

After discovering a point-source in *Fermi* data (1FGL J1745.6 – 2900), which could be consistent with the H.E.S.S. TeV source (HESS J1745 – 290), Chernyakova

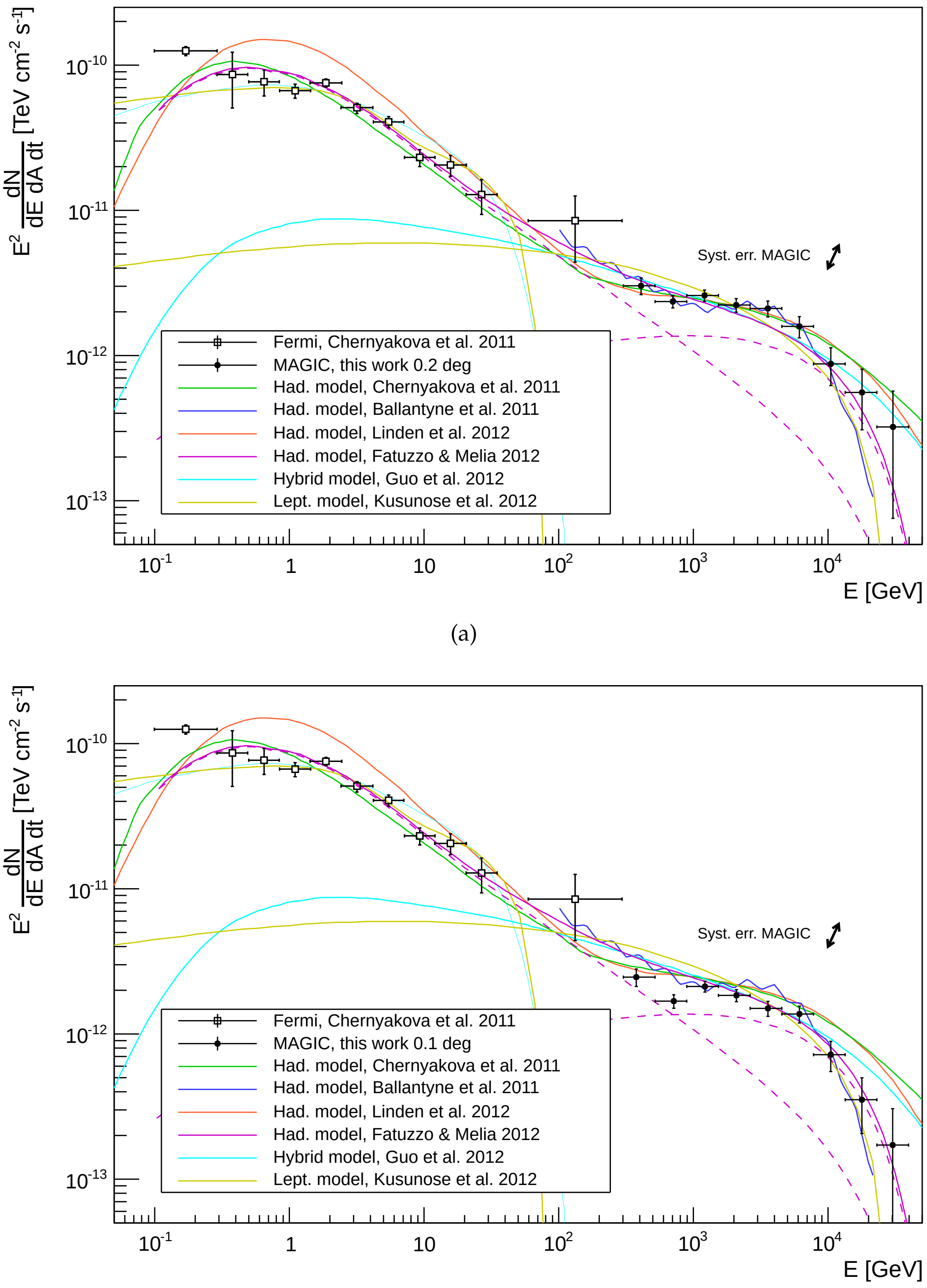

(a)

(b)

Figure 12.1: MAGIC and *Fermi* (Chernyakova et al., 2011) SED of the GC γ-ray source compared to several model predictions. The models are compared to MAGIC SEDs extracted from two integration radii (0.2 ° (a) and 0.1 ° (b)). The shown leptonic model by Kusunose & Takahara (2012) is based on two independent electron populations, one for explaining the GeV part and one for the TeV part of the SED (thin magenta, dashed lines).

et al. (2011) and later Linden et al. (2012) were proposing similar hadronic models, able to explain both, the GeV and the TeV emission. In both models a injection spectrum from CR acceleration close to the SMBH with spectral index $\alpha \sim -2$ and exponential cut-off at 100 TeV is used. Variation of the spectral index of the γ-ray emission throughout the spectrum is explained by the difference in the diffusion for GeV compared to TeV CRs. Both models are assuming a dense configuration of interstellar gas at distances from one to a few parsec from SgrA*. The γ-ray flux for a given energy is then proportional to the time the CRs stay inside the region of dense material and interact, producing pions. For low energies, diffusion is slow and the time spent in the emission region is of the order of the timescale of activity of the particle accelerator. Therefore they should mimic the spectral shape of the injected CRs and the total flux should depend on the duration of the accelerator being active. A low energy cut-off is expected below 100 MeV, due to the π_0 production limit. At higher energies there is a transition with steeper spectral index as diffusion is getting faster. At TeV energies the CRs move nearly rectilinearly through the emission zone, all spending the same time and therefore again mimicking the injection spectrum.

In their hadronic model Fatuzzo & Melia (2012) include a simplified description of the particle acceleration in their numeric simulation of the diffusion of CRs through turbulent magnetic fields. They assume a torus of dense material around the GC BH of about 2 pc radius, embedded inside a wind zone of lower density, about 10 pc in diameter. Particles are accelerated throughout their diffusion history and eventually react with ambient protons, either in the torus or in the wind zone. The protons in their model are originating from the extremely-high energy tail of the thermal distribution near the BH and are further accelerated subsequently. The torus is mainly populated by lower energy particles that have a high probability for hadronic reactions due to the high ambient density, generating the *Fermi* peak of the SED. TeV protons have a much higher probability to react in the wind zone, leading to the high energy hump in the SED. This model, which does not even need time variability for explaining the observations, fits both the *Fermi* and the MAGIC points, with surprising precision (see figure 12.1).

Leptonic scenarios on the other hand have difficulties explaining both, the GeV and the TeV spectrum with a single population of electrons. Recently Kusunose & Takahara (2012) suggested a model where high energy electrons accelerated close to the central BH are interacting via IC scattering with soft photons emitted by the dense population of stars and dust inside the central few parsecs from the GC. By adapting their model parameters they are able to fit either the high energy or the low energy bump. In this scenario the electron populations would have to originate from different acceleration mechanisms or sources, as it is proposed by the authors and also Hinton & Aharonian (2007).

int. radius	$F_{E>1\mathrm{TeV}}$ [cm$^-2$ s$^-1$]	ΔF [cm$^-2$ s$^-1$]	$F_{E>1\mathrm{TeV}}/F_{E>1\mathrm{TeV},0.1^\circ}$
0.1 °	$1.711 \cdot 10^{-12}$	$0.068 \cdot 10^{-12}$	1.000
0.2 °	$2.127 \cdot 10^{-12}$	$0.089 \cdot 10^{-12}$	1.243
0.4 °	$3.089 \cdot 10^{-12}$	$0.154 \cdot 10^{-12}$	1.805

Table 12.1: Integral flux ($E > 1$ TeV) from GC for the three different integration radii (0.1 °, 0.2 ° and 0.4 °).

A lepto-hadronic hybrid scenario was recently suggested by Guo et al. (2013). In their model the GeV part of the spectrum as observed by *Fermi* is due to IC scattering of relativistic electrons and the TeV part is due to CRs, both accelerated in the vicinity of the BH.

As it can be seen from figure 12.1, all models are able to describe well the MAGIC data within errors. The *Fermi* spectrum is also described with reasonable precision by most models, except for the hadronic model by Linden et al. (2012). The *Fermi* point at around 150 MeV seems a bit problematic, especially for the hadronic models that must include the π_0 cut-off only slightly below that energy. These circumstances are already mentioned by Chernyakova et al. (2011), who recommend to interpret this point with caution, since the angular resolution of *Fermi* is very low at this energy, which could lead to large systematic errors due to source confusion. It should also be noted that in case of the leptonic model by Kusunose & Takahara (2012), the two SEDs, one for the GeV and one for the TeV spectrum are generated by two distinct electron populations and could therefore be modeled independently.

One might think the the high energy cut-off at ~ 10 TeV represents a good possibility for testing the difference between specific models, especially after even longer observations and therefore smaller statistical error bars. Unfortunately this cut-off has been introduced ad hoc in most scenarios, assuming a seed CR/e^- spectrum with exactly the right properties.

One can conclude that in order to distinguish between different models, time variations, as predicted by most of the hadronic models, have the highest potential for ruling out some of them. It is therefore necessary to continue monitoring the source, especially at the highest energies, close to the cut-off (~ 10 TeV), where variability on a timescale of the order of 10 y or even less is predicted. The detection of the gas cloud G2 on its trajectory, which brings it close to SgrA* and might cause a flare of freshly accelerated CRs, presents a unique chance for studying the nature this source.

12.2 THE EXTENSION OF THE GC SOURCE

The claim that the γ-ray emission from the direction of SgrA is actually extended is based on the fact that the flux increases with increasing integration radius. By integrating over a larger area the number of events is automatically increasing due to the limited angular resolution of the instrument, even for a point source. This effect should be compensated by the increasing effective collection area, which is determined based on MC. A good match between data and MC has to be assumed in order to keep up this claim.

For not having to rely on MC only, the same analysis has been tried on contemporary Crab Nebula data, also observed at very large Zd (see appendix C). The Crab analysis shows an increase of the flux by 9 % if going from 0.1 ° to 0.2 ° and 11 % if going from 0.1 ° to 0.4 ° integration radius. The flux from the GC is increasing by $\sim$ 24 % if going from 0.1 ° to 0.2 ° and 81 % if going from 0.1 ° to 0.4 ° integration radius (see table 12.1).

In case of the Crab Nebula, the biggest jump happens between 0.1 ° to 0.2 °, probably because the MC data do not perfectly reproduce the PSF. On the other hand, the angular extension of the Crab Nebula in radio/optical/X-ray is between 0.05 ° and 0.1 °. If the extension of the γ-ray source is of the same order, then even this physical extension could be responsible for flux increase when going to larger radii.

For the GC on the other hand the biggest change happens when going to very large integration radii, a clear hint for extended emission. The same picture is supported by the skymaps, where clear evidence for extended emission, especially along the Galactic plane, can be found. In conclusion one can say that there might be a small systematic data/MC mismatch, but it is still safe to claim an extended source at the direction of SgrA.

12.3 THE NEW SOURCE

The probably most interesting by-product of the GC monitoring campaign was the discovery of a significant γ-ray counting excess at the position of the Galactic Center Arc (GCA). If systematic effects can be excluded there is a number of interesting scenarios that could explain a source with a very hard spectrum in TeV energies at this location.

12.3.1 *Is the Arc feature real?*

A topic related to the extension of the GC γ-ray source is the question if one can safely exclude a systematic effect that could have caused the remaining, statistically significant excess at the coordinates of the radio Arc discovered by Yusef-Zadeh et al. (1984). As already mentioned, tests performed on the Crab data sample could not reproduce any excess of similar relative magnitude. When fitting a two dimensional Gaussian to the Crab Nebula skymaps, a similar pointing mismatch of the order of 0.02 ° has been found. The maximum residual relative flux after subtraction of a 2D Gaussian is on the order of 5% of the pre-subtraction value, while for the GC it is about 25% that remain at the location of the GCA. The TS value significance of the GCA emission is more than 5σ, for nearly all energy thresholds, except for $E > 10\,\text{TeV}$ (see also appendix C).

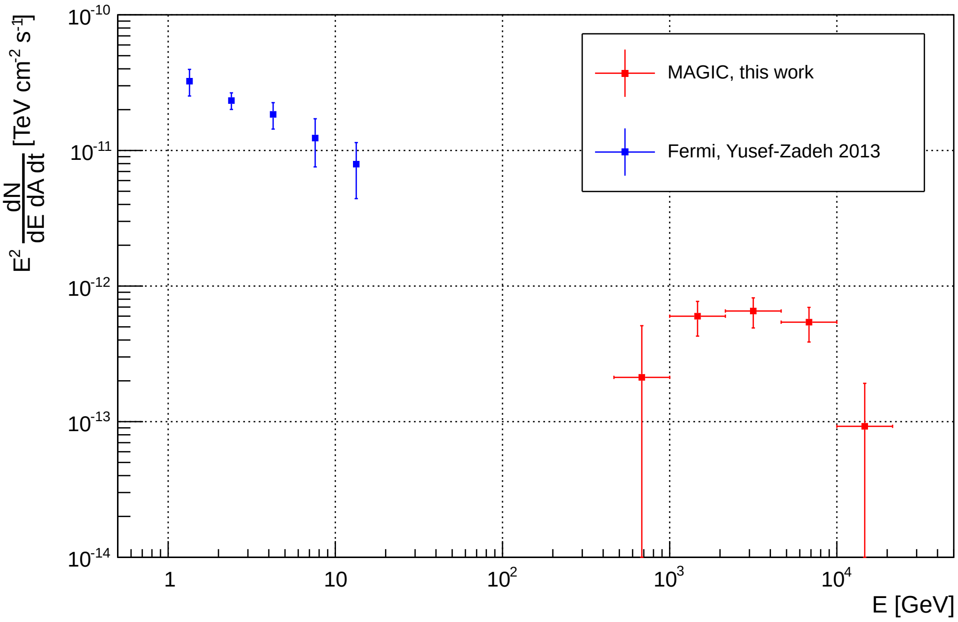

Figure 12.2: MAGIC and *Fermi* (Yusef-Zadeh et al., 2013) SED of the GC Arc.

Therefore it is relatively safe to claim the detection of a new source of VHE γ-radiation. Already in the Galactic Center Ridge discovery paper by H.E.S.S. (Aharonian et al., 2006a), there is a strong - however unclaimed - hint for γ-ray emission from the same location. Also Macias & Gordon (2014) hint to a correlation of an excess in H.E.S.S. and *Fermi* data with the coordinates of the GCA.

12.3.2 *Possible counterparts of the new source*

The radio Arc as source of the high energy γ-ray emission from the corresponding region is only one possible explanation. Another good – maybe even better – candidate is the giant molecular cloud (GMC) G0.11-0.11 (Tsuboi et al., 1997), which is located very close to the southern half of the GCA, between the Arc and SgrA. γ-rays could either originate form electrons that are being accelerated in the interaction of G0.11-0.11 with the GCA (Tsuboi et al., 1997), or they could originate from CR interactions inside the dense molecular material. Those cosmic rays could either originate from past flaring activity of the GC BH SgrA*, several 100 or 1000 years ago. Or they could have been accelerated in shocks associated with the numerous supernova explosions driving the expansion of the GMC.

Yusef-Zadeh et al. (2013) show a *Fermi* spectrum of the GCA source. In their paper they assume Bremsstrahlung of CR electrons as the dominant mechanism responsible for the γ-ray emission in several of the GC molecular clouds. For some of the objects, like for example SgrB2, also the H.E.S.S. TeV spectrum is available. They argue that the harder TeV part of the spectrum is due to a younger electron population, while the softer *Fermi* spectrum is due

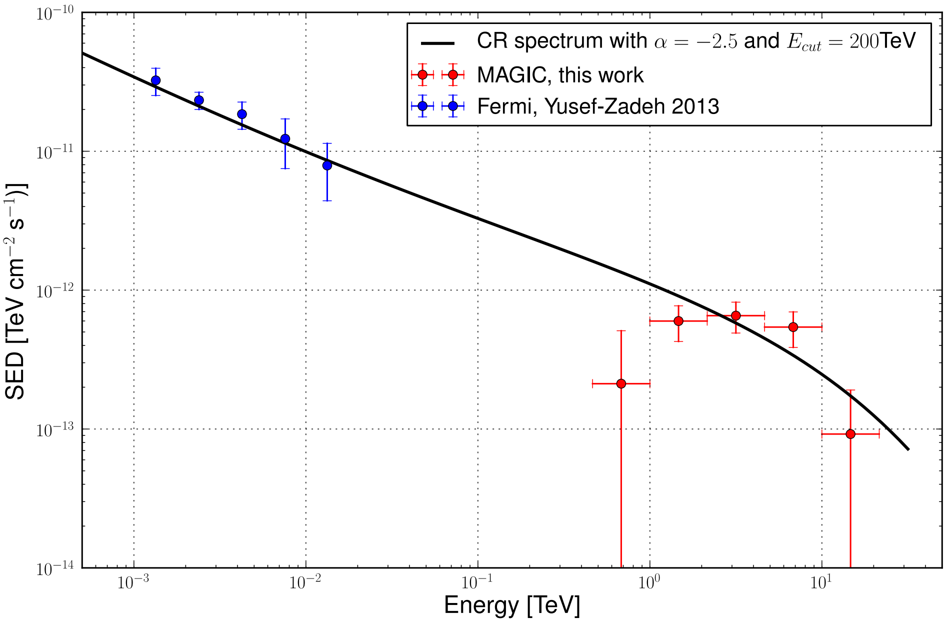

(a)

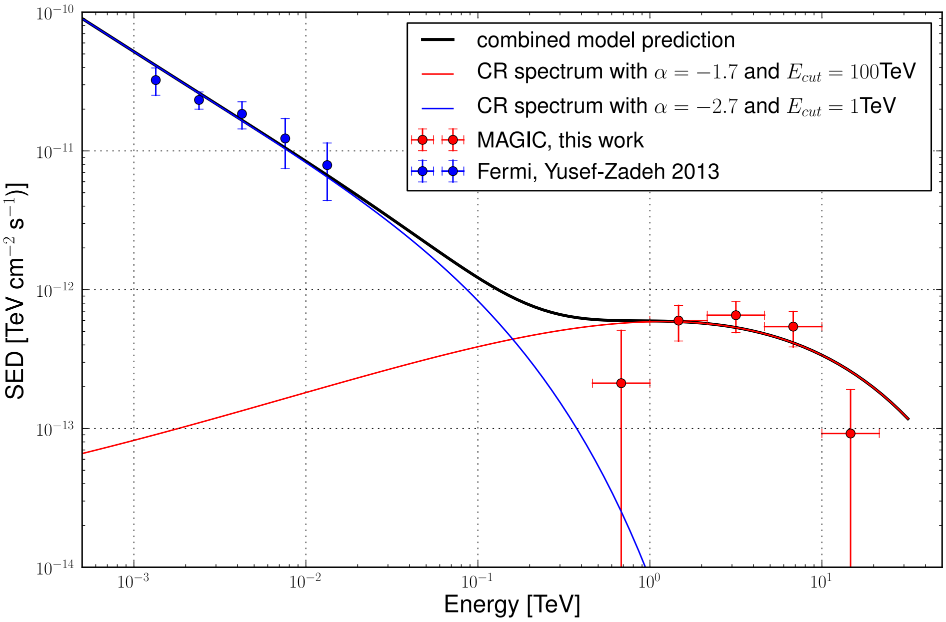

(b)

Figure 12.3: γ-ray emission from pp-interaction in the GMC G0.11-0.11 modeled with a single component seed CR spectrum, visually fitted to match MAGIC and *Fermi* (Yusef-Zadeh et al., 2013) data (a). Same, using two components (b). Values for χ^2 have been calculated, giving 21 over 7 d.o.f. and 8 over 5 d.o.f., respectively.

to an older, already synchrotron-cooled population. A similar scenario would probably also work for the *Fermi* and MAGIC SED (figure 12.2) of the GCA source.

In the following I will show that the GCA SED can in principle also be reproduced assuming pp-interaction inside the molecular cloud G0.11-0.11. Handa et al. (2006) estimate the total molecular mass of G0.11-0.11 to $6.3 \cdot 10^5\, M_\odot$. Using the formulae in Aharonian et al. (2013), one can show that the *Fermi* part of the GCA SED can be explained by assuming the same cosmic ray spectrum that is observed at Earth (spectral index $\alpha = -2.7$, see also chapter 2.2) with a flux normalization that is increased by a factor 20. If one also wants to simultaneously match the MAGIC data points one has to introduce a second component with spectral index -1.7 and an exponential cutoff at 100 TeV. The resulting γ-ray spectrum visually matches best the data-points if also assuming a cutoff in the GeV spectrum at about 1 TeV (see figure 12.3 (b)). The following spectral parameters were used for the seed CR spectra.

$$\left(\frac{\mathrm{d}F}{\mathrm{d}E\,\mathrm{d}\Omega}\right)_1 = 2.86 \cdot \left(\frac{E}{\mathrm{TeV}}\right)^{-2.7} \exp\left(-\frac{E}{1\,\mathrm{TeV}}\right)\ \mathrm{m^{-2}s^{-1}sr^{-1}TeV^{-1}}\,,$$
$$\left(\frac{\mathrm{d}F}{\mathrm{d}E\,\mathrm{d}\Omega}\right)_2 = 0.36 \cdot \left(\frac{E}{\mathrm{TeV}}\right)^{-1.7} \exp\left(-\frac{E}{100\,\mathrm{TeV}}\right)\ \mathrm{m^{-2}s^{-1}sr^{-1}TeV^{-1}}\,.$$

Alternatively, the spectrum can be modeled with a single component CR spectrum (figure 12.3 (a)) with

$$\frac{\mathrm{d}F}{\mathrm{d}E\,\mathrm{d}\Omega} = 5.0 \cdot \left(\frac{E}{\mathrm{TeV}}\right)^{-2.5} \exp\left(-\frac{E}{200\,\mathrm{TeV}}\right)\ \mathrm{m^{-2}s^{-1}sr^{-1}TeV^{-1}}\,.$$

In both cases χ^2 has been minimized by hand giving values of 21 over 7 d.o.f. for the single power-law spectrum and 8 over 5 d.o.f. for the two component spectrum. Finally one can conclude that explaining the emission from the GCA with a single CR component is quite appealing due to its simplicity, but for ruling out any of the possible scenarios, more precise measurements of the SED are necessary.

12.4 DARK MATTER INTERPRETATION OF THE GC SPECTRUM

Without any doubt, the GC region is an important candidate region for the detection of γ-ray signals from the interaction or decay of dark matter. There have been already a number of publications which examine the possibility of explaining the TeV spectrum observed in the GC by secondary particles from DM interaction/decay. Some examples are Aharonian et al. (2006b), Cembranos et al. (2012) and Gammaldi et al. (2014).

In scenarios like the one described in Gammaldi et al. (2014), a very heavy Wimp has to be assumed with $M_\chi \sim 50\,\mathrm{TeV}$. γ-rays are produced in cascading reactions after annihilation of two DM particles into $W^+ W^-$. With these prerequisites the authors manage to explain well the spectral shape of the H.E.S.S. spectrum, using a power-law extension of the *Fermi* spectrum as background. Another problem is explaining the obviously relatively small extension and necessarily high central density of the hypothetical DM halo. A very pronounced central cusp or spike like it is proposed by Fields et al. (2014), together with a very large WIMP mass of the order of several 10 TeV, could possibly explain the IACT observations.

The new MAGIC observations, given the very asymmetric morphology of the extended part of the γ-ray signal, do not support the idea of a pure DM interpretation. It is not excluded that DM plays a role in the GC emission, even at TeV energies. But most probably other astrophysical sources are dominating the γ-ray emission in that region.

12.5 CONCLUSIONS

No effect of the gas cloud G2 on the VHE γ-ray emission from the GC could be observed during the 3 year observation campaign with MAGIC. Nevertheless, re-observation of the GC with MAGIC allowed for studying the spectrum and morphology of the GC γ-ray source with excellent precision. The spectral results of the H.E.S.S. telescope on SgrA* and the SNR G 0.9+0.1 could be confirmed.

Most of the recent leptonic and hadronic models are able to explain the GeV to TeV spectrum observed by *Fermi* and IACTs, assuming particle acceleration close to the SMBH associated with SgrA*. Leptonic models however need to assume two distinct electron populations or sources in order to describe the two bump structure.

It could be shown that the emission from the GC source is clearly extended, with however a dominant point-like contribution from the location of HESS J1745-290. There is significant evidence for extended emission from the location of the radio feature called the Arc. Using a novel method, which allows for extracting energy spectra from skymap regions, the spectrum could be reconstructed (spectral index: -2.3 ± 0.1). Further observations are needed in order to better constrain the spectral parameters of the Arc source.

Part IV

SUMMARY AND CONCLUSIONS

13

SUMMARY AND CONCLUSIONS

In this thesis I am presenting the scientific results that I derived with three years of observations of the Galactic Center (GC) in TeV γ-rays with the MAGIC telescopes. Additionally, I also developed several techniques for extending the capabilities of observations by Imaging Air Cherenkov Telescopes (IACTs). Those developments include:

- Production of transmission profiles derived with LIDAR data, which can then be used in the analysis of IACT data.
- Determination of a procedure to correct the energy of events from IACT observations during non-optimal atmospheric conditions.
- Determination of an algorithm for adjusting the instrument response model, from Monte Carlo simulations, to the actual atmospheric conditions.
- Development of a technique for computing the energy spectra of extended (and possibly off-center) gamma-ray sources through the extraction of events from spatial regions in energy-binned skymaps.

The main goal of the GC observations was to search for possible variability of the γ-ray flux from the source associated with the SMBH in the center of our galaxy, SgrA*. Variability in the multi-TeV radiation is one possible scenario that could result from the interaction of the SMBH with the compact gas cloud G2, which approached SgrA* during the last years, getting as close as a few thousand Schwarzschild radii.

The evaluation of flux/spectral variability during long time intervals require a precise knowledge of the instrument response and its stability (or potential variation) with time. One of the main sources of error in the measurement of the gamma-ray flux is the uncertainty in the light transmission of the atmosphere, which is used as a gigantic calorimeter by IACTs. One of my goals was to account for variations in the atmospheric transmission (due to clouds, aerosol or Calima) through the usage of a low-power LIDAR instrument (built by the MPP group), and through the development of suitable analysis procedures. During my PhD thesis program I succeeded to do so for some IACT observations at low zenith angles (Zd). The technique is based on the determination of the atmospheric cloud/aerosol transmission profile through LIDAR measurements simultaneous to the IACT observations, which is then used to estimate the transmission losses on a shower-by-shower basis.

The transmission losses can be directly translated into an energy estimation bias, which would otherwise lead to a deformation of the reconstructed energy spectrum. The estimated energy of each event is scaled accordingly and the collection area model, which is obtained from MC simulations is adopted to this energy correction.

Using Crab Nebula observations during adverse atmospheric conditions, I could demonstrate that this new technique is able to reconstruct the known spectrum with good precision. For future observations, this method will allow for reducing the systematic errors of IACT observations and extending the useful observation time window into periods with thin clouds or high aerosol content, which could extend the available telescope observing time by up to 20%.

This is the first time in the history of γ-ray astronomy that LIDAR-based corrections have been successfully applied to energy spectra obtained with IACTs. All tools are now available to the MAGIC collaboration within the standard data analysis framework. This is an important step towards establishing high precision calibration for CTA, where several LIDAR systems will be operated together with the array and any gain in observation time will be highly valuable considering the high costs of the project.

The GC had to be observed under special circumstances, due to its low culmination altitude at the MAGIC site. The Zd range of the observations (59°-70°) has strong effect on the data taken under such conditions. It implies an increased energy threshold by nearly one order of magnitude. At the same time also the effective collection area for γ-rays scales by a similar factor. I validated the the performance of the MAGIC data analysis chain for energies $\gtrsim$ 1 TeV using dedicated MC simulations and observations of the Crab Nebula under similarly large Zd range. Unfortunately, by the time of the MAGIC observations on the GC, the LIDAR instrument had some hardware limitations which prevented observations at large Zd, and hence this technique could not be used to correct the MAGIC GC data presented in this PhD thesis. The LIDAR instrument was upgraded in August 2014, which will allow its usage in forthcoming observations of the GC with MAGIC.

The overall data set from three years of observations that was used for the analysis covers 66 h of good quality data. Based on this data set, so far no hint for variability could be detected in the light curve. The source energy spectrum between 400 GeV and 20 TeV could be measured with good precision, largely confirming previous measurements with the H.E.S.S. telescopes. The strong dependence of the flux on the angular integration radius, as well as the structure seen in the skymap provide strong evidence for extended emission from the region. When subtracting a point source from the coordinates of SgrA*, apart from extended emission along the direction of the Galactic plane, also two other coordinates show significant excess. One coinciding with the pulsar wind nebula G0.9+0.1, already known from observations by the H.E.S.S. telescopes, and a new source coinciding with the coordinates of the GC radio Arc (GCA) and the molecular cloud G0.11-0.11, both at about 0.2° from the GC. The new source appears to be slightly elongated in the direction perpendicular to the Galactic plane, although systematic effects from the subtraction of the SgrA* source cannot be completely ruled out.

I developed a new method for calculating the energy spectrum of off-center and possibly extended objects. The method uses signal extraction regions in energy binned skymaps for determining the number of excess events, and relies on the standard MC based tools for estimating the effective collection area and effective observation time. Using this technique, a spectrum for G0.9+0.1 and the new GCA source has been calculated. The spectrum of G0.9+0.1, with a spectral index of about -2.7 ± 0.4, is in good agreement with the H.E.S.S. measurements. The spectrum of the new GCA source is relatively hard (spectral index: -2.3 ± 0.1) and shows hints for a turnover or cutoff at around 3 TeV.

The γ-ray emission of SgrA* has been compared to several theoretical scenarios where the emission is dominated by hadrons, by leptons and by the combination of these two particle populations. While it is generally easier to explain the emission with at least one hadronic component, none of the models can be completely ruled out on the basis of the new MAGIC observations. No dedicated model exists for the TeV emission from the GCA. However, two possible sources have been identified: the radio Arc itself and the GMC G0.11-0.11. The GCA is a very bright source of electron synchrotron radiation, therefore IC or Bremsstrahlung scenarios are possible. The GMC G0.11-0.11 on the other hand, with its high hydrogen density, offers an excellent target for electron Bremsstrahlung or pp-interaction. I could show that a single power-law CR population with an index of -2.5, producing γ-radiation via π_0 decay can produce the observed emission within errors.

Despite the non-detection of variability in the VHE γ-ray emission from the GC, I think MAGIC should continue with these observations because the effects of the interaction between the GC and the gas cloud G2 might only be observable in a few years from now. Additionally, the increase in the VHE data set from this region would permit to improve the studies related to the gamma-ray production mechanisms in SgrA* as well as in the newly discovered GCA source.

I was also responsible for the analysis of the MAGIC data from the type Ia supernova (SN) explosion that occurred in the starburst galaxy M82 on January 21th 2014. This SN (dubbed SN 2014J) is the closest of this type that occurred since the late 80s, and hence the first one that could be observed with IACTs, which triggered large interest in the astrophysics community. While no significant VHE γ-ray excess could be detected from the location of SN 2014J, the most stringent upper limit for prompt emission from a SN of this type could be established ($1.5 \cdot 10^{-12}\,\mathrm{cm}^{-2}\mathrm{s}^{-1}$ for $E > 300\,\mathrm{GeV}$ and $3.9 \cdot 10^{-13}\,\mathrm{cm}^{-2}\mathrm{s}^{-1}$ for $E > 700\,\mathrm{GeV}$, at 95% confidence level). I have also been appointed to lead a scientific publication with these MAGIC observations.

Moreover, this PhD thesis also reports the hardware studies I did for the CTA project, where I characterized the angular acceptance of the Winston Cones (WC) using the photomultipliers (PMTs) that will actually be installed in the camera of the Large Size Telescopes (LST).

Part V

APPENDIX

A

OBSERVING M82 AFTER THE EXPLOSION OF SN2014J

A.1 TYPE IA SUPERNOVAE

The first reports about the observation of exceptionally bright stars, suddenly appearing in the sky, staying visible for months until slowly fading away, have been found in the records of Chinese astronomers from the first few centuries after Christ. Historical observations of the supernovae SN 1572 by Tycho Brahe and SN 1604 by Johannes Kepler had big influence on the conception of the world at that time. They were brought up against the Aristotelian geocentric model, in which the skies were thought to be static and eternal, persistently changing the scientific worldview (Weiler, 2003).

According to our current understanding, two different types of events can be responsible for the observed phenomena. The, core collapse or type II, is triggered by massive stars ($M \gtrsim 8M_{\odot}$) running out of fuel for nuclear fusion. The energy for the explosion is extracted from the gravitational potential during the formation of a compact object, such as a black hole or a neutron star. The second scenario, which leads to the explosion of thermonuclear or type Ia supernovae is a close binary system of a CO white dwarf, close to the Chandrasekhar mass limit, and a red giant star. The explosion is triggered when the mass of the white dwarf exceeds the Chandrasekhar limit after accretion of material from the hulls of the red giant. While the white dwarf collapses, gravitational energy, which is released in this process allows for carbon fusion to take place, burning the whole star and leaving no compact remnant (Mazzali et al., 2007).

It is generally assumed that some of the brightest SNRs, like the ones of Kepler, Tycho and SN 1006, are actually remnants of type Ia supernovae (Reynolds et al., 2007; Krause et al., 2008; Branch & Tammann, 1992). SNRs are classical sources of VHE-γ radiation, among them also such of type Ia, for example SN 1006 (Acero et al., 2010a). On the other hand little is known about possible particle acceleration in type Ia supernova explosions themselves at very early stage.

A.2 SN 2014J

SN 2014J has been discovered by Fossey et al. (2014) inside the starburst galaxy M82 on January 21th 2014. It has later been classified as type Ia supernova (SN) by Cao et al. (2014). SN 2014J is the closest SN of this type, at least since 1986 (Nielsen et al., 2014) and therefore the brightest within the era of large IACT arrays.

Date (yyyy mm dd)	[MJD]	Eff. Time [h]	Z_d [deg]	UL (E>300GeV) [$\mathrm{cm}^{-2}\,\mathrm{s}^{-1}$]	UL (E>700GeV) [$\mathrm{cm}^{-2}\,\mathrm{s}^{-1}$]
2014-01-27	56684	0.98	47-53	$1.18\mathrm{x}10^{-11}$	$1.51\mathrm{x}10^{-12}$
2014-01-28	56685	1.41	40-43	$2.35\mathrm{x}10^{-12}$	$1.14\mathrm{x}10^{-12}$
2014-01-29	56686	1.30	40-42	$2.16\mathrm{x}10^{-12}$	$6.51\mathrm{x}10^{-13}$
2014-02-01	56689	0.98	40-42	$2.49\mathrm{x}10^{-12}$	$5.63\mathrm{x}10^{-13}$
2014-02-02	56690	1.30	40-42	$3.82\mathrm{x}10^{-12}$	$2.12\mathrm{x}10^{-12}$

Table A.1: MAGIC observation times and daily flux upper limits for SN 2014J

A.3 THE HOST GALAXY M82

The host galaxy M82 is one of the closest starburst galaxies, located at 3.6 Mpc from our galaxy in the constellation Ursa Mayor (Freedman et al., 1994). The SN rate in this galaxy has been estimated to be on the order of $0.1\,\mathrm{y}^{-1}$ (Fenech et al., 2008). The high star formation rate ($2\,M_\odot\,\mathrm{y}^{-1}$) and SN rate, together with its proximity, make M82 a good candidate for a γ-ray source. Indeed, the galaxy was discovered to produce VHE γ-rays after 137 h of observations with the VERITAS telescope (Acciari et al., 2009). In this publication it is suggested that the γ-ray flux is due to CR interaction. The CRs are thought to be accelerated inside the numerous SNRs throughout the galaxy.

A.4 OBSERVATIONS WITH MAGIC

SN 2014J was observed by the MAGIC telescopes for the first time six days after the discovery (January 21th 2014) and observed for a total of five nights accumulating 6 h of good quality data. The dates and duration of the observations can be found in table A.1. The observation campaign was treated as target of opportunity observation, given the rarity of such an event.

The observations were carried out at medium Zd (47-53 ° in the first and 40-43 ° in the following nights) and during weak moonlight conditions from January 27th to 29th and during dark conditions on February 1st and 2nd.

The data quality was generally very good. Even the data affected by weak moonlight was fulfilling the requirements for being analyzed as dark-night data. No bad weather cuts had to be applied and all 5.96 h could be used in the higher level analysis.

A.5 RESULTS

No significant γ-ray excess could be detected from the direction of M82 (see figure A.1). Daily flux upper limits for γ-ray events with $E > 300\,\mathrm{GeV}$ and $E > 700\,\mathrm{GeV}$ were calculated (see table A.1 and figure A.2). The overall flux upper limits are $1.5 \cdot 10^{-12}\,\mathrm{cm}^{-2}\mathrm{s}^{-1}$ for $E > 300\,\mathrm{GeV}$ and $3.9 \cdot 10^{-13}\,\mathrm{cm}^{-2}\mathrm{s}^{-1}$ for $E > 700\,\mathrm{GeV}$, at 95% confidence level. These values correspond to 1.2%

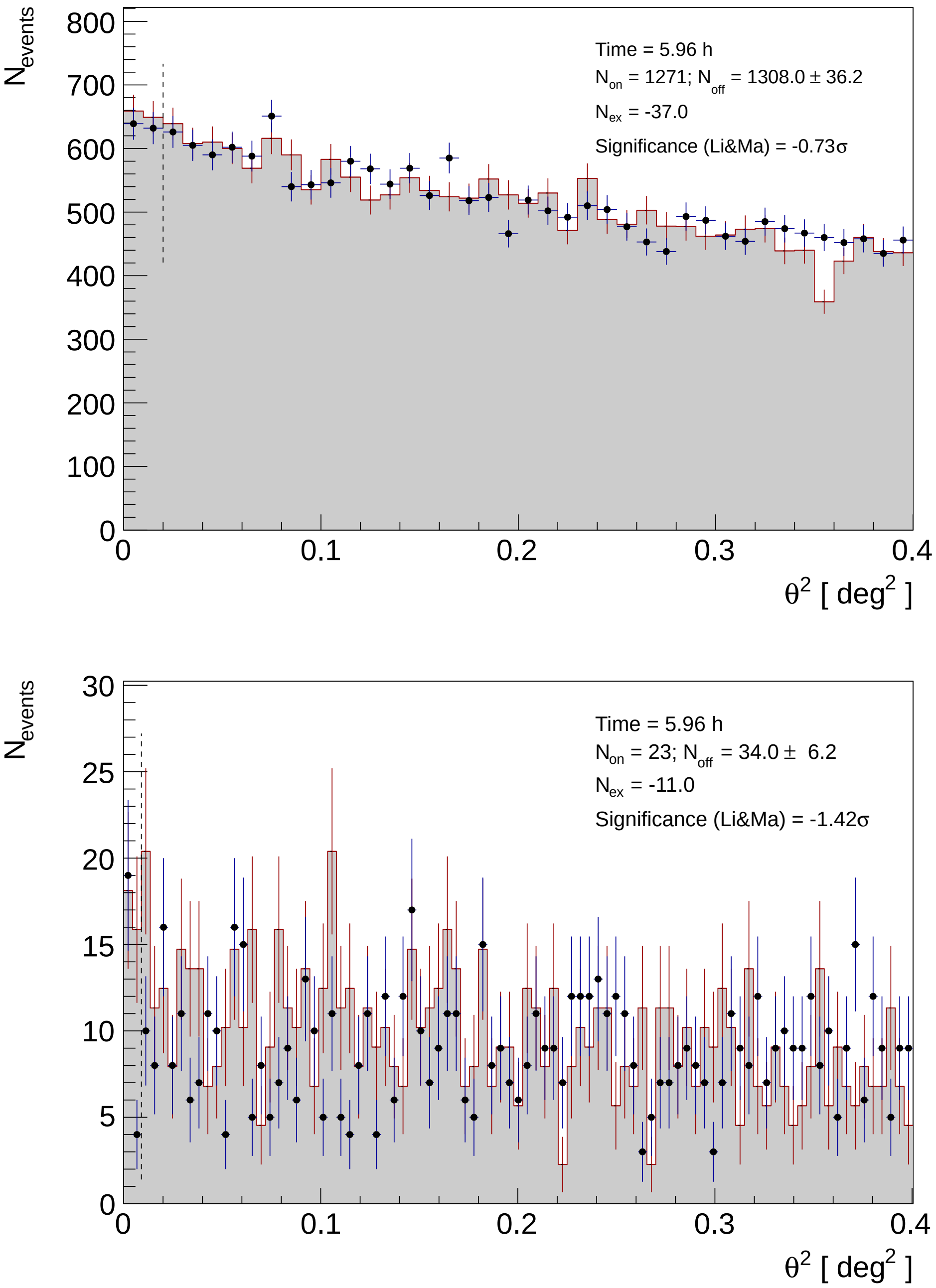

Figure A.1: θ^2 plots for SN 2014J with low energy (a) and full range (b) cuts. No γ-ray excess could be detected.

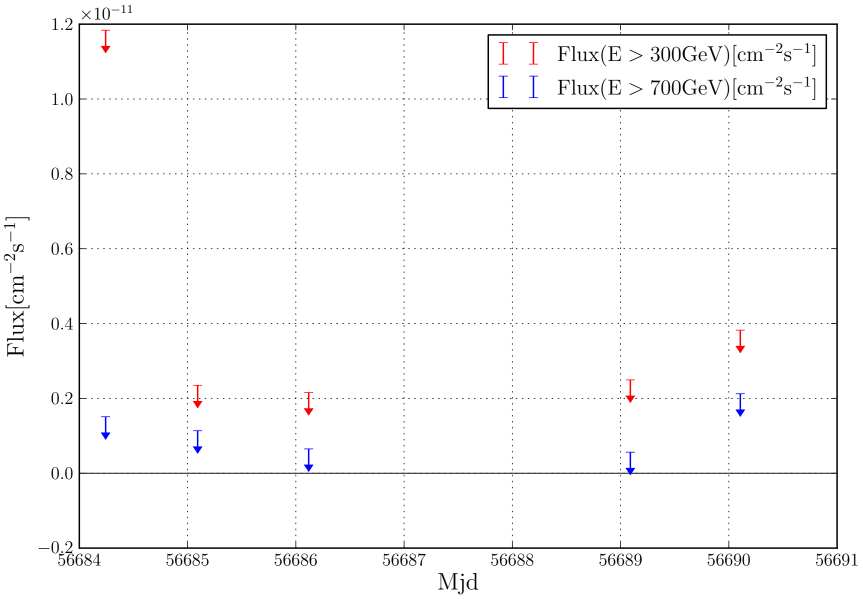

Figure A.2: Daily flux upper limits for SN 2014J for events with more that 300 GeV (red) and more than 700 GeV (blue)

and 1.0% respectively, in units of the Crab Nebula flux, assuming a Crab-like spectral shape.

A.6 DISCUSSION

The γ-ray flux from M82 should have acted as background for our observations. Given the short observations by MAGIC, no significant excess, neither from the host galaxy, nor from any superposed source could be discovered. VERITAS was measuring a flux of $(3.7 \pm 0.8_{stat} \pm 0.7_{syst}) \cdot 10^{-13}\,\mathrm{cm}^{-2}\mathrm{s}^{-1}$ for $E > 700\,\mathrm{GeV}$ (Acciari et al., 2009). Given the effective collection area of the MAGIC observations ($1.46 \cdot 10^9\,\mathrm{cm}^2$) and the observation time ($19.5 \cdot 10^3\,\mathrm{s}$) MAGIC should have seen an excess of 11.6 ± 3.3 events[1], while the actually observed excess was -4.0 ± 6.0 events. The 95% confidence level upper limit is 11.1 excess events, which still includes the VERITAS measurement given their errors. Given the possible large downward fluctuation in the MAGIC data, the background from the host galaxy M82 was not considered further in the upper limits on the flux from SN 2014J.

The closest ever observed SN in the modern scientific era was SN 1987A (Type II), which was already observed with Cherenkov telescopes by (Bond et al., 1989) using the JANZOS cosmic ray facility, with an energy threshold of $E > 75\,\mathrm{TeV}$. They give an upper limit for the energy emitted as γ-radiation in that band of $E < 10^{37}\,\mathrm{erg\,s}^{-1}$, assuming a spectral index of -2 over the whole

---

[1] The statistical and the systematic error of the VERITAS measurement have been added quadratically.

energy range. Here the flux UL for $E > 300\,\mathrm{GeV}$ shall serve for calculating an upper limit on the total power, which the SN emits in the VHE regime. Assuming a Crab like spectral index of -2.6, the mean γ-ray energy is

$$\overline{E_\gamma} = \frac{\int_{300\,\mathrm{GeV}}^{\infty} E\, E^{-2.6}\, \mathrm{d}E}{\int_{300\,\mathrm{GeV}}^{\infty} E^{-2.6}\, \mathrm{d}E} = 487.5\,\mathrm{GeV}\,. \tag{A.6.1}$$

This allows for calculating an upper limit for the power density at earth.

$$\begin{aligned} S_{E_\gamma > 300\,\mathrm{GeV},max} &= F_{E_\gamma > 300\,\mathrm{GeV},max} \cdot \overline{E}_{\gamma,E>300\,\mathrm{GeV},\alpha=2.6} \\ &= 1.5 \cdot 10^{-12}\,\mathrm{cm}^{-2}\mathrm{s}^{-1} \cdot 487.5\,\mathrm{GeV} \\ &= 1.17 \cdot 10^{-12}\,\mathrm{erg}\,\mathrm{cm}^{-2}\mathrm{s}^{-1}\,. \end{aligned} \tag{A.6.2}$$

For isotropic emission and the distance to M82, $d_{M82} = 3.6\,\mathrm{Mpc}$ (Freedman et al., 1994), the total power upper limit is

$$\begin{aligned} P_{E_\gamma > 300\,\mathrm{GeV},max} &= 4\,\pi\, d_{M82}^2\, S_{E_\gamma > 300\,\mathrm{GeV},max} \\ &= 4\,\pi \cdot (1.11 \cdot 10^{25}\,\mathrm{cm})^2 \cdot 1.17 \cdot 10^{-12}\,\mathrm{erg}\,\mathrm{cm}^{-2}\mathrm{s}^{-1} \\ &= 1.8 \cdot 10^{39}\,\mathrm{erg}\,\mathrm{s}^{-1}\,. \end{aligned} \tag{A.6.3}$$

One can compare this to the total energy yield of a SN explosion of type Ia, generated by carbon fusion, $E_{tot} = 1 \cdot 10^{51}$ erg (Falta et al., 2011). Assuming a timescale for the observations of 10 days, the fraction of the total energy yield emitted as VHE-γ radiation during that time is $E_{E_\gamma > 300\,\mathrm{GeV}} / E_{tot} < 10^{-6}$. Being a bit more conservative and assuming the γ-radiation would be emitted over a period of 100 days, one can still constrain that the fraction of the energy going into that channel is less than 10^{-5}. This should be the most stringent upper limit on the γ-ray flux emitted directly after a type Ia SN explosion.

B

MORE TABLES AND FIGURES OF THE GC ANALYSIS

In the following I am presenting some additional material concerning the data sample and analysis of the GC observations. Tables B.1, B.2, and B.3 show the exact remaining observation times after data quality selection for the years 2012, 2013, and 2014 respectively. Figures B.1 and B.2 show the GC differential energy spectra and SEDs for different integration radii (0.1 °, 0.2 °, and 0.4 °) and using different unfolding methods. Figure B.3 illustrates the new experimental technique for extracting energy spectra from skymap regions.

obs. day	eff. time	obs. day	eff. time	obs. day	eff. time
2012-04-14	1.41 h	2012-04-15	1.59 h	2012-04-17	1.26 h
2012-04-24	0.69 h	2012-04-26	0.66 h		
total	6 h				

Table B.1: Remaining observation days/time after quality cuts for the 2012 observations of the GC.

obs. day	eff. time	obs. day	eff. time	obs. day	eff. time
2013-03-10	0.03 h	2013-03-11	0.25 h	2013-03-19	0.37 h
2013-03-20	0.78 h	2013-03-21	0.30 h	2013-04-06	0.66 h
2013-04-07	1.09 h	2013-04-16	0.41 h	2013-04-17	0.35 h
2013-04-18	0.89 h	2013-05-02	0.65 h	2013-05-05	1.20 h
2013-05-06	1.63 h	2013-05-07	0.04 h	2013-05-11	0.14 h
2013-05-12	0.21 h	2013-05-13	1.18 h	2013-05-14	0.61 h
2013-05-15	1.06 h	2013-05-16	1.22 h	2013-05-17	0.89 h
2013-05-18	0.33 h	2013-05-19	0.29 h	2013-05-20	0.08 h
2013-05-31	0.70 h	2013-06-01	1.00 h	2013-06-02	1.18 h
2013-06-03	0.81 h	2013-06-04	0.48 h	2013-06-06	1.24 h
2013-06-08	1.09 h	2013-06-13	1.12 h	2013-06-14	1.15 h
2013-06-15	1.17 h	2013-06-16	1.67 h	2013-06-17	0.24 h
2013-06-26	0.39 h	2013-06-27	1.34 h	2013-07-02	0.49 h
2013-07-03	0.11 h	2013-07-04	0.15 h	2013-07-08	0.72 h
2013-07-09	0.63 h	2013-07-10	0.11 h		
total	31 h				

Table B.2: Remaining observation days/time after quality cuts for the 2013 observations of the GC.

obs. day	eff. time	obs. day	eff. time	obs. day	eff. time
2014-03-01	0.56 h	2014-03-02	0.68 h	2014-03-03	0.70 h
2014-03-05	0.78 h	2014-03-06	0.87 h	2014-03-07	0.90 h
2014-03-12	0.82 h	2014-03-14	0.53 h	2014-03-27	0.96 h
2014-04-05	1.56 h	2014-04-07	1.24 h	2014-04-08	0.93 h
2014-04-09	1.15 h	2014-04-23	1.45 h	2014-04-24	1.48 h
2014-04-25	0.62 h	2014-04-27	0.65 h	2014-04-29	1.21 h
2014-04-30	0.08 h	2014-05-02	0.79 h	2014-05-03	0.86 h
2014-05-04	0.74 h	2014-05-06	0.58 h	2014-05-08	0.49 h
2014-05-21	0.83 h	2014-05-24	0.96 h	2014-05-26	0.59 h
2014-05-27	0.98 h	2014-05-30	0.96 h	2014-05-31	1.05 h
2014-06-01	0.65 h	2014-06-02	0.49 h	2014-06-03	0.65 h
2014-06-04	0.17 h	2014-06-05	0.63 h		
total	29 h				

Table B.3: Remaining observation days/time after quality cuts for the 2014 observations of the GC.

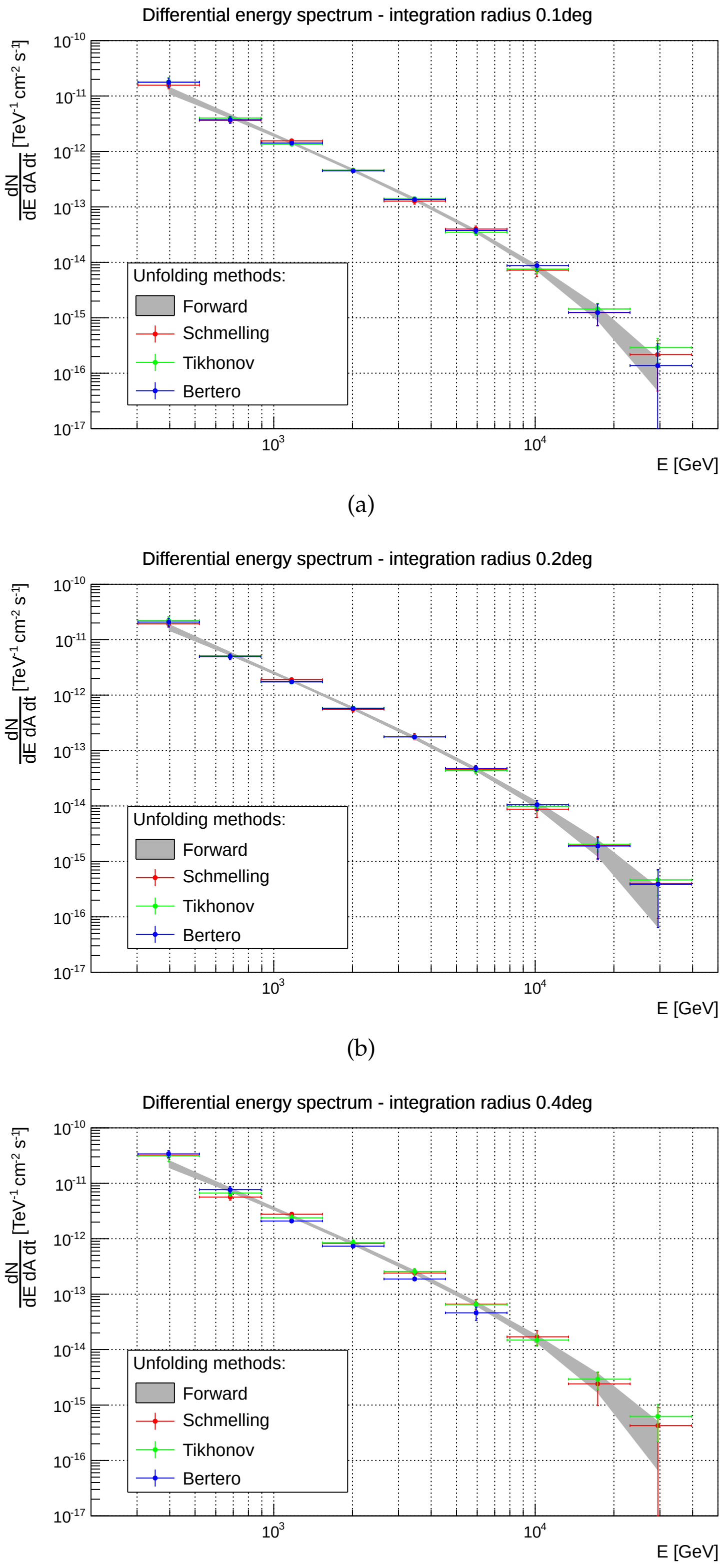

(a)

(b)

(c)

Figure B.1: Differential energy spectra for three different integration radii (0.1 ° (a), 0.2 ° (b) and 0.4 ° (c)) around the Galactic Center. The plots are showing spectra unfolded with three different algorithms (datapoints: Bertero, Schmelling, Tikhonov) and the result of the forward folding method using a power-law with exponential cut-off as assumed spectrum (shaded uncertainty area).

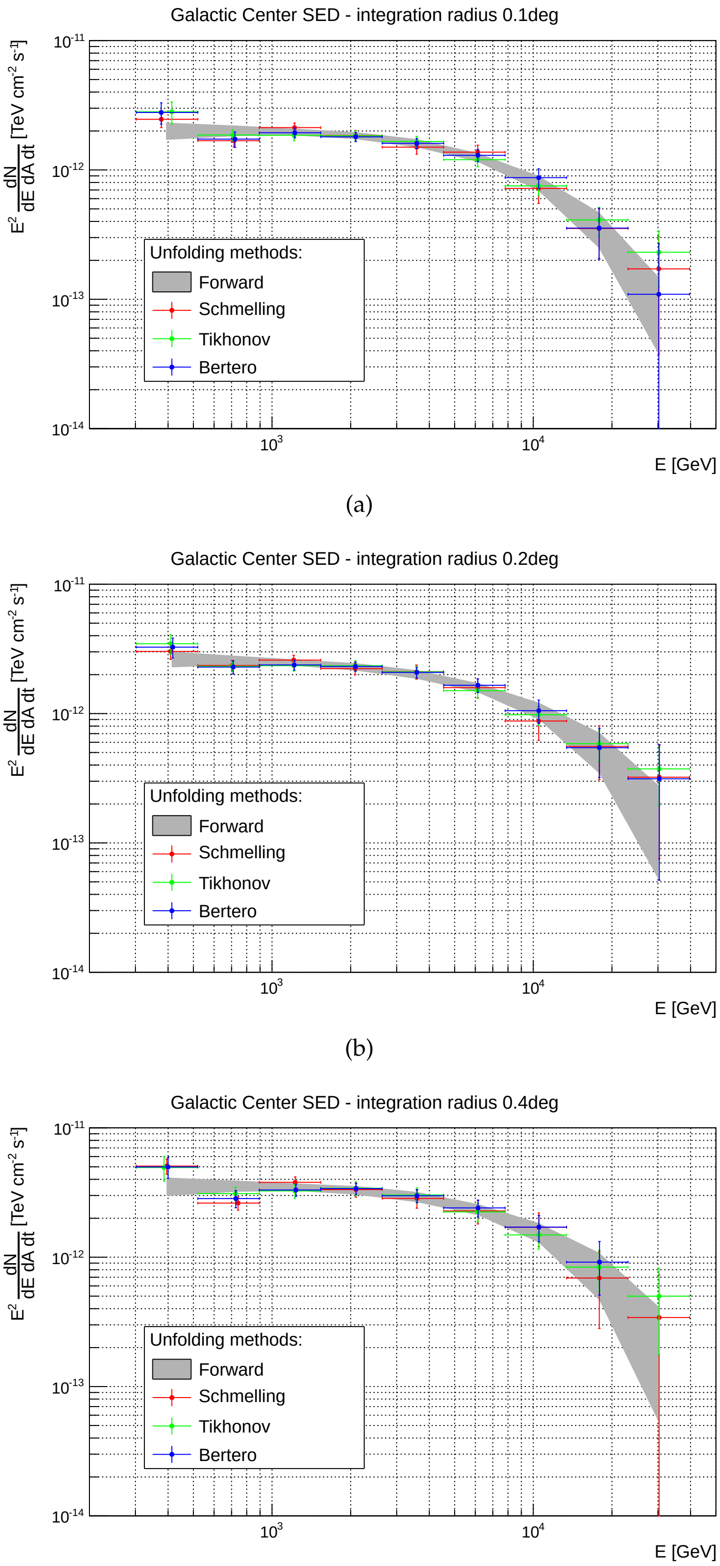

(a)

(b)

(c)

Figure B.2: Galactic center SEDs for three different integration radii (0.1 ° (a), 0.2 ° (b) and 0.4 ° (c)) and three different unfolding methods (datapoints: Bertero, Schmelling, Tikhonov) plus the result of the forward folding method using a power-law with exponential cut-off as assumed spectrum (shaded uncertainty area).

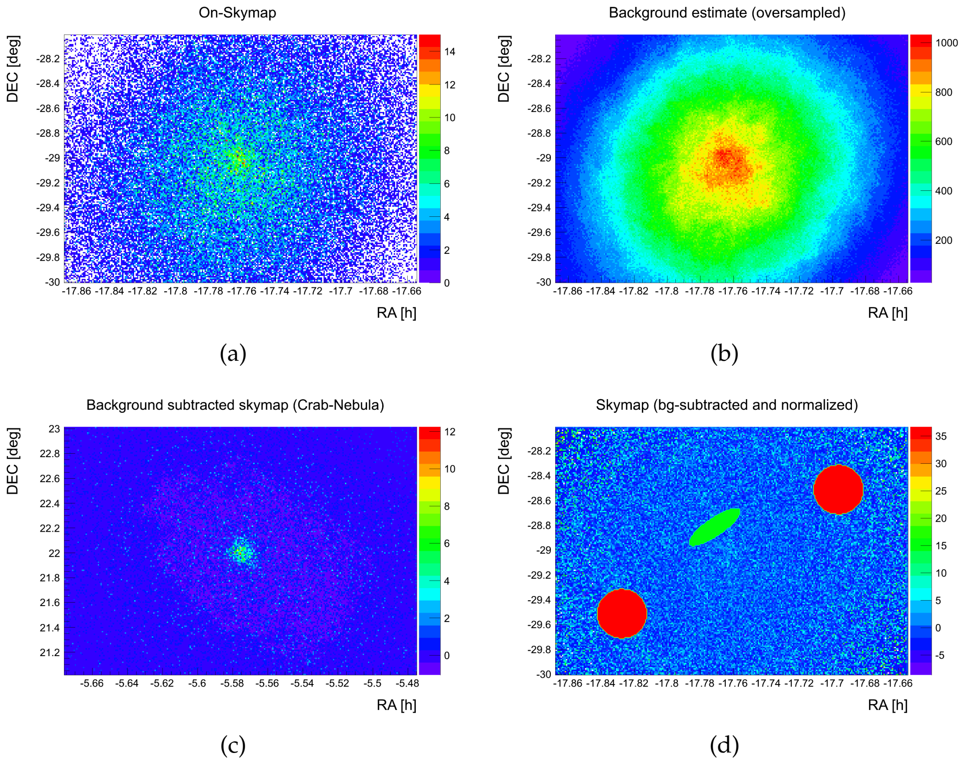

On-Skymap

Background estimate (oversampled)

Background subtracted skymap (Crab-Nebula)

Skymap (bg-subtracted and normalized)

(a) (b)

(c) (d)

Figure B.3: New experimental method extracting energy spectra from skymaps: In a first step the oversampled background estimation (b) is scaled to match the raw on-skymap (a) within user defined regions with no expected signal (red circles in d). The scaled background map is then subtracted bin-wise from the on-skymap. The on-skymap is then divided by the normalized background map, correcting for inhomogeneities of the camera acceptance. A scaled version of a background subtracted Crab Nebula skymap (c) can be used as template for subtracting point-sources. Finally, user defined shapes (green ellipse in d) can be used for extracting an acceptance corrected number of excess events from the skymap (d). For the GCA SED the contribution of a point source at the coordinates of SgrA* has been subtracted.

C

CRAB CROSS-CHECK ANALYSIS

In order to justify the quality selection and data analysis parameters used for the GC, they were tested on Crab Nebula data. The Crab sample was recorded during about the same period (spring 2013/14), also at very high zenith distance (VHZD).

C.1 THE CRAB DATA SAMPLE

The Crab Nebula has been observed at very large zenith distance in the beginning of the years 2013 and 2014. These observations were conducted for two reasons. First, in order to cross-check the GC data analysis with a known source observed with similar conditions. Second, for studying the high energy part of the Crab Nebula spectrum, as well as searching for possible variability.

C.1.1 *2013 data sample and quality*

The observation dates and times during the 2013 campaign can be found in table[1] C.1. The whole sample contains about 10 h of good quality data. Data selection was performed with the same cuts that were then for the GC data. LIDAR measurements were evaluated on the relevant days, showing a very good overall picture of the atmosphere during the observations. LIDAR data could neither be used systematically for data selection nor for corrections. For part of the data, the LIDAR was not ready for that task yet and more importantly for observations beyond 60 ° Zd the LIDAR cannot properly track the telescopes.

obs. day	eff. time	obs. day	eff. time	obs. day	eff. time
2013-01-09	0.77 h	2013-01-18	0.85 h	2013-02-08	0.76 h
2013-02-09	0.71 h	2013-02-10	0.84 h	2013-02-11	0.81 h
2013-02-12	0.17 h	2013-02-13	0.56 h	2013-02-14	0.24 h
2013-02-16	0.30 h	2013-03-09	0.73 h	2013-03-10	0.09 h
2013-03-11	0.78 h	2013-03-12	0.49 h	2013-12-30	0.60 h
total	10 h				

Table C.1: Remaining observation days/time after quality cuts for the 2013 observations of the Crab Nebula.

obs. day	eff. time	obs. day	eff. time	obs. day	eff. time
2014-01-01	0.37 h	2014-01-02	0.83 h	2014-01-03	0.90 h
2014-01-04	0.69 h	2014-01-05	0.90 h	2014-01-06	0.90 h
2014-01-07	0.72 h	2014-02-03	0.85 h	2014-02-04	0.79 h
2014-02-06	0.93 h	2014-03-28	0.86 h	2014-04-03	0.87 h
2014-04-23	0.78 h	2014-04-25	0.36 h	2014-04-26	0.57 h
total	11 h				

Table C.2: Remaining observation days/time after quality cuts for the 2014 observations of the Crab Nebula.

	RA [°]	Dec [°]	δRA [°]	δDec [°]	offset [°]
Crab Nebula	83.6334	22.0144	0.0000	0.0000	0.0000 ± 0.0000
($E > 500\,\mathrm{GeV}$)	83.6202	22.0065	-0.0132	-0.0080	0.0145 ± 0.0011
($E > 1\,\mathrm{TeV}$)	83.6219	22.0043	-0.0115	-0.0102	0.0147 ± 0.0010
($E > 2\,\mathrm{TeV}$)	83.6217	22.0008	-0.0117	-0.0136	0.0174 ± 0.0012
($E > 3\,\mathrm{TeV}$)	83.6231	22.0015	-0.0103	-0.0130	0.0161 ± 0.0015
($E > 5\,\mathrm{TeV}$)	83.6237	22.0066	-0.0097	-0.0078	0.0119 ± 0.0020
($E > 10\,\mathrm{TeV}$)	83.6169	21.9936	-0.0165	-0.0208	0.0258 ± 0.0026

Table C.3: Position fit results of the signal centroid in the Crab Nebula skymaps with different energy thresholds. The central 0.15 ° radius has been fitted with a 2D Gaussian in order to determine the location of the γ-ray emission.

C.1.2 *2014 data sample and quality*

Table C.2 shows a summary of all observations conducted in 2014. The size of the sample is about 11 h after quality cuts. Similarly to 2013 data, all cuts are the same as for the GC. Again, LIDAR data on the relevant days shows a very clear atmosphere for a dominating fraction of the observations.

C.2 SOURCE DETECTION PLOTS

The θ^2 plots presented in figure C.1 are for the whole 2013/14 sample. The cuts in Odie are the same as for the GC analysis. As for the rest of the analysis, the same random forests and the same MC events have been used.

C.3 SKYMAPS

As for the GC, six different energy cuts were used for making skymaps of the Crab Nebula observed at VHZD. Test statistic or "significance" maps can be found in figure C.2 and the relative flux map is shown in figure C.4. The signal in the skymaps is slightly offset from the expected source coordinates and shows elongation in one direction. The strong asymmetry can be probably explained by the wobble mode with which the Crab Nebula has been observed.

---

[1] The last day in 2013 is actually already belonging to the 2014 campaign.

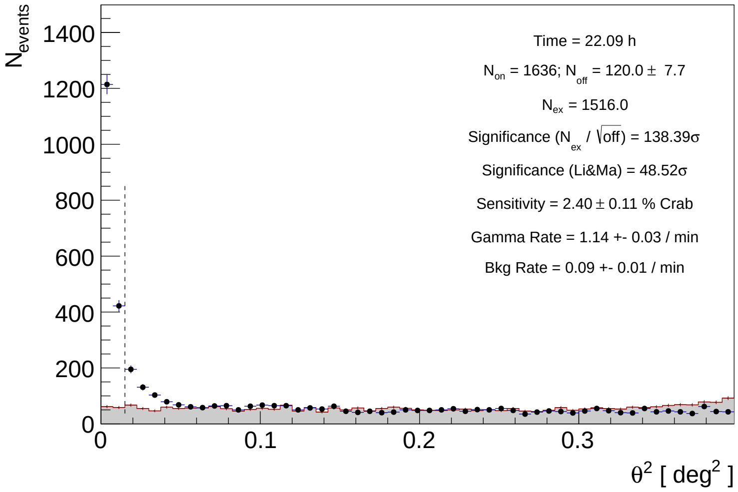

(a)

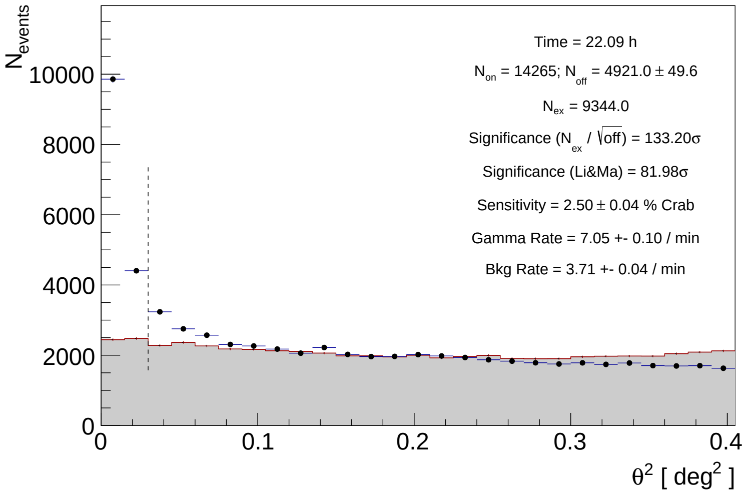

(b)

Figure C.1: Detection (θ^2) plots for the VHZD Crab Nebula observations in spring 2013 and 2014. The detection plots were made with different sets of cuts, optimized for maximum sensitivity over the full spectral range (a) and optimized for best sensitivity close to the energy threshold (b). The on-source histogram is displayed as data-points only, while the background histogram is displayed with data-points and gray bars.

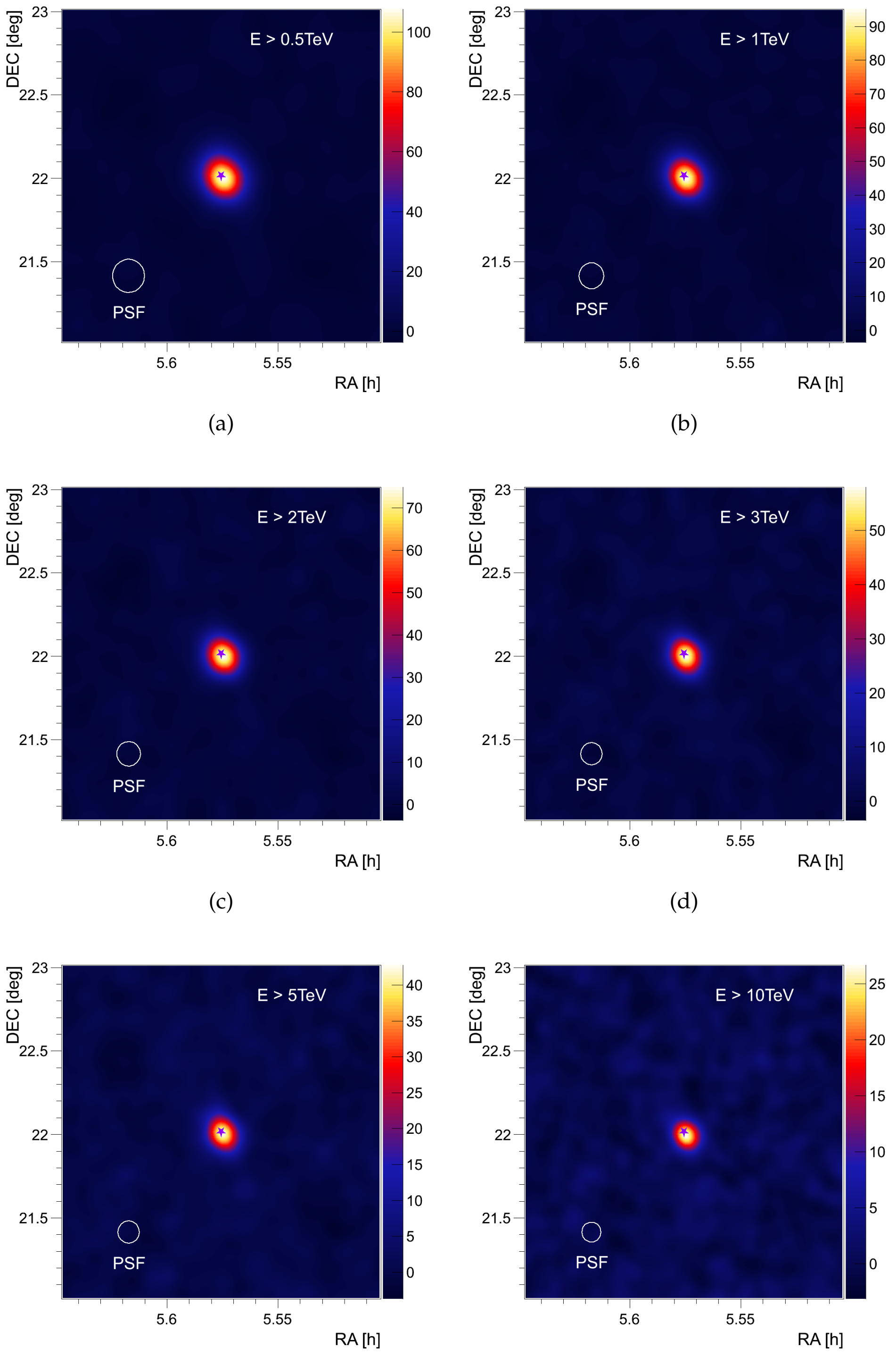

(a) (b)

(c) (d)

(e) (f)

Figure C.2: Test statistic (TS)-value maps of $2^\circ \times 2^\circ$ around the Crab Nebula for different energy thresholds. The TS value can be interpreted as a local significance of the smeared γ-ray excess, assuming a Gaussian distribution of the background. The star symbol marks the expected source coordinates.

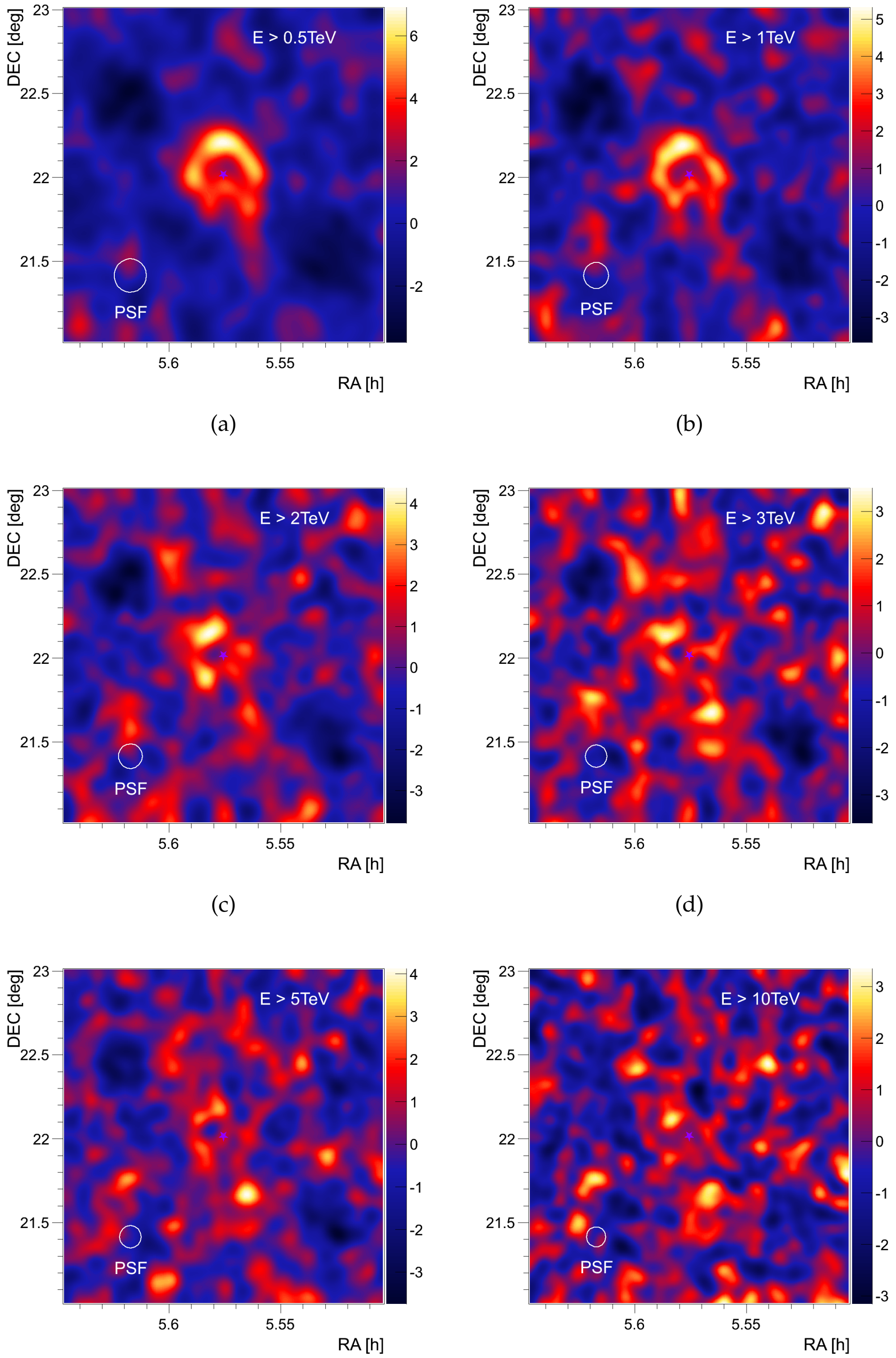

(a) (b) (c) (d) (e) (f)

Figure C.3: Test statistic (TS)-value maps of 2° × 2° around the Crab Nebula for different energy thresholds. A point source located at the coordinates marked with a star has been subtracted from the skymap. The skymap shows residuals due to the not perfectly Gaussian PSF of the instrument.

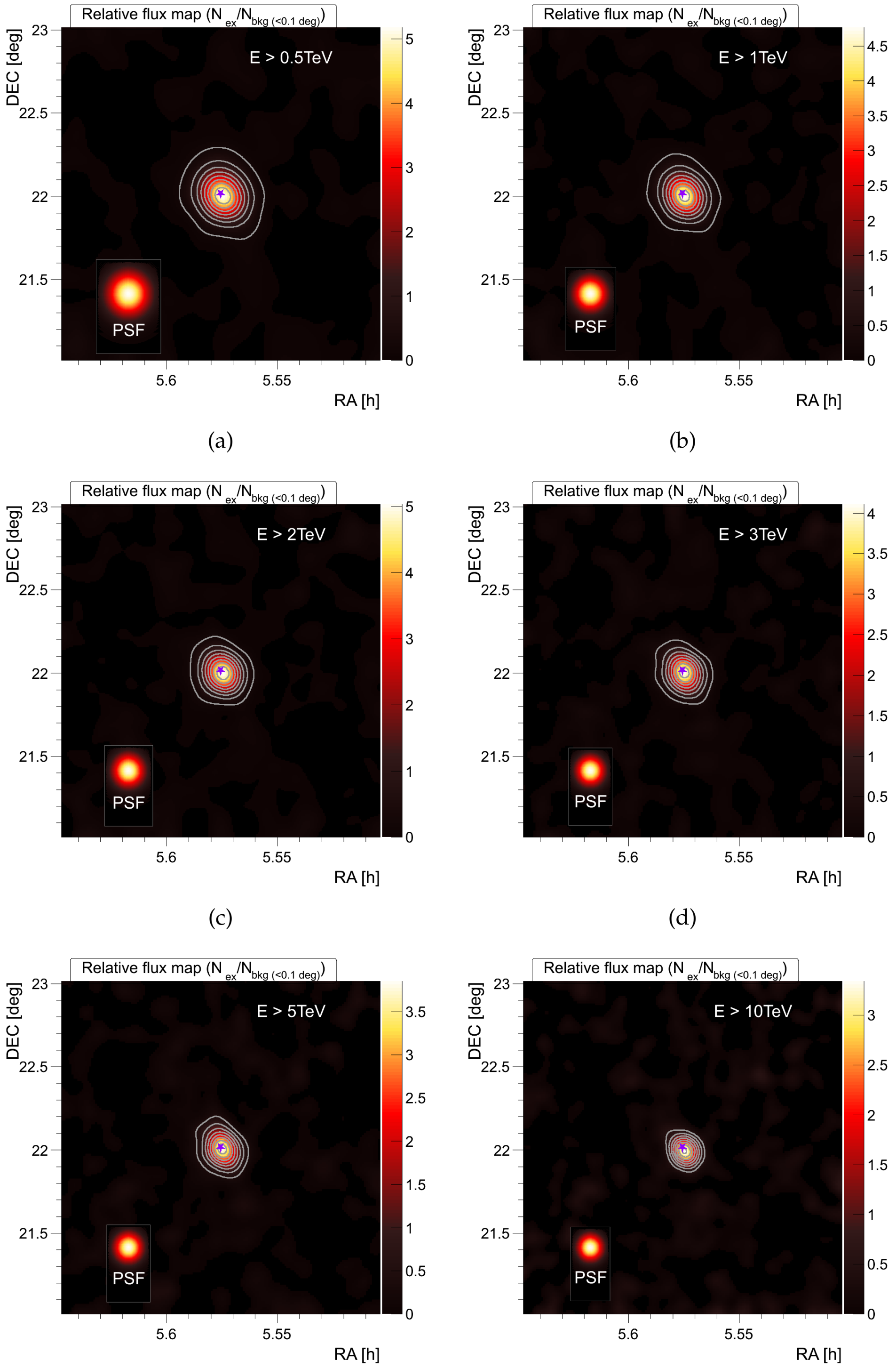

(a) (b)

(c) (d)

(e) (f)

Figure C.4: Relative flux maps of the 2 ° × 2 ° around the Crab Nebula for different energy thresholds. The relative flux is the smeared excess map divided by the background map. The gray contours indicate the local significance of the excess starting from 5σ.

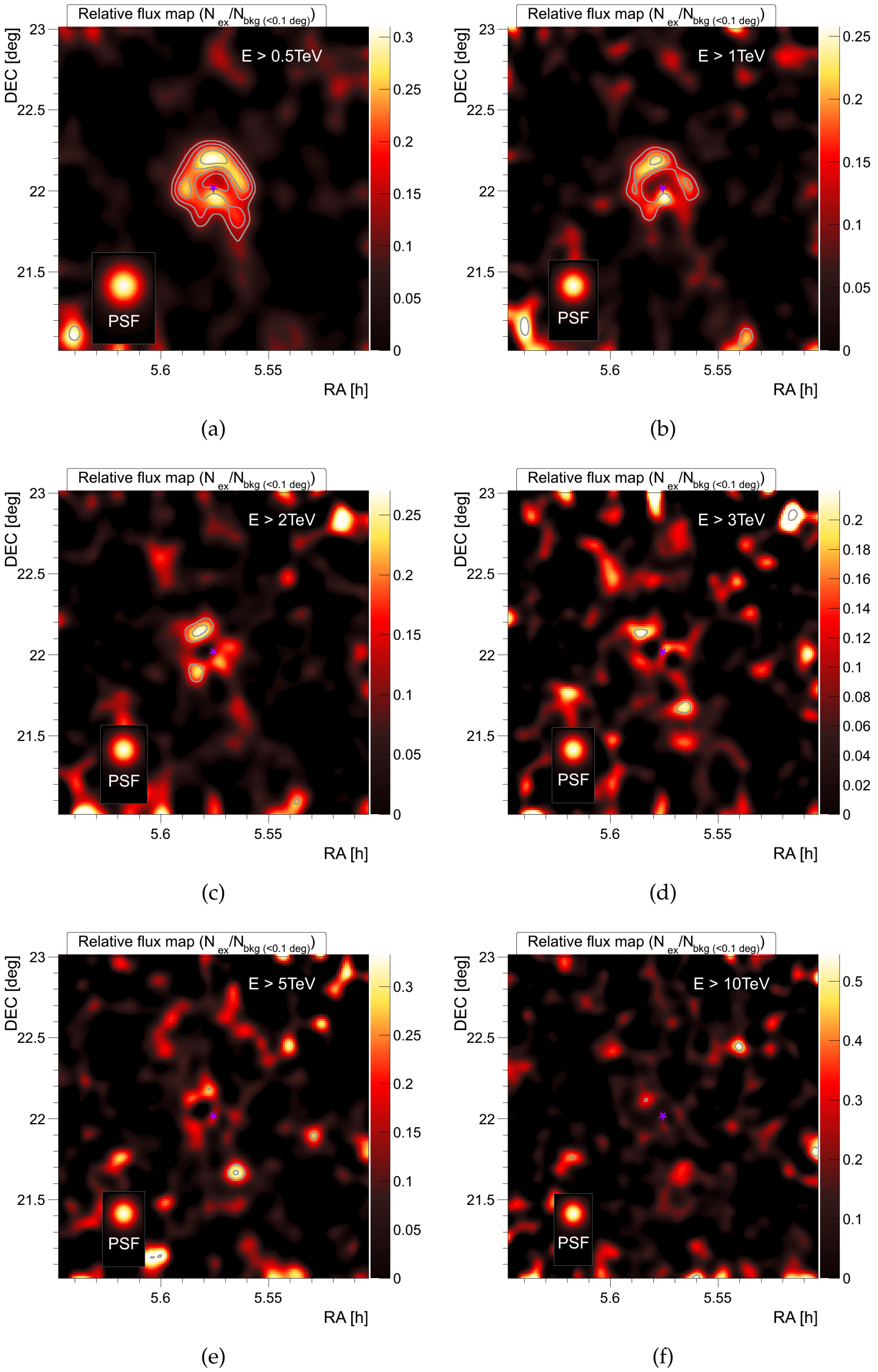

(a) (b)

(c) (d)

(e) (f)

Figure C.5: Relative flux maps of the 2° × 2° around the Crab Nebula for different energy thresholds. A point source located at the coordinates marked with a star has been subtracted from the skymap. The skymap shows residuals due to the not perfectly Gaussian PSF of the instrument.

In order to avoid a bright star (ζ Tauri) in the FoV, in contrast to most sources, the Crab Nebula is usually observed with only two instead of four symmetric wobble positions. The offset of the centroid of the signal in respect to the expected coordinates could be an effect of the large zenith distance.

The signal has been fitted with a 2D Gaussian. The offsets of the fits from the observed coordinates for the single energy ranges is listed in table C.3. The measured offset is covered by the typical systematic uncertainty on the reconstructed source position ($\lesssim 0.02\,^{\circ}$, see 3.2.5).

The fitted Gaussian has been removed from the skymaps (see figure C.3 and C.5). One can compare this test to the point source subtraction in the case of the GC. As for the GC, not all of the signal gets removed from the skymap, especially at lower energies. This is due to the none Gaussian shape of the real PFS of the Instrument. Still, the remnant is much smaller and much more symmetric compared to the residual skymap of the GC.

C.4 ENERGY SPECTRUM AND SED

The differential energy spectrum of the Crab Nebula was fitted with a single log-parabola function,

$$\frac{\mathrm{d}F}{\mathrm{d}E} = f_0 \cdot \left(\frac{E}{1\,\mathrm{TeV}}\right)^{\alpha+\beta\,\log\left(\frac{E}{1\,\mathrm{TeV}}\right)} \quad . \tag{C.4.1}$$

The parameter results can be found in table C.4. In contrast to observations with lower energy threshold, the curvature is negligible within errors. Unfolded energy spectra of the Crab Nebula for the integration radii $0.1\,^{\circ}$, $0.2\,^{\circ}$ and $0.4\,^{\circ}$ observed at VHZD can be found in figures C.6 and C.7. The SED representations of those spectra are shown in figures C.8 and C.9. Table C.5 shows the integral flux for $E > 1\,\mathrm{TeV}$ and the three different integration radii.

In figures C.7 and C.9 also three different previously published spectral shapes of the Crab Nebula are shown for comparison. For the lower energy part of the spectra ($E > 10\,\mathrm{TeV}$) the agreement with the most recently published MAGIC spectrum (Aleksić et al., 2014), as well as with the H.E.S.S. spectrum (Aharonian et al., 2006c) is good. Above 10 TeV, the VHZD spectrum seems too hard and does not show enough curvature, as in the MAGIC spectrum or even a cut-off as suggested by the H.E.S.S. measurements. However, very recent H.E.S.S. publication by Abramowski et al. (2014), about observations, which were conducted in about the same time period (March 2013) as the MAGIC VHZD observations, show a very similar spectrum of the highest energies like the one presented in this work. It can thus not be excluded that the observed hardening of the Crab Nebula spectrum is actually a real physical rather than systematic effect.

Another important observation that can be made from the Crab Nebula data in comparison to the GC SEDs are the relatively small flux differences

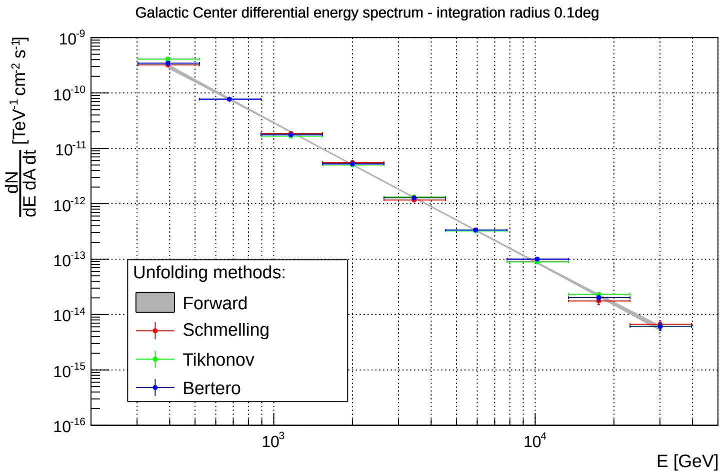

(a)

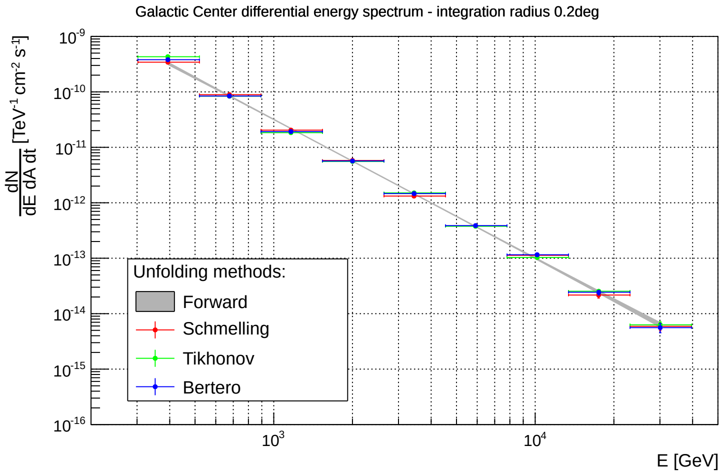

(b)

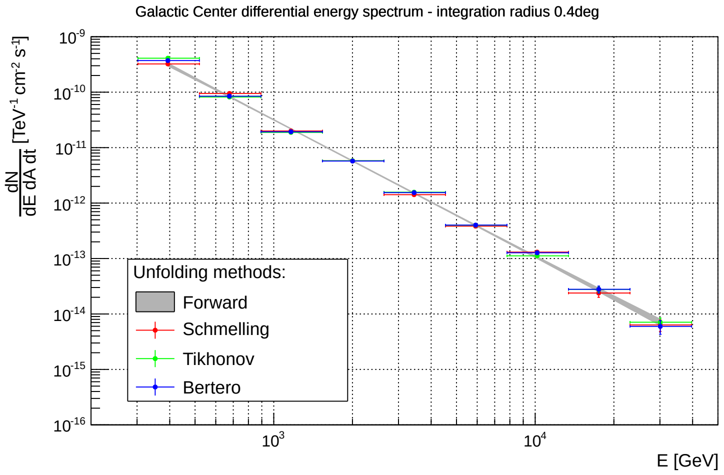

(c)

Figure C.6: Differential energy spectra for three different integration radii (0.1 ° (a), 0.2 ° (b) and 0.4 ° (c)) around the Crab Nebula. The plots are showing spectra unfolded with three different algorithms (datapoints: Bertero, Schmelling, Tikhonov) and the result of the forward folding method using a log-parabola as assumed spectrum (shaded uncertainty area).

integration radius 0.1 °

unfolding method	f_0 [cm$^{-2}s^{-1}$TeV^{-1}]	α	β	χ^2/n.d.f
Bertero	$(6.07 \pm 0.59) \cdot 10^{-10}$	-2.57 ± 0.09	0.04 ± 0.04	15.5/6
Forward	$(6.02 \pm 0.75) \cdot 10^{-10}$	-2.53 ± 0.12	0.01 ± 0.06	—
Schmelling	$(6.21 \pm 0.52) \cdot 10^{-10}$	-2.56 ± 0.08	0.02 ± 0.04	11.7/6
Tikhonov	$(6.07 \pm 0.59) \cdot 10^{-10}$	-2.57 ± 0.09	0.04 ± 0.04	19.0/6

integration radius 0.2 °

unfolding method	f_0 [cm$^{-2}s^{-1}$TeV^{-1}]	α	β	χ^2/n.d.f
Bertero	$(6.47 \pm 0.54) \cdot 10^{-10}$	-2.54 ± 0.08	0.04 ± 0.04	19.8/6
Forward	$(6.38 \pm 0.66) \cdot 10^{-10}$	-2.49 ± 0.10	0.00 ± 0.03	—
Schmelling	$(6.76 \pm 0.45) \cdot 10^{-10}$	-2.55 ± 0.07	0.02 ± 0.03	12.8/6
Tikhonov	$(6.85 \pm 0.70) \cdot 10^{-10}$	-2.60 ± 0.11	0.06 ± 0.05	25.4/6

integration radius 0.4 °

unfolding method	f_0 [cm$^{-2}s^{-1}$TeV^{-1}]	α	β	χ^2/n.d.f
Bertero	$(6.53 \pm 0.65) \cdot 10^{-10}$	-2.56 ± 0.10	0.06 ± 0.05	14.8/6
Forward	$(6.12 \pm 0.73) \cdot 10^{-10}$	-2.46 ± 0.13	0.00 ± 0.07	—
Schmelling	$(6.68 \pm 0.49) \cdot 10^{-10}$	-2.55 ± 0.08	0.04 ± 0.04	15.0/6
Tikhonov	$(6.68 \pm 0.79) \cdot 10^{-10}$	-2.57 ± 0.13	0.06 ± 0.06	13.9/6

Table C.4: Parameter results of the correlated fits to the VHZD Crab Nebula energy spectra for three different integration radii and 3 different unfolding methods plus forward folding. The fitted function is always a log-parabola. The flux normalization is at 1 TeV.

int. radius	$F_{E>1\mathrm{TeV}}$ [cm^{-}2 s^{-}1]	ΔF [cm^{-}2 s^{-}1]	$F_{E>1\mathrm{TeV}}/F_{E>1\mathrm{TeV},\,0.1\,^\circ}$
0.1 °	$2.093 \cdot 10^{-11}$	$0.038 \cdot 10^{-11}$	1.000
0.2 °	$2.273 \cdot 10^{-11}$	$0.037 \cdot 10^{-11}$	1.086
0.4 °	$2.318 \cdot 10^{-11}$	$0.050 \cdot 10^{-11}$	1.108

Table C.5: Integral flux ($E > 1$ TeV) from HZD Crab Nebula observations for the three different integration radii (0.1 °, 0.2 ° and 0.4 °).

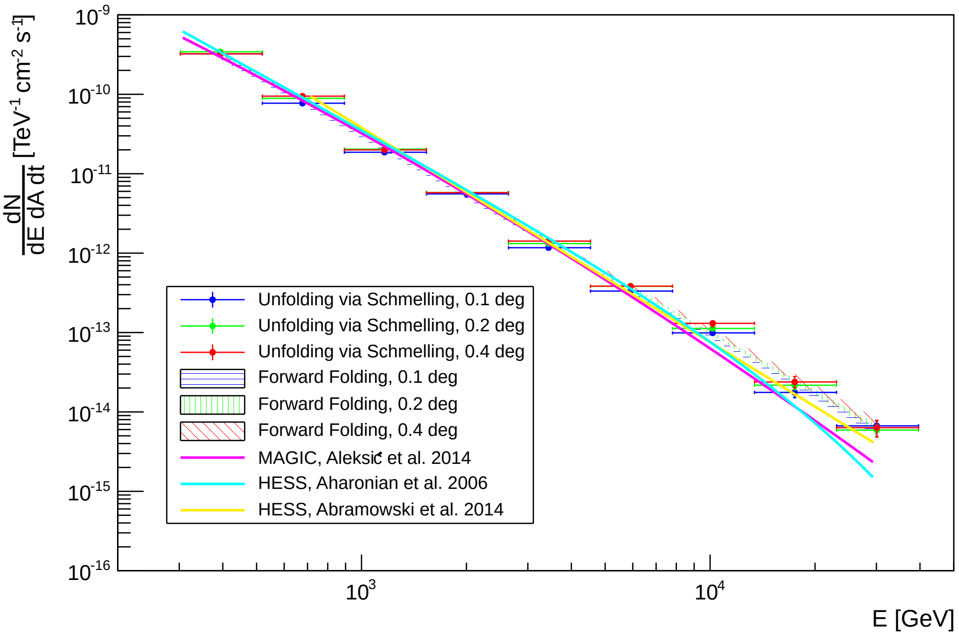

Figure C.7: Differential energy spectra for different integration radii in one plot. The data-points are for the Schmelling unfolding method and the shaded regions correspond to the uncertainty areas of the forward folding method.

in-between the different integration radii. The flux from the GC increases by about a factor two when integrating 0.4 ° instead of 0.1 ° around the source. In case of the Crab Nebula data, this increase is only 11%, most of it happening when going from 0.1 ° to 0.2 °, where the change in the collection efficiency is still large. This means that there is a small systematic miss-match between real and MC-events, concerning the reconstruction of the direction of origin. This miss-match does by far not explain the observed extension of the GC source, which can therefore be considered as physical.

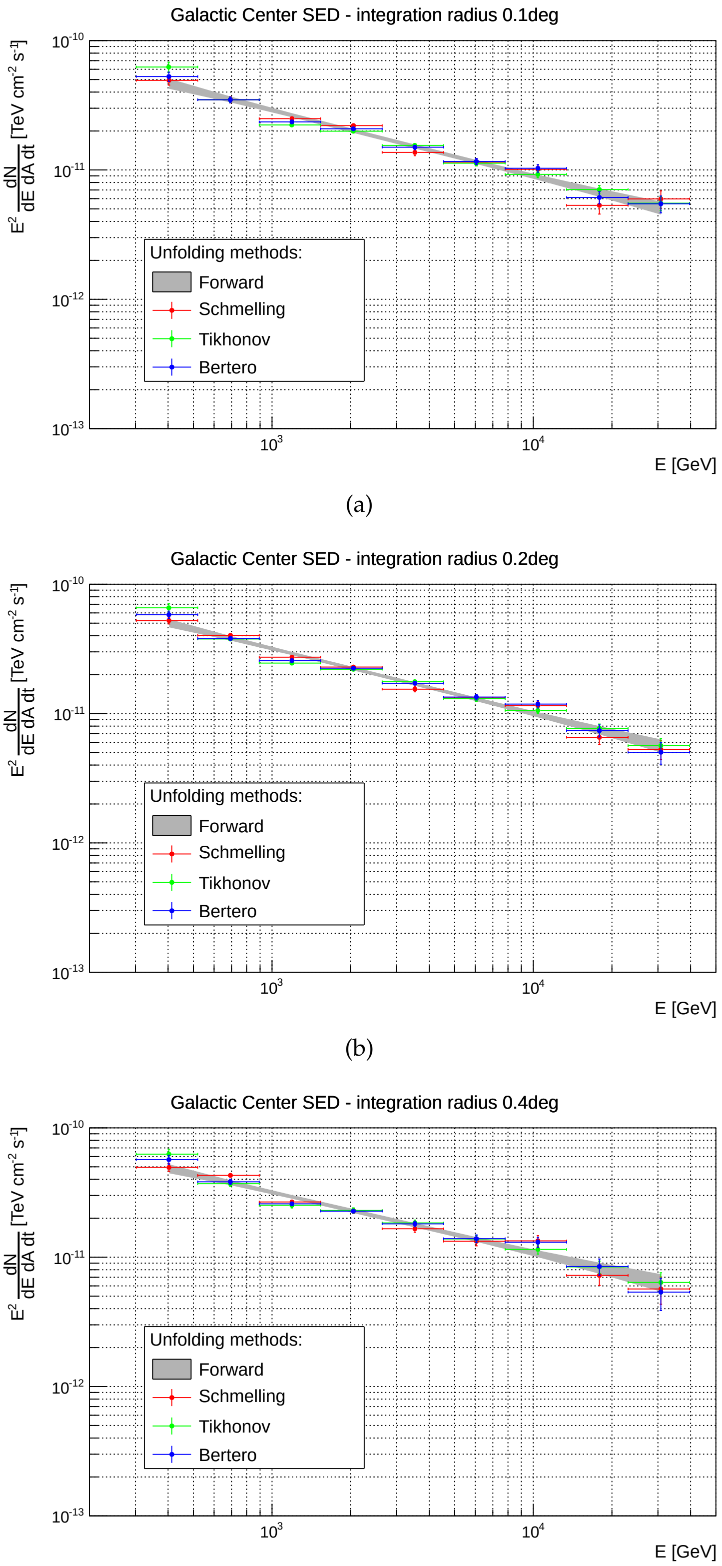

(a)

(b)

(c)

Figure C.8: Crab Nebula SEDs for three different integration radii (0.1 ° (a), 0.2 ° (b) and 0.4 ° (c)) and three different unfolding methods (datapoints: Bertero, Schmelling, Tikhonov) plus the result of the forward folding method using a power-law with exponential cut-off as assumed spectrum (shaded uncertainty area).

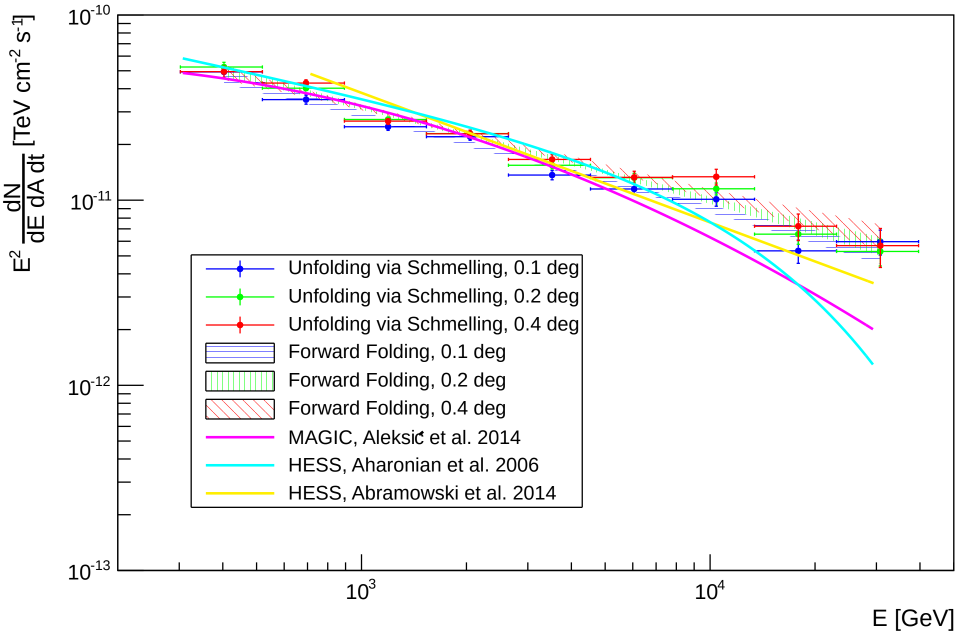

Figure C.9: Crab Nebula SEDs for the three different integration radii in one diagram. The data-points were obtained using the Schmelling unfolding algorithm and the shaded regions correspond to the uncertainty area of the forward folding method, using a log-parabola as spectral assumption.

D

DATA ANALYSIS TOOLS OF MAGIC

In this chapter I will explain some of the final analysis steps for MAGIC data in more detail. This is to motivate the analysis techniques that were used for obtaining the results, which are presented in the two main parts of this thesis.

D.1 SOURCE DETECTION

In the MAGIC data analysis framework MARS, for probing the excess from a given position in the sky and calculating its significance, the program Odie is used. The program produces two histograms in θ^2, one with respect to the source position (on) and one with respect to the background positions (off). θ^2 is the squared angular distance with respect to certain sky coordinates. The sky coordinates which contain the other wobble positions, other than the one containing the source, are used for the background histogram. The data filled into the histograms have usually been reduced by applying γ-hadron separation cuts, in order to strongly suppress the background. One expects the θ^2 histogram of the on-position to be peaked around zero if there is a γ-ray signal from the source candidate. The off-histogram on the other hand is expected to be comparably flat (see figure D.1).

The same cut in θ^2 is now applied to the on- and to the off-histogram and defines the number of events in the on-source N_{on} and in the corresponding off-source N_{off} region. The significance of the excess can be calculated using equation 17 in Li & Ma (1983).

$$\sigma = \sqrt{2}\sqrt{N_{\text{on}}\,\ln\left(\frac{1+\alpha}{\alpha}\,\frac{N_{\text{on}}}{N_{\text{on}}+N_{\text{off}}}\right)+N_{\text{off}}\,\ln\left((1+\alpha)\,\frac{N_{\text{off}}}{N_{\text{on}}+N_{\text{off}}}\right)}. \qquad \text{(D.1.1)}$$

α is the oversampling ratio of the off-histogram e.g. how many symmetric positions w.r.t. the camera center were used for the off-histogram.

D.2 SKYMAPS

Within MARS, a program called Caspar is used for producing skymaps of γ-ray sources. Very generally, a skymap is produced by filling pre-selected events into a 2D sky coordinates (RA, Dec) histogram. The resulting skymap, also called exposure map, contains γ-ray events as well as hadronic events that passed the γ-hadron separation as well as other cuts. In order to separate the γ-ray excess from the hadronic background one needs to find a background model for the observations.

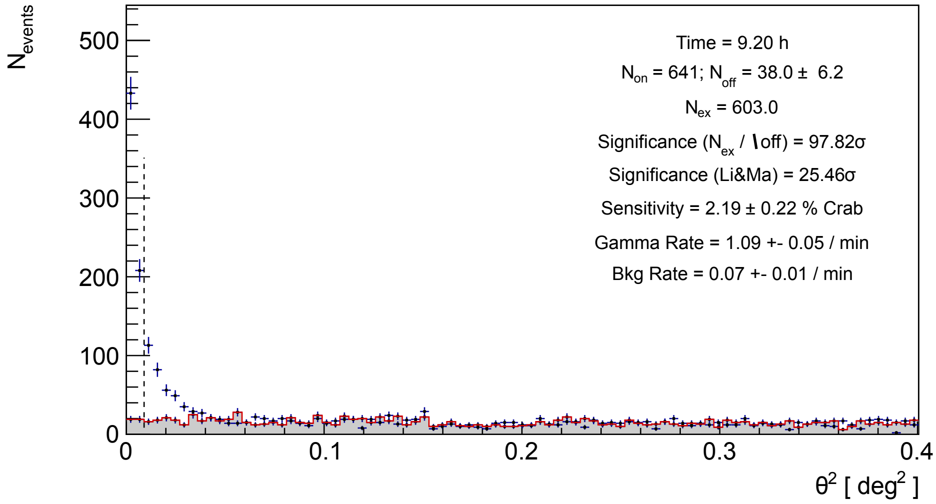

Figure D.1: θ^2-histogram of the Crab Nebula. The gray bars represent the background (off) histogram. The dashed line marks the θ^2 cut which was used to determine the significance or 25σ according to equation D.1.1.

In Caspar there are two methods available for performing this task: blind map and the wobble map. Both methods make use of the fact that each position in the sky has been observed with different parts of the camera due to the wobble observation scheme.

For the wobble map, it is assumed, that any signal from the source is coming from one half of the camera only, while the other half contains only background. In this case the background is estimated by sampling the off-side, in camera coordinates, of the exposure map.

In case when the observed source extends beyond the central 0.4° circle or the extension is unknown, the blind map option has to be used. Here the background in camera coordinates is obtained by sampling the whole exposure map always for two different wobble positions and selecting the lower value. By doing this one systematically underestimates the background by

$$\Delta = -\frac{\sigma}{\sqrt{\pi}}, \tag{D.2.1}$$

assuming that both values are following the same normal distribution with standard deviation σ. The background model for the camera is obtained by correcting for this bias.

The background model for the observations is obtained by applying the camera background model to the actual exposure during the observations. From this background model, for each event in the exposure map, 200 background events are generated randomly. The actual background map is obtained by normalization to the exposure map. The difference between expo-

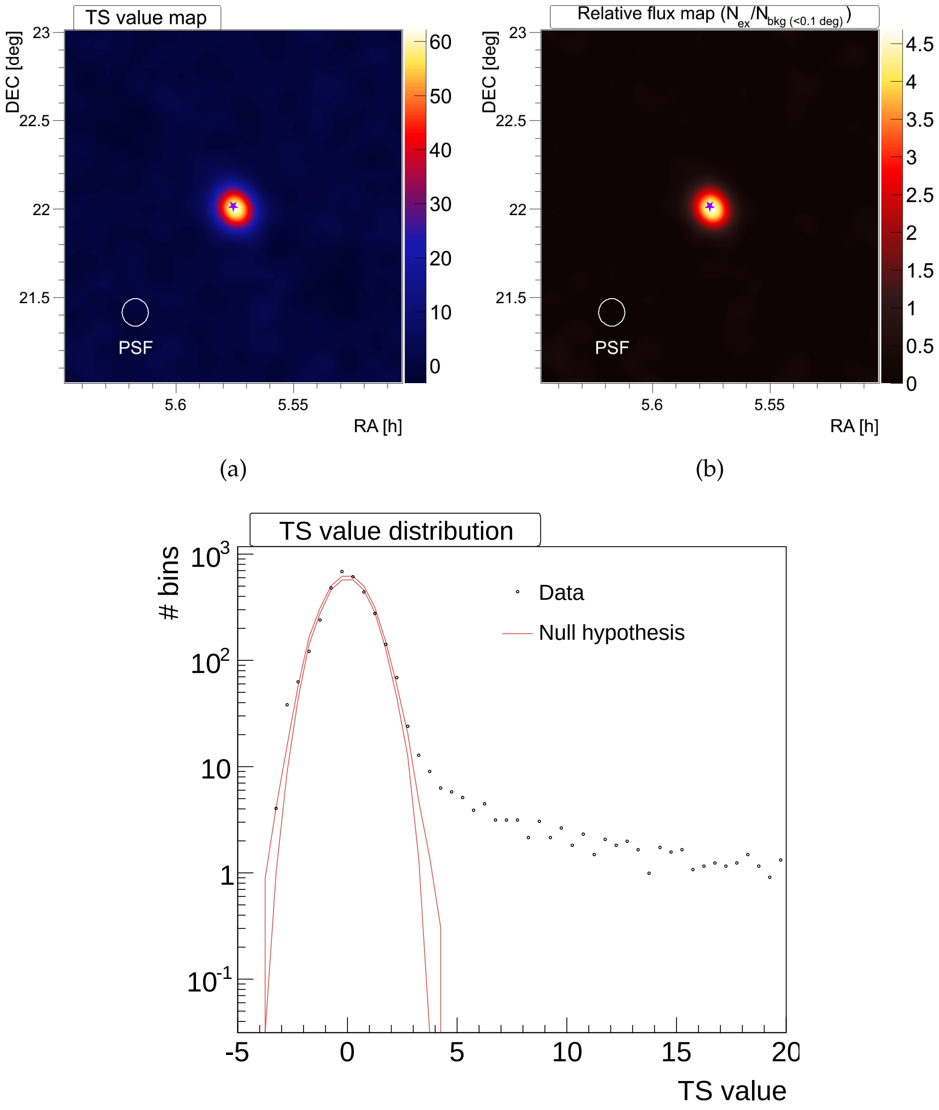

(a)

(b)

(c)

Figure D.2: Skymaps of the Crab Nebula produced with Caspar. (a) shows the TS-value map, (b) shows the relative flux map and (c) shows the test statistic histogram. The few bins on the right, well above the null-hypothesis correspond to the excess form the Crab Nebula in the center of the skymaps.

sure map and background map leads to the excess map. The excess map is smeared with a Gaussian kernel, similar to the PSF of the instrument, in order to reduce noise in case of low statistics within single bins.

From the smeared skymap a test statistic (TS) value is calculated using equation D.1.1 (Li & Ma, 1983), α being 200 (the oversampling of the background map). This TS value has similar meaning as the commonly used (local) significance. But due to the strong oversampling and the non perfect Gaussian shape of the test statistic, its absolute value is not 100% reliable and tends to slightly overestimate significances (see figure D.2 (c)).

In addition to the TS value map (figure D.2 (a)), also a relative flux map (figure D.2 (b)) is generated. This is the ratio between the exposure map and the background map.

$$N_{\text{rel.flux}} = -\frac{N_{\text{exposure}}}{N_{\text{background}}}, \tag{D.2.2}$$

This map is useful for studying the morphology of extended sources, since it cancels out the differences in exposure of different regions in the sky. Caspar does also allow for the subtraction of a point source from the skymap. This is done by subtracting a Gaussian with σ_{map}, the effective PSF of the skymap

$$\sigma_{\text{map}} = \sqrt{\sigma^2_{\text{instr.}} + \sigma^2_{\text{smear.}}}\,. \tag{D.2.3}$$

D.3 ENERGY SPECTRA AND LIGHT-CURVES

In MARS the program Flute serves for calculating differential energy spectra, spectral energy distributions (SED) and light-curves. In order to calculate the physical γ-ray flux

$$F = \frac{N}{T_{\text{eff}}\,A_{\text{eff}}} \tag{D.3.1}$$

it is necessary to determine the effective observation time T_{eff} and the effective collection area A_{eff}. The observation time is relatively easy to determine, but one has to take into account the dead time introduced by the readout system ($26 \cdot 10^{-6}$ s for the new DRS4 chip) per event. The collection area on the other hand is not so easy to calculate. It is strongly energy dependent, especially close to the trigger threshold. It also depends on the cuts, both in θ^2 and in hadronnes and therefore has to be determined using MC simulations in a dedicated way for each data set and set of cuts (see figure D.3). The cuts in θ^2 and hadronnes can be requested from Flute to be defined in an automatic way. Therefore a target survival probability for MC-γs is defined and the cuts are tuned by Flute in order to match that probability for each energy bin.

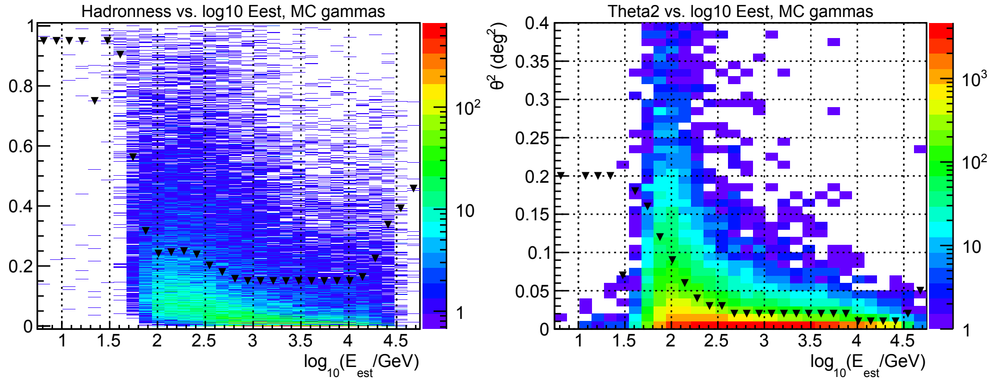

(a)

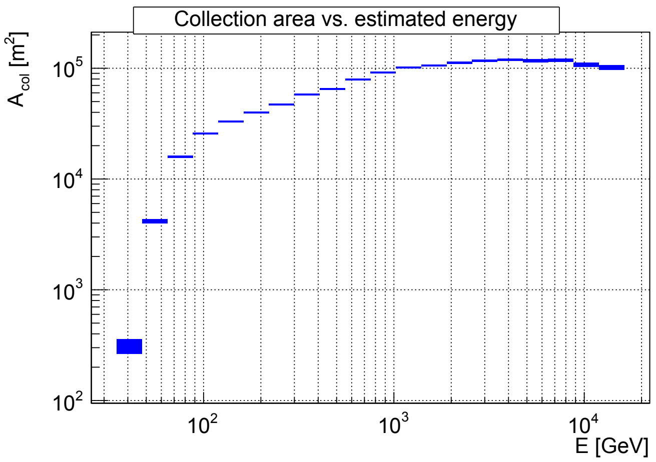

(b)

Figure D.3: Hadronness and θ^2 distributions for MC-events binned in energy. The black triangles indicate the corresponding cuts (a). The effective collection area for each energy bin using these cuts is shown in (b).

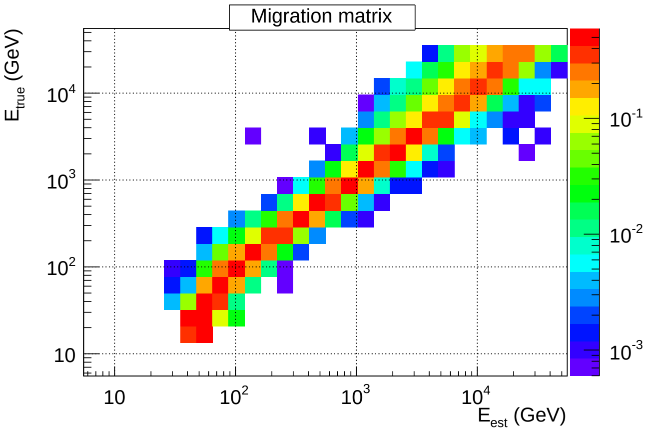

Figure D.4: Typical energy migration matrix for MAGIC observations at low zenith distance. The migration matrix has been determined from MC-simulated events by the program Flute. The assumption behind this method is that the MC simulation is reproducing the real instrument response with reasonable precision.

Using the effective collection area of the observation, Flute calculates the differential energy spectrum, which defined as

$$\frac{\mathrm{d}F}{\mathrm{d}E} = \frac{\mathrm{d}N}{\mathrm{d}E\, T_{\mathrm{eff}}\, A_{\mathrm{eff}}}, \tag{D.3.2}$$

and the SED, defined as

$$E^2 \frac{\mathrm{d}F}{\mathrm{d}E} = E^2 \frac{\mathrm{d}N}{\mathrm{d}E\, T_{\mathrm{eff}}\, A_{\mathrm{eff}}}. \tag{D.3.3}$$

The SED is a measure for the power emitted per logarithmic bandwidth. This means that the SED is always comparing fluxes in intervals with the same $\Delta E_\gamma / E_\gamma$.

Apart from spectra and SEDs, Flute can also be used for calculating lightcurves for γ-ray emission above a certain energy threshold. Therefore the effective on-time and collection area calculation needs to be done for each time bin separately in order to calculate the integral flux for each bin.

D.4 SPECTRAL DECONVOLUTION

In general, the energy spectra obtained in the way, which is described above are correlated to the true energy spectrum of the observed object by convolution of the true event distribution with the instrument response function or migration matrix $M_{\mathrm{mig}}(E_{\mathrm{true}}, E_{\mathrm{est}})$ (see figure D.4 for a discrete real data example).

$$\left(\frac{\mathrm{d}N}{\mathrm{d}E_{\mathrm{est}}}\right)_{\mathrm{obs}} = M_{\mathrm{mig}}(E_{\mathrm{true}}, E_{\mathrm{est}}) \otimes \left(\frac{\mathrm{d}N}{\mathrm{d}E_{\mathrm{true}}}\right)_{\mathrm{true}} . \tag{D.4.1}$$

The true event distribution and therefore energy spectrum can be recovered if $M^{-1}_{\mathrm{mig}}(E_{\mathrm{est}}, E_{\mathrm{true}})$, the inverse of M_{mig} exists and is known.

$$\left(\frac{\mathrm{d}N}{\mathrm{d}E_{\mathrm{true}}}\right)_{\mathrm{true}} = M^{-1}_{\mathrm{mig}}(E_{\mathrm{est}}, E_{\mathrm{true}}) \otimes \left(\frac{\mathrm{d}N}{\mathrm{d}E_{\mathrm{est}}}\right)_{\mathrm{obs}} . \tag{D.4.2}$$

In practice, there is usually no analytic solution to the matrix inversion problem. It is however possible to solve the problem for the event distribution in true energy via minimization and regularization (Albert et al., 2007).

Inside the MARS framework there is a ROOT macro containing some tools (see Albert et al., 2007, for details) for spectral deconvolution or unfolding called "CombUnfold.C". This macro allows for unfolding spectra using the algorithms of Bertero (1989), Schmelling (1998) and Tikhonov & Arsenin (1977), as well as the forward folding method. The forward folding method uses a parametric function for describing the unfolded spectrum. The parameters are varied and the energy migration matrix is applied to the spectral assumption, trying to minimize the difference between the folded spectrum and the observed spectrum.

The unfolding methods by Bertero (1989), Schmelling (1998) and Tikhonov & Arsenin (1977) mainly differ in the way, the regularization is performed. The use of more than one such algorithm on the same data set serves as a kind of cross-check, in order to avoid a wrong spectral reconstruction in case one algorithm fails for the given set of parameters.

E

F-FACTOR METHOD FOR PMT CHARGE CALIBRATION

The F-factor of a photo detector can be understood as spoiling factor of width of the charge distribution at the output when illuminated by a Poissonian process like for example a pulsed laser. It originates from the additional statistical uncertainty coming from the charge multiplication mechanism of a light detector. This additional uncertainty results in a broader charge distribution compared to the Poisson distribution from photon statistics. The F-factor method allows to calculate the charge gain of a light sensor, assuming that the F-factor of this sensor is known. A very comprehensive description can be found in Mirzoyan & Lorenz (1997); Mirzoyan (2000).

The relative width of the charge distribution of a PMT, which is illuminated by a pulsed light source, such that it on average produces $\overline{N_{\mathrm{phe}}}$ photoelectrons is – for $\overline{N_{\mathrm{phe}}} \gtrapprox 10$ (Gaussian approximation) – given by

$$\frac{\sigma_Q}{\overline{Q}} = \frac{1}{\sqrt{\overline{N_{\mathrm{phe}}}}} \cdot F\,. \tag{E.0.3}$$

$\overline{Q}$ and σ_Q are the mean value and the standard deviation of the output charge of the PMT respectively. F is the F-factor, which is defined in terms of

$$F = \sqrt{(1 + \frac{\mathrm{Var}(G)}{\overline{G}^2})}\,, \tag{E.0.4}$$

where G is the gain of the PMT. Given a pulsed illumination of the PMT with unknown gain but known F, the average number of detected photoelectrons can always be calculated as

$$\overline{N_{\mathrm{phe}}} = \left(2\,\sqrt{2\,\ln(2)}) \cdot F \cdot \frac{FWHM}{\overline{Q}}\right)^2\,, \tag{E.0.5}$$

under the assumption that $\overline{N_{\mathrm{phe}}}$ is large enough to approximate $p(Q)$ with a Gauss-like distribution.

F

SIMPLE 1D AIR-SHOWER SIMULATION

For studying some aspect of the LIDAR energy corrections (chapter 7) it was more convenient to use a simple 1D MC approach than using a full-scale MC setup, like it is provided by CORSIKA (Heck et al., 1998). Such simulations can be adapted and run very fast and contain information about the longitudinal structure of air-showers with reasonable accuracy (see also Matthews, 2005).

The main questions to be studied for the LIDAR corrections were the following: How well can an extensive air-shower be approximated with a Gaussian profile? What is the typical energy dependent width of this profile? The model, which was applied here is similar to the Heitler model (Heitler, 1954), but with some modifications making it slightly more realistic. It makes the following assumptions:

- The electromagnetic air-shower will produce secondaries until a last step with N particles is reached with $N = E_{\mathrm{primary}} / E_{\mathrm{th}}$, where E_{th} is the threshold energy below which the radiative energy loss becomes less than the collisional one.
- The track length of a single particle is a random number, following an exponentially decaying distribution, of which the PDE drops to half of its initial value every $\ln 2 \cdot \lambda_{\mathrm{r}}$, where λ_{r} is the radiation length in air.
- The end point of every track defines the starting point of a new one. This continues until the maximum number of secondary particles is reached, which defines the number of tracks in the last generation of tracks.

The track lengths are subsequently transformed into physical distance to the telescope by applying a simple exponential density profile. The number of active tracks is counted for every height bin and the Cherenkov light emissivity $I(\omega)$ is calculated using

$$I(\omega) = \frac{\omega\, e^2\, v}{4\pi\, \epsilon_0\, c^3} \left(1 - \frac{c^2}{n^2\, v^2}\right) , \tag{F.0.6}$$

where v is the particle velocity and n is the local refractive index (Longair, 2011). For the refractive index, $n(h) = 1 + 0.000292 \cdot \frac{\rho(h)}{\rho_0}$ is used, with $\rho(h)$ being the altitude dependent density of the atmosphere. Example 1 TeV γ shower profiles obtained with this model can be found in figure F.1. The distribution of fitted widths (for a larger sample) can be found in figure F.2. Figure F.3 shows the energy dependence of the shower width.

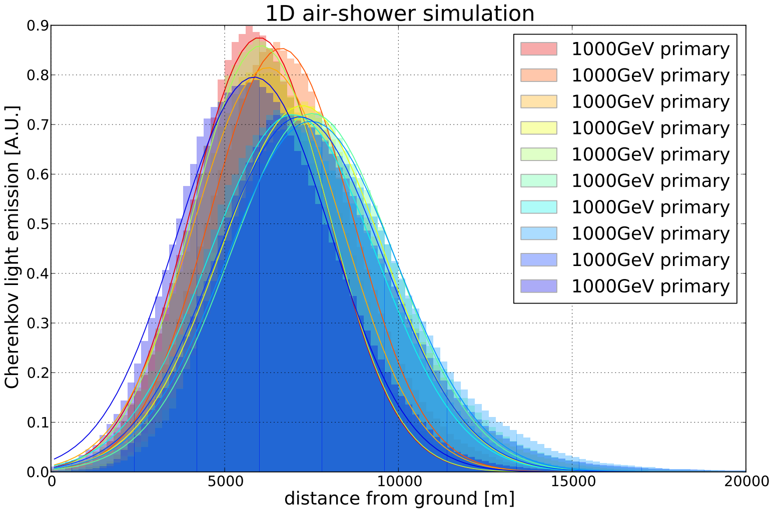

Figure F.1: Result of 10 times simulating a 1 TeV air-shower with a simple 1D cascade model. The plot shows Cherenkov light emissivity of all "active" particles in arbitrary units as function of altitude above the MAGIC telescopes. The showers are simulated coming from zenith. The colored lines show the best fitting Gaussian approximation of the Cherenkov light emission profile.

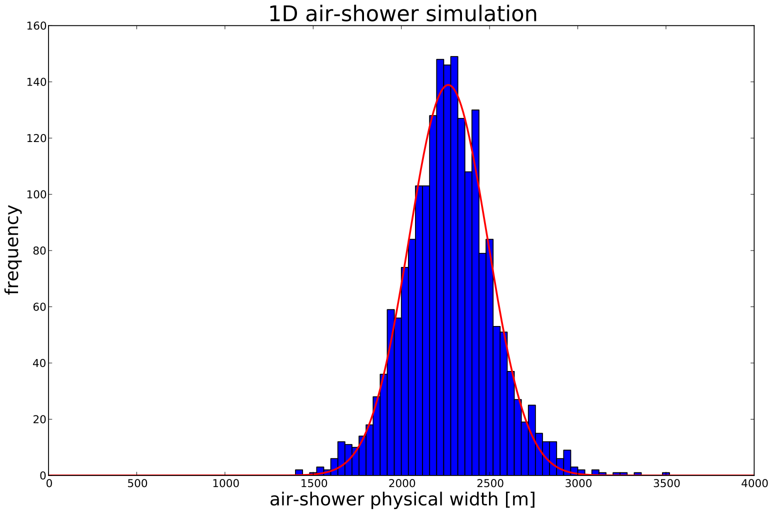

Figure F.2: Result of 2000 times simulating a 1 TeV air-shower with a simple 1D cascade model. The plot shows the distribution of widths of the Cherenkov light emission profiles (blue). The distribution can be fitted with a Gaussian ($\mu = 2300$ m and $\sigma = 230$ m).

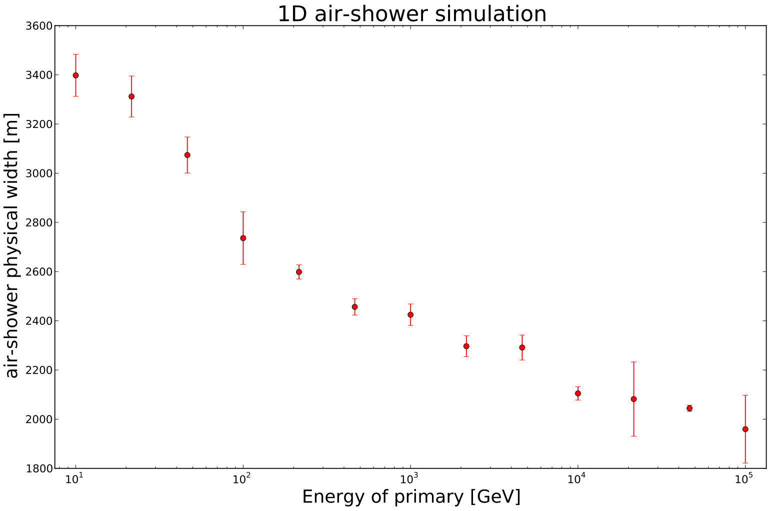

Figure F.3: Result of simulating air-showers of different energies, 200 times each, with a simple 1D cascade model. The plot shows the energy dependence of the width of the Cherenkov light emission profiles.

G

SCALING OF THE LIGHT YIELD WITH ZD

For estimating the true geometric scaling of the Cherenkov light pool with zenith distance of the observations, one has to determine the distance from the shower core to the observer. Numbers for the atmospheric depth of shower maxima of primary γ-rays of different energies can be found for example in Wagner (2006). A typical value is $X_{\mathrm{max}} = 350\,\mathrm{gcm}^{-2}$ for a primary γ-ray of about one TeV.

Given an idealized atmosphere with a scale length h_{s} of 10 km and a mass density ρ_0 of $0.96\,\mathrm{kgm}^{-3}$ at the altitude of the MAGIC telescopes, the distance to the shower maximum d_{x} is defined by the following equation:

$$\int_{d_{\mathrm{x}}}^{\infty} \rho_0 \exp\left(\frac{-r\cos(\mathrm{Zd})}{h_{\mathrm{s}}}\right) \mathrm{d}r = X_{\mathrm{max}}\,. \tag{G.0.7}$$

This can be solved for d_{x}, giving

$$d_{\mathrm{x}} = -\frac{h_{\mathrm{s}}}{\cos(\mathrm{Zd})} \ln\left(\frac{X_{\mathrm{max}}\cos(\mathrm{Zd})}{h_{\mathrm{s}}\,\rho_0}\right)\,. \tag{G.0.8}$$

Figure G.1 shows the dependence distance to the shower maximum, geometric collection area, and light yield with Zd. Different powers of $\cos(\mathrm{Zd})$ are drawn for comparison. In conclusion one can say that the light yield is scaling like $\cos^{-(3.5..4)}(\mathrm{Zd})$, only for geometrical reasons. The geometric collection area - or area of the light pool, in correspondence, is scaling like $\cos^{3.5..4}(\mathrm{Zd})$. Additionally, effects like increased atmospheric absorption and reduced trigger efficiency are further reducing the effective collection area. These effects can be better studied using MC simulations.

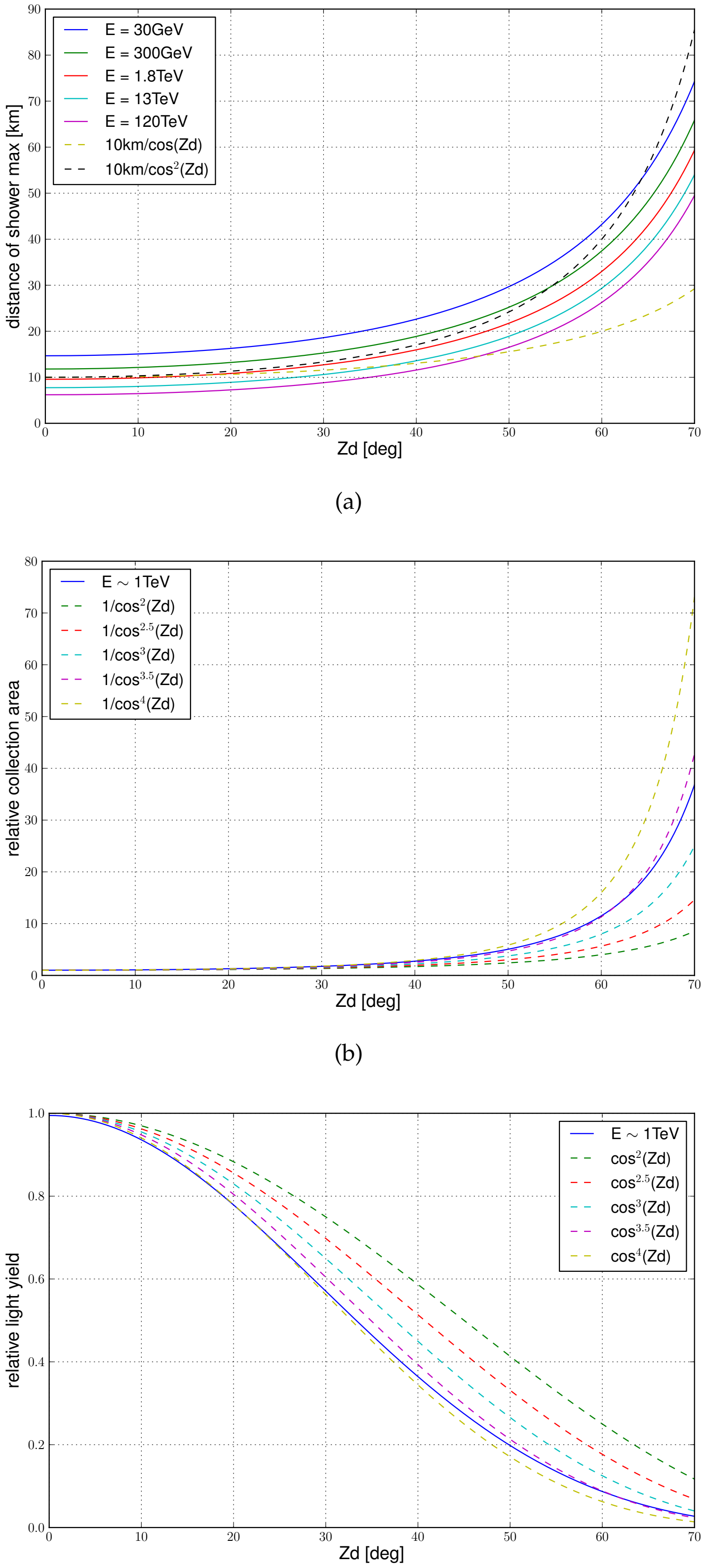

(a)

(b)

(c)

Figure G.1: Scaling of the distance to the shower core with Zd (a). Scaling of the effective collection area (area of light pool) with Zd (b). Scaling of the light yield with Zd, neglecting absorption effects (c).

H

TESTS OF WINSTON CONE PROTOTYPES FOR CTA

Different light concentrator prototype geometries for the application in CTA photomultiplier cameras were tested in the lab. The main focus was on their angular acceptance and light collection efficiency when operated under "real conditions", meaning in front of a CTA prototype PMT.

The geometry of these non-imaging light concentrators – also known as Winston cones (WC) – is based on an arrangement of reflective surfaces with parabolic shape that are inclined with respect to the symmetry axis, in order to increase the solid angle, from which light is accepted by one opening and guided through the output on the other side (Winston et al., 2005). Ideal WCs are rotationally symmetric. For the application in CTA, where a hexagonal pixel layout of the camera will be used, also hexagonal-shaped entrance window cones are required. This deviation from the ideal geometry comes at the cost of a perfectly sharp angular acceptance cutoff, but allows for a better light collection efficiency by avoiding dead areas.

H.1 THE MEASUREMENT SETUP

The main idea behind the lab measurements of the angular acceptance of various WC geometries was studying also the interplay of the WC and PMT under realistic conditions. This was done in order to not have to rely only on idealized ray tracing simulations as for example performed by Hénault et al. (2013). The influence of the surface texture of the PMT entrance window was of particular interest.

The experimental setup consists of a laser light source (532 nm) equipped with a Spectralon transmitting diffuser and the Winston cone sample, as well as a flux monitoring PIN diode at a distance of 3 m from the light source. The WC sample is mounted on a turntable driven by a stepping motor (see figure H.1)[1]. The PMT is connected to a standard voltage divider and operated at a typical voltage of -1.1 kV. The DC current is recorded using a Keithly picoammeter. This way of operation should simulate best the real operational conditions for the WCs in an IACT camera.

For reducing systematic errors to a minimum, the measurement was conducted in an absolutely dark room, reference dark currents were recorded before and after each measurement and the light output of the laser was

---

[1] The turntable setup was originally designed by Hanna Kellermann for characterizing Spektralon samples (Kellermann, 2011). It proved to be very useful also for this measurement.

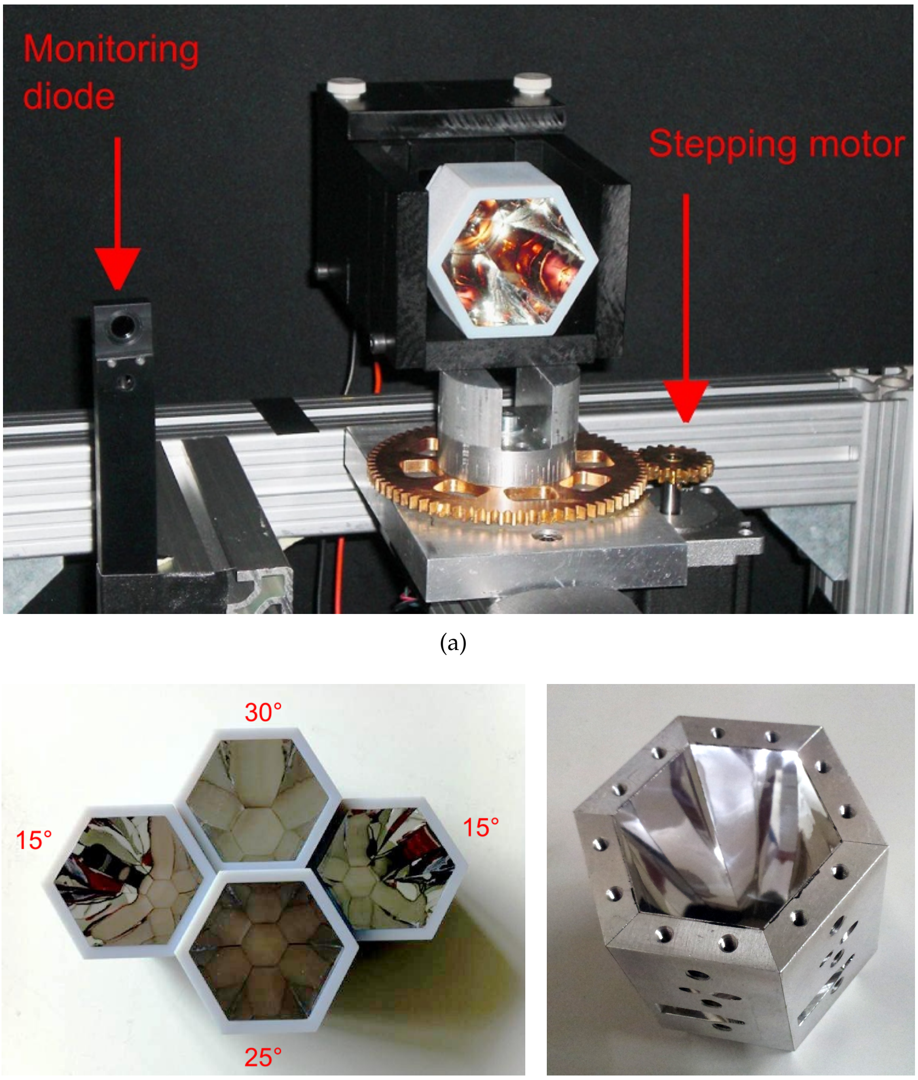

(a)

(b)

(c)

Figure H.1: Setup for the Winston cone measurements (a) (image: courtesy Hanna Kellermann), Mylar/Vikuiti prototype Winston cones (b), and Alanod Winston cone prototype (c).

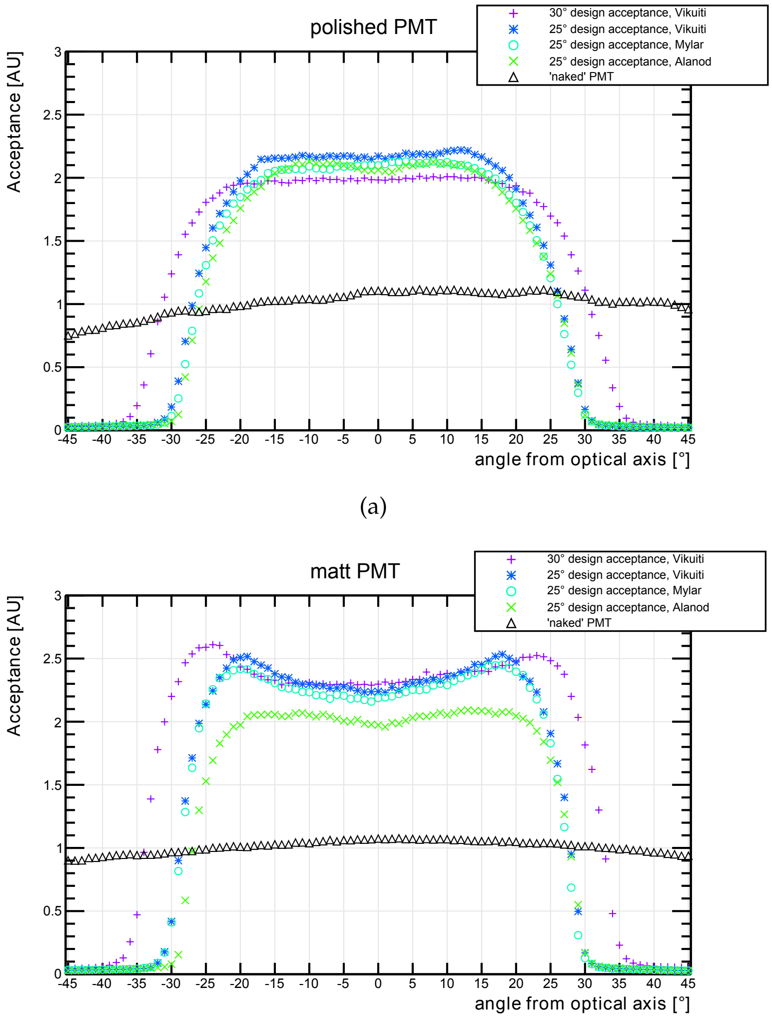

(a)

(b)

Figure H.2: Angular acceptance of different Winston cones/PMT surfaces. The y-axis scale is in units of relative anode current, when compared to the corresponding 'naked' PMT, averaged over the angles of the typical FoV.

constantly monitored using a PIN photodiode connected to a second picoammeter.

Three different WC materials and different geometries were tested. The three materials were: anodized Mylar foil, Vikuiti foil with high reflectance coating and physical vapour deposition (PVD) coated Aluminum (Alanod). The tested geometries had design angular acceptances of 15, 25, and 30 degrees from the optical axis.

H.2 RESULTS

Here, the results of the measurements are presented in arbitrary units, normalized in a way that the polished PMT without light concentrator will give

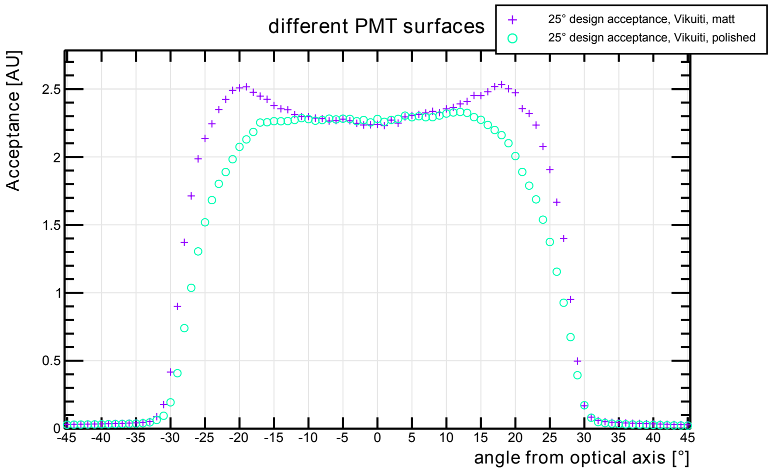

Figure H.3: Angular acceptance of Winston cone with polished / matt finish PMT. The y-axis scale is in units of relative anode current, when compared to the corresponding 'naked' PMT, averaged over the angles of the typical FoV.

about unity acceptance in the central part of the scanned angular region. Only results from the 25 ° and 30 ° WCs will be shown here since the narrower acceptance cones were discarded in the ongoing design phase of CTA.

In figure H.2 the results of the angular acceptance measurements are shown for the polished PMT surface (a) and the matt PMT surface (b). It was found that the Vikuiti foil has a slightly better reflectivity compared to the Mylar foil, which in turn is better than the Alanod material. Probably the most important finding was that the surface finishing of the PMT entrance window has big influence on the light collection efficiency and the angular acceptance of the WC PMT system. For all WC samples the acceptance at the edge of the FoV is enhanced for the matt surface. This effect leads to a very desirable sharper acceptance cutoff at the edge of the FoV combined with a slightly increased overall collection efficiency (see figure H.3).

It is not so easy to explain this effect, especially given its remarkable magnitude. However, two effects probably play an important role. First, for extreme angles, close to the acceptance limit, light is guided to the PMT surface under very small angles. This, in case of a polished surface, leads to a large reflected component. For the rough PMT on the other hand, it is much easier to enter the glass because the average angle under which the photons reach the surface are closer to normal. The second effect comes from the curved photocathode surface of the PMT. The curvature allows for photons that are entering the inner part of the PMT under extreme angles, to cross the photocathode a second time, without being absorbed by the photocatode material, increasing their probability of being absorbed. Such photon trajectories are more likely in case of a rough surface, which randomizes the direction under which the photons enter the tube.

BIBLIOGRAPHY

Aab A. et al. (2013). Highlights from the Pierre Auger Observatory. *arXiv preprint arXiv:1310.4620*.

Aartsen M. et al. (2014). Search for a diffuse flux of astrophysical muon neutrinos with the IceCube 59-string configuration. *Physical Review D*, 89(6):062007.

Abbasi R. et al. (2008). First observation of the Greisen-Zatsepin-Kuzmin suppression. *Physical Review Letters*, 100(10):101101.

Abdo A. et al. (2009a). Fermi large area telescope measurements of the diffuse gamma-ray emission at intermediate galactic latitudes. *Physical Review Letters*, 103(25):251101.

Abdo A.A. et al. (2009b). Measurement of the cosmic ray e++ e-spectrum from 20 GeV to 1 TeV with the Fermi Large Area Telescope. *Physical Review Letters*, 102(18):181101.

Abraham J. et al. (2010). The fluorescence detector of the Pierre Auger Observatory. *Nuclear Instruments and Methods in Physics Research Section A: Accelerators, Spectrometers, Detectors and Associated Equipment*, 620(2):227–251.

Abramowski A. et al. (2014). HESS observations of the Crab during its March 2013 GeV gamma-ray flare. *Astronomy and Astrophysics*, 562:L4.

Acciari V. et al. (2009). A connection between star formation activity and cosmic rays in the starburst galaxy M82. *Nature*, 462(7274):770–772.

Acero F. et al. (2010a). First detection of VHE gamma-rays from SN 1006 by HESS. *Astronomy and Astrophysics*, 516.

Acero F. et al. (2010b). Localizing the VHE γ-ray source at the Galactic Centre. *Monthly Notices of the Royal Astronomical Society*, 402(3):1877–1882.

Acharya B. et al. (2013). Introducing the CTA concept. *Astroparticle physics*, 43:3–18.

Ackermann M. et al. (2011). Constraining dark matter models from a combined analysis of Milky Way satellites with the Fermi Large Area Telescope. *Physical Review Letters*, 107(24):241302.

Ackermann M. et al. (2012). The imprint of the extragalactic background light in the gamma-ray spectra of blazars. *Science*, 338(6111):1190–1192.

Ade P. et al. (2013). Planck 2013 results. XVI. Cosmological parameters. *arXiv preprint arXiv:1303.5076*.

Aharonian F., Bogovalov S. & Khangulyan D. (2012). Abrupt acceleration of a/cold/'ultrarelativistic wind from the Crab pulsar. *Nature*, 482(7386):507–509.

Aharonian F. et al. (2004). Very high energy gamma rays from the direction of Sagittarius A*. *Astronomy & astrophysics.*, 425(1):L13–L17.

Aharonian F. et al. (2005). Very high energy gamma rays from the composite SNR G0. 9+ 0.1. *Astronomy and Astrophysics*, 432.

Aharonian F. et al. (2006a). Discovery of very-high-energy γ-rays from the Galactic Centre ridge. *Nature*, 439(7077):695–698.

Aharonian F. et al. (2006b). HESS observations of the galactic center region and their possible dark matter interpretation. *Physical Review Letters*, 97(22):221102.

Aharonian F. et al. (2006c). Observations of the Crab nebula with HESS. *Astronomy and Astrophysics*, 457:899–915.

Aharonian F. et al. (2008). Energy spectrum of cosmic-ray electrons at TeV energies. *Physical Review Letters*, 101(26):261104.

Aharonian F. et al. (2009). Spectrum and variability of the Galactic center VHE γ-ray source HESS J1745–290. *Astronomy & Astrophysics*, 503(3):817–825.

Aharonian F. et al. (2013). *Astrophysics at Very High Energies*. Springer.

Ahn H. et al. (2010). Discrepant hardening observed in cosmic-ray elemental spectra. *The Astrophysical Journal Letters*, 714(1):L89.

Albert J. et al. (2006). Observation of gamma rays from the galactic center with the MAGIC telescope. *The Astrophysical Journal Letters*, 638(2):L101.

Albert J. et al. (2007). Unfolding of differential energy spectra in the MAGIC experiment. *Nuclear Instruments and Methods in Physics Research Section A: Accelerators, Spectrometers, Detectors and Associated Equipment*, 583(2):494–506.

Albert J. et al. (2008). VHE γ-Ray Observation of the Crab Nebula and its Pulsar with the MAGIC Telescope. *The Astrophysical Journal*, 674(2):1037.

Aleksić J. et al. (2011). Searches for Dark Matter annihilation signatures in the Segue 1 satellite galaxy with the MAGIC-I telescope. *Journal of Cosmology and Astroparticle Physics*, 2011(06):035.

Aleksic J. et al. (2012). Performance of the MAGIC stereo system obtained with Crab Nebula data. *Astroparticle Physics*, 35:435–448.

Aleksic J. et al. (2014). The major upgrade of the MAGIC telescopes, Part II: The achieved physics performance using the Crab Nebula observations. *arXiv preprint arXiv:1409.5594*.

Aleksić J. et al. (2014). Measurement of the Crab Nebula spectrum over three decades in energy with the MAGIC telescopes. *arXiv preprint arXiv:1406.6892*.

Aliu E. et al. (2008). Observation of pulsed γ-Rays above 25 GeV from the Crab Pulsar with MAGIC. *Science*, 322(5905):1221–1224.

Allekotte I. et al. (2008). The surface detector system of the Pierre Auger Observatory. *Nuclear Instruments and Methods in Physics Research Section A: Accelerators, Spectrometers, Detectors and Associated Equipment*, 586(3):409–420.

Anderson C.D. (1933). The Positive Electron. *Phys. Rev.*, 43:491–494. doi: 10.1103/PhysRev.43.491.

Archer A. et al. (2014). Very-high Energy Observations of the Galactic Center Region by VERITAS in 2010-2012. *The Astrophysical Journal*, 790(2):149.

Arons J. (1983). Pair creation above pulsar polar caps: geometrical structure and energetics of slot caps. *Astrophys. J.;(United States)*, 266(1).

Arons J. & Scharlemann E. (1979). Pair formation above pulsar polar caps-Structure of the low altitude acceleration zone. *The Astrophysical Journal*, 231:854–879.

Atoyan A. & Dermer C.D. (2004). TeV emission from the galactic center black hole plerion. *The Astrophysical Journal Letters*, 617(2):L123.

Atwood W. et al. (2009). The large area telescope on the Fermi gamma-ray space telescope mission. *The Astrophysical Journal*, 697(2):1071.

Baganoff F. et al. (2000). Chandra Detects X-ray Emission from Sgr A*. In *Bulletin of the American Astronomical Society*, volume 32, page 1184.

Balick B. & Brown R.L. (1974). Intense sub-arcsecond structure in the galactic center. *The Astrophysical Journal*, 194:265–270.

Ballantyne D., Schumann M. & Ford B. (2011). Modelling the time-dependence of the TeV γ-ray source at the Galactic Centre. *Monthly Notices of the Royal Astronomical Society*, 410(3):1521–1526.

Barrio J.A. et al. (1998). The MAGIC Telescope - Design study for the construction of a 17m Cherenkov telescope for Gamma-Astronomy above 10 GeV. Technical report.

Bartos I. et al. (2013). Gas Cloud G2 Can Illuminate the Black Hole Population Near the Galactic Center. *Physical review letters*, 110(22):221102.

Bell A. (1978). The acceleration of cosmic rays in shock fronts. I. *Monthly Notices of the Royal Astronomical Society*, 182:147–156.

Benn C. & Ellison S. (1998). Brightness of the night sky over La Palma. *New Astronomy Reviews*, 42(6):503–507.

Bergström L. et al. (2013). New Limits on Dark Matter Annihilation from Alpha Magnetic Spectrometer Cosmic Ray Positron Data. *Physical review letters*, 111(17):171101.

Beringer J. et al. (2012). Review of particle physics. *Physical Review D*, 86(1).

Bernlöhr K. (2000). Impact of atmospheric parameters on the atmospheric Cherenkov technique. *Astroparticle Physics*, 12(4):255–268.

Bertero M. (1989). Advances in Electronics and Electron Physics, Vol. 75.

Biagi S. (2013). Updated limits on diffuse fluxes of cosmic neutrinos with 2008-2011 ANTARES data. *arXiv preprint arXiv:1305.6442*.

Biland A. et al. (2008). The Active Mirror Control of the MAGIC Telescopes. In *International Cosmic Ray Conference*, volume 3, pages 1353–1356.

Blackett P. (1948). A possible contribution to the night sky from the Cerenkov radiation emitted by cosmic rays. In *The Emission Spectra of the Night Sky and Aurorae*, volume 1, page 34.

Blandford R.D. & Ostriker J.P. (1978). Particle acceleration by astrophysical shocks. *The Astrophysical Journal*, 221:L29–L32.

Blasi P. (2013). The origin of galactic cosmic rays. *The Astronomy and Astrophysics Review*, 21(1):1–73.

Bond I. et al. (1989). Upper limit for ultra-high-energy gamma rays from SN 1987A obtained by Cerenkov technique at large zenith angles. *The Astrophysical Journal*, 344:L17–L19.

Bower G.C. et al. (2014). The Intrinsic Two-Dimensional Size of Sagittarius A*. *arXiv preprint arXiv:1405.1456*.

Branch D. & Tammann G. (1992). Type Ia Supernovae as Standard Candles. *Annual Review of Astronomy and Astrophysics*, 30(1):359–389.

Breiman L. (2001). Random forests. *Machine learning*, 45(1):5–32.

Bromberg O. et al. (2012). An Observational Imprint of the Collapsar Model of Long Gamma-Ray Bursts. *The Astrophysical Journal*, 749(2):110.

Brun R. & Rademakers F. (1997). ROOT — An object oriented data analysis framework. *Nuclear Instruments and Methods in Physics Research Section A: Accelerators, Spectrometers, Detectors and Associated Equipment*, 389(1–2):81 – 86. ISSN 0168-9002. doi:http://dx.doi.org/10.1016/S0168-9002(97)00048-X.

Bruno A. et al. (2013). PRECISE COSMIC RAYS MEASUREMENTS WITH PAMELA. *Acta Polytechnica*, 53.

Cabrera-Lavers A. et al. (2008). The long Galactic bar as seen by UKIDSS Galactic plane survey. *Astronomy and Astrophysics*, 491:781–787.

Cao Y. et al. (2014). Classification of Supernova in M82 as a young, reddened Type Ia Supernova. *The Astronomer's Telegram*, 5786:1.

Carslaw K. (2009). Atmospheric physics: Cosmic rays, clouds and climate. *Nature*, 460(7253):332–333.

Cembranos J., Gammaldi V. & Maroto A. (2012). Possible dark matter origin of the gamma ray emission from the galactic center observed by HESS. *Physical Review D*, 86(10):103506.

Chang J. et al. (2008). An excess of cosmic ray electrons at energies of 300–800 GeV. *Nature*, 456(7220):362–365.

Cherenkov P.A. (1934). Visible emission of clean liquids by action of γ radiation. *Doklady Akademii Nauk SSSR*, 2:451.

Chernyakova M. et al. (2011). The high-energy, Arcminute-scale galactic center gamma-ray source. *The Astrophysical Journal*, 726(2):60.

Chiba N. et al. (1992). Akeno Giant Air Shower Array (AGASA) covering 100 km< sup> 2</sup> area. *Nuclear Instruments and Methods in Physics Research Section A: Accelerators, Spectrometers, Detectors and Associated Equipment*, 311(1):338–349.

Chowdhury D., Vempati S.K. & Jog C.J. (2011). Results from PAMELA, ATIC and FERMI: Pulsars or dark matter? *Pramana*, 76(1):1–22.

Cocke W., Disney M. & Taylor D. (1969). Discovery of optical signals from pulsar NP 0532.

Cucinotta F.A. & Durante M. (2006). Cancer risk from exposure to galactic cosmic rays: implications for space exploration by human beings. *The lancet oncology*, 7(5):431–435.

d'Ambrosio C. & Leutz H. (2000). Photoelectron backscattering from silicon anodes of hybrid photodetector tubes. *Nuclear Science, IEEE Transactions on*, 47(4):1685–1690.

Darlington E. (1975). Backscattering of 10-100 keV electrons from thick targets. *Journal of Physics D: Applied Physics*, 8(1):85.

Davies R., Walsh D. & Booth R. (1976). The radio source at the galactic nucleus. *Monthly Notices of the Royal Astronomical Society*, 177(2):319–333.

Derbina V. et al. (2005). Cosmic-ray spectra and composition in the energy range of 10-1000 TeV per particle obtained by the RUNJOB experiment. *The Astrophysical Journal Letters*, 628(1):L41.

Diaz-Castro F.J. (1998). Adaptation of streetlighting on La Palma. *New Astronomy Reviews*, 42(6):509–513.

Doeleman S.S. et al. (2008). Event-horizon-scale structure in the supermassive black hole candidate at the Galactic Centre. *Nature*, 455(7209):78–80.

Drury L.O. (1983). An introduction to the theory of diffusive shock acceleration of energetic particles in tenuous plasmas. *Reports on Progress in Physics*, 46(8):973.

Eisenhauer F. et al. (2008). GRAVITY: getting to the event horizon of Sgr A*. In *SPIE Astronomical Telescopes+ Instrumentation*, pages 70132A–70132A. International Society for Optics and Photonics.

Ekers R. et al. (1983). The radio structure of SGR A. *Astronomy and Astrophysics*, 122:143–150.

Emmanoulopoulos D., McHardy I.M. & Uttley P. (2010). On the use of structure functions to study blazar variability: caveats and problems. *Monthly Notices of the Royal Astronomical Society*, 404(2):931–946.

Enomoto R. et al. (2003). *The Universe Viewed in Gamma-rays: International Science Symposium on the Universe Viewed in Gamma-Rays, Held on September 25 - 28, 2002, in Kashiwa, Chiba, Japan*. Frontiers science series. Universal Academy Press. ISBN 9784946443756.

Fairbairn M. et al. (2014). The CTA sensitivity to Lorentz-violating effects on the gamma-ray horizon. *Journal of Cosmology and Astroparticle Physics*, 2014(06):005.

Falta D., Fisher R. & Khanna G. (2011). Gravitational Wave Emission from the Single-Degenerate Channel of Type Ia Supernovae. *Phys. Rev. Lett.*, 106:201103. doi:10.1103/PhysRevLett.106.201103.

Fatuzzo M. & Melia F. (2012). Diffusive Cosmic-Ray Acceleration in Sagittarius A*. *The Astrophysical Journal Letters*, 757(1):L16.

Fenech D. et al. (2008). Deep MERLIN 5 GHz radio imaging of supernova remnants in the M82 starburst. *Monthly Notices of the Royal Astronomical Society*, 391(3):1384–1402.

Fermi E. (1949). On the Origin of the Cosmic Radiation. *Phys. Rev.*, 75:1169–1174. doi:10.1103/PhysRev.75.1169.

Fernandopullé D. (1976). Climatic characteristics of the Canary Islands. In *Biogeography and ecology in the Canary Islands*, pages 185–206. Springer.

Fields B.D., Shapiro S.L. & Shelton J. (2014). Galactic Center Gamma-Ray Excess from Dark Matter Annihilation: Is There A Black Hole Spike? *arXiv preprint arXiv:1406.4856*.

Finkbeiner D.P., Su M. & Weniger C. (2013). Is the 130 GeV line real? A search for systematics in the Fermi-LAT data. *Journal of Cosmology and Astroparticle Physics*, 2013(01):029.

Fish V.L. et al. (2011). 1.3 mm wavelength VLBI of Sagittarius A*: detection of time-variable emission on event horizon scales. *The Astrophysical Journal Letters*, 727(2):L36.

Fleetwood D.M., Winokur P.S. & Dodd P.E. (2000). An overview of radiation effects on electronics in the space telecommunications environment. *Microelectronics Reliability*, 40(1):17–26.

Fossey J. et al. (2014). Supernova 2014J in M82= Psn J09554214+ 6940260. *Central Bureau Electronic Telegrams*, 3792:1.

Frank I. & Tamm I. (1937). Coherent visible radiation of fast electrons passing through matter. *Doklady Akademii Nauk SSSR*, 14:109–114.

Freedman W.L. et al. (1994). First Hubble Space Telescope observations of the brightest stars in the Virgo galaxy M100= NGC 4321. *The Astrophysical Journal*, 435:L31–L34.

Fritz G. et al. (1969). X-ray Pulsar in the Crab Nebula. *Science*, 164(3880):709–712.

Fruchter A. et al. (2006). Long γ-ray bursts and core-collapse supernovae have different environments. *Nature*, 441(7092):463–468.

Fruck C. (2010). *A new LIDAR system for the MAGIC telescopes and site search instrumentation for CTA*. Diplomarbeit, Technical University Munich.

Fruck C. et al. (2015). Instrumentation for CTA site characterization. *arXiv preprint arXiv:1501.02156*.

Gammaldi V. et al. (2014). Gamma-ray and neutrino fluxes form Heavy Dark Matter in the Galactic Center. *arXiv preprint arXiv:1404.2067*.

Genzel R. & Eckart A. (1999). The Galactic Center Black Hole. In *The Central Parsecs of the Galaxy*, volume 186, page 3.

Genzel R., Eisenhauer F. & Gillessen S. (2010). The Galactic Center massive black hole and nuclear star cluster. *Reviews of Modern Physics*, 82(4):3121.

Genzel R. et al. (2003). Near-infrared flares from accreting gas around the supermassive black hole at the Galactic Centre. *Nature*, 425(6961):934–937.

Giannios D. & Sironi L. (2013). The S2 star as a probe of the accretion disc of Sgr A*. *Monthly Notices of the Royal Astronomical Society: Letters*, 433(1):L25–L29.

Gillessen S. et al. (2009). Monitoring stellar orbits around the Massive Black Hole in the Galactic Center. *The Astrophysical Journal*, 692(2):1075.

Gillessen S. et al. (2012). A gas cloud on its way towards the supermassive black hole at the Galactic Centre. *Nature*, 481(7379):51–54.

Gillessen S. et al. (2013a). New Observations of the Gas Cloud G2 in the Galactic Center. *The Astrophysical Journal*, 763(2):78.

Gillessen S. et al. (2013b). Pericenter Passage of the Gas Cloud G2 in the Galactic Center. *The Astrophysical Journal*, 774(1):44.

Goldreich P. & Julian W.H. (1969). Pulsar electrodynamics. *The Astrophysical Journal*, 157:869.

Goudie A. & Middleton N. (2001). Saharan dust storms: nature and consequences. *Earth-Science Reviews*, 56(1):179–204.

Guo Y.Q. et al. (2013). A hybrid model of GeV–TeV gamma ray emission from the Galactic center. *Journal of Physics G: Nuclear and Particle Physics*, 40(6):065201.

Guzik T. et al. (2004). The ATIC long duration balloon project. *Advances in Space Research*, 33(10):1763–1770.

Haefner D. et al. (2011). New improved Sum-Trigger system for the MAGIC telescopes. *arXiv preprint arXiv:1111.1299*.

Haefner D. et al. (2012). A Tunable Delay Line for Fast Analog Pulses as Key Element of a New Sum-Trigger for Cherenkov Telescopes. *Nuclear Science, IEEE Transactions on*, 59(2):289–293. ISSN 0018-9499. doi:10.1109/TNS.2011.2182619.

Handa T. et al. (2006). Thermal SiO and H13CO+ Line Observations of the Dense Molecular Cloud G0. 11–0.11 in the Galactic Center Region. *The Astrophysical Journal*, 636(1):261.

Hanlon W.F. (2013). Updated cosmic ray spectrum. http://www.physics.utah.edu/ whanlon/spectrum.html. [Online; accessed 6-December-2013].

Heck D. et al. (1998). *CORSIKA: A Monte Carlo code to simulate extensive air showers*, volume 6019. FZKA.

Heitler W. (1954). *The quantum theory of radiation*. DoverPublications. com.

Heitronics (2013). HEITRONICS Infrarot Messtechnik GmbH. http://www.heitronics.com. [Online; accessed 28-November-2013].

Hénault F. et al. (2013). Design of light concentrators for Cherenkov telescope observatories. In *SPIE Optical Engineering+ Applications*, pages 883405–883405. International Society for Optics and Photonics.

Hewish A. et al. (1968). Observation of a rapidly pulsating radio source. *Nature*, 217(5130):709–713.

Hillas A.M. (1985). Cerenkov light images of EAS produced by primary gamma. In *International Cosmic Ray Conference*, volume 3, pages 445–448.

Hinton J. & Aharonian F. (2007). Inverse compton scenarios for the TeV gamma-ray emission of the galactic center. *The Astrophysical Journal*, 657(1):302.

Hirotani K. (2008). Outer-gap versus slot-gap models for pulsar high-energy emissions: the case of the Crab pulsar. *The Astrophysical Journal Letters*, 688(1):L25.

Hopper V.D. & Biswas S. (1950). Evidence Concerning the Existence of the New Unstable Elementary Neutral Particle. *Phys. Rev.*, 80:1099–1100. doi: 10.1103/PhysRev.80.1099.

Jabiri A. et al. (2000). A meteorological and photometric study of the Oukaimeden site. *Astronomy and Astrophysics Supplementary Series*, 146:271–284.

Jakobsson P. et al. (2006). A mean redshift of 2.8 for Swift gamma-ray bursts. *Astronomy & Astrophysics*, 447(3):897–903.

Jelley J. (1958a). **C**erenkov radiation in the atmosphere and its application to the study of extensive air showers. *Il Nuovo Cimento (1955-1965)*, 8:578–584.

Jelley J.V. (1958b). Cherenkov radiation and its applications.

Karle A. et al. (2014). IceCube-status and recent results. *arXiv preprint arXiv:1401.4496*.

Kassim N.E. et al. (1998). Wide Field Radio Imaging of the Galactic Center. http://www.nrl.navy.mil/media/news-releases/1998/wide-field-radio-imaging-of-the-galactic-center. [Online; accessed 3-April-2014].

Kawai H. et al. (2008). Telescope array experiment. *Nuclear Physics B-Proceedings Supplements*, 175:221–226.

Kellermann H. (2011). *Präzise Vermessung der fokussierten Reflektivität der MAGIC-Teleskopspiegel und Charakterisierung des hierfür verwendeten diffusen Reflektors*. Diplomarbeit, Munich University for Applied Sciences.

Klett J.D. (1981). Stable analytical inversion solution for processing lidar returns. *Applied Optics*, 20:211–220.

Kosack K. et al. (2004). TeV gamma-ray observations of the galactic center. *The Astrophysical Journal Letters*, 608(2):L97.

Kouveliotou C. et al. (1993). Identification of two classes of gamma-ray bursts. *The Astrophysical Journal*, 413:L101–L104.

Krabbe A. et al. (1995). The nuclear cluster of the Milky Way: Star formation and velocity dispersion in the central 0.5 parsec. *The Astrophysical Journal Letters*, 447(2):L95.

Krause J. (2012). *Resolved gamma ray emission of the supernova remnant W51C and HESS J1857+026 obtained with the MAGIC telescopes*. Ph.d. thesis, Ludwig-Maximilians-Universität München.

Krause O. et al. (2008). Tycho Brahe's 1572 supernova as a standard Type Ia as revealed by its light-echo spectrum. *Nature*, 456(7222):617–619.

Krymskii G. (1977). A regular mechanism for the acceleration of charged particles on the front of a shock wave. In *Akademiia Nauk SSSR Doklady*, volume 234, pages 1306–1308.

Kunneriath D. et al. (2012). The Galactic centre mini-spiral in the mm-regime. *Astronomy & Astrophysics*, 538:A127.

Kunz G.J. & de Leeuw G. (1993). Inversion of lidar signals with the slope method. *Appl. Opt.*, 32(18):3249–3256. doi:10.1364/AO.32.003249.

Kusunose M. & Takahara F. (2012). A Leptonic Model of Steady High-energy Gamma-Ray Emission from Sgr A*. *The Astrophysical Journal*, 748(1):34.

Laken B.A. et al. (2014). Saharan mineral dust outbreaks observed over the North Atlantic island of La Palma in summertime between 1984 and 2012. *Quarterly Journal of the Royal Meteorological Society*, 140(680):1058–1068.

Law C. et al. (2008). Green Bank Telescope multiwavelength survey of the Galactic center region. *The Astrophysical Journal Supplement Series*, 177(1):255.

Li T.P. & Ma Y.Q. (1983). Analysis methods for results in gamma-ray astronomy. *The Astrophysical Journal*, 272:317–324.

Li Z., Morris M.R. & Baganoff F.K. (2013). Evidence for A parsec-scale jet from the galactic center black hole: interaction with local gas. *The Astrophysical Journal*, 779(2):154.

Linden T., Lovegrove E. & Profumo S. (2012). The Morphology of Hadronic Emission Models for the Gamma-Ray Source at the Galactic Center. *The Astrophysical Journal*, 753(1):41.

Longair M. (2011). *High Energy Astrophysics*. Cambridge University Press. ISBN 9781139494540.

Lorenz E. (2004). Status of the 17 m Ø MAGIC telescope. *New Astronomy Reviews*, 48(5–6):339 – 344. ISSN 1387-6473. doi:http://dx.doi.org/10.1016/j.newar.2003.12.059. 2nd VERITAS Symposium on the Astrophysics of Extragalactic Sources.

Macias O. & Gordon C. (2014). Contribution of cosmic rays interacting with molecular clouds to the Galactic Center gamma-ray excess. *Physical Review D*, 89(6):063515.

Maeda Y. et al. (2002). A Chandra Study of Sagittarius A East: A Supernova Remnant Regulating the Activity of Our Galactic Center? *The Astrophysical Journal*, 570(2):671.

Margiotta A. (2013). The KM3NeT project: status and perspectives. *Geoscientific Instrumentation, Methods and Data Systems*, 2(1):35–40.

Martinez-Valpuesta I. & Gerhard O. (2011). Unifying A Boxy Bulge and Planar Long Bar in the Milky Way. *The Astrophysical Journal Letters*, 734(1):L20.

Matthews J. (2005). A Heitler model of extensive air showers. *Astroparticle Physics*, 22(5):387–397.

Mazin D. et al. (2013). Potential of EBL and cosmology studies with the Cherenkov Telescope Array. *Astroparticle Physics*, 43:241–251.

Mazzali P.A. et al. (2007). A common explosion mechanism for type Ia supernovae. *Science*, 315(5813):825–828.

Measures R.M. (1992). *Laser remote sensing: fundamentals and applications*. Krieger.

Mezger P.G., Duschl W.J. & Zylka R. (1996). The Galactic Center: a laboratory for AGN? *The Astronomy and Astrophysics Review*, 7(4):289–388.

Mirzoyan R. (2000). Conversion Factor Calibration for MAGIC Based on the Use of Measured F-Factors of PMTs. Internal MAGIC memo.

Mirzoyan R. & Lorenz E. (1997). On the Calibration Accuracy of Light Sensors in Atmospheric Cherenkov, Fluorescence and Neutrino Experiments. In *Proceedings of the 25th International Cosmic Ray Conference*, volume 7, pages 265–268.

Morrison P. (1958). On gamma-ray astronomy. *Il nuovo cimento*, 7(6):858–865.

Muslimov A.G. & Harding A.K. (2003). Extended acceleration in slot gaps and pulsar high-energy emission. *The Astrophysical Journal*, 588(1):430.

Neronov A.Y., Semikoz D. & Tkachev I. (2009). Ultra-high energy cosmic ray production in the polar cap regions of black hole magnetospheres. *New Journal of Physics*, 11(6):065015.

Neto J. et al. (2013). Review of the anisotropy working group at UHECR-2012. *arXiv preprint arXiv:1306.4998*.

Nielsen M. et al. (2014). Upper limits on the luminosity of the progenitor of type Ia supernova SN2014J. *arXiv preprint arXiv:1402.2896*.

Orito R. et al. (2009). Development of HPD Clusters for MAGIC-II. *arXiv preprint arXiv:0907.0865*.

Panov A. et al. (2007). Elemental energy spectra of cosmic rays from the data of the ATIC-2 experiment. *Bulletin of the Russian Academy of Sciences: Physics*, 71(4):494–497.

Paoletti R. et al. (2007). The Trigger System of the MAGIC Telescope. *Nuclear Science, IEEE Transactions on*, 54(2):404–409. ISSN 0018-9499. doi:10.1109/TNS.2007.892649.

Peixdto J.P. & Oort A.H. (1992). Physics of climate. *American institute of physics, New York*.

Petrov L. et al. (2011). The Very Long Baseline Array Galactic Plane Survey—VGaPS. *The Astronomical Journal*, 142(2):35.

Pian E. et al. (2006). An optical supernova associated with the X-ray flash XRF 060218. *Nature*, 442(7106):1011–1013.

Pittori C. & Tavani M. (2004). Scientific goals and instrument performance of the gamma-ray imaging detector AGILE. *Nuclear Physics B-Proceedings Supplements*, 134:72–74.

Reinhardt (2013). REINHARDT System- und Messelectronic GmbH. http://www.reinhardt-testsystem.de. [Online; accessed 28-November-2013].

Reynolds S.P. et al. (2007). A deep Chandra observation of Kepler's supernova remnant: a type Ia event with circumstellar interaction. *The Astrophysical Journal Letters*, 668(2):L135.

Rochester G.D. & Butler C.C. (1947). Evidence for the Existence of New Unstable Elementary Particles. *nature*, 160:855–857. doi:10.1038/160855a0.

Ruderman M. & Sutherland P.G. (1975). Theory of pulsars-Polar caps, sparks, and coherent microwave radiation. *The Astrophysical Journal*, 196:51–72.

Rybicki G.B. & Lightman A.P. (2008). *Radiative processes in astrophysics*. John Wiley & Sons.

Saito T. et al. (2009). Very high QE HPDs with a GaAsP photocathode for the MAGIC telescope project. *Nuclear Instruments and Methods in Physics Research Section A: Accelerators, Spectrometers, Detectors and Associated Equipment*, 610(1):258–261.

Schartmann M. et al. (2012). Simulations of the origin and fate of the Galactic Center cloud G2. *The Astrophysical Journal*, 755(2):155.

Schmelling M. (1998). Numerische Methoden der Datenanalyse. *MPI-K Heidelberg*, pages 1998–01.

Schmidt F. (2014). CORSIKA Shower Images. http://www.ast.leeds.ac.uk/ fs/showerimages.html. [Online; accessed 13-January-2014].

Schödel R. et al. (2002). A star in a 15.2-year orbit around the supermassive black hole at the centre of the Milky Way. *Nature*, 419(6908):694–696.

Simpson J. (1983). Elemental and isotopic composition of the galactic cosmic rays. *Annual Review of Nuclear and Particle Science*, 33(1):323–382.

Sitarek J. et al. (2013). Physics performance of the upgraded MAGIC telescopes obtained with Crab Nebula data. *arXiv preprint arXiv:1308.0141*.

Snow T.P. & McCall B.J. (2006). Diffuse atomic and molecular clouds. *Annu. Rev. Astron. Astrophys.*, 44:367–414.

Sokolsky P. et al. (2010). Final Results from the High Resolution Fly's Eye (HiRes) Experiment. *arXiv preprint arXiv:1010.2690*.

Stecker F.W. (2013). Ice Cube Observed PeV Neutrinos from AGN Cores. *Phys. Rev. D*, 88(arXiv: 1305.7404):047301.

Stone E. et al. (1977). Cosmic ray investigation for the Voyager missions; energetic particle studies in the outer heliosphere—And beyond. *Space Science Reviews*, 21(3):355–376.

Tescaro D. (2012). The upgraded readout system of the MAGIC telescopes. In *Nuclear Science Symposium and Medical Imaging Conference (NSS/MIC), 2012 IEEE*, pages 1901–1904. ISSN 1082-3654. doi:10.1109/NSSMIC.2012.6551440.

Thompson D. (2008). Gamma ray astrophysics: the EGRET results. *Reports on Progress in Physics*, 71(11):116901.

Tikhonov A.N. & Arsenin V.Y. (1977). Solutions of ill-posed problems.

Tridon D.B. et al. (2010). The MAGIC-II gamma-ray stereoscopic telescope system. *Nuclear Instruments and Methods in Physics Research Section A: Accelerators, Spectrometers, Detectors and Associated Equipment*, 623(1):437 – 439. ISSN 0168-9002. doi:http://dx.doi.org/10.1016/j.nima.2010.03.028.

Tridon D.B. et al. (2011). Measurement of the cosmic electron plus positron spectrum with the MAGIC telescopes. *arXiv preprint arXiv:1110.4008*.

Trimble V. (1987). Existence and nature of dark matter in the universe. *Annual review of astronomy and astrophysics*, 25(1):425–472.

Tsuboi M., Ukita N. & Handa T. (1997). An expanding shell-like molecular cloud near the Galactic center arc. *The Astrophysical Journal*, 481(1):263.

Tsuchiya K. et al. (2004). Detection of sub-TeV gamma rays from the Galactic center direction by CANGAROO-II. *The Astrophysical Journal Letters*, 606(2):L115.

Wagner R. (2006). *Measurement of VHE γ-ray emission from four blazars using the MAGIC telescope and a comparative blazar study*. Ph.d. thesis, Technische Universität München.

Weekes T.C. et al. (1989). Observation of TeV gamma rays from the Crab nebula using the atmospheric Cerenkov imaging technique. *The Astrophysical Journal*, 342:379–395.

Weiler K. (2003). *Supernovae and gamma-ray bursters*. Springer.

Weisskopf M.C. et al. (2000). Chandra X-ray Observatory (CXO): overview. In *Astronomical Telescopes and Instrumentation*, pages 2–16. International Society for Optics and Photonics.

Weniger C. (2012). A tentative gamma-ray line from dark matter annihilation at the Fermi Large Area Telescope. *Journal of Cosmology and Astroparticle Physics*, 2012(08):007.

Wilson E. (1996). Fifty years of synchrotrons. In *Proceedings of the 1996 European Particle Accelerator Conference (EPAC'96)*, pages 135–139.

Winston R., Miñano J.C. & Benitez P. (2005). *Nonimaging optics*. Academic Press.

Yusef-Zadeh F., Morris M. & Chance D. (1984). Large, highly organized radio structures near the galactic centre.

Yusef-Zadeh F. et al. (2012). A 3 pc Scale Jet-driven Outflow from Sgr A*. *The Astrophysical Journal Letters*, 758(1):L11.

Yusef-Zadeh F. et al. (2013). Interacting Cosmic Rays with Molecular Clouds: A Bremsstrahlung Origin of Diffuse High-energy Emission from the Inner $2^\circ \times 1^\circ$ of the Galactic Center. *The Astrophysical Journal*, 762(1):33.

ACKNOWLEDGEMENTS

I want take this opportunity to show my appreciation to everyone who supported me during the time I spent working on this thesis. First of all I want to thank Prof. Masahiro Teshima for accepting me as PhD student in his group at the MPP, offering me the chance to work in this great environment for my research. Many thanks also go to Razmik Mirzoyan, my day-to-day supervisor, for his continuous support, his valuable comments, and the many fruitful discussions in his office. At the same time I want to thank Prof. Allen Caldwell for accepting the official supervision of my thesis and for giving me important comments in his final review. Thanks also to David Paneque, who despite his limited time and many obligations, in a situation when he was even just about to move to Japan for a while, took his time and read over my theses, giving me very useful advice.

Thank you, to everyone in the MAGIC group at MPP, for the warm and friendly working atmosphere. Thanks for the countless discussions about our work but also on every other imaginable topic in science, life and politics during our lunch and coffee breaks. I want to thank also to those of you with whom I spent part of my free time, skiing, climbing and going out. Thanks to my fellow PhD/diploma/master students from the now not even anymore existing office 026, also to those whose career paths led them elsewhere already years ago, for always giving me this feeling that I am not alone in my situation, mastering my first steps in science, especially: Dennis Häfner, Hanna Kellermann, Matthias Kurz, Max Knötig, Uta Menzel.

Here I also want to express my gratitude for having had the chance working together with the late Eckart Lorenz, "father" of the MAGIC telescopes, great scientist and inspiring personality. I think that I am by far not the only one missing his advice.

I also want to acknowledge the excellent work of the MPI workshops. Without their prompt and professional support it would have been impossible to work on the hardware projects presented in this thesis.

I want to thank all members of the MAGIC collaboration. I will always remember MAGIC as excellent example for an international collaboration with everyone working hard and with great ambition, but always keeping this spirit of being a big family. Special thanks go to Markus Gaug for helping me with the implementation of the LIDAR correction code in MARS and the on-site crew Martin Will and Javier Herrera for always helping me out in case of technical problems with the LIDAR on La Palma.

Thanks to everyone with whom I spent time on the island, talking, cooking and keeping the telescopes running, but also enjoying some free time swimming in the sea and eating at Casa Goyo.

I want to thank my old friends from school who did not see me very often in the last years, but still thought about me when meeting or organizing a party even though my participation was often highly uncertain.

Finally, I want to express my deepest thanks to Hanna and my family, especially to my parents Alfred and Brigitte for their unconditional love and support, and for giving me this invaluable feeling that there is a place where I am always welcome, which I can call home.